Carnegie Mellon University
MELLON COLLEGE OF SCIENCE

THESIS

SUBMITTED IN PARTIAL FULFILLMENT OF THE REQUIREMENTS
FOR THE DEGREE OF

DOCTOR OF PHILOSOPHY IN THE FIELD OF PHYSICS

TITLE: "Mysteries of Universe imprinted on Redshifts"

PRESENTED BY: Shadab Alam

ACCEPTED BY THE DEPARTMENT OF PHYSICS

SHIRLEY HO	7/29/16
SHIRLEY HO, CHAIR PROFESSOR	DATE

STEPHEN GAROFF	7/29/19
STEPHEN GAROFF, DEPT HEAD	DATE

APPROVED BY THE COLLEGE COUNCIL

FRED GILMAN	7/29/16
FRED GILMAN, DEAN	DATE

Mysteries of Universe imprinted on Redshift

by

Shadab Alam

Submitted in partial fulfillment of the

requirements for the degree of

Doctor of Philosophy

at

Carnegie Mellon University

Department of Physics

Pittsburgh, Pennsylvania

Advised by Professor Shirley Ho

June 8, 2016

I certify that I have read this thesis and that in my opinion it is fully adequate, in scope and in quality, as a dissertation for the degree of Doctor of Philosophy.

————————————————

Shirley Ho

(Principal Advisor)

I certify that I have read this thesis and that in my opinion it is fully adequate, in scope and in quality, as a dissertation for the degree of Doctor of Philosophy.

————————————————

Rupert A. C. Croft

I certify that I have read this thesis and that in my opinion it is fully adequate, in scope and in quality, as a dissertation for the degree of Doctor of Philosophy.

————————————————

Rachel Mandelbaum

ii

I certify that I have read this thesis and that in my opinion it is fully adequate, in scope and in quality, as a dissertation for the degree of Doctor of Philosophy.

_____

Martin White

Approved for the Carnegie Mellon University Department of Physics:

_____

Head of the Physics Department

iii

To Mom and Dad...

For Eveything

Acknowledgments

Caring is the word I would like to use to describe Carnegie Mellon University's (CMU) physics community. Even in a foreign land, though with a shared desire to learn physics, the CMU community made me feel at home. This thesis is possible only because of the many people who have heard me with patience, appreciated my experiences, validated my identity and allowed me to prosper. This acknowledgement is my attempt to thank constant support I have received. I would like to thank everyone with all my sincerity for making this thesis possible.

Shirley has been the most cheerful advisor I have met. She is very knowledgeable, intelligent, well known, resourceful, and encouraging, which are all the qualities I hoped for in my advisor. She is also very friendly, caring, cheerful and understanding, which were never on my list of expectation as a naive first-year graduate student. She has such high excitement and energy levels that even in the most gloomy days, one feels that all is well. She has been providing insightful direction and support which has shaped each and every chapter of this thesis. She has patiently seen innumerable incomprehensible plots and has painstakingly gone through crude texts of every write-up I produced. One of the very valuable thing in my experience of working with her has been the amount of freedom she provided and the highly interacting working group she has nurtured at CMU. I would like to thank her for inspiring and enabling us to do exciting science.

I would like to thank Rupert Croft and Rachel Mandelbaum, who are not only a part

of my thesis committee but have also continuously guided me during my Ph.D. Rupert has been instrumental in making me see beyond my cynicism and lack of confidence while working on gravitational redshift project. Also, chapter 7, which is the project I enjoyed the most, was developed with the help of his insight and has been the most adventurous research idea in my Ph.D. He was also very patient when for months I was not able to make much progress. I owe thanks to Rachel for her constructive criticism, which helped me develop my writing skills. I have lost count of the number of revisions we have done and the number of flaws I discovered in the initial draft of my project with her. I am inspired by her deep insight into the gravitational lensing studies. She has an eye for details which I can only dream of possessing.

I would like to thank Martin White for being involved with my PhD. from the beginning, even before we met for the first time. He has been instrumental in not only creating the knowledge base on which my thesis rests but also shaping my papers. He patiently went through many of my papers and provided incredibly insightful comments regarding the science as well as the organization of the articles. He also generously became the external member of my thesis committee. I still remember about one of the very first emails I sent to him late in the night, and how he responded almost immediately with profound questions which took me days to understand. Such interactions with Martin not only helped improved my understanding but also motivated me to work harder.

I would like to thank Ayesha for being the rock of Gibraltar of my life. I wonder how I would have managed the ups and downs of graduate life without she being beside me. I am indebted to her for constant support in every aspect. She has worked relentlessly on improving my English speaking and writing skills. She has always been available to talk to me. whether I am sad or happy, sometimes at the cost of her own work. She has listened to me patiently for numerous hours when I excitedly gave long monologues about my research. She is the most interesting person, who can discuss about almost any topic in

seminars, processing our salaries, travel reimbursements, documents requests and many other things which are essential for functioning of the department. Last three years of my graduate life have been an incredibly rewarding journey. I feel delighted to be part of CMU physics community.

I grew up in a small town called Tatanagar in India, which was where a great visionary called Jamshedji Nusserwanji Tata started their first steel plant (Tata Steel) more than 100 years ago. My education was funded by the philanthropic schemes that were undertaken by Tata Steel. I am here because of the dream that this organization has for every child. I also pay regards to all the people who make possible the various scholarships of Govt. of India, which funded my undergraduate education. I want to thank Ramana Athreya, my Master's thesis advisor at IISER Pune, who inspired me to pursue astrophysics, Sutirth Dey for showing me wonders of evolution and adding great value to my undergraduate experience. My graduate degree is supported by CMU physics graduate program and research grants of my mentors. I thank my mentors who worked relentlessly to obtain these highly competitive grants and the funding agencies which made my research possible.

I would like to take this opportunity to thank my mom, dad, sisters and brother. They have always shown me the right path and utmost trust in my abilities. They celebrated each of my small achievements so hard that I felt embarrassed of my laziness and got motivated to work harder. I largely owe the person I am to the values that my parents have cultivated in me.

I would like to end with this last thought. Our research group at CMU is involved in addressing some of the very fundamental questions about the origin, functioning and ultimate fate of the universe. The human race has developed a very neat story of the universe starting from Big Bang 13.7 billion years ago, to the formation of our galaxy, Milky way, our solar system, planets till the origin of life and evolution of human race. This story makes me realize that our existence is insignificant in space and time of the universe, but

the human intellect can reach the vastness of the universe and even beyond. The story of the universe is far from perfect. I am sure my graduate experience will play a significant role in my journey to make the story of the universe a little closer to perfection.

Thank You, Everyone!!

Preamble

FASCINATION is one of the essential qualities which has driven the development of human civilization and knowledge. But it is just the necessary step and is far from sufficient. The combination of fear and fascination motivated humans to start studying the heavens very early on. These efforts produced tremendous excitement when we began to explain what we see with logic and rationality, combined with the rigor of physics. Also, nature turns out to be an amazing scriptwriter enticing the humans at every step with a new mystery. Through centuries of efforts to chase these mysteries, humans have developed an amazingly simple story of the universe with lots of new puzzles to be pursued. My time as a graduate student at Carnegie Mellon University was spent in learning what is already understood about the theory of the universe and trying to chase some of the mysteries. This thesis consists of seven episodes which occurred during my graduate life. I worked on large galaxy redshift surveys in order to extract the information content of redshift to explore the nature of universe and hence the title "Mysteries of Universe imprinted on Redshift".

I will begin by answering a few questions pertaining to a story which fascinates me and is the focus of my research. This is the story of the universe as given by the most successful model of it, which is based on Einstein's general theory of relativity (GR). This story is not yet complete, with many mysteries and details remaining to be worked out.

Our universe started 13.7 billion years ago when the "Big Bang" happened and produced all the energy we see in the universe. Immediately after the big bang the universe

had nothing but pure energy. This event was followed by a time during which our universe expanded faster than the speed of light, for reasons which remain to be understood. After this the universe began to convert energy into other forms like subatomic particles, photons, which led to the creation of an extremely hot and dense plasma. This plasma expanded and eventually resulted in the formation of nuclei and electrons, pairs of which combined and formed the neutral hydrogen (the simplest atom) as the universe expanded and cooled. This marks a remarkable event in the history of the universe and is called recombination. The recombination, which happened almost 0.38 million years after the big bang, was the first time the photons became decoupled from matter and started streaming freely. The radiation of the free flowing photons, called Cosmic Microwave Background (CMB), is the first ever image of the baby universe. The recently concluded NASA/ESA Plank Mission provides the most precise measurement of CMB so far. This also helps us figure out the initial condition of the universe and forms a solid foundation for the current understanding of the story of the universe.

Following this event, the universe was full of neutral hydrogen, whose inherent tiny quantum fluctuations made the universe a playing field for gravity. These small density fluctuations grew exponentially whenever the conditions were conducive and formed balls of hydrogen everywhere. These balls got so dense and hot with time that they initiated the first nuclear fission at the core and turned themselves into stars. This made the other fundamental forces to act, giving them the opportunity to contribute to shaping the universe by creating more and more complex structures. Some stars exploded and cooled down to become white dwarfs while some stars were so massive that they exploded and became black holes, an ultimate trap from where nothing can escape, not even light. Though, quantum mechanics does allow the possibility of Hawking radiations escaping black holes, which is yet to be observed. These black holes, which are singular points in space-time, led to the formation of many more complicated structures like galaxies, galaxy clusters, Quasi-

Stellar Objects (QSO), etc. Some stars in the galaxies formed planets which revolved around them and hence formed a solar system. One of such stars is our sun, and one of its planets is Earth, which had the appropriate conditions to form very complex molecules. These complex molecules finally led to the origin of life on earth, which evolved for many billions of years to the present state in which the most dominant species are the human beings.

It is a fascinating story we have built together about our origin through centuries of scientific efforts. There are two major observations we have with us which can be used to answer many of the questions about universe. The first one is the extremely precise measurement of cosmic microwave background and second one is the millions of galaxies observed as a part of the galaxy redshift surveys. These two together provide excellent data to make the ground for testing the most important prescription of our story, "Gravity". This can be set-up as a standard physics problem where the initial condition (CMB) is provided, and the equations of motion (General Theory of Relativity) is known (thanks to Einstein), and the final state (the galaxy redshift survey) is observed. The initial condition and the equations of motion could be used to predict the final state and checked against observations, which is major part of my thesis.

The data set for my research basically comes from Sloan Digital Sky Survey III (SDSS-III) which has taken images of millions of galaxies and has observed their spectra to infer line-of-sight distances and locate the galaxies in three-dimensional space. These observations are then simplified in terms of summary statistics, which is the two-point correlation function for us. The two-point correlation function basically asks a simple question: what is the probability of finding a pair of galaxies separated by a distance r which subtend an angle θ from line-of-sight. This function helps us study two important physical properties known as Baryon Acoustic Oscillation (BAO) and Redshift Space Distortions (RSD)

BAO is a characteristic scale at which the two-point correlation function shows an ex-

cess probability (similar to camel's hump) and could be used as a standard ruler. The redshift quantifies the wavelength shift in the atomic line of galaxy spectra and hence requires observing galaxys spectral energy distributions (SED). The redshift measured in a spectroscopic survey has two major components. The first is due to the expansion of the universe (recession velocity) which should be used to estimate the line of sight distance and the second is due to the local gravitational interaction (peculiar velocity). In particular, the line of sight distance inferred from the redshift is biased due to the peculiar velocity component of galaxy redshift, which is observed as an anisotropy in the correlation function. The anisotropy observed due to peculiar motion of galaxy is known as Redshift Space Distortions (RSD).

We measure all the parameters of the standard model of cosmology by combining our measurement of galaxy correlation function with Planck CMB measurements. We have also measured the linear growth rate ($f\sigma_8$) at 5.5 billion light years (redshift = 0.57) away from us. The measured $f\sigma_8$ is a measure of the strength of gravity at the epoch of measurement. We arrive at a measurement of $f\sigma_8 = 0.462 \pm 0.041$ (9% accuracy) when we include Planck Cosmic Microwave Background (CMB) likelihood while marginalizing over all the other cosmological parameters.

We have combined our RSD measurements from CMASS sample with $f\sigma_8$ from 6 different surveys between redshifts 0 and 1 to obtain an evolution of growth rate with redshift. These combined measurements were used to analyze different extensions of ΛCDM and modified gravity models. We have showed that these measurements combined could provide current best constraints on dark energy, the curvature of the universe, modifications to gravity and an upper limit on redshift of reionization. It will be good to pause here for a moment and understand the implication of this analysis. The general theory of relativity with minimal cosmological model (ΛCDM) successfully passes with flying colors in predicting the evolution of the universe from the beginning to almost the current universe, that

is over entire cosmic history!

For the past few decades, we have been pushing the noise to lower and lower levels in our measurements. so much so that the curvature of the universe is known to be zero up to three decimal places. The measurements are only going to get better in the next decade with multiple large surveys coming online.

What we have been talking about so far was mostly about the gravitational interactions between matter. Another, important aspect of the theory is to understand the interaction between light and matter. One of the most powerful probes which could tell us about such interactions is called gravitational lensing. It turns out that we can also measure a quantity which probes both the strength of light-matter interaction and matter-matter interaction. We have written three chapters on such measurements. We learned that relative amplitude for the two interactions, a relatively less studied aspect of the theory, is consistent with our measurements at a scale above the size of a galaxy cluster and smaller than ~ 100 Mpc. The theoretical understanding fails at the scale smaller than the size of galaxy cluster due to more complicated baryonic physics. The scales larger than ~ 100 Mpc show inconsistency with our current understanding. This inconsistency might be a hint towards new physics or maybe towards some not well-understood aspect of our measurements. It will be exciting to see what happens with a similar analysis in future.

Galaxies are known to live in dark matter haloes which possess strong gravitational potentials (ϕ). The light emitted from a galaxy experiences gravitational shift $z_g = -\phi/c^2$, as it climbs out of the potential well, in the observed redshift. The gravitational redshift is one of the most fundamental prediction of GR. The manifestation of the phenomenon as mentioned earlier was first observed in a nuclear resonance experiment. The gravitational redshift has also been measured in astrophysical systems, e.g. a red giant star sirius B, in the solar system and in galaxy clusters. We have measured the relativistic effects, dominantly gravitational redshift signal, using the cross-correlation of two galaxy populations with

different masses. This measurement adds another victory to the success story of GR in explaining the observed universe and predicting the unobserved. In this project we extract the information about gravitation potential imprinted on the redshift.

My main goal has been to fill the gaps in the understanding of the story of the universe from the cosmological perspective. These gaps are filled by advancing the measurement to next level of precision and improving the modeling, which is achieved with a better understanding of the theory and will allow us to start making precision test of general theory of relativity at large scale. I hope that better understanding of redshift combined with improved measurements will open new doors towards the unknown.

Preface

This thesis consists of 7 chapters.

Chapters 1-3 have been published, and chapter 4 have been submitted for publication in the Monthly Notices of the Royal Astronomical Society (MNRAS). Chapters 5-7 are papers in preparation to be submitted for publication in next few weeks. I provide brief description of each chapter including details about publication, collaborators and my contribution to each chapter.

Chapter 1: "Testing General Relativity with Growth rate measurement from Sloan Digital Sky Survey III Baryon Oscillations Spectroscopic Survey galaxies"

Alam, S., Ho, S., Vargas-Magaña, M., Schneider, D. P.

2015, Monthly Notices of the Royal Astronomical Society , **453**, 1754, arXiv:1504.02100

This chapter provides a redshift space distortions (RSD) analysis of galaxy clustering using Sloan Digital Sky Survey III (SDSS) Baryon Oscillation Spectroscopic Survey (BOSS) CMASS sample from data release 11. I used a perturbation theory model to measure linear growth rate and also constrain other cosmological parameters especially matter density. I performed the principal analysis and wrote the paper with the help from Mariana Vargas-Magaña and Shirley Ho. When Shirley assigned me this project for the first time, I saw it as a simple regression analysis and underestimated its challenges. This project has helped me learn so many aspect of large scale structure analysis, which is impossible to understand just by reading papers. This also helped me appreciate the work done by the

collaboration a lot more than I did before.

Chapter 2: "Testing deviations from ΛCDM with growth rate measurements from 6 Large Scale Structure Surveys at $z = 0.06$ to 1"

Alam, S., Ho, S., Silvestri, A.

2015, Monthly Notices of the Royal Astronomical Society , **456**, 3743 , arXiv:1509.05034

This chapter looks at the assumptions of ΛCDM and variety of other alternate gravity model in the light of growth rate measurements over last one decade with 6 different galaxy redshift surveys. We provide one of the best constraints for almost all the models considered. We also proposed that a lower τ from CMB could potentially resolve the tension due to lower growth rate observed in the various analysis. I performed the analysis and wrote the paper with the help from Alessandra Silvestri and Shirley Ho. This project gave me the opportunity to sit down and work out some of the modified gravity equations with expert guidance from Alessandra. We also pointed out one issue regarding the understanding of Chameleon gravity parametrization in literature, while working on this project.

Chapter 3: "Probing Gravity at Large Scales through CMB Lensing"

Pullen, A. R., **Alam, S.**, Ho, S.

2015, Monthly Notices of the Royal Astronomical Society , **449**, 4326 , arXiv:1412.4454

This chapter develops the theory for combining galaxy clustering measurements with redshift space distortion and galaxy-CMB lensing cross-correlation to measure E_G. It also provides the forecast for several different modified gravity models and future surveys. I worked on the redshift space distortion and theoretical development of modified gravity aspects in this chapter. This chapter was lead by Anthony Pullen. This project introduced me to the idea of CMB lensing and showed the power of cross-correlation for the first time.

Chapter 4: "Constraining Gravity at the Largest Scales through CMB Lensing and Galaxy Velocities"

Pullen, A. R., **Alam, S.**, He, S., Ho, S.

2015, Monthly Notices of the Royal Astronomical Society , **submitted**, arXiv:1511.04457

This chapter uses the theoretical estimator and models developed in the previous chapter and perform the first measurement of E_G using CMB lensing from Planck and galaxy clustering from SDSS BOSS CMASS sample. In this chapter, I worked on the RSD measurements, error estimation from data using jackknife and mocks. I also worked on developing N-body simulation with HOD with a lot of help from Sebastien Fromenteau, which is used to make theoretical predictions and systematic corrections in the analysis. This chapter was lead by Anthony Pullen. I for the first time used raw N-body simulation output. It provided me the opportunity to handle large simulation files and also learn and implement the process of painting galaxies on simulations.

Chapter 5: "Testing gravity at large scales by combining galaxy-galaxy lensing with redshift space clustering"

Alam, S., Miyatake, H., More, S., Ho, S., Mandelbaum, R.

in preperation

This chapter also measures E_G similar to the previous chapter but using galaxy lensing in place of CMB lensing. We used data from SDSS CMASS sample and CFHTLenS survey. We performed a very detailed systematic error estimates and corrections using N-body simulations. I performed the RSD analysis and clustering measurement. I also worked on populating N-body with HOD and used them to estimate all the systematic corrections. I finally combined all the component to get our final constraint. I learned a lot about lensing systematics while writing this paper with the coauthors especially from Rachel Mandelbaum. This chapter took the shortest time to execute and longest time to write with a great learning experience.

Chapter 6: "Relativistic distortions using the large-scale clustering of massive galaxies in SDSS-III BOSS CMASS sample"

Alam, S., Zhu, H., Croft, R. A. C., Ho, S., Giusarma, E.

in preperation

This chapter provides the first detection of relativistic distortion in large scale structure. We detect line-of-sight asymmetry in the cross-correlation of the two galaxy populations with different halo mass at better than 3σ level. This measurement is the mixture of multiple relativistic effects but dominated by gravitational redshift. I performed this analysis based on the ideas proposed by Rupert Croft in one of his paper using simulations. This project was possible because I had Rupert providing his great insights about relativistic effects and Shirley Ho guiding me through the details of large scale structure catalog. This project made me realize the difficulty and importance of writing multiple independent pipelines providing same answers.

Chapter 7: "Relativistic effects on the Target Selection"

Alam, S., Croft, R. A. C., Ho, S., Zhu, H., Giusarma, E.

in preperation

This chapter discusses the possible effects of galaxy velocity on the target selection due to relativistic Doppler effect and beaming. This study was motivated to answer questions regarding the previous chapter about contributions of sample selection and survey geometry to our observed asymmetry. We found that these effects are quite small and also motivated the forms of such effects in our companion paper (Zhu et. al. 2016) using simulations. We also came up with numbers of galaxies getting affected due to such effects being of the order of 0.2% ($\sim$ 1000 galaxies) of the full sample. I really enjoyed working on this project. This project was one of the most adventurous during my Ph.D. I never understood the big picture in this project until I started writing this chapter. The final story came out of this project was quite simple and intuitively.

Contents

xxiv

List of Tables

List of Figures

Chapter 1

Testing General Relativity with Growth rate measurement from Sloan Digital Sky Survey III Baryon Oscillations Spectroscopic Survey galaxies

Shadab Alam, Shirley Ho, Mariana Vargas-Magaña, Donald P. Schneider

1.1   Abstract

The measured redshift (z) of an astronomical object is a combination of Hubble recession, gravitational redshift and peculiar velocity. In particular, the line of sight distance to a galaxy inferred from redshift is affected by the peculiar velocity component of galaxy redshift, which can also be observed as an anisotropy in the correlation function. This anisotropy allows us to measure the linear growth rate of matter ($f\sigma_8$). In this paper,

we measure the linear growth rate of matter ($f\sigma_8$) at $z = 0.57$ using the CMASS sample from Data Release 11 of Sloan Digital Sky Survey III (SDSS III) Baryon Oscillations Spectroscopic Survey (BOSS). The galaxy sample consists of 690,826 Luminous Red Galaxies (LRGs) in the redshift range 0.43 to 0.7 covering 8498 deg^2. Here we report the first measurement of $f\sigma_8$ and cosmology using Convolution Lagrangian Perturbation Theory (CLPT) with Gaussian streaming model (GSRSD). We arrive at a constraint of $f\sigma_8 = 0.462 \pm 0.041$ (9% accuracy) at effective redshift ($\bar{z} = 0.57$) when we include Planck CMB likelihood while marginalizing over all other cosmological parameters. We also measure $b\sigma_8 = 1.19 \pm 0.03$, $H(z = 0.57) = 89.2 \pm 3.6$ km s^{-1} Mpc^{-1} and $D_A(z = 0.57) = 1401 \pm 23$ Mpc. Our analysis also improves the constraint on $\Omega_c h^2 = 0.1196 \pm 0.0009$ by a factor of 3 when compared to the Planck only measurement($\Omega_c h^2 = 0.1196 \pm 0.0031$). Our results are consistent with Planck ΛCDM-GR prediction and all other measurements using the same data, even though our theoretical models are fairly different. This consistency suggests that measurement of $f\sigma_8$ from Redshift space distortions at multiple redshift will be a sensitive probe of the theory of gravity that is largely model independent, allowing us to place model-independent constraints on alternative models of gravity.

1.2 Introduction

The evolution of our universe appears to be well described by the theory of general relativity(GR) [254, 95]. The predictions appear to be consistent with all the observations except the mysterious accelerated expansion of the universe [306, 262], and the dark matter [417, 178, 316] . The accelerated expansion of the universe proposed in ΛCDM-GR is in good agreement with Baryon Acoustic Oscillation (BAO) [113, 85, 167, 184, 259, 300], Hubble constant [308] and Cosmic Microwave Background (CMB) [39, 268]. Within the

current paradigm, the primordial fluctuations in the early universe were amplified into structures we observe today via gravitational interactions. These gravitational interactions are the sum of the motions of matter and the expansion of the universe. Therefore, one would only need to specify the initial conditions, the spatial geometry and the contents of the universe to use Einstein's theory to predict the large-scale growth rate of the matter density in the universe. We can compare such predictions to the observations in redshift surveys [328, 54, 47, 258, 99]. The velocity field from maps of galaxies in such surveys can be measured because the galaxy redshifts, from which distances are inferred, include components from both the Hubble flow and peculiar velocities from the comoving motions of galaxies. Such surveys thus reveal an anisotropic distribution of objects [84, 252, 320]; the anisotropy in the clustering encodes information about the formation of structure and provides a sharp test of the theory.

In galaxy redshift surveys, the distortion produced in the two-point correlation function due to the peculiar velocity component in the galaxy redshift is known as "Redshift Space Distorion (RSD)". Kaiser [180] first developed a formalism that describes redshift space power spectrum by modifying the linear theory of large scale structure. Hamilton [138] extended this approach to the two-point correlation function in real space. In the seminal work of Scoccimarro [336] describes more general dispersion model, which improves the Kaiser linear model by including higher order terms. Scoccimarro [336] also invoked the concept of general streaming model which was first introduced by Davis and Peebles [95] and further developed by Fisher [119]. A combination of the Lagrangian Perturbation Theory model by Scoccimarro [336] and the Gaussian Streaming model was used to measure the linear growth rate ($f\sigma_8$) of the universe in Baryon Oscillation Spectroscopic Survey [BOSS; 328], which is part of Sloan Digital Sky Survey III [SDSS-III; 115], DR9 [299, 301] and DR11 [324] data releases. Other methods and models of the correlation functions or power spectrum are also used to derive $f\sigma_8$ with BOSS data [77, 48, 159, 327]. Other galaxy

redshift surveys such as 6-degree Field Galaxy Redshift Survey (6dFGRS,[47]), 2-degree Field Galaxy Redshift Survey (2dFGRS,[258]), WiggleZ [54], and VIMOS Public Extragalactic Redshift Survey (VIPERS,[99]) have also measured redshift space distortion at different redshifts.

In this paper we employ a model called Convolution Lagrangian Perturbation Theory with Gaussian Streaming Redshift Space Distortions (hereafter CLPT-GSRSD) to analyze BOSS DR11 [20]. In order to test the model and the analysis method presented in this paper to a high accuracy, we have used a relatively large number of mock galaxy catalogs [222] with clustering properties similar to those of the higher redshift BOSS galaxies. We also provide systematic errors based on the results of analyzing these mock galaxy catalogs. In addition, we have participated in the BOSS galaxy working group Redshift Space Distortion Data Challenges (Tinker et. al. in preperation).

1.3 Theory

In this section we describe the model with which we fit both the mock galaxy catalogs and BOSS data. Throughout the paper, we adopt the standard "plane-parallel" or "distant-observer" approximation, in which the line-of-sight direction to each object is taken to be the fixed direction $\hat{z}$. This approach has been shown to be a good approximation at the level of current observational error bars (e.g., Figure 10 of Samushia et al. [322] or Figure 8 of Yoo and Seljak [403]).

1.3.1 CLPT

Convolution Lagrangian Perturbation Theory (CLPT) is a non-perturbative resummation of Lagrangian perturbation theory [72]. With CLPT, Carlson identified a few terms that asymptote to constants in the large-scale limit and hence need not be expanded with ap-

proximations. The authors showed that CLPT performs better than all the other methods when compared to N-body simulations of dark matter halos. The monopole of correlation function matches N-body up to a very small scale; the quadrupole has less than a few percent error for scale above 20 h^{-1}Mpc (see Figure 1 and 2 of [72]) . Unfortunately, the CLPT doesn't perform well in the quasi-linear regime for the quadrupole of biased tracer (see Figure 5 of [72]). To overcome this problem with the quadrupole for a biased tracer we use CLPT in combination with the Gaussian Streaming Model (GSM) as it has been demonstrated to model the galaxy correlation functions more accurately [386].

1.3.2   The Gaussian streaming model

The Gaussian Streaming Model (GSM) developed by Reid and White [299], fits the monopole and quadrupole of the correlation functions of mock galaxies with a large-scale bias $b \simeq 2$ to the percent level on scales above $25\,h^{-1}$Mpc. This model has been used to interpret the clustering of galaxies measured in BOSS [301, 324, 325].

The GSM is inspired by the Eulerian streaming models. It enforces pair conservation, assuming that the functional form of the halo velocity distribution is Gaussian, centered at μv_{12}, where μv_{12} is mean line of sight velocity between a pair of tracers as a function of their real space separation. Specifically we assume that the redshift-space halo correlation function is

$$1 + \xi^s(s_\perp, s_\parallel) = \int \frac{dy}{\sqrt{2\pi}\sigma_{12}} [1 + \xi(r)] \exp\left\{ -\frac{[s_\parallel - y - \mu v_{12}]^2}{2(\sigma_{12}^2 + \sigma_{FOG}^2)} \right\} , \qquad (1.1)$$

where $\xi(r)$, v_{12} and σ_{12} are provided from an analytic theory. In the model of Reid and White [299], Reid et al. [301] intergrated Lagrangian perturbation theory with scale-dependent but local Lagrangian bias [225] was used for the real-space correlation function ($\xi(r)$) of halos, but the halo infall velocity ($v_{12}(r)$) and dispersion($\sigma_{12}(r)$) were computed

in standard perturbation theory with scale-independent bias. In order to move from halos to galaxies, Reid et al. [301] showed that it suffices to introduce a single additional parameter, σ_{FOG}, akin to the σ in Eq. (1.1). This quantity is taken to be an isotropic, scale-independent dispersion that is added in quadrature to σ_{12} that modifies the scale-dependence of the quadrupole moment on small scales. There are more comprehensive simulation based models for describing the velocity distribution of galaxies around groups and clusters [416] and at large scales [50], but it is relatively difficult to embed them into the halo model to explain the kinematics of the galaxies.

1.3.3 CLPT-GSRSD

The quadrupole prediction on quasi-linear scales from CLPT for a biased tracer is not as accurate as its predictions for N-body simulations. CLPT was further improved by the model proposed by Wang et al. [386], which combines the velocity statistics and correlation function from CLPT with GSM in order to produce a more accurate monopole and quadrupole for biased tracer. This model has less than 5% error in quadrupole for pair separation greater than 20 h^{-1}Mpc for a biased tracer [386]. This model is similar to the Zeldvoich Streaming Model (ZSM) [390] and Lagrangian Streaming Model (LSM) [398]. None of these models has been yet used to interpret the clustering of any galaxy sample. We will be using the analytical model described by Wang et al. [386] to extract constraints on cosmological parameters; we denote this model CLPT-GSRSD.

1.4 SDSS III- BOSS data

We use data included in data releases 10 (DR10;[5]) and 11 (DR11;[9]) of the Sloan Digital Sky Survey (SDSS; [407]). Together, SDSS I, II [1] and III [115] used a drift-scanning mosaic CCD camera [132] to image over one-third of the sky (14555 square degrees) in

five photometric bandpasses [122, 351, 104] to a limiting magnitude of $r < 22.5$ using the dedicated 2.5-m Sloan Telescope [134] located at the Apache Point Observatory in New Mexico. The imaging data were processed through a series of pipelines that perform astrometric calibration [265], photometric reduction [218], and photometric calibration [248]. All of the imaging was reprocessed as part of SDSS Data Release 8 (DR8; [6]). BOSS [96]is designed to obtain spectra and redshifts for 1.35 million galaxies over a footprint covering 10,000 square degrees. These galaxies are selected from the SDSS DR8 imaging and are being observed together with 160,000 quasars and approximately 100,000 ancillary targets. The targets are assigned to tiles using a tiling algorithm that is adaptive to the density of targets on the sky [61]. Spectra are obtained using the double-armed BOSS spectrographs [349]. Each observation is performed in a series of 900-second exposures, integrating until a minimum signal-to-noise ratio is achieved for the faint galaxy targets. This ensures a homogeneous data set with a high redshift completeness of more than 97% over the full survey footprint. Redshifts are extracted from the spectra using the methods described in Bolton et al. [65]. A summary of the survey design appears in Eisenstein et al. [115], and a full description is provided in Dawson et al. [96].

We use the CMASS sample of galaxies [65] from data release 11 [9]. The CMASS sample has 690,826 Luminous Red Galaxies (LRGs) covering 8498 square degrees in the redshift range $0.43 < z < 0.70$, which correspond to an effective volume of 6 Gpc^3.

1.5 Investigating the Systematics Budget

In this section we will examine possible sources for the systematics. We will first describe the result of fitting PTHalo mocks and then the systematic introduced by various approximations used in the analysis. We will conclude this section by describing the possible observational systematics.

1.5.1 Mock Galaxy catalogs

To validate CLPT-GSRSD we have used mock catalogs derived from N-body simulations. Such validations have been performed by Wang et al. [386] in the paper in which they were introduced. However, our goal is to test the model for mock galaxies with properties similar to those of BOSS galaxies at $z \simeq 0.5$.

The perturbation theory mock (PTHalo mock) is generated by populating matter field of second order Lagrangian perturbation theory and calibrating the masses of dark matter halos by comparing it to detailed numerical simulations [337, 222]. We are using the PTHalo mocks generated and validated by Manera et al. [222] for DR11 footprint of SDSS-III survey. There are 600 PTHalo mocks available, which we employed to validate the model and decide upon some constraints on the model parameters. The simulations used to produce PTHalo mocks cover the same volume as that of the CMASS sample. These mocks are designed to have a bias similar to the bias of CMASS sample. It is important to note that both, mocks and our model, are based on similar kind of perturbation theory.

1.5.2 Fitting PTHalo mocks

We have examined the result of fitting 600 PTHalo mocks. We fixed the cosmology while fitting these mocks because we precisely know the cosmology of simulation. The mocks are constructed in such a way that they mimic the CMASS sample . We have computed the monopole and quadruple of correlation function for each of the 600 mocks using Landy-Szalay estimator [194] with bins of 8 h^{-1}Mpc in pair separation. The monopole and quadruple are fit with the CLPT-GSRSD model for fixed fiducial cosmology and three freely-floating RSD parameters, $\{F', F'', f\}$, where the parameters represent the first and the second order Lagrangian bias and the derivative of logarithm of the growth factor, respectively. Figure 1.1 shows the result of fitting 600 PTHalo mocks using CLPT-

8

GSRSD model. The top panel demonstrates that we recover the expected value of $f = d(\ln D)/d(\ln a)$ within a few percent for the entire range of s_{min} shown in the figure. The bottom panel reveals that the $\chi^2/d.o.f$ increases as we include smaller scales in the fit. The solid blue lines in these plots are the mode of the results from 600 mocks and the shaded region corresponds to 1σ limit. We have also performed this analysis with bins of 2 h^{-1}Mpc in monopole and quadruple and found similar results. Wang et al. [386] has shown that the prediction of correlation function by CLPT-GSRSD agrees at few percent level down to $r = 15$ h^{-1}Mpc with N-body simulation. We have used 30 h^{-1}Mpc as minimum fitting scale on the basis of results from N-body simulation and our fit to the mocks as shown in Figure 1.1.

Figure 1.2 demonstrates that the observed scatter in the parameter produced by fitting the mocks is completely consistent with the model degeneracy. The black points are the best fit obtained from the mock (some of the mocks are outside of the region shown in the plot). The red dashed contours in the figure are an estimate of the model degeneracy. We have evaluated the theoretical correlation function on the 100×100 grid in the region covered in Figure 1.2. We have used correlation function evaluated for $F' = 1.0$ and $f = 0.76$ as the reference model to evaluate the χ^2 at each point of the grid using the covariance matrix evaluated from the mocks. The $\chi2$ surface constructed in this manner should reveal the degeneracy of the model. The red dashed line in Figure 1.2 represents the contour of χ^2 while using fitting scale 30 h^{-1}Mpc $< s < 126$ h^{-1}Mpc. We designate this as model degeneracy and show that almost all the scatter in the mocks can be explained by the model degeneracy. We have found 17 mocks with $F\prime < 0.8$ (outliers). The χ^2/dof for the outlier mocks is relatively high. The mean of quadruple moment of these mocks shows stronger variation around $r = 100$ h^{-1}Mpc.
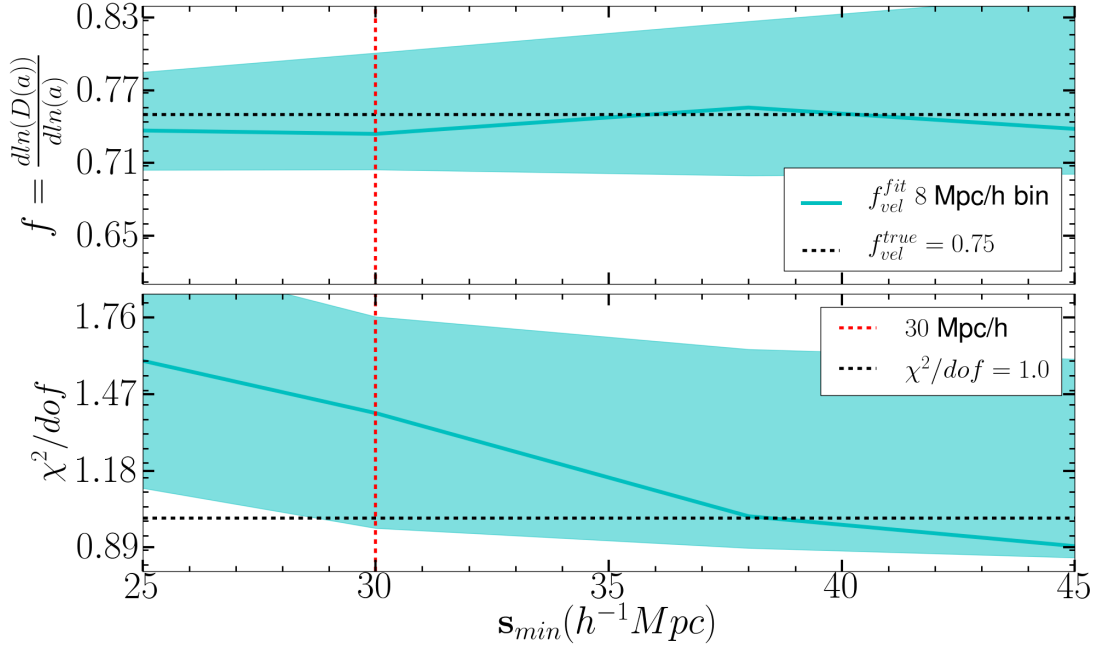
Figure 1.1: The result of fitting 600 PTHalo mocks. The two panels show the mode and 1σ spread of $\{f, \chi^2/dof\}$ as the function of s_{min} minimum scale used for fitting the correlation function. In the top panel for f, we recover the expected value of the parameter within a few percent. The vertical dashed line indicates the minimum scale used in this paper $s_{min} = 30$ h^{-1}Mpc. The lower panel demonstrates that the model and data do not agree as we move to smaller(more non-linear) scale
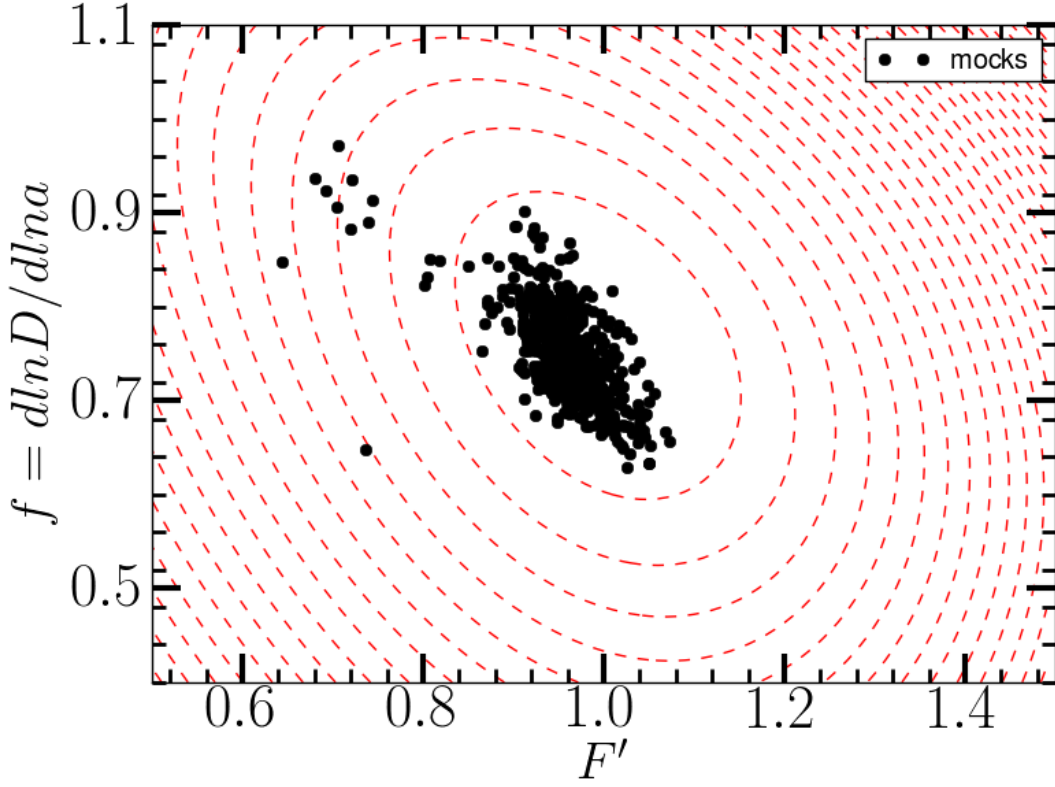
Figure 1.2: The scatter shown by black points is the result of fitting 600 PTHalo mocks. Seven out of 600 mocks showed best fit which is outside the region shown in the plot. The red-dashed contour lines represent the model degeneracy. This plot demonstrates that most of scattering in the mock can be explained by the model degeneracy. We have found 17 outlier mocks with $F\prime < 0.8$ and relatively high χ^2.

Table 1.1: The shift in the parameter $\{f\sigma_8, \alpha_\parallel, \alpha_\perp\}$ for each weight application from the default of applying all weights in units of error on the parameter. The stellar weight is most important for the full shape analysis.

Weights	$\Delta f\sigma 8/\sigma_{f\sigma_8}$	$\Delta\alpha_\parallel/\sigma_{\alpha_\parallel}$	$\Delta\alpha_\perp/\sigma_{\alpha_\perp}$
$w_{star} * (w_{cp} + w_{zf} - 1)$	−0.03	0.02	0.03
$w_{see} * (w_{cp} + w_{zf} - 1)$	0.54	0.82	0.12
$w_{cp} + w_{zf} - 1$	0.51	0.82	0.13
w_{zf}	0.79	0.71	-0.20
w_{cp}	0.44	0.94	0.36
None (uniform weighting)	0.72	0.82	0.06

1.5.3 Observational effects

There are several possible sources of observational systematics in the measurement of correlation function. These systematics have been studied in great detail for the SDSS DR9 and DR11 samples in Ross et al. [312], Anderson et al. [23, 20]. They have introduced two different systematic weights to reduce the cross correlation of ξ_l with the star density, seeing and sky brightness. We have adopted the weights w_{star} and w_{see} in our measurement to remove these systematic effects. We have also used the weights to account for redshift failure (w_{zf}) and close pairs (w_{cp}). w_{cp} accounts for the fact that the spectrum of only one of the galaxies is observed for galaxies separated by less than 62" due to the finite size of fiber fittings. Ross et al. [312] demonstrates that these weights don't change the cosmological result for Baryon Acoustic Oscillation (BAO) but do remove the systematic effects in the measurement of ξ_l and improve the goodness of fit. Ross et al. [312] have also shown that ξ_l for scales above $150\,\mathrm{h}^{-1}\mathrm{Mpc}$ has a systematic error larger than the statistical error. This issue is not a concern for our study because our maximum scale of interest is $126\,\mathrm{h}^{-1}\mathrm{Mpc}$.

We have also examined the effect of using different weighting on the measured RSD parameters (similar to Osumi and Ho [245]). We have calculated the correlation function with different weighting, these correlation functions are fit for RSD and BAO parameters

$\{f\sigma_8, bias, \sigma_{FOG}, \alpha_\parallel, \alpha_\perp\}$. Table 1.1 lists the observed shift compared to the default case of using all weights. The stellar weight has the important effects in our measurements. If we do not use any weights the shifts are of the order of 1σ for $f\sigma_8$ and $\alpha_\parallel$ but is small for $\alpha_\perp$.

1.6 Analysis

In this section we describe the steps of our analysis starting from galaxy position to the parameter constraints. We first briefly mention the different steps then elaborate on the procedure in the following subsections.

We first measure the galaxy correlation function using SDSS-DR11 (CMASS) galaxy sample. We have used 600 PTHalo mocks to generate an estimate of the covariance matrix. We start our optimization problem with nine-dimensional parameter space consisting of four cosmological parameters and three RSD parameters, and run Markov Chain Monte Carlo(MCMC) to explore this parameter space using COSMOMC [202]. In every MCMC step, we first evaluate the Planck likelihood, and then evaluate the linear power spectrum for the current sampled(grid) point if it has not been evaluated previously. This linear power spectrum is fed to the CLPT theory to calculate the correlation function($\xi(r)$) and velocity statistics. The CLPT $\xi(r)$ and velocity statistics are used by the Gaussian streaming model GSRSD with the three RSD parameters to evaluate the redshift space two-dimensional correlation function. This two-dimensional correlation function is rescaled according to the difference in the fiducial cosmology and the current MCMC cosmology to determine the final model correlation function. The final correlation function is used as the theoretical model (CLPT-GSRSD) to calculate the χ^2_{RSD} with data correlation function and mock covariance matrix. The χ^2_{RSD} is converted to a likelihood, which is multiplied to the Planck likelihood in order to calculate the total likelihood, which is maximized using COSMOMC.

The basic approach is to estimate the cosmological parameters by fitting the monopole and quadrupole of correlation function from SDSS CMASS DR11 using the correlation function of CLPT-GSRSD in combination with Planck likelihood computed from CMB power spectrum.

1.6.1 Measuring the correlation function and covariance matrix

We first assumed the fiducial cosmology as flat ΛCDM-GR cosmological model with $\Omega_m = 0.274$, $H_0 = 0.7$, $\Omega_b h^2 = 0.0224$, $n_s = 0.95$ and $\sigma_8 = 0.8$ [20] in order to convert observed celestial coordinates (α, δ) and redshift to the position of the galaxy in three-dimensional space. These galaxy positions are used to estimate the two point statistic (correlation function) of the galaxy using the minimum variance estimator Landy-Szalay estimator [194].

$$\hat{\xi}(\Delta r) = \frac{DD(\Delta r) - 2DR(\Delta r) + RR(\Delta r)}{RR(\Delta r)} \tag{1.2}$$

where DD, DR and RR represent weighted pair count of galaxy, cross pair count of galaxy-random and pair counts of randoms, respectively. We used $w_{tot} = w_{fkp}w_{star}w_{see}(w_{cp} + w_{zf} - 1)$ to weight each galaxy, as described in Anderson et al. [20] to account for systematic and minimize variance. The correlation function is function of r, which is the distance between a pair of galaxies and $\mu = cos(\theta)$, where θ is the angle between separation vector and line of sight. We compress the information by projecting the correlation function to the Legendre polynomial $L_l(\mu)$ of order l as follows.

$$\hat{\xi}_l(r) = \frac{2l+1}{2} \int_{-1}^{1} d\mu \hat{\xi}(r, \mu) L_l(\mu) \approx \frac{2l+1}{2} \sum_k \Delta\mu_k \hat{\xi}(r, \mu) L_l(\mu_k) \tag{1.3}$$

Wang et al. [386] reported that the CLPT-GSRSD model is a good fit to N-body simulation for $l = 0$ and $l = 2$ but not for higher l, therefore, we will limit our analysis up to

$l = 2$. The signal measured in the correlation function should evolve with redshift due to the evolution of $\sigma_8(z)$, but a good approximation is to use an effective redshift for DR11 sample $\bar{z} = 0.57$ as shown in equation[10-12] of Samushia et al. [324].

To estimate the uncertainty in our measurement of the correlation function, we constructed the covariance matrix using 600 PTHalo mocks. The inverse of the sample covariance estimated form finite number of mocks is a biased estimator. We will adopt the correction for covariance matrix as described in Vargas Magaña et al. [380], Percival [257]. The sample covariance matrix is calculated as follows.

$$\hat{C}_{i,j} = \frac{\sum_{m=1}^{300}(\xi_i - \bar{\xi})(\xi_j - \bar{\xi}) + \sum_{m=301}^{600}(\xi_i - \bar{\xi})(\xi_j - \bar{\xi})}{2 \times 299} \tag{1.4}$$

where $\hat{C}_{i,j}$ represents the covariance between bin i and j and $\bar{\xi}$ is the mean of the mocks and the sum is over different mocks. The corrected inverse covariance matrix is

$$C_{i,j} = (1 - 0.62(2 \times n_{r_{bin}} + 1)/(N_{mock} - 1))\hat{C}_{i,j} \tag{1.5}$$

where N_{mock} is the total number of mocks which is 600 for us, and $n_{r_{bin}}$ is the number of bins of the correlation function used in the analysis.

1.6.2 Parameter space

Our model parameters can be subdivided into two subsets. The first set is of cosmological parameter $(\Omega_b h^2, \Omega_c h^2, n_s, A_s, H_0)$, where Ω_b, Ω_c and H_0 are baryon density, dark matter density and hubble constant, respectively, with h being $H_0/100$. The quantity A_s is the scalar amplitude of primordial power spectrum. This choice of parameters requires us to assume an evolution model in order to evaluate the theoretical model at the galaxy redshift.We want our measurement to be independent of such an assumption, which is nec-

essary to be able to use these results to test various models of gravity. This goal can be accomplished by fixing H_0 to the best fit and allowing two extra parameters, $H(z)$ and $D_A(z)$, at the effective redshift. This can be modeled using Alcock-Paczynski parameters $\alpha_\parallel, \alpha_\perp$. The second set of parameters are the redshift space distortion (RSD) parameters $(F', F'', f, \sigma_{FOG})$, where F', F'' and f represent the first and the second order Lagrangian bias, and the logarithmic derivative of the growth factor, respectively. The parameter σ_{FOG} is an additional isotropic velocity dispersion to account for the finger-of-god effect [299]. The second order Lagrangian bias is not well constrained because it is more important for small scale quadrupole. We have considered two cases. In the first one we have marginalized over F'' with hard prior covering $[-5, 5]$ in the second case we have sampled overdensity ν which determines both F' and F'' using peak background split [390].

$$F' = \frac{1}{\delta_c} \left[a\nu^2 - 1 + \frac{2p}{1 + (a\nu^2)^p} \right] \tag{1.6}$$

$$F'' = \frac{1}{\delta_c^2} \left[a^2\nu^4 - 3a\nu^2 + \frac{2p(2a\nu^2 + 2p - 1)}{1 + (a\nu^2)^p} \right] \tag{1.7}$$

where a = 0.707, p = 0.3 gives the Sheth-Tormen mass function [343], and $\delta_c = 1.686$ is the critical density for collapse. Independent of whether we use peak background split or marginalize over F'', we obtain consistent results .

1.6.3 Calculating Theoretical model

We first calculate the linear matter power spectrum using Code for Anisotropies in the Microwave Background (CAMB) [204]. This approach requires the knowledge of cosmological parameters of the model we are evaluating. The linear power spectrum is then sampled according to the sampling scheme for k described in Appendix 1.9. The sampled power spectra is used to calculate the real space correlation function ($\xi(r)$), pairwise veloc-

ity statistics ($v_{12}(r)$) and the dispersion of pairwise velocity statistics ($\sigma_{12}(r)$) as described in Wang et al. [386] and Carlson et al. [72].

$$1 + \xi(r) = \int d^3q M_o(r, q) \tag{1.8}$$

$$v_{12}(r) = [1 + \xi(r)]^{-1} \int d^3q M_{1,n}(r, q) \tag{1.9}$$

$$\sigma_{12,nm}^2(r) = [1 + \xi(r)]^{-1} \int d^3q M_{2,nm}(r, q) \tag{1.10}$$

$$\sigma_{\parallel}^2(r) = \sum_{nm} \sigma_{12,nm}^2 \hat{r}_n \hat{r}_m \tag{1.11}$$

$$\sigma_{\perp}^2(r) = \sum_{nm} (\sigma_{12,nm}^2 \delta_{nm}^K - \sigma_{\parallel}^2)/2 \tag{1.12}$$

where $M_o(r, q)$,$M_{1,n}(r, q)$ and $M_{2,nm}(r, q)$ are integrals of the CLPT perturbation theory that depend on the linear matter power spectra. The $\hat{r}_n$,$\hat{r}_m$ are unit vectors along the galaxies position vectors. Please refer to Wang et al. [386] for details of these integrals and derivation of these equations.

The real space correlation function and velocity statistics calculated from CLPT together with the RSD parameters are supplied to the Gaussian Streaming Model (GSM) [299] in order to evaluate the redshift space correlation function as follows.

$$1 + \xi^{model}(s_\perp, s_\parallel) =$$

$$\int \frac{dy[1 + \xi(r)]}{[2\pi\sigma_{12}^2(r, \mu)]^{1/2}} \times exp\left\{-\frac{[s_\parallel - r_\parallel - \mu v_{12}(r)]^2}{2\sigma_{12}^2(r, \mu)}\right\} \tag{1.13}$$

$$\sigma_{12}^2(r, \mu) = \mu^2 \sigma_{\parallel}^2(r) + (1 - \mu^2)\sigma_{\perp}^2(r) + \sigma_{FOG}^2 \tag{1.14}$$

17

where $s_\perp$ is the transverse separation in both real and redshift space. The quantities $s_\parallel$ and $r_\parallel$ are the LOS (line of sight) separation in redshift and real space, respectively.

We want our measurement to be independent of any particular model of gravity. This can be achieved by avoiding the use of any model for the evolution of structure formation under the assumption of small deviation from widely accepted ΛCDM-GR. We will model this deviation by using two parameters $(\alpha_\parallel, \alpha_\perp)$ which are defined as follows.

$$\alpha_\parallel = \frac{H_{fiducial}}{H(z_{eff})}, \alpha_\perp = \frac{D_A(z_{eff})}{D_A^{fiducial}} \tag{1.15}$$

We will rescale the model redshift space correlation function to account for this extra distortion as follow.

$$\xi_l^{RSD}(s) =$$

$$\frac{\displaystyle\sum_{|s-s_o|<\Delta s/2} (2l+1)\xi^{model}(\alpha_\parallel s_\parallel, \alpha_\perp s_\perp)P_l(\mu)\sqrt{1-\mu^2}}{\frac{2}{\pi}\text{Number of bins used in sum}} \tag{1.16}$$

where $\{H_{fiducial}, H\}$ and $\{D_A^{fiducial}, D_A\}$ are the hubble expansion rate and angular diameter distance for the fiducial and model cosmology, respectively, $s_o = \sqrt{\alpha_\parallel^2 s_\parallel^2 + \alpha_\perp^2 s_\perp^2}$ and $\Delta s = 5\,\text{h}^{-1}\text{Mpc}$. The above rescaling is simply the application of Alcock-Paczynski effect [16].

1.6.4   MCMC and Likelihood estimation

We use COSMOMC to perform Markov Chain Monte-Carlo likelihood analysis [202] and explore nine-dimensional parameter space. We have four cosmological parameters $\{\Omega_b h^2, \Omega_c h^2, n_s, A_s\}$. These parameters have flat prior centered at best fit value of Planck

with width $\pm 5\sigma_{planck}$ (see Table 1.2). The other set of parameters are five redshift space distortion parameters $\{\nu, f, \sigma_{FOG}, \alpha_\parallel, \alpha_\perp\}$, where ν is overdensity, which determines the first and the second order bias using peak background split relation. When we marginalize over second order Lagrangian bias F'' in place of using the peak background split, then our second set of parameters is replaced by $\{F', F'', f, \sigma_{FOG}, \alpha_\parallel, \alpha_\perp\}$.

We calculate the model monopole and quadrupole of the galaxy correlation function as described in the previous section for each point in the parameter space visited by the MCMC sampler. We have optimized our model evaluations with some assumptions, discussed in the Appendix 1.9, in order to make time per MCMC iteration smaller. The likelihood constraint from RSD is calculated using χ^2 as follows.

$$\chi^2_{RSD} = (\xi_{model} - \xi_{data})^T C^{-1} (\xi_{model} - \xi_{data}) \tag{1.17}$$

$$\mathcal{L}_{RSD} = \exp(-\chi^2/2) \tag{1.18}$$

where $\xi_{model} = [\xi_0^{RSD}; \xi_2^{RSD}]$, $\xi_{data} = [\xi_0^{data}; \xi_2^{data}]$ and C^{-1} is the inverse of corrected covariance matrix calculated from 600 PTHalo mocks. The cosmological parameters are well constrained from Planck satellite CMB data, which are mostly independent of the gravity and growth of structure parameters. Therefore, we will multiply our RSD likelihood by the Planck likelihood to obtain the joint constraint on our parameters.

$$\mathcal{L}_{total} = \mathcal{L}_{planck}\mathcal{L}_{RSD} \tag{1.19}$$

The Planck likelihood is calculated using the constraint reported from planck temperature anisotropy data [274]. The Planck parameter covariance is obtained from the correlation matrix given in Figure 21 of [275]. We employ a multivariate Gaussian approximation

Table 1.2: The list of parameters used in our analysis. For each parameter we provide their symbol, prior range, central value and 1σ error. We report the results of using peak background split to relate the first and second order bias and also the result of using sampling of the two bias independently. The results in both case are consistent. We also list the result when Planck prior is replaced by WMAP prior, which predicts 2% shift in $f\sigma_8$.

Parameter	prior range	Peak background split		First and Second order bias
		with WMAP prior	with Planck prior	with Planck prior
Sampling Parameters				
$\Omega_b h^2 \ldots$	[0.02042 , 0.02372]	0.02267 ± 0.00036	0.02206 ± 0.00026	0.02206 ± 0.00026
$\Omega_c h^2 \ldots$	[0.1041 , 0.1351]	0.1141 ± 0.0021	0.11956 ± 0.00086	0.11956 ± 0.00086
$n_s \ldots$	[0.914 , 1.008]	0.9741 ± 0.0085	0.9614 ± 0.0058	0.9613 ± 0.0058
$log(10^{10}A_s) \ldots$	[2.67 , 3.535]	3.178 ± 0.029	3.093 ± 0.066	3.103 ± 0.070
$\alpha_\parallel$	[0.8 ,1.2]	1.003 ± 0.039	1.051 ± 0.043	1.058 ± 0.047
$\alpha_\perp$	[0.8 ,1.2]	0.997 ± 0.018	1.03 ± 0.016	1.032 ± 0.016
$f = dlnD/dlna$	[0.3 , 1.2]	0.739 ± 0.067	0.747 ± 0.072	0.729 ± 0.073
σ_{FOG}	[0 , 10]	2.26 ± 1.46	1.91 ± 1.28	2.70 ± 1.69
v_{RSD}	[1.5 , 2.0]	1.83 ± 0.038	1.80 ± 0.05	
$F1$	[0.5 , 1.5]			0.93 ± 0.07
$F2$	[0.5 , 1.5]			1.0 ± 1.78
Derived Parameters				
$f\sigma_8$	$\ldots$	0.454 ± 0.041	0.462 ± 0.041	0.453 ± 0.041
$b\sigma_8$	$\ldots$	1.21 ± 0.030	1.194 ± 0.032	1.20 ± 0.032
$D_A(z = 0.57)$	$\ldots$	1356.0 ± 24.0	1400.9 ± 22.7	1403 ± 21.9
$H(z = 0.57)$	$\ldots$	93.4 ± 3.6	89.2 ± 3.6	88.5 ± 3.9
F_{AP}	$\ldots$	0.663 ± 0.033	0.654 ± 0.033	0.651 ± 0.034
$D_V(z = 0.57)$	$\ldots$	2024.5 ± 27.2	2101.4 ± 25.6	2108 ± 29.4

to the full Planck likelihood. This approximation is close to the actual likelihood in the

parameter space in which we are working.

$$\Omega_b h^2 = 0.02207, \Omega_c h^2 = 0.1196, n_s = 0.9616, A_s = 3.098$$

$$C_{planck} = \begin{pmatrix} 1.089\times10^{-7} & -4.501\times10^{-7} & 1.365\times10^{-6} & 3.564\times10^{-6} \\ -4.501\times10^{-7} & 9.610\times10^{-6} & -2.215\times10^{-5} & 1.562\times10^{-5} \\ 1.365\times10^{-6} & -2.215\times10^{-5} & 8.836\times10^{-5} & 2.030\times10^{-5} \\ 3.564\times10^{-6} & 1.562\times10^{-5} & 2.030\times10^{-5} & 5.184\times10^{-3} \end{pmatrix}$$
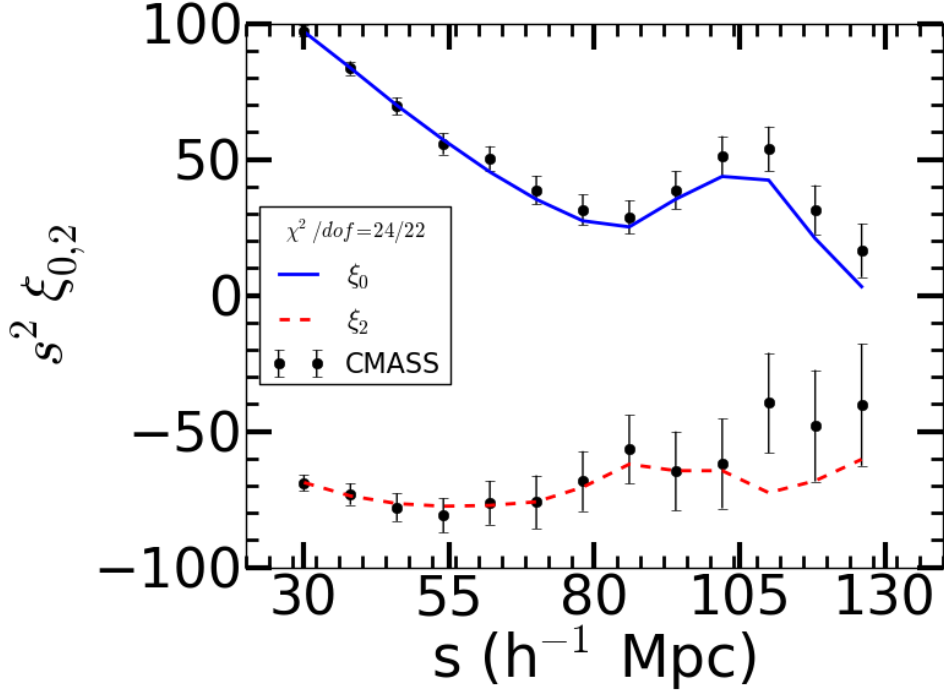
Figure 1.3: This figure shows the projection of two-dimensional correlation function in legendre basis. The black data points are measured correlation function for DR11 CMASS sample and the error bars are the diagonal terms of covariance matrix calculated using 600 PTHALO mocks. The blue and red lines are the best fit monopole and quadruple, respectively, with $\chi^2/dof = 24/22$.

Planck+peak

Planck+F1,F2
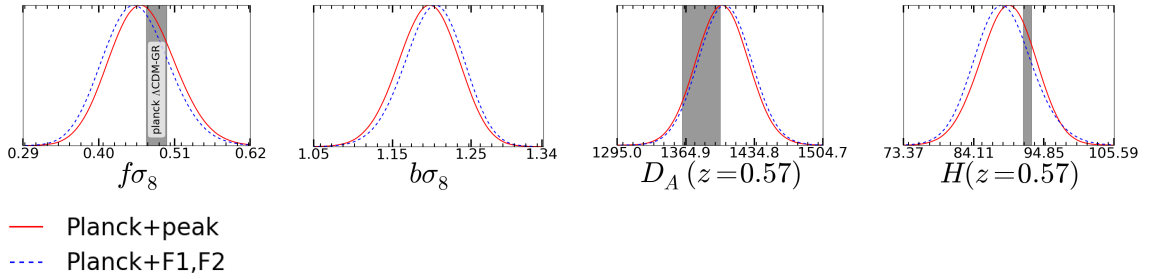
Figure 1.4: The four panels show the one-dimensional marginalized likelihood for the parameters $\{f\sigma_8, b\sigma_8, D_A, H\}$ at effective redshift 0.57 . The red solid line shows the result with peak background split, and the blue dashed line is the result when we fit for both first and second order Lagrangian bias. The grey shaded region shows 1σ constraint from Planck with ΛCDM-GR. We detect 1.9% shift in $f\sigma_8$ and less than 1% for other parameters between the analysis with and without peak background split.

1.7 Results

Figure 1.3 presents the monopole and quadrupole of the galaxy correlation function. The black data points are measurements from BOSS CMASS DR11 galaxy sample. The error bars on the measurements are the diagonal elements of mock covariance matrix. The blue and red lines are the best fit of monopole and quadrupole, respectively, using the fitting range $30 \text{ h}^{-1}\text{Mpc} \leq s \leq 126 \text{ h}^{-1}\text{Mpc}$ with $8 \text{ h}^{-1}\text{Mpc}$ sampling. The best fit $\chi^2/dof = 24/22$ is achieved after marginalizing over essentially all the relevant parameters as listed in Table 1.2. The Figures 1.4 and 1.5 show the one dimensional and two dimensional marginalized likelihood for some of the parameters. The final results of this analysis are given in Table 1.2. We have measured $f\sigma_8(z = 0.57) = 0.462 \pm 0.041$, $b\sigma_8 = 1.19 \pm 0.03$, $D_A(z = 0.57) = 1401 \pm 23$ Mpc and $H(z = 0.57) = 89.2 \pm 3.6$ km s^{-1} Mpc^{-1}. The galaxy correlation function doesn't improve the constraints on the baryon density ($\Omega_b h^2$), scalar spectral index(n_s) and amplitude of primordial curvature perturbation (A_s) at $k_0 = 0.05$ Mpc^{-1}h over the already tight constraints from Planck, however we do improve the measurement of cold dark matter density ($\Omega_c h^2 = 0.1196 \pm 0.0009$) ,which is a 0.7% measurement, this is an improvement in measurement of cold dark matter density compared to Planck ($\Omega_c h^2 = 0.1196 \pm 0.0031$) by a factor of 3.6 . We have also studied the impact of second order bias on growth rate measurement. We found consistent constraint while allowing both of first and second order Lagrangian bias to be free (shown by blue dashed line in Figure 1.4). It is interesting to note that we have found covariance between second order Lagrangian bias (F'') and growth rate. This suggest that a better modeling of higher-order bias including local and non-local contributions (for a recent work along this line, see e.g. Saito et al. [318]) will become more important as the clustering statistics become more precise with future surveys.We have also repeated our analysis by replacing the Planck prior with WMAP prior [39] and found 2% shift in $f\sigma_8$, which is much smaller than the

estimated error.

Our measurement of $f\sigma_8$ is consistent with all the other measurements reported from the same data set, as shown in Figure 1.6. [324] has reported $f\sigma_8(z = 0.57) = 0.44\pm0.044$, which is similar to our analysis. One major difference is in the theoretical model used in the two studies. We have used CLPT-GSRSD to evaluate our model correlation function, whereas Samushia et al. [324] use Lagrangian perturbation theory (LPT) as the model to predict correlation function. Beutler et al. [48] used the monopole and quadrupole of power spectrum and reported $f\sigma_8(z = 0.57) = 0.419 \pm 0.044$, whereas Chuang et al. [77] performs the analysis in configuration space with a different fitting model and obtained $f\sigma_8 = 0.391 \pm 0.044$. Sánchez et al. [327] used wedges to measure the RSD signal and reported $f = 0.719 \pm 0.094$. Reid et al. [302] has done the analysis at small scale 0.8 $h^{-1}Mpc < s < 32 \ h^{-1}Mpc$ with halo occupation distribution model and Planck best fit cosmology and measured $f\sigma_8(z = 0.57) = 0.45 \pm 0.011$. Reid et al. [302] provides the strongest constraint on the growth rate but this analysis has significant modeling and cosmological assumptions. More et al. [235] measured the constraint on Ω_m and σ_8 using a combination of abundance, clustering and galaxy-galaxy lensing. They have reported a constraint on $f\sigma_8$ by assuming the General Relativity linear theory prediction for growth rate ($f = \Omega_m^{0.545}$). Our measurement is competitive with all RSD measurements from large scale.

1.8 Discussion

We have presented an analysis of Redshift Space Distortion (RSD) using the SDSS-III BOSS DR11 CMASS sample, and have measured the monopole and quadruple moments of galaxy auto correlation function at effective redshift of 0.57. We have used CLPT-GSRSD to model the Legendre moments of redshift space galaxy auto correlation function. The
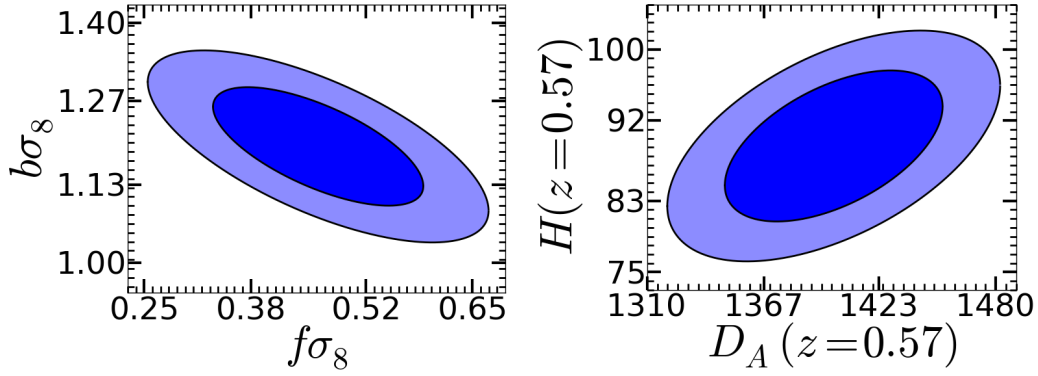
Figure 1.5: Two-dimensional 68% (1σ) and 95% (2σ) confidence limits obtained on $f\sigma_8$—$b\sigma_8$ and D_A—H at effective redshift of 0.57 recovered from Planck CMB and CMASS ($\xi_{0,2}$) datasets with peak background split assumption.
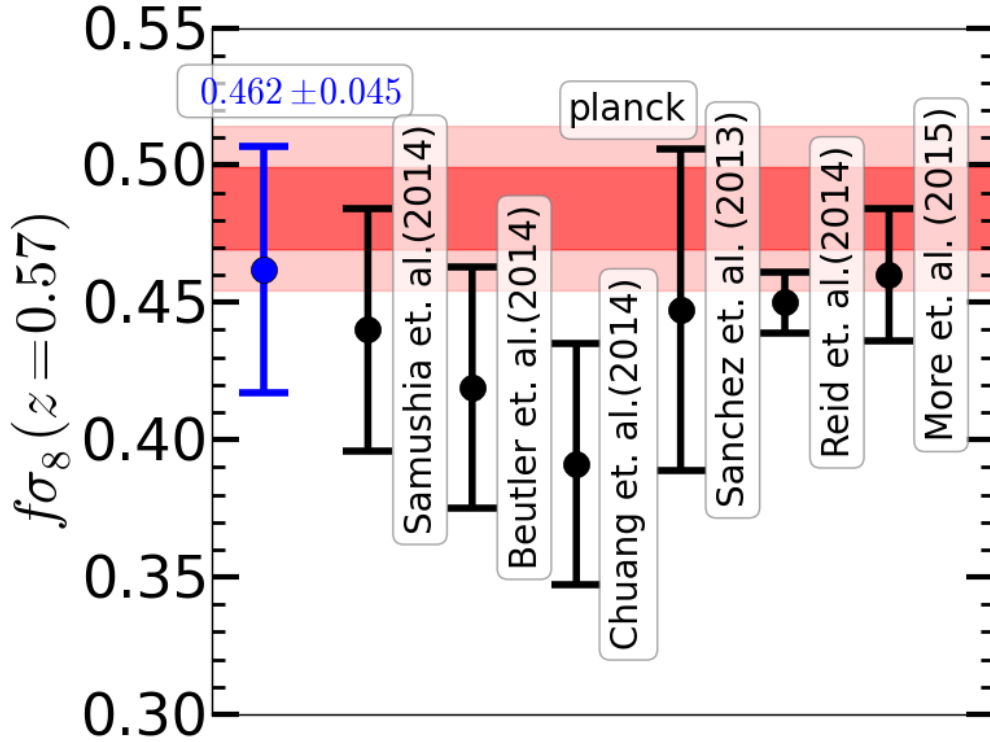
Figure 1.6: Comparison of $f\sigma_8$ with other analysis on the same DR11 CMASS sample. The blue point present the result from our analysis. Our measurement is consistent with other clustering analysis and Planck ΛCDM-GR prediction.

model used here does not work at small scales due to non-linearity, and measurement of correlation function from data shows systematic error at large scales. Therefore, we have adopted a conservative fitting scale between 30 h^{-1}Mpc and 126 h^{-1}Mpc, which we chose with the aid of a suite of perturbation theory mocks. Our measurements of linear growth rate ($f\sigma_8$), angular diameter distance (D_A) and Hubble constant (H) at effective redshift of 0.57 don't assume ΛCDM-GR evolution by virtue of using Alcock-Paczynski parameters ($\alpha_\parallel, \alpha_\perp$) independent of cosmology at current epoch ($z = 0$). This approach makes these measurements suitable to test the predictions of various alternate models of gravity and cosmology.

Our results are consistent with Samushia et al. [324], who performed a similar analysis on the same data set. However, the perturbation theory models used in the two analyses are different. Our model (CLPT) performed better on N-body simulation compared to the Lagrangian Perturbation Theory (LPT) model used in Samushia et al. [324], . We have seen marginal improvement in the measurement uncertainty compared to the previous analyses. This is the first use of CLPT-GSRSD to measure both cosmology and growth from the galaxy redshift survey. It has been used by Howlett et al. [159] to measure the growth rate with fixed cosmology for SDSS main galaxy sample. We couldn't use our model at smaller scales because our mocks cannot be trusted in this range. In the future we may be able to extend this model to scales as low as 20 h^{-1}Mpc if a reliable technique to test them on realistic mocks can be developed.

The linear growth factor has been measured in many redshift surveys between redshift of 0 and 1. Our measurement provides an important data point to study the evolution of the linear growth factor with redshift. The absolute value of $f\sigma_8$ and its evolution with redshift is quite sensitive to the model of gravity. These measurements will provide a good test of the general theory of relativity and the standard model of cosmology on the largest distance and time scales. It is possible to use these measurements to constrain flatness of

the universe and the dark energy equation of state parameter. These measurements also have the ability to constrain the parameters of alternate theories of gravity and dark energy.

The next-generation surveys are going to be even more powerful, which will provide better measurement of correlation function and measurement of $f\sigma_8$, hence better understanding of cosmology and gravity. The error in the measurement of the correlation function is much smaller at small scales, which has not yet been explored in this paper due to our inability to test the theoretical model in this range. We can tap into the potential of small-scale clustering using RSD measurement when we can model the nonlinear clustering at small scale either analytically or using fast simulations.

26

Dame/JINA Participation Group, Johns Hopkins University, Lawrence Berkeley National Laboratory, Max Planck Institute for Astrophysics, Max Planck Institute for Extraterrestrial Physics, New Mexico State University, New York University, Ohio State University, Pennsylvania State University, University of Portsmouth, Princeton University, the Spanish Participation Group, University of Tokyo, University of Utah, Vanderbilt University, University of Virginia, University of Washington, and Yale University.

1.9   Appendix A: Improving the efficiency of MCMC

The most computationally expensive part of likelihood analysis is the calculation of CLPT correlation function and velocity statistics. In order to make this high dimensional optimization problem reasonably efficient, we have adopted two modifications. First we optimized the sampling of k in the linear power spectrum used as the input to the CLPT perturbation theory. Second , we have discretized a small subspace of the parameter required for the perturbation theory in order to avoid doing almost the same calculation thousands of times.

1.9.1   Power Spectrum Sampling

The CLPT's runtime depends on the number of k points sampled in linear power spectrum. However, if we reduce the sampling of power spectrum too much, the integrals involved in the CLPT theory might not converge. Therefore, we need to minimize the sampling in k to reduce the calculation time but keep the sampling sufficiently high to avoid the convergence problem. We have run an optimization of the sampling in k by checking the convergence of the correlation function produced by CLPT and achieved the best case runtime of about 1 min for CLPT correlation function, which doesn't have any convergence issues in the scale of interest, which is up to $130 \, \mathrm{h}^{-1}\mathrm{Mpc}$.
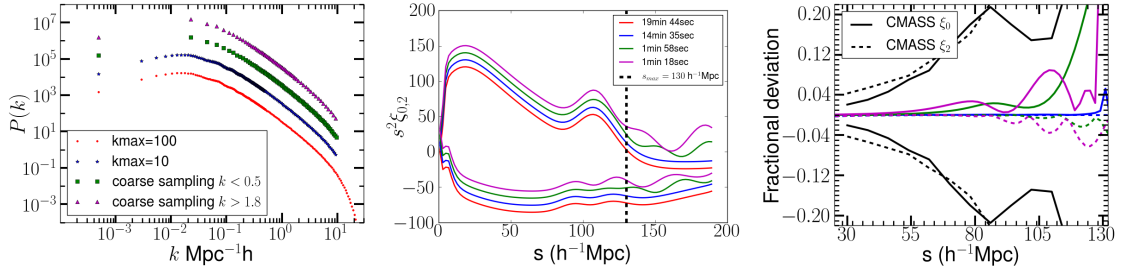
Figure 1.7: Input power spectrum and output correlation function for four different run times . The power spectrum and correlation functions are vertically shifted in order to show the changes clearly. It is clear from the curves that as we sample the power spectrum more sparsely the correlation function does not converge at large scale. This result decides our maximum fitting scale as 126 h^{-1}Mpc for this analysis. The lower panel shows the fractional deviation of correlation function from the completely converged (red line) correlation function. The solid lines represents monopole and the dashed lines quadruple. The black line demonstrates the fractional error in our measurement. The error in theoretical model is much smaller than the measurement error.

We start with the finely-sampled power spectrum and $k_{max} > 100$ Mpc^{-1}h. The initial power spectrum (Figure 1.7 shown in red) has linear sampling for $k < 0.5$ with 1030 points. The sampling is logarithmic for $k > 0.5$ with 500 points until $k_{max} = 100$. The CLPT takes 20 minutes to run with this sampling of power spectrum. The correlation function converges until $r = 200$ h^{-1}Mpc with the above mentioned sampling. We start with this power spectrum and attempt to resample it in such a way that the run time decreases without introducing any error within the scale of interest which is assumed to be $r < 130$ h^{-1}Mpc. The results of this optimization are summarized in Figure 1.7.

Figure 1.7 shows the power spectra, which are vertically shifted for clarity. As we reduce the sampling of linear matter power spectrum, the computation time (shown in the legend of correlation function panel) decreases. As we reduce the sampling in k the correlation function fails to converge for large scale. The fastest runtime (1min 18 seconds) produces a correlation function that doesn't converge above 130 h^{-1}Mpc. The corresponding sampling of linear matter power spectrum is as follows (shown in purple in Figure 1.7):

$$\mathbf{k < 0.5} : \text{linear sampling, 150 points}$$

$$\mathbf{0.5 < k < 1.8} : \text{logarithmic sampling, 90 points}$$

$$\mathbf{1.8 < k < 10} : \text{logarithmic sampling, 90 points}$$

1.9.2   Discretizing a subspace of the full parameter space

We wish to perform the likelihood minimization on the full parameter space of Planck and RSD parameters. This approach creates a nine-dimensional parameter space, which requires millions of likelihood evaluations; hence, the perturbation theory best case runtime of 1 minute is still too long to achieve convergence in a reasonable time with feasible computing resources.The CLPT, however, depends only on the input linear power spectrum which is the function of four cosmological parameters $\{\Omega_b h^2, \Omega_c h^2, n_s, H_0\}$. Therefore, we can significantly reduce the number of evaluations of the CLPT correlation function if it is done on the subspace of the full nine-dimensional parameter space. In order to avoid evaluating the CLPT repeatedly for the same cosmology, we have discretized the four-dimensional subspace and run the CLPT calculation only once for each grid in this subspace. Any repetitive call of CLPT for the same grid point will use the stored result from the previous evaluation for that grid point, Significantly increasing the speed of the entire optimization problem.

Chapter 2

Testing deviations from ΛCDM with growth rate measurements from 6 Large Scale Structure Surveys at z $= 0.06$ to 1

Shadab Alam, Shirley Ho and Alessandra Silvestri

2.1 Abstract

We use measurements from the Planck satellite mission and galaxy redshift surveys over the last decade to test three of the basic assumptions of the standard model of cosmology, ΛCDM: the spatial curvature of the universe, the nature of dark energy and the laws of gravity on large scales. We obtain improved constraints on several scenarios that violate one or more of these assumptions. We measure $w_0 = -0.94 \pm 0.17$ (18% measurement) and $1+w_a = 1.16\pm0.36$ (31% measurement) for models with a time-dependent equation of state, which is an improvement over current best constraints [27]. In the context of modified

gravity, we consider popular scalar tensor models as well as a parametrization of the growth factor. In the case of one-parameter $f(R)$ gravity models with a ΛCDM background, we constrain $B_0 < 1.36 \times 10^{-5}$ (1σ C.L.), which is an improvement by a factor of 4 on the current best [401]. We provide the very first constraint on the coupling parameters of general scalar-tensor theory and stringent constraint on the only free coupling parameter of Chameleon models. We also derive constraints on extended Chameleon models, improving the constraint on the coupling by a factor of 6 on the current best [157] . The constraints on coupling parameter for Chameleon model rule out the value of $\beta_1 = 4/3$ required for $f(R)$ gravity. We also measure $\gamma = 0.612 \pm 0.072$ (11.7% measurement) for growth index parametrization. We improve all the current constraints by combining results from various galaxy redshift surveys in a coherent way, which includes a careful treatment of scale-dependence introduced by modified gravity.

2.2   Introduction

Since its development a century ago, General Relativity (GR) has consistently provided a very successful framework to describe the evolution of our Universe [254, 95]. Nowadays, the prediction of GR for the growth of the large scale structure that we observe around us, is reaching great precision as cosmic microwave background (CMB) measurements are providing us with impressively accurate estimates of the cosmological parameters [282]. Yet, the excitement about the advances of observational cosmology is accompanied by the awareness that we face some major challenges. While the standard cosmological model, based on the laws of GR, provides a very good fit to existing data, it relies on a universe of which we understand only $\sim 5\%$ of the content. The remaining energy budget comes in the form of dark matter ($\sim 27\%$), responsible for the clustering of structure, and the cosmological constant Λ [110] ($\sim 68\%$), responsible for the phase of accelerated expan-

sion recently entered by the universe. In particular, the physical understanding of cosmic acceleration represents one of the most important challenges in front of modern physics. While Λ is in good agreement with available data, e.g. baryon acoustic oscillations (BAO) [113, 85, 167, 184, 259, 300, 27, 21, 24], Supernovae [261, 88, 129, 365, 309], and CMB (Planck Collaboration et al. [282], WMAP9 Bennett et al. [39]) observations, it suffers from the coincidence and fine tuning problems [388, 73]. Several alternatives to Λ have been proposed in the two decades since the discovery of cosmic acceleration [306, 262], and they can be roughly divided into two classes. The first class, to which we will refer as *modified gravity* (MG), corresponds to modifications of the laws of gravity on large scales, designed to achieve self accelerating solutions when matter becomes negligible [344, 79]; alternatively, one can introduce a dynamical degree of freedom, commonly dubbed *dark energy* (DE; first coined by [165]), which is smoothly distributed and starts to dominate the evolution of the Universe at late times [92].

Undoubtedly, one of the important tasks for modern cosmologists, is to perform precision tests of the standard model of cosmology (ΛCDM) and identify areas of tension. In a joint effort, one needs also to explore the parameter space of alternative models. Even though with the current constraints from data, any departure from ΛCDM is likely to be small and challenging to detect, we are in a unique position to test GR, and the other assumptions of ΛCDM, to unprecedented precision with modern observational probes. The three basic assumptions of ΛCDM which are popularly tested are the curvature of the universe, the nature of dark energy and the laws of gravitational interaction on large scales. The curvature of the universe can be explored by allowing a curvature density parameter, Ω_K, to be different from zero and free to vary. As for the nature of dark energy, we will focus on smoothly distributed models where it suffices to test for the deviation of the equation of state parameter, w, from -1, which is the value it assumes if the acceleration is driven by Λ. We will consider both a constant w as well as a time-dependent one, resorting to the

popular CPL parametrization in terms of w_0 and w_a, i.e. $w = w_0 + w_a \frac{z}{1+z}$ [76, 208]. Finally, we will explore the nature of gravity by replacing GR with various modified gravity models, including Chameleon-type scalar-tensor theories and popular parametrizations of the growth rate. All these alternatives that we consider in our analysis, affect, in one way or another, the rate at which large scale structures grow. Models of smoothly distributed dark energy, which does not cluster, modify only the background dynamics of the universe, but this still has an impact on the rate at which structure forms. On the other hand, models of modified gravity generally modify both the background and perturbation dynamics, leading to a significant effect on the growth rate.

Modern galaxy redshift surveys, have successfully measured the growth rate using Redshift Space Distortions (hereafter RSD ; Kaiser [180]), which is the distortion induced in the galaxy correlation function by the peculiar velocity component of the galaxy redshift. Hence, on linear scales, RSD offers a handle both on the distribution of matter over-density and peculiar velocity of galaxies. Recent galaxy redshift surveys have provided the measurement of $f\sigma_8(z)$ up to redshift $z = 0.8$, where f is the growth rate, i.e. the logarithmic derivative of the growth factor, and σ_8 is the rms amplitude of matter fluctuations in a sphere of radius 8 h^{-1}Mpc. In this paper, we will test all the three assumptions of ΛCDM listed above using the Planck CMB measurement [267] and latest RSD measurement from BOSS CMASS [12], SDSS LRG [323], 6dFGRS[47], 2dFGRS [258], WiggleZ [53] and VIMOS Public Extragalactic Redshift Survey (VIPERS,[99]) . It is difficult to use the measurement from different surveys as they have different assumptions. We have looked into these assumptions and possible systematic while combining results from the different survey and also proposed a way to test scale dependence for modified gravity models using these results.

2.3 Theory

In exploring the power of RSD data to constrain deviations from the standard cosmological scenario, we consider several alternative models, divided into dark energy models that modify the background expansion history without introducing any clustering degree of freedom, and those that instead modify only the dynamics of perturbations while keeping the background fixed to ΛCDM. In the former case we consider one and two parameter extensions of the standard scenario, corresponding to different equations of state for dark energy or a non zero spatial curvature. More specifically we consider: a wCDM universe, where the equation of state for dark energy is a constant parameter that can differ from the ΛCDM value $w = -1$; a (w_0, w_a)CDM universe, in which the equation of state for dark energy is a function of time and is approximation to exact solutions of the scalar field equation of motion, i.e. the Chevallier-Polarski-Linder (CPL) parameterization $w = w_0 + w_a(1 - a)$; a $o\Lambda$CDM universe which can have a spatial curvature different from zero, parameterized in terms of the corresponding fractional energy density Ω_K. In the case of models that modify the equations for the evolution of perturbations, we analyze Chameleon-type scalar-tensor theories, $f(R)$ gravity and a time dependent parametrization of the growth rate.

We use the publicly available Einstein-Boltzmann solver MGCAMB [157][1] to evolve the dynamics of scalar perturbations and obtain predictions to fit to our data set for all the models considered, except for the (w_0, w_a)CDM case. This latter needs to be treated instead through the PPF module [117] in CAMB [2]. While the implementation of the non-clustering dark energy models is trivial, in the following we shall describe in more detail the implementation of the modified gravity models.

---

[1] http://www.sfu.ca/~aha25/MGCAMB.html
[2] http://camb.info

2.3.1 Scalar-tensor theories

Going beyond simple extensions of the standard model and non-clustering dark energy models, one needs to take into consideration also the modifications to the equations for cosmological perturbations. Given the cosmological probes that we consider in our analysis, it suffices for us to focus on linear scalar perturbations. In this context, it is possible to generally parametrize deviations from the standard cosmological scenario in the dynamics of perturbations by mean of two functions of time and scale introduced in the set of Einstein and Boltzmann equations for metric and matter perturbations. More precisely, in the absence of anisotropic stress, one can write the Poisson and anisotropy equations as follows:

$$k^2\Psi = -\frac{a^2}{2M_P^2}\mu(a,k)\rho\Delta \; , \quad \frac{\Phi}{\Psi} = \gamma_{slip}(a,k) \, , \tag{2.1}$$

where $\rho\Delta \equiv \rho\delta + 3\frac{aH}{k}(\rho+P)v$ is the comoving density perturbation of matter fields and we have selected the conformal Newtonian gauge with Ψ and Φ representing the perturbation to respectively the time-time and space-space diagonal component of the metric. And then combine them with the unmodified Boltzmann equations for matter fields.

We shall focus on scalar-tensor theories where the metric and the additional scalar degree of freedom obey second order equations of motion and will adopt the parametrization introduced in [46] (BZ) to describe the corresponding form of (μ, γ_{slip}), i.e.:

$$\mu = \frac{1 + \beta_1\lambda_1^2\,k^2a^s}{1 + \lambda_1^2\,k^2a^s} \, ,$$

$$\gamma_{\text{slip}} = \frac{1 + \beta_2\lambda_2^2\,k^2a^s}{1 + \lambda_2^2\,k^2a^s} \tag{2.2}$$

where we have adopted the convention of [411] and β_1, β_2 are dimensionless contants representing couplings, λ_1, λ_2 have dimensions of length and $s > 0$ to ensure that at early times GR is recovered. This parametrization gives a very good representation of scalar-

tensor theories in the quasi-static regime, where time derivates of the perturbations to the metric and scalar degree of freedom are neglected with respect to their spatial gradients on sub-horizon scales [411, 158, 98, 18, 345]. This is a good approximation given the observables that we are considering. Additionally, (2.2) sets the evolution of the characteristic lenghtscales of the models to a power law in the scale factor. This is of course a choice of parametrization for the time dependence of the mass scale of the scalar degree of freedom, and other choices are possible. Nevertheless, as we will discuss in the following, it is a good approximation for several scalar-tensor models, and data are not that sensitive to the specific choice of the time dependence.

Equations (2.2) are built-in in MGCAMB and allow to easily extract predictions for scalar-tensor models on a ΛCDM background for different observables, including the growth rate.

2.3.2   Chameleon models

Chameleon models are a class of scalar-tensor theories for which the additional scalar field has a standard kinetic term and is conformally coupled to matter fields as follows:

$$
\begin{aligned}
S = \quad & \int d^4x \sqrt{-\tilde{g}} \left[\frac{M_P^2}{2} \tilde{R} - \frac{1}{2} g^{\tilde{\mu}\nu} (\tilde{\nabla}_\mu \phi) \tilde{\nabla}_\nu \phi - V(\phi) \right] \\
& + S_i \left(\chi_i, e^{-\kappa\alpha_i(\phi)} \tilde{g}_{\mu\nu} \right) ,
\end{aligned} \tag{2.3}
$$

where $\alpha_i(\phi)$ is the coupling between the scalar field ϕ and the i-th matter species. The coupling(s) in general can be a non-linear function(s) of the field ϕ; however, since the value of the field ϕ typically does not change significantly on the time scales associated to the epoch of structure formation, we will assume it to be linear in ϕ. Since we are dealing with clustering of matter in the late universe, it is safe to consider one coupling, i.e. to dark matter; that amounts to neglecting differences between baryons and dark matter, or simply

neglecting baryons, which is safe for the observables under consideration.

In the quasi-static regime, (μ, γ_{slip}) for Chameleon-type theories can be well represented by a simplified version of (2.2) for which:

$$1 + \frac{1}{2}\left(\frac{d\alpha}{d\phi}\right)^2 = \beta_1 = \frac{\lambda_2^2}{\lambda_1^2} = 2 - \beta_2\frac{\lambda_2^2}{\lambda_1^2}, \quad 1 \leq s \leq 4 \tag{2.4}$$

Therefore the effects of Chameleon-type theories on the dynamics of linear scalar perturbations on sub-horizon regimes can be described with good accuracy in terms of three parameters: $\{\beta_1, \lambda_1, s\}$. The last condition in (2.4) is broadly valid for models with runaway and tracking type potentials [411]. Following a convention which is commonly used for $f(R)$ theories, let us express the lengthscale λ_1^2 in terms of a new parameter B_0, which corresponds to the value of the inverse mass scale today in units of the horizon scale [355]:

$$B_0 \equiv \frac{2H_0^2\lambda_1^2}{c^2}, \tag{2.5}$$

so that we will work with $\{\beta_1, B_0, s\}$.

Let us notice that Chameleon theories as defined in action (2.3), have necessarily $\beta_1 \geq 1$. However, in previous analysis of Chameleon models under the BZ parametrization, such theoretical prior has not been generally imposed and a wider range of β_1 has been explored (see e.g. [157, 101]). Hence, in our analysis we will consider both the case with $\beta_1 > 1$ and the case for which β_1 is allowed to be smaller than unity, to facilitate comparison. We will refer to the former as the *Chameleon* model, and the latter as the extended Chameleon model (*eChameleon*). We shall emphasize that we consider the eChameleon as a purely phenomenological model within (2.2), without linking it to action (2.3), since it would not be viable case of the latter. While the eChameleon might correspond to a very special subcase of the parametrization (2.2), it still represents a possible choice for (μ, γ_{slip}) and,

as we will discuss in Section 2.7, it will be interesting to see what data can say about it.

2.3.3 $f(R)$ **gravity**

$f(R)$ theories of gravity correspond to the simple modification of the Einstein-Hilbert action by the addition of a nonlinear function of the Ricci scalar. In the past decade they have been extensively explored as candidate models for cosmic acceleration (see e.g. [344, 98] and references therein). They represent a subcase of the larger class of models described by action (2.3), corresponding to a universal fixed coupling $\alpha_i = \sqrt{2/3}\,\phi$ and are therefore well represented in the quasi-static regime by the functions (2.2) and conditions (2.4). However, the fixed coupling $\alpha_i = \sqrt{2/3}\,\phi$ implies that $\beta_1 = 4/3$ and viable $f(R)$ models that closely mimic ΛCDM have been shown to correspond to $s \sim 4$ [411, 158]. Therefore the number of free parameters in Eqs. (2.2) can be effectively reduced to λ_1, which is then expressed in terms of B_0. The latter is in fact the only free parameter needed to label the family of $f(R)$ models that reproduce a given expansion history, in our case the ΛCDM one, and can be usually reconstructed via the so-called designer approach [355, 289]. Alternatively, one could adopt the recently developed EFTCAMB package for an exact implementation of designer $f(R)$ models that does not rely on the quasi-static approximation [161, 296] [3]. The latter method allows to choose different bacgkround histories, however for the data and cosmology involved in our analysis, MGCAMB provides enough accuracy.

---

[3]http://wwwhome.lorentz.leidenuniv.nl/~hu/codes/

2.3.4 Growth index parametrization of the growth rate

In the cosmological concordance model, as well as in non-clustering dark energy models, the growth rate of structure is well approximated by:

$$f \equiv \frac{d \ln \delta_m}{d \ln a} \approx \Omega_m(a)^{6/11} \tag{2.6}$$

where $\Omega_m(a) \equiv \rho_m(a)/3M_P^2 H^2(a)$, ρ_m is the background density of matter and $\delta_m \equiv \delta\rho_m/\rho_m$. This inspired the following parametrization for deviations in the growth of structure [385, 209, 210]

$$f = \Omega_m(a)^\gamma \tag{2.7}$$

where γ is commonly referred to as growth index (not to be confused with the γ_{slip} defined above, which represents instead the gravitational slip).

The idea behind this parametrization is that of capturing independently in Ω_m and γ the information from, respectively, the expansion and the growth history. Since in our analysis we fix the background to ΛCDM, $\Omega_m(a)$ is determined by that and the only parameter of interest will be γ. While for models of modified gravity and clustering dark energy in general γ will be a function of time and scale, in several cases for the regime of interest it can still be safely approximated by a constant, which can differ significantly from the ΛCDM value. See [210] for more details and some forms of γ in alternative theories of gravity.

In our analysis we will assume γ is constant and explore constraints on it after extracting predictions for the CMB and growth of structure from MGCAMB.
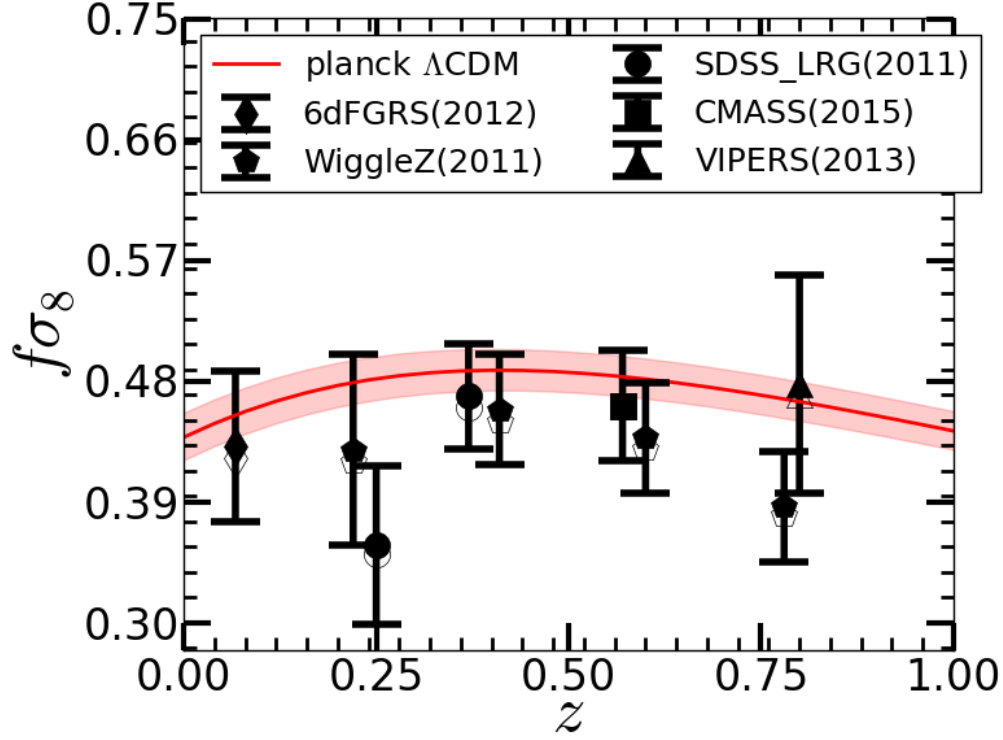
Figure 2.1: The measured $f\sigma_8$ from different surveys covering redshift range $0.06 < z < 0.8$. The empty markers represent the reported measurement of $f\sigma_8$ and the filled markers are for the corrected values for Planck Comsology. The red band shows the Planck ΛCDM 1σ prediction.

2.4 Observations

We use measurements of CMB angular power spectrum (C_l) from Planck 2013 [272] combined with the measurement of $f(z)\sigma_8(z)$ from various redshift surveys covering between $z = 0.06$ to $z = 0.8$ listed in Table 2.1 as our main data points. The Figure 2.1 shows the measurements used with and without corrections and Planck 2013 prediction. We briefly describe each of the surveys and $f\sigma_8$ measurements in the following sections.

Table 2.1: Measurement of $f(z)\sigma_8(z)$ from various galaxy redshift surveys covering redshift between 0.06 to 0.8.

z	$f\sigma_8(z)$	1/k[h /Mpc]	Survey
0.067	0.42 ± 0.05	16.0 –30	6dFGRS(2012)
0.17	0.51 ± 0.06	6.7 – 50	2dFGRS(2004)
0.22	0.42 ± 0.07	3.3 – 50	WiggleZ(2011)
0.25	0.35 ± 0.06	30 – 200	SDSS LRG (2011)
0.37	0.46 ± 0.04	30 – 200	SDSS LRG(2011)
0.41	0.45 ± 0.04	3.3 – 50	WiggleZ(2011)
0.57	0.462 ± 0.041	25 –130	BOSS CMASS
0.6	0.43 ± 0.04	3.3 – 50	WiggleZ(2011)
0.78	0.38 ± 0.04	3.3 – 50	WiggleZ(2011)
0.8	0.47 ± 0.08	6.0 – 35	Vipers(2013)

2.4.1 6dFGRS

The 6dFGRS (6 degree Field Galaxy Redshift Survey has observed 125000 galaxies in near infrared band across 4/5th of southern sky [177]. The surveys covers redshift range $0 < z < 0.18$, and has an effective volume equivalent to 2dFGRS [258] galaxy survey. The RSD measurement was obtained using a subsample of the survey consisting of 81971 galaxies [47]. The measurement of $f\sigma_8$ was obtained by fitting 2D correlation function using streaming model and fitting range 16-30 Mpc/h. The Alcock-Paczynski effect [16] has been taken into account and it has a negligible effect [47]. The final measurement uses WMAP7 [39] likelihood in the analysis. To be able to use this $f\sigma_8$ measurement we need to account for the transformation to the Planck best fit cosmology [267].

2.4.2 2dFGRS

The 2dFGRS (2 degree Field Galaxy Redshift Survey) obtained spectra for 221414 galaxies in visible band on the southern sky [86]. The survey covers redshift range $0 < z < 0.25$ and has a effective area of 1500 square degree. The RSD measurement was obtained by linearly modeling the observed distortion after splitting the over-density into radial and angular components [258]. The parameters were fixed at different values $n_s = 1.0$, $H_0 = 72$. The results were marginalized over power spectrum amplitude and $b\sigma_8$. We are not using this measurement in our analysis for two reasons. First, the survey has a huge overlap with 6dFGRS which will lead to a strong correlation between the two measurements. Second, the cosmology assumed is quite far from WMAP7 and Planck which may cause our linear theory approximation used to shift the cosmology to fail.

2.4.3 WiggleZ

The WiggleZ Dark Energy Survey is a large scale galaxy redshift survey of bright emission line galaxies. It has obtained spectra for nearly 200,000 galaxies. The survey covers redshift range $0.2 < z < 1.0$, covering effective area of 800 square degrees of equatorial sky [54]. The RSD measurement was obtained using a sub-sample of the survey consisting of 152,117 galaxies. The final result was obtained by fitting the power spectrum using Jennings et al. [170] model in four non-overlapping slices of redshift. The measured growth rate is $f\sigma_8(z) = (0.42 \pm 0.07, 0.45 \pm 0.04, 0.43 \pm 0.04, 0.38 \pm 0.04)$ at effective redshift $z = (0.22, 0.41, 0.6, 0.78)$ with non-overlaping redshift slices of $z_{slice} = ([0.1, 0.3], [0.3, 0.5], [0.5, 0.7], [0.7, 0.9])$ respectively. We can assume the covariance between the different measurements to be zero because they have no volume overlap.

2.4.4 SDSS-LRG

The Sloan Digital Sky Survey (SDSS) data release 7 (DR7) is a large-scale galaxy redshift survey of Luminous Red Galaxies (LRG) [115]. The DR7 has obtained spectra of 106,341 LRGs, covering 10,000 square degree in redshift range $0.16 < z < 0.44$. The RSD measurement was obtained by modeling monopole and quadruple moment of galaxy auto-correlation function using linear theory. The data was divided in two redshift bins: $0.16 < z < 0.32$ and $0.32 < z < 0.44$. The measurements of growth rate are $f\sigma_8(z) = (0.3512 \pm 0.0583, 0.4602 \pm 0.0378)$ at effective redshift of 0.25 and 0.37 respectively [323]. These measurements are independent because there is no overlapping volume between the two redshift slices.

2.4.5 BOSS CMASS

Sloan Digital Sky Survey (SDSS) Baryon Oscillation Spectroscopic Survey (BOSS; Dawson et al. [96]) targets high redshift ($0.4 < z < 0.7$) galaxies using a set of color-magnitude cuts. The growth rate measurement uses the CMASS (Reid et al. [298], Anderson et al. [21]) sample of galaxies from Data Release 11 [9]. The CMASS sample has 690,826 Luminous Red Galaxies (LRGs) covering 8498 square degrees in the redshift range $0.43 < z < 0.70$, which correspond to an effective volume of 6 Gpc^3. The $f\sigma_8$ is measured by modeling the monopole and quadruple moment of galaxy auto-correlation using Convolution Lagrangian Perturbation Theory (CLPT; Carlson et al. [72]) in combination with Gaussian Streaming model [386]. The reported measurement of growth rate is $f\sigma_8 = 0.462 \pm 0.041$ at effective redshift of 0.57 [12].

We are also using the combined measurement of growth rate ($f\sigma_8$), angular diameter distance (D_A) and Hubble constant (H) measured from the galaxy auto correlation in CMASS sample at an effective redshift of 0.57 [12]. The measurement and its covariance are given below and it's called eCMASS.

$$f\sigma_8 = 0.46, D_A = 1401, H = 89.15$$

$$C_{eCMASS} = \begin{pmatrix} 0.0018 & -0.6752 & -0.1261 \\ -0.6752 & 550.61 & 45.881 \\ -0.1261 & 45.881 & 14.019 \end{pmatrix} \quad (2.8)$$

2.4.6 VIPERS

VIMOS Public Extragalactic Redshift Survey (VIPERS,[99]) is a high redshift small area galaxy redshift survey. It has obtained spectra for 55,358 galaxies covering 24 square

degree in the sky from redshift range $0.4 < z < 1.2$. The measurement of growth factor uses 45,871 galaxies covering the redshift range $0.7 < z < 1.2$. The $f\sigma_8$ measurement is obtained by modeling the monopole and quadruple moments of galaxy auto-correlation function between the scale 6 h^{-1}Mpc and 35 h^{-1}Mpc. They have reported $f\sigma_8 = 0.47 \pm 0.08$ at effective redshift of 0.8. The perturbation theory used in the analysis has been tested against N-body simulation and shown to work at mildly non-linear scale below 10 h^{-1}Mpc [99].

2.4.7 Planck *CMB*

Planck is a space mission dedicated to the measurement of CMB anisotropies. It is the third-generation of all sky CMB experiment following COBE and WMAP. The primary aim of the mission is to measure the temperature and polarization anisotropies over the entire sky. The Planck mission provides a high resolution map of CMB anisotropy which is used to measure the cosmic variance limited angular power spectrum C_ℓ^{TT} at the last scattering surface. The Planck measurements helps us constrain the background cosmology to unprecedented precision [267, 273, 282]. We are using the CMB measurements from Planck satellite in order to constrain cosmology. We have assumed that Planck measurements is independent of the measurement of growth rate from various galaxy redshift surveys.

2.4.8 Correlation Matrix

We use the measurements of $f\sigma_8$ from 6 different surveys. Although these surveys are largely independent, and in some cases they probe different biased tracers, they are measuring inherently the same matter density field. Therefore, the parts of the survey observing same volume of sky cannot be treated as independent. We have predicted an upper limit
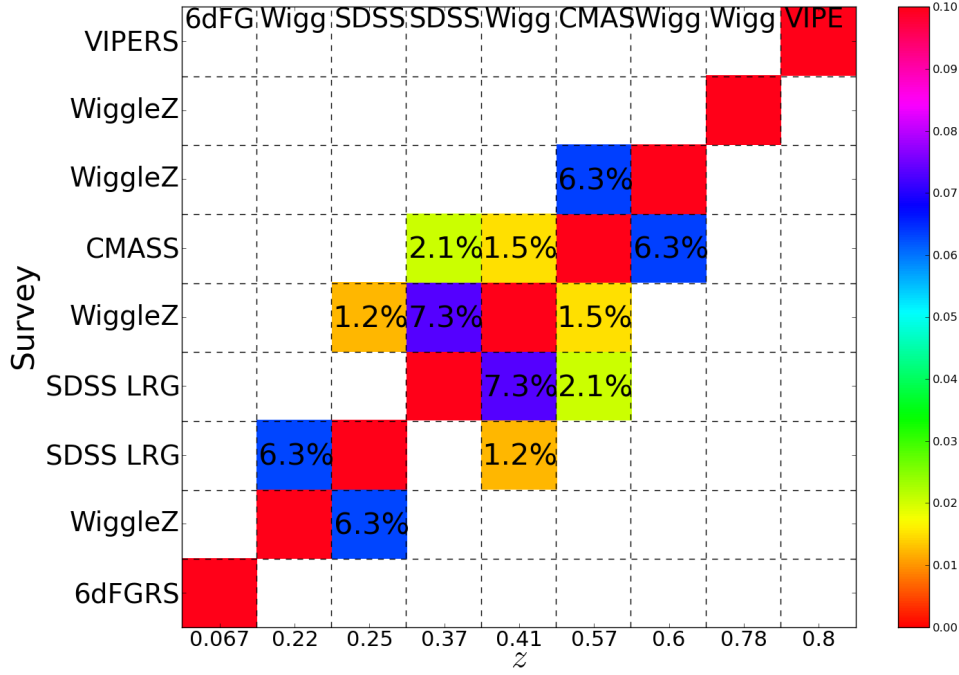
Figure 2.2: Correlation matrix between all the measurements used in our analysis. We have estimated the correlation as the fraction of overlap volume between two survey to the total volume of the two surveys combined.

to the overlap volume using the data from different surveys. We have estimated the fractional overlap volume between any two samples as the ratio of the overlap volume to the total volume of the two samples. We estimate the correlation between two measurements as the fractional overlap volume between the two measurements. Figure 2.2 shows our estimate of the correlation between the surveys. The four measurements of WiggleZ survey cover the redshift range between 0.1 to 0.9 and hence show most correlation with other measurements like SDSS LRG and CMASS in the same redshift range.

2.5 Potential Systematics

The collection of $f\sigma_8$ data points that we are using in this analysis contain measurements from several different surveys, obtained during the last decade, each with a different

pipeline. Furthermore, often the latter implicitly assumes a GR modeling, which does not take into account the different predictions for the growth factor in modified theories of gravity. It is important to account for some crucial differences in order to use these measurements in our analysis. We have looked at following different aspects of measurements and theoretical prediction before using them in our analysis.

2.5.1 Fiducial Cosmology of the growth rate ($f\sigma_8$)

The measurements of $f\sigma_8$ have been obtained over the time when we had transition from WMAP best fit cosmology [146] to the Planck best fit cosmology [267]. Since we are using Planck likelihood [272] in our analysis, we have decided to convert all the measurements to Planck cosmology. The 3 dimensional correlation function can be transformed from WMAP to the Planck cosmology using Alcock-Paczynski effect (Alcock and Paczynski [16]),

$$\xi_{planck}(r_\parallel, r_\perp, \phi) = \xi_{WMAP}(\alpha_\parallel r_\parallel, \alpha_\perp r_\perp, \phi), \tag{2.9}$$

where $\alpha_\parallel$ is the ratio of the hubble parameters ($\alpha_\parallel = H_{planck}/H_{WMAP}$) and $\alpha_\perp$ is the ratio of the angular diameter distances ($\alpha_\perp = D_A^{WMAP}/D_A^{planck}$). The $r_\parallel$, $r_\perp$ are pair separations along the line of sight and perpendicular to the line of sight and ϕ is the angular position of pair separation vector in the plane perpendicular to the line of sight from a reference direction. In practice the correlation function is isotropic along ϕ. We can calculate the corresponding power spectrum by applying Fourier transform to correlation function.

$$P_{planck}(k_{\parallel}, k_{\perp}, k_{\phi}) = \int dr_{\parallel} dr_{\perp} r_{\perp} d\phi \xi_{planck}(r_{\parallel}, r_{\perp}, \phi) e^{-i\vec{k}.\vec{r}} \tag{2.10}$$

$$= \int dr'_{\parallel} dr'_{\perp} \frac{r'_{\perp}}{\alpha_{\parallel} \alpha_{\perp}^2} \xi_{WMAP}(r'_{\parallel}, r'_{\perp}, \phi) e^{-i\vec{k'}.\vec{r'}} \tag{2.11}$$

$$= \frac{P_{WMAP}(k_{\parallel}/\alpha_{\parallel}, k_{\perp}/\alpha_{\perp}, k_{\phi})}{\alpha_{\parallel} \alpha_{\perp}^2} \tag{2.12}$$

The Kaiser formula for RSD gives the redshift space correlation function as $P_g^s(k, \mu) = b^2 P_m(k)(1 + \beta\mu^2)^2$ [180]. Using the linear theory kaiser prediction and the above approximation between WMAP and planck power spectrum, we can get a relation to transform the growth function from WMAP to planck cosmology.

$$\frac{1 + \beta_{planck}\mu'^2}{1 + \beta_{WMAP}\mu^2} = C\sqrt{\frac{P_{planck}(k', \mu')}{P_{WMAP}(k, \mu)}} \tag{2.13}$$

$$= C\sqrt{\frac{1}{\alpha_{\parallel} \alpha_{\perp}^2}} \tag{2.14}$$

where C is the ratio of isotropic matter power spectrum with WMAP and planck cosmology integrated over scale used in β measurement.

$$C = \int_{k_1}^{k_2} dk \sqrt{\frac{P_{WMAP}^m(k)}{P_{planck}^m(k')}} \tag{2.15}$$

where $k'_{(\parallel, \perp)} = k_{(\parallel, \perp)}/\alpha_{(\parallel, \perp)}$ .When right hand side of equaion(2.14) is close to 1, then we can approximate the above equation as follows:

$$\beta_{planck} = \beta_{WMAP} C \frac{\mu^2}{\mu'^2} \sqrt{\frac{1}{\alpha_{\parallel} \alpha_{\perp}^2}} \tag{2.16}$$

The ratio $\frac{\mu^2}{\mu'^2}$ can be obtained using simple trigonometry which gives following equa-

tions, where the last equation is aprroximation for $\alpha_{\parallel}^2 \approx \alpha_{\perp}^2$.

$$\frac{\mu^2}{\mu'^2} = \frac{1}{\alpha_{\perp}^2} \left(\alpha_{\parallel}^2 + (\alpha_{\perp}^2 - \alpha_{\parallel}^2)\mu^2\right) \approx \left(\frac{\alpha_{\parallel}}{\alpha_{\perp}}\right)^2 \tag{2.17}$$

We can substitute equation (2.17) in equation (2.16) in order to get the required scaling for f(growth factor) assuming that bias measured is proportional to the σ_8 of the cosmology used.

$$\beta_{planck} = \beta_{WMAP} C \left(\frac{\alpha_{\parallel}}{\alpha_{\perp}^2}\right)^{(3/2)} \tag{2.18}$$

$$f\sigma_{8 planck} = f\sigma_{8 WMAP} C \left(\frac{\alpha_{\parallel}}{\alpha_{\perp}^2}\right)^{(3/2)} \left(\frac{\sigma_8^{planck}}{\sigma_8^{WMAP}}\right)^2 \tag{2.19}$$

We have tested prediction of equation (2.19) against the measurement of $f\sigma_8$ reported in Table 2 of Alam et al. [12] at redshift 0.57 using both Planck and WMAP cosmology. In principle the bias in the measurements of $f\sigma_8$ should be corrected for the each step of MCMC to the chosen cosmology. But, we choose not to incorporate that and apply only an overall correction. Because the corrections are negligible compared to the error on measurements.

2.5.2   Scale dependence

General Relativity predicts a scale independent growth factor. One of the important features of the modified gravity theories we are considering is that they predict a scale dependent growth factor which has a transition from high to low growth at certain scale which depends on the redshift z and the model parameters. The mesurements we use from the different surveys, assumes a scale-independent $f\sigma_8$ and uses characteristic length scale while analyzing data. In order to account for all these effects we have done our analysis in two

different ways. In the first method, we assume that the measurements corresponds to an effective k and in the second method, we treat the average theoretical prediction over range of k used in $f\sigma_8$ analysis.

Figures 2.11 and 2.12 show the parameters constraint for Chameleon models and $f(R)$ gravity. The grey and red contours result from using two different model predictions to test the scale dependence. The grey contours correspond to the model where we average $f\sigma_8$ over k used in respective $f\sigma_8$ analysis and red contours correspond to $f\sigma_8$ evaluated at $k = 0.2h$ Mpc^{-1}. It is evident from the plots that, at the current level of uncertainty, we obtain very similar constraint and hence do not detect any significant effect of scale dependence of $f\sigma_8$.

2.5.3   Other systematics

The measurements of $f\sigma_8$ are reported at the mean redshift of the surveys. But the galaxies used have a redshift distribution which in principle can be taken into account by integrating the theoretical prediction. This should be a very small effect because the $f\sigma_8(z)$ is relatively smooth and flat (see Figure 2.1 and Huterer et al. [166])for the redshift range of the survey and also because the survey window for every individual measurement is small. Another important point is the assumption of GR based modeling for the measurement. We have looked at the modeling assumption for each of the measurements. All measurements of $f\sigma_8$ except WiggleZ and VIPERS, allow the deviation from GR through Alcock-Paczynski effect [16] which justifies our use of *modified gravity* models. The inclusion of AP in WiggleZ and VIPERS will marginally increase the error on the measurements. Different surveys use different ranges of scale in the RSD analysis. This will be important espe-cially while analyzing *modified gravity* models. To account for the different scales used we evaluate the prediction for each survey averaged over the scale used in the respective

analysis.

2.6 Analysis

We have measurement of $f\sigma_8$ from various surveys covering redshift range 0.06-0.8 (see Table: 2.1). We first correct these measurements for the shift from WMAP cosmology to planck cosmology as described in section(2.5.1). The next step is to evaluate prediction from different modified gravity theories by evolving a full set of linear perturbation equations. The theoretical predictions for $f\sigma_8$ is generally scale and redshift dependent (see section 2.5.2). Therefore, we consider two cases for theoretical prediction: 1) evaluate $f\sigma_8$ at effective k and 2) evaluate $f\sigma_8$ averaged over range of k used in measurements. We also predict C_l^{TT} for different modified gravity theories. Finally we define our likelihood, which consists of three parts one by matching planck temperature fluctuation C_l^{TT} , second by matching growth factor from Table 2.1 and third by using eCMASS data as shown in equation 2.8. Therefore, we define the likelihood as follows:

$$\mathcal{L} = \mathcal{L}_{planck}\mathcal{L}_{f\sigma_8}\mathcal{L}_{eCMASS} \tag{2.20}$$

$$\mathcal{L}_{f\sigma_8} = e^{-\chi^2_{f\sigma_8}/2} \tag{2.21}$$

$$\chi^2_{f\sigma_8} = \Delta f\sigma_8 C^{-1}\Delta f\sigma_8^T \tag{2.22}$$

The $\Delta f\sigma_8$ is the deviation of the theoretical prediction from the mesurement and C^{-1} is the inverse of covariance which has diagonal error for different surveys and correlation between measurement as described in section[2.4.8]. Note that we do not include $f\sigma_8$ from CMASS while using eCMASS with $f\sigma_8(z)$ to avoid double counting. This likelihood is sampled using modified version of COSMOMC [202, 157]. We sample over 6 cos-

51

Table 2.2: The list of extension parameters for all the models used in our analysis. For each parameter we provide their symbol, prior range, central value and 1σ error.

Model	Parameter	prior range	posterior
w**CDM**	w_0	-2.0 - 0.0	-0.873 ± 0.077
$w_0 w_a$**CDM**	w_0	-2.0 - 0.0	-0.943 ± 0.168
	w_a	-4.0 - 4.0	0.156 ± 0.361
$o\Lambda$**CDM**	Ω_k	-1.0 - 1.0	-0.0024 ± 0.0032
Scalar-tensor	β_1	0 - 2.0	1.23 ± 0.29
	β_2	0 - 2.0	0.93 ± 0.44
	$\lambda_1^2 \times 10^{-6}$	0 - 1	0.49 ± 0.29
	$\lambda_2^2 \times 10^{-6}$	0 - 1	0.41 ± 0.28
	s	1.0 - 4.0	2.80 ± 0.84
Chameleon	β_1	1.0 - 2.0	< 1.008
	B_0	0 - 1.0	< 1.0
	s	1.0 - 4.0	$2.27 < s < 4.0$
eChameleon	β_1	0 - 2.0	0.932 ± 0.031
	B_0	0 - 1.0	< 0.613
	s	1.0 - 4.0	$2.69 < s < 4.0$
f(R)	$B_0^{\dagger}$	10^{-10} - 10^{-4}	$< 1.32 \times 10^{-5}$
Growth index	γ	0.2 - 0.8	0.611 ± 0.072

$\dagger$ We have tried using both logarithmic and linear prior on B_0 for $f(R)$ model and obtained similar results for on the upper limit on B_0. But, our final results are using logarithmic prior on B_0 because the linear prior never converged due huge range strong constraint.

mology parameters $\{\Omega_b h^2, \Omega_c h^2, 100\Theta_{MC}, \tau, n_s, log(10^{10} A_s)\}$ and all 18 planck nuisance parameters as described in Planck Collaboration et al. [267] with the respective extension parameters or modified gravity parameters. The priors we have used on all the parameters are the same as the priors in Planck Collaboration et al. [267] and the priors we used on the parameters of modified gravity model are given in Table [2.2].

2.7   Results

We have combined CMB data set and measurements of growth from various redshift surveys in order to constrain the parameters of standard cosmology (ΛCDM), extended cos-

Table 2.3: The list of standard ΛCDM parameters used in our analysis. For each parameter we provide its symbol, prior range, central value and 1σ error. We have used the same prior as Planck2013 on these parameters. We have also marginalized over all the nuisance parameters of Planck likelihood. We report the results for each of the model analyzed in this paper.

Models	$\Omega_b h^2$	$\Omega_c h^2$	$100\theta_{MC}$	τ	n_s	$\ln(10^{10}A_s)$
prior range	0.005-0.10	0.001-0.99	0.50-10.0	0.01-0.8	0.9-1.1	2.7-4.0
Λ**CDM**	0.0219 ± 0.0002	0.1208 ± 0.0020	1.0410 ± 0.0006	0.0442 ± 0.0236	0.953 ± 0.0068	3.0007 ± 0.0450
w**CDM**	0.0221 ± 0.0003	0.1183 ± 0.0028	1.0414 ± 0.0006	0.0911 ± 0.0449	0.9615 ± 0.0097	3.0884 ± 0.0843
$w_0 w_a$**CDM**	0.0221 ± 0.0003	0.1181 ± 0.0029	1.0415 ± 0.0007	0.0906 ± 0.0454	0.9619 ± 0.0099	3.0871 ± 0.0850
$o\Lambda$**CDM**	0.0220 ± 0.0003	0.1191 ± 0.0031	1.0413 ± 0.0007	0.0518 ± 0.0278	0.9582 ± 0.0094	3.0118 ± 0.0514
Scalar-tensor	0.0221 ± 0.0003	0.1199 ± 0.0020	1.0412 ± 0.0006	0.0333 ± 0.0198	0.9591 ± 0.0071	2.9769 ± 0.0377
Chameleon	0.0219 ± 0.0002	0.1205 ± 0.0020	1.0411 ± 0.0006	0.0390 ± 0.0222	0.9539 ± 0.0067	2.9894 ± 0.0425
eChameleon	0.0218 ± 0.0003	0.1222 ± 0.0023	1.0409 ± 0.0006	0.1313 ± 0.0467	0.9537 ± 0.0079	3.1780 ± 0.0914
$f(R)$	0.0221 ± 0.0004	0.1182 ± 0.0033	1.0414 ± 0.0008	0.0733 ± 0.0354	0.9607 ± 0.0101	3.0526 ± 0.0663
growth index (γ)	0.0218 ± 0.0003	0.1214 ± 0.0023	1.0409 ± 0.0006	0.0699 ± 0.0400	0.9525 ± 0.0075	3.0534 ± 0.0788
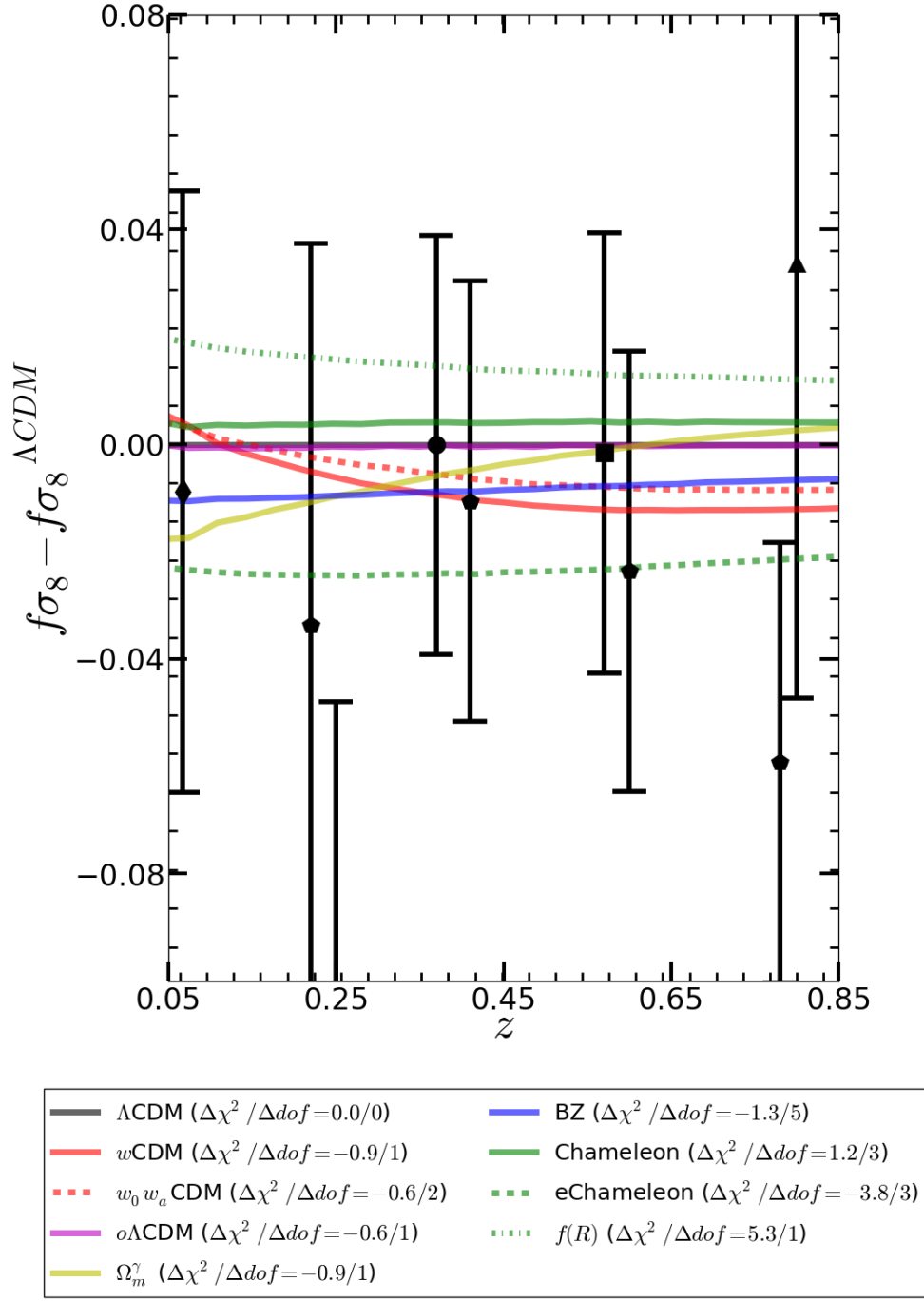
Figure 2.3: The black points show the corrected $f\sigma_8$ used in our analysis, along with the errorbar. Lines of different colors show the best fit for the various models used in our analysis. The best fit and χ^2 are for the case of Planck $+f\sigma_8$ + eCMASS fits. Notice that the eChameleon model predicts the smallest growth rate by preferring lower values of the coupling constant (β_1), even though the scalar amplitude of primordial power spectrum is high.
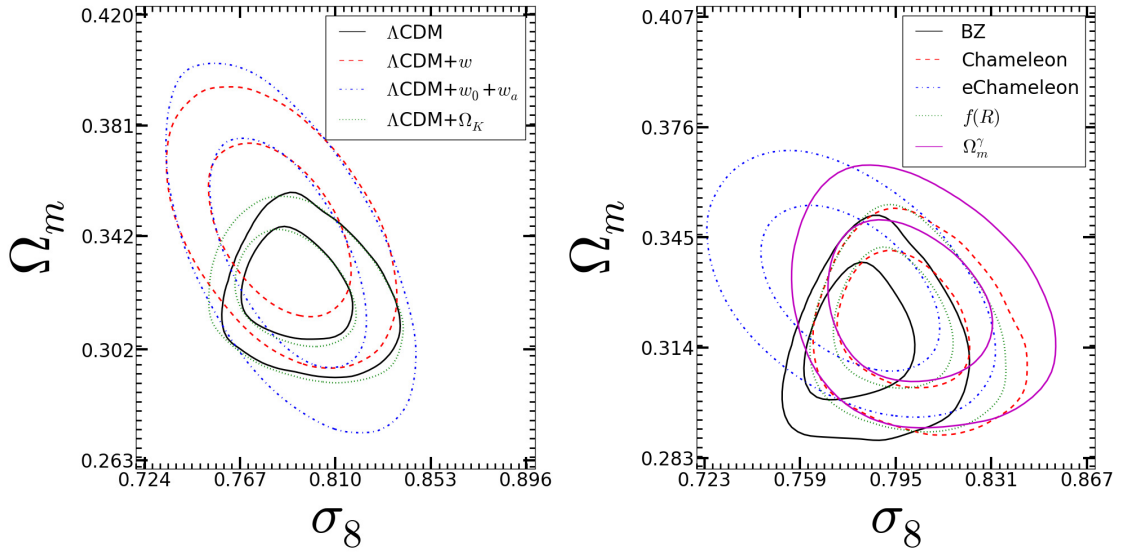
Figure 2.4: The figure shows the 1σ and 2σ regions for each of the models considered in this paper in Ω_m-σ_8 plane. It shows that the posterior likelihood is consistent for each of the model in this parameter space. The top plots shows the models which are extension to ΛCDM and the bottom plot shows the *modified gravity* models.

mology models and *modified gravity*. Our analysis gives consistent constraints for the standard ΛCDM parameters $\{\Omega_b h^2, \Omega_c h^2, 100\Theta_{MC}, \tau, n_s, log(10^{10}A_s)\}$ as shown in Table 2.3. Figure 2.4 shows the constraint on Ω_m-σ_8 plane for ΛCDM, wCDM, $o\Lambda$CDM, Scalartensor model, Chameleon gravity, eChameleon, $f(R)$ and growth index parametrization. Theses are our best constraints obtained using planck +eCMASS + $f\sigma_8(z)$. Figure 2.3 shows the theoretical predictions of $f\sigma_8(z)$ for each of the model considered in this paper.

2.7.1 ΛCDM

Figure 2.5 shows the one dimensional marginalized likelihood for standard ΛCDM cosmology. The black line shows the contraints from Planck 2013 alone. The red ,blue and magenta lines are posterior obtained for the data set combinations planck+eCMASS, planck+$f\sigma_8(z)$ and planck+eCMASS+$f\sigma_8(z)$ respectively. Our parameter constraints are completely consistent with the Planck 2013 results. Adding measurements of the growth rate to Planck data does not improve the results (see Figure 2.5) due to already tight constraints from Planck observations (see Figure 2.1).

2.7.2 Dark Energy Equation of state (wCDM)

We have looked at the wCDM, i.e the one parameter extension of ΛCDM where the dark energy equation of state is a constant, w. Figure 2.6 shows the two dimensional likelihood of w_0 and Ω_m. The grey contours are Planck only constraint ($w_0 = -1.27 \pm 0.42$), red contours are Planck and eCMASS ($w_0 = -0.92 \pm 0.10$) and blue contours show Planck combined with eCMASS and growth factor measurements ($w_0 = -0.87 \pm 0.077$). We obtain $w_0 = -0.87 \pm 0.077$ (8.8% measurement) which is consistent with the fiducial value of $w = -1$ for ΛCDM. The constraint we obtained is similar in precision as compared to BAO only, but has different degeneracy. Therefore combined measurement of growth rate
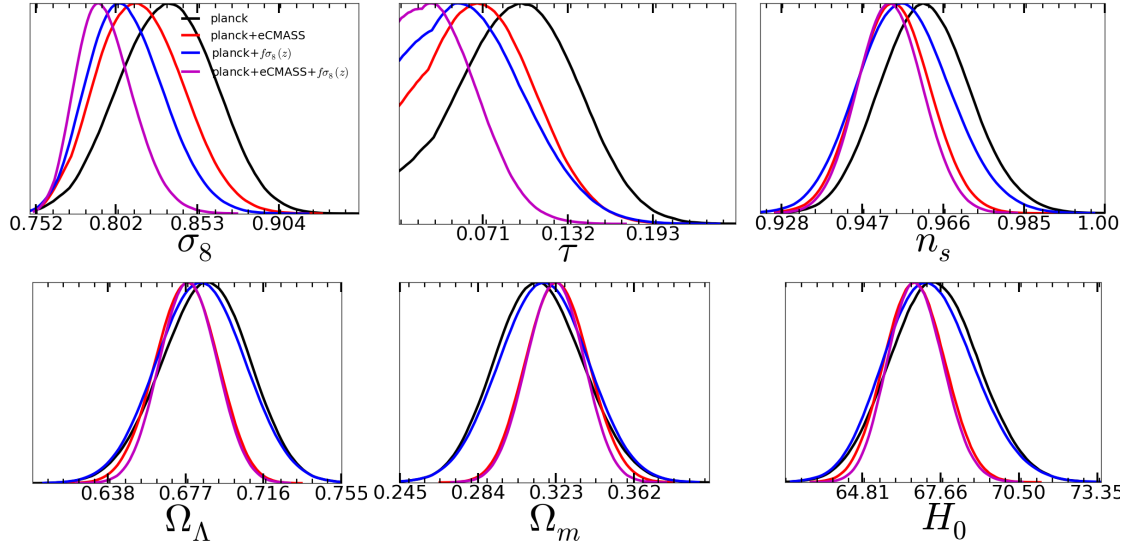
Figure 2.5: Λ**CDM:** We use GR as the model for gravity to determine the growth factor and fit for $f\sigma_8(z)$ and eCMASS measurement with Planck likelihood. The black line shows the contraints from Planck 2013 alone. The red ,blue and magenta lines are posterior obtained for the data set combinations planck+eCMASS, planck+$f\sigma_8(z)$ and planck+eCMASS+$f\sigma_8(z)$ respectively. The two most prominent effect are in optical depth τ and scalar amplitude of primordial power spectrum A_s. Which is also reflected in the derived parameter σ_8 and mid redshift of re-ionization z_{re}.
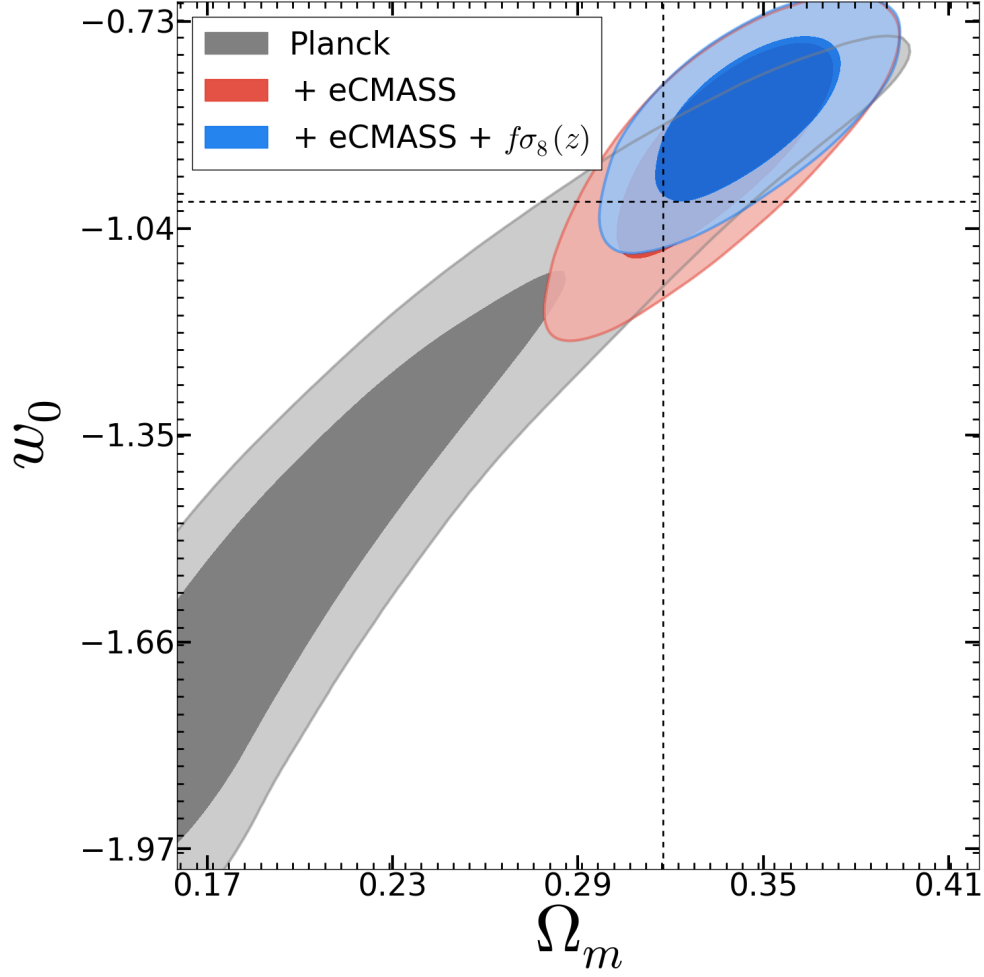
Figure 2.6: **wCDM:** The two dimensional posterior likelihood w and Ω_m for wCDM. The grey contour is for Planck ($w_0 = -1.27 \pm 0.42$), red contour is combined constraint from Planck and eCMASS ($w_0 = -0.92 \pm 0.10$). The blue contour represents constraint from combining Planck with eCMASS and $f\sigma_8(z)$ ($w_0 = -0.87 \pm 0.077$).
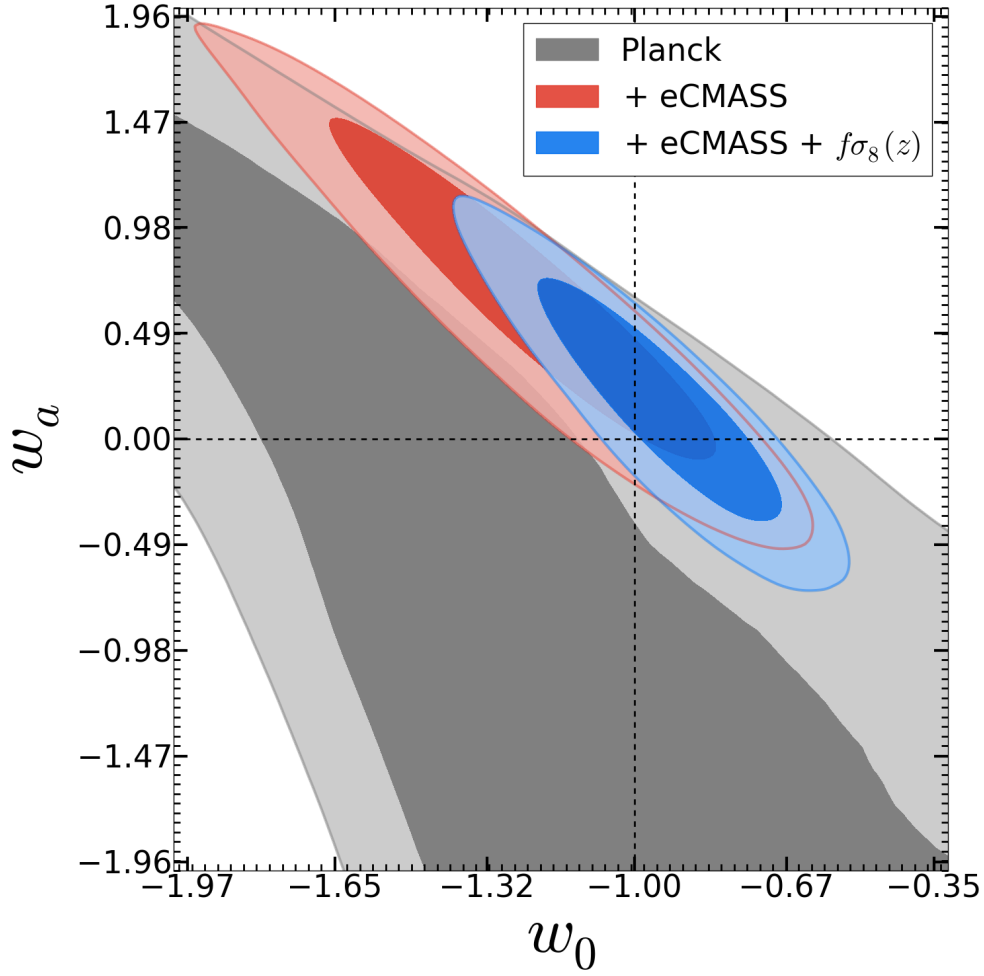
Figure 2.7: **w0waCDM:** The two dimensional posterior likelihood of w_0 and w_a for time-dependent dark energy model. The grey contour is for Planck ($w_0 = -0.99 \pm 0.52, w_a = -1.50 \pm 1.46$), red contour is combined constraint from Planck and eCMASS ($w_0 = -1.23 \pm 0.26, w_a = 0.63 \pm 0.49$). The blue contour represents results from combining Planck with eCMASS and $f\sigma_8(z)$ ($w_0 = -0.94 \pm 0.17, w_a = 0.16 \pm 0.36$).

and anisotropic BAO for all of these surveys will help us improve the precision of w_0.

2.7.3 Time-dependent Dark Energy (w_0w_aCDM)

The wCDM model which proposes a constant dark energy is limited in its physical characteristics. Many models propose time-dependent dark energy which is popularly tested using linear relation $w(z) = w_0 + w_a\frac{z}{1+z}$ with w_0 and w_a as free parameters. This model

has been shown to match exact solutions of distance, Hubble, growth to the 10^{-3} level of accuracy [100] for a wide variety of scalar field (and *modified gravity*) models. The dynamical evolution of $w(z)$ can change the growth factor significantly and leave an imprint on the CMB. The combination of CMB and collection of growth factor at different redshifts is a unique way to test the time-dependent dark energy model.

Figure 2.7 shows the 1σ and 2σ region for (w_0, w_a). The grey contour is from the Planck temperature power spectrum data alone ($w_0 = -0.99 \pm 0.52, w_a = -1.50 \pm 1.46$). The red contours are from Planck and eCMASS ($w_0 = -1.23 \pm 0.26, w_a = 0.63 \pm 0.49$) and blue contour shows planck combined with eCMASS and growth factor measurement ($w_0 = -0.94 \pm 0.17, w_a = 0.16 \pm 0.36$). The ΛCDM prediction of $(w_0, w_a) = (-1, 0)$ is completely consistent with our posterior. We have obtained constraint on $w_0 = -0.94 \pm 0.17$ (18% measurement) and $1 + w_a = 1.16 \pm 0.36$ (31% measurement) which is stronger constraint than the current best measurement of $w_a = -0.2 \pm 0.4$ from Aubourg et al. [27].

2.7.4   Spatial Curvature ($o\Lambda$CDM)

We consider a model with spatial curvature parametrized with Ω_K as free parameter called $o\Lambda$CDM along with ΛCDM parameters. Figure 2.8 shows the posterior for the Ω_K and Ω_m plane. The grey contour is from the Planck temperature power spectrum data alone ($\Omega_k = -0.060 \pm 0.047$). The red contours are from Planck and eCMASS ($\Omega_k = -0.0024 \pm 0.0034$) and blue contour shows Planck combined with eCMASS and growth factor measurements ($\Omega_k = -0.0024 \pm 0.0032$). The ΛCDM prediction of $\Omega_k = 0$ is completely consistent with our posterior. We have obtained constraint on $1 + \Omega_k = 0.9976 \pm 0.0032$ (0.3% measurement) which is competitive with the current best measurements [27]. It will be interesting to see if combined RSD and BAO at all redshifts will give any improvement on the precision of curvature.
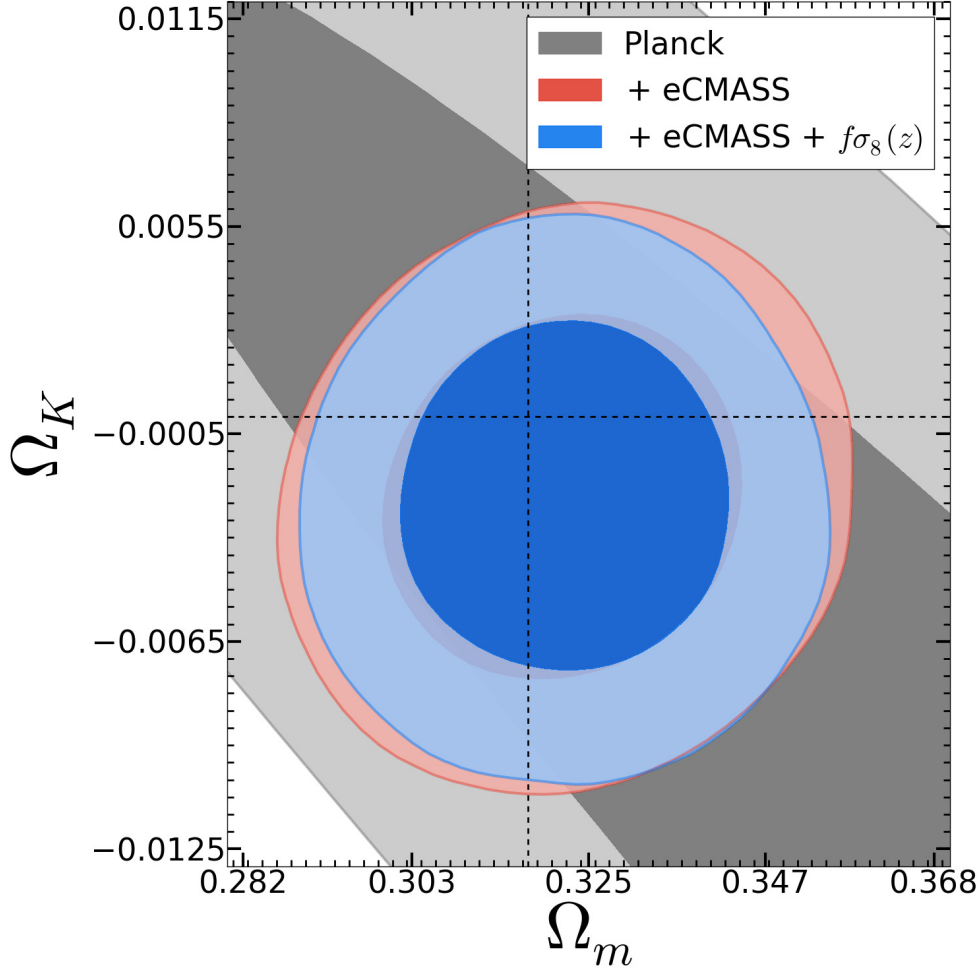
Figure 2.8: $o\Lambda$**CDM:** The two dimensional posterior likelihood of Ω_k and Ω_m for $o\Lambda$CDM. The grey contour is for Planck ($\Omega_k = -0.060 \pm 0.047$), red contour is combined constraint from Planck and eCMASS ($\Omega_k = -0.0024 \pm 0.0034$). The blue contour represents results from combining Planck with eCMASS and $f\sigma_8(z)$ ($\Omega_k = -0.0024 \pm 0.0032$).
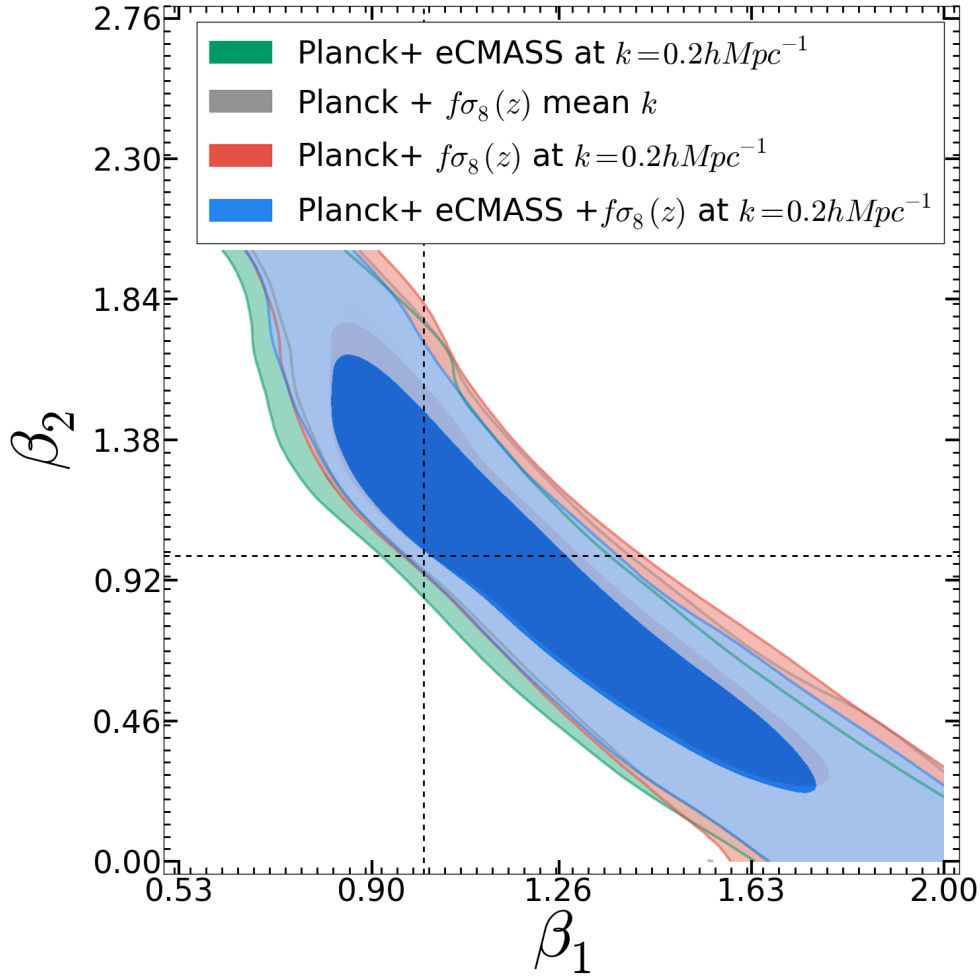
Figure 2.9: **BZ:** The two dimensional posterior likelihood of β_1-β_2 for five parameter Scalar-tensor theory parametrized through the BZ form of (2.2). The green contour is the combined constraint from Planck and eCMASS ($\beta_1 = 1.18 \pm 0.29$, $\beta_2 = 0.95 \pm 0.43$).The grey contour is the combined constraint from Planck and $f\sigma_8(z)$ with averaged over k ($\beta_1 = 1.24 \pm 0.3$, $\beta_2 = 0.96 \pm 0.45$), red contour is the combined constraint from Planck and $f\sigma_8(z)$ at effective $k = 0.2h$ Mpc^{-1} ($\beta_1 = 1.24 \pm 0.3$, $\beta_2 = 0.95 \pm 0.45$). The blue contour represents results from the combination of Planck, $f\sigma_8(z)$ and eCMASS ($\beta_1 = 1.23 \pm 0.29$, $\beta_2 = 0.93 \pm 0.44$).

2.7.5 Scalar-Tensor Gravity (BZ parametrization)

The general Scalar-tensor theories of gravity is analyzed using five parameter model called BZ parametrization . The five parameters of Scalar-tensor gravity ($\beta_1, \beta_2, \lambda_1, \lambda_2, s$) are constrained along with the standard ΛCDM parameters using Planck, $f\sigma_8(z)$ and eCMASS

measurements. BZ model predicts a scale dependent growth rate ($f\sigma_8(k, z)$), whereas the measurements are at some effective k. In order to incorporate the k-dependence in our analysis, we use the two different approaches described in Section 2.5.2. Figure 2.9 shows two dimensional posterior in the plane (β_1, β_2). The green contour is combined constraint from Planck and eCMASS ($\beta_1 = 1.18 \pm 0.29, \beta_2 = 0.95 \pm 0.43$). The grey contour is the combined constraint from Planck and $f\sigma_8(z)$ with averaged over k ($\beta_1 = 1.24 \pm 0.3, \beta_2 = 0.96 \pm 0.45$); the red contour is the combined constraint from Planck and $f\sigma_8(z)$ at effective $k = 0.2h$ Mpc^{-1} ($\beta_1 = 1.24 \pm 0.3, \beta_2 = 0.95 \pm 0.45$). The blue contour represents results from the combination of Planck, $f\sigma_8(z)$ and eCMASS ($\beta_1 = 1.23 \pm 0.29, \beta_2 = 0.93 \pm 0.44$). We obtain the following joint constraint on the five BZ parameters: $\beta_1 = 1.23 \pm 0.29$, $\beta_2 = 0.93 \pm 0.44$, $\lambda_1^2(\times 10^{-6}) = 0.49 \pm 0.29$, $\lambda_2^2(\times 10^{-6}) = 0.41 \pm 0.28$ and $s = 2.80 \pm 0.84$. By looking at the joint 2D likelihood for (β_1, β_2) in Fig. 2.9, we notice that there is a strong degeneracy between the two parameters which reflects the degeneracy between μ and γ for the observables that we are using. Similar results have been found in [158, 285]. For the next models that we will discuss, β_1 and β_2 are not independent and this will allow data to place more stringent constraints.

While the constraints on the length scale of the scalar field (λ_1, λ_2) and (s) are very broad, the one on the coupling, β_1 and β_2, is the first ever constraint obtained on these parameters for general Scalar-tensor gravity. The discrepancy in the strength of the constraints on the coupling and on the length scale, can be linked to the fact that data strongly prefer values of the coupling constants close to 1. For such values, the scale and time dependences in (μ, γ) becomes less important and therefore are loosely constrained. We will encounter this again in the Chameleon and $f(R)$ gravity cases.
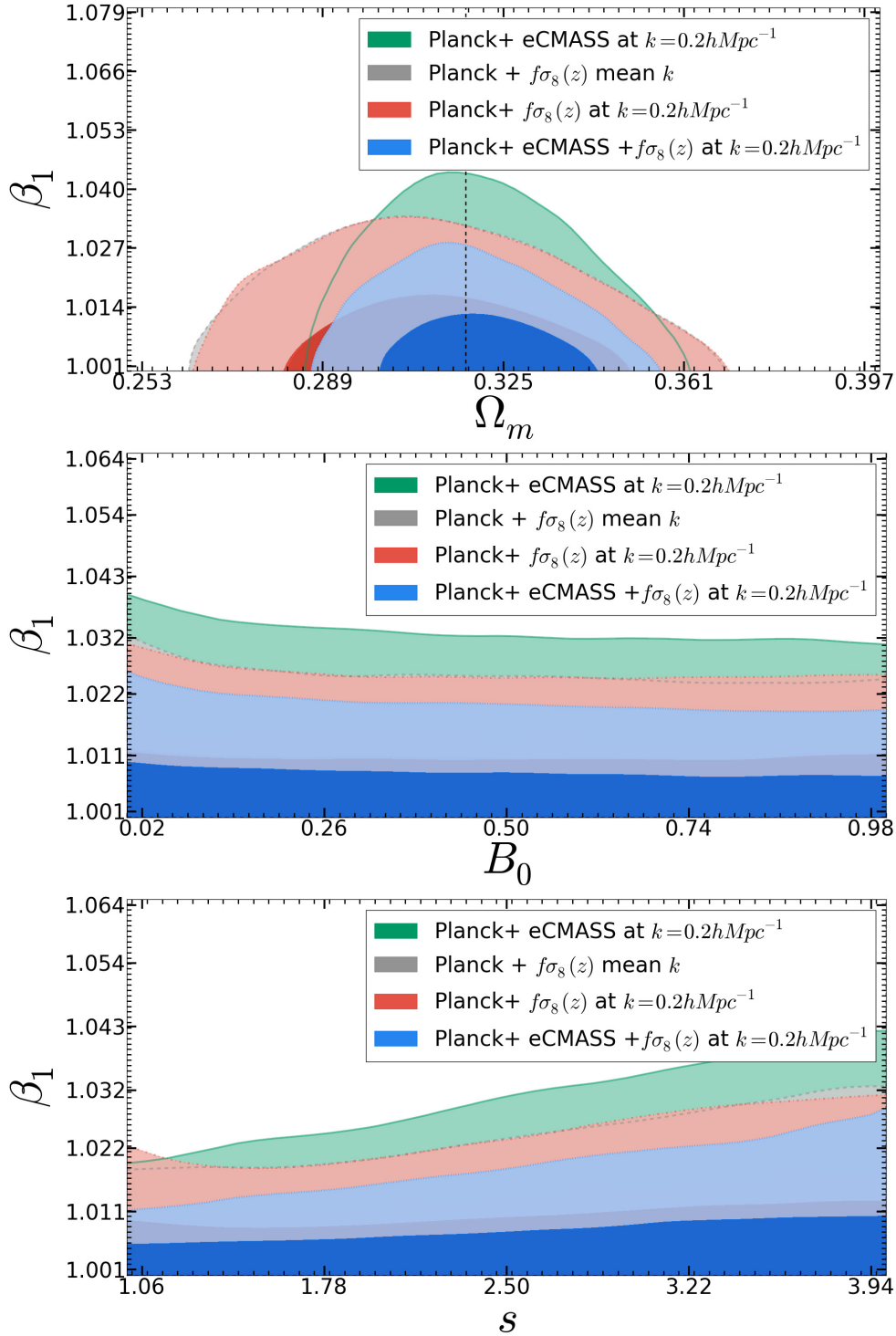
Figure 2.10: **Chameleon Theory:** The two dimensional posterior likelihood for Chameleon gravity. The green contour is the combined constraint from Planck and eC-MASS ($\beta_1 < 1.013$).The grey contour is the combined constraint from Planck and $f\sigma_8(z)$ with averaged over k ($\beta_1 < 1.010$), the red contour is the combined constraint from Planck and $f\sigma_8(z)$ at effective $k = 0.2h$ Mpc^{-1} ($\beta_1 < 1.010$). The blue contour represents results from the combination of Planck, eCMASS and $f\sigma_8(z)$ ($\beta_1 < 1.008$).
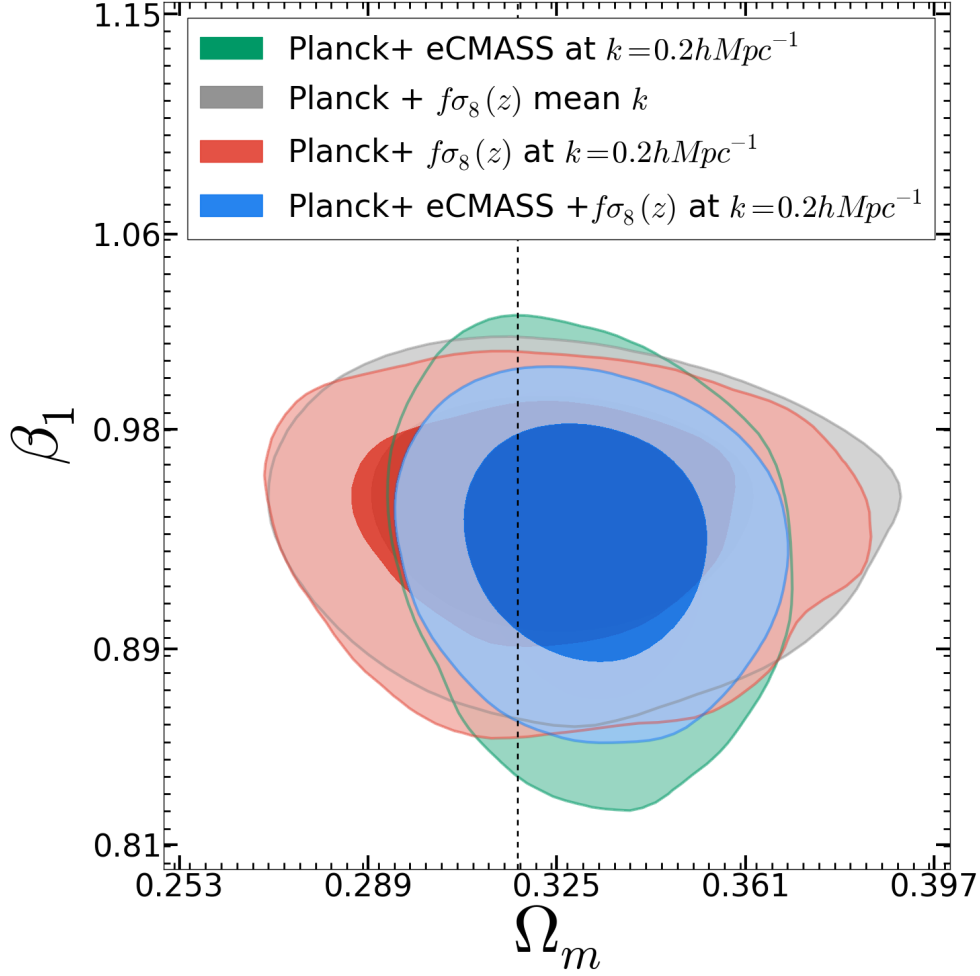
Figure 2.11: **eChameleon Theory:** The two dimensional posterior likelihood of β_1 and Ω_m for extended Chameleon gravity. The green contour is the combined constraint from Planck and eCMASS ($\beta_1 = 0.932 \pm 0.04$). The grey contour is the combined constraint from Planck and $f\sigma_8(z)$ with averaged over k ($\beta_1 = 0.940 \pm 0.032$), red contour is combined constraint from Planck and $f\sigma_8(z)$ at effective $k = 0.2h$ Mpc^{-1} ($\beta_1 = 0.936 \pm 0.032$). The blue contour represents results from the combination of Planck, $f\sigma_8(z)$ and eCMASS ($\beta_1 = 0.932 \pm 0.031$).

2.7.6 Chameleon Gravity

The three parameters of Chameleon gravity (β_1, B_0, s) are constrained along with the standard ΛCDM parameters using Planck, $f\sigma_8(z)$ and eCMASS measurements. Chameleon models predict a scale dependent growth rate $(f\sigma_8(k,z))$, whereas the measurements are at some effective k. In order to incorporate the k-dependence in our analysis, we use the two different approaches described in Section 2.5.2. Figure 2.10 shows the two dimensional posterior in the plane (Ω_m, β_1), (B_0, β_1) and (s, β_1). The grey and red contours show the posteriors from combined data set of Planck and growth rate measurements. The red contours are likelihood while evaluating the growth rate at an effective k ($\beta_1 < 1.010$), whereas grey contours are for the case when we use an effective growth rate, averaged over the scales used in the actual $f\sigma_8$ measurement ($\beta_1 < 1.010$). The green contour is combined constraint from Planck and eCMASS ($\beta_1 < 1.013$). Finally, the blue contours show the posterior from combined data of Planck, eCMASS and growth rate ($\beta_1 < 1.008$). We obtain the following joint constraint on the three Chameleon parameters: $\beta_1 < 1.008$, $B_0 < 1.0$ and $2.27 < s < 4$. While the constraints on the length scale of the scalar field, B_0 and s is very broad, the one on the coupling, β_1, is very strong and predicts $\beta_1 = 1$ to 0.8%, bringing μ to its GR value. As we already discussed for the Scalar-tensor case, the discrepancy in the strenght of these constraints is due to the fact that data prefer values of the coupling constant close to 1, for which the time and scale dependence of (μ, γ_{slip}) become negligible. This is even more the case for Chameleon models, where the theoretical prior forces $\beta_1 > 1$, which corresponds to enhanced growth, and data consequently require very small values for this coupling, pushing μ very close to its GR value.

We have also looked at the extended Chameleon model where we allow β_1 to be less than 1 following previous analysis of this model. Figure 2.11 shows the two dimensional posterior in the plane (Ω_m, β_1). The red contours are likelihood while evaluating the growth

rate at an effective k ($\beta_1 = 0.940 \pm 0.032$), whereas grey contours are for the case when we use an effective growth rate, averaged over the scales used in the actual $f\sigma_8$ measurement ($\beta_1 = 0.936 \pm 0.032$). The green contour is combined constraint from Planck and eCMASS ($\beta_1 = 0.932 \pm 0.04$). Finally, the blue contours show the posterior from combined data of Planck, eCMASS and growth rate ($\beta_1 = 0.932 \pm 0.031$). We obtain the following joint constraint on the three eChameleon parameters: $\beta_1 = 0.932 \pm 0.031$, $B_0 < 0.613$ and $2.69 < s < 4$. Like in the more general Scalar-tensor case, while the constraints on the length scale of the scalar field, B_0 and s are very broad, the one on the coupling, β_1, is an huge improvement on the previous constraint of $\beta_1 = 1.3 \pm 0.25$ (19.2 % measurement) using WMAP CMB, SNe and ISW dataset [157]. Let us notice that when we constrain jointly the three eChameleon parameters, data select a region in the parameter space which corresponds to $\beta_1 < 1$, i.e. to suppressed growth. This region excludes standard Chameleon models, including $f(R)$ theories, for which $\beta_1 > 1$ and the growth is enhanced. After all, as we have seen above and will see in the next Section, the same data place very stringent constraints on Chameleon and $f(R)$ models, forcing them to be very close to ΛCDM (see Figure 2.11 and 2.12). Hence the combination of data sets that we employ favor models with a suppressed growth rate, which adopting the BZ parametrization can be obtained with $\beta_1 < 1$; a suppressed growth was favored also by the data set used in [285], although in that case the authors employed a time-dependent parametrization. Theoretically viable scalar-tensor models with a suppressed growth are discussed in [260], where they are analyzed via a scale-independent parametrization in the effective field theory language.

2.7.7 $f(R)$ theory

We consider one parameter (B_0) model of $f(R)$ gravity. The parameter B_0 parameter-izes the deviation from ΛCDM. The model approaches GR when B_0 is zero. Similar to
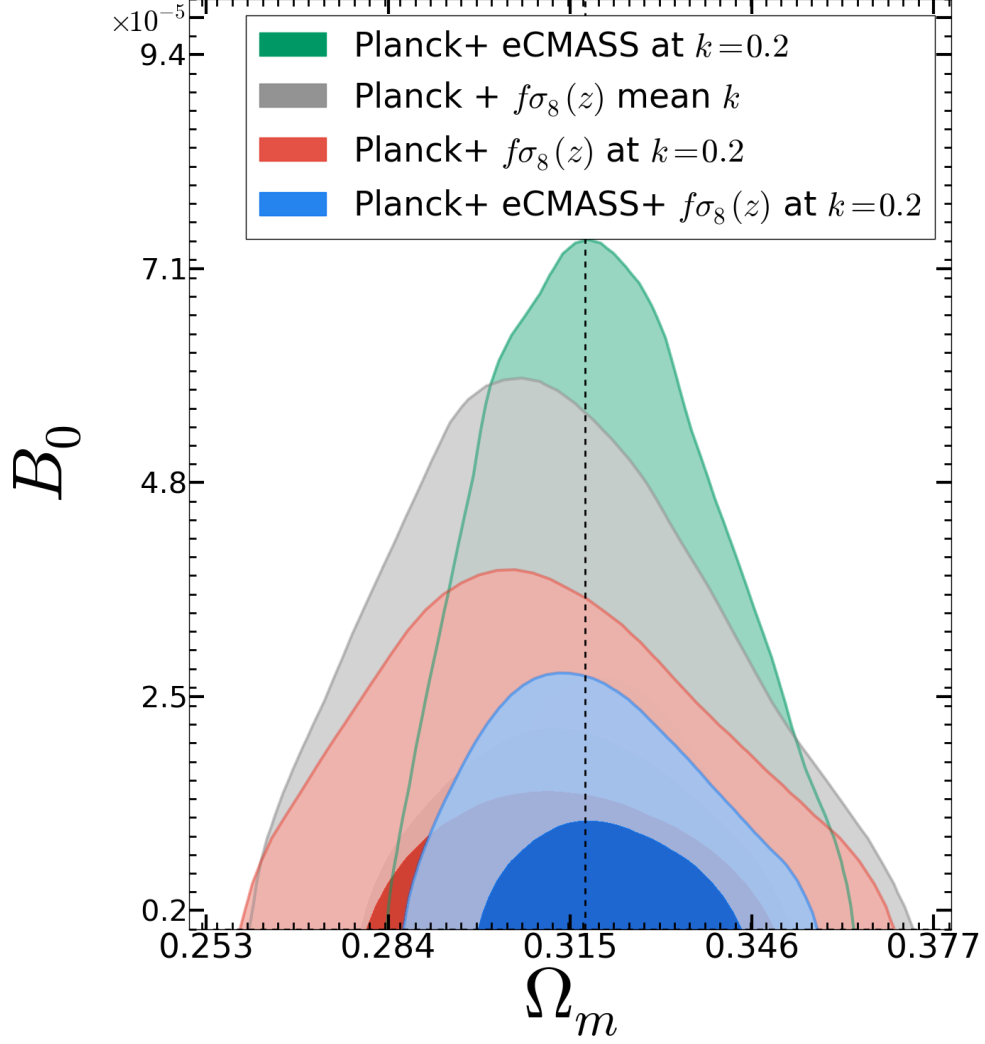
Figure 2.12: $f(R)$ **Gravity:** The two dimensional posterior likelihood of B_0 and Ω_m for $f(R)$ gravity. The green contour is combined constraint from Planck and eCMASS ($B_0 < 3.43 \times 10^{-5}$). The grey contour is the combined constraint from Planck and $f\sigma_8(z)$ with averaged over k ($B_0 < 2.77 \times 10^{-5}$), the red contour is the combined constraint from Planck and $f\sigma_8(z)$ at effective $k = 0.2h$ Mpc^{-1} ($B_0 < 1.89 \times 10^{-5}$). The blue contour represents results from the combination of Planck, $f\sigma_8(z)$ and eCMASS ($B_0 < 1.36 \times 10^{-5}$)

Chameleon theory, $f(R)$ gravity predicts a scale dependent growth rate ($f\sigma_8(k, z)$). Figure 2.12 shows the two dimensional posterior in B_0 and Ω_m plane. The green contour is combined constraint from Planck and eCMASS ($B_0 < 3.43 \times 10^{-5}$). The grey and red contours show posterior from combined data set of Planck and growth rate measurements. The red contours are likelihood while evaluating the growth rate at an effective k ($B_0 < 1.89 \times 10^{-5}$) where as grey contours are for the case when we use effective growth rate, which is averaged over scales used in the actual $f\sigma_8$ measurements ($B_0 < 2.77 \times 10^{-5}$). The blue contours show the posterior from combined data of Planck, eCMASS and growth rate ($B_0 < 1.36 \times 10^{-5}$). We obtained $B_0 < 1.36 \times 10^{-5}$ (1σ C.L.), which is an improvement by a factor of 4 on the most recent constraint from large scale structure of $B_0 = 5.7 \times 10^{-5}$ (1σ C.L.) [401]. Our constraint is competitive with the constraint from solar system tests and clusters [163, 331, 75].

2.7.8 Growth index (γ) parametrization

The standard cosmological model, based on GR, predicts a precise value for the growth factor in the linear regime, i.e. $f = \Omega_m^{0.55}$. In order to test deviations from GR, we have parameterized the growth factor using growth index γ (Linder and Cahn [210]) as $f = \Omega_m^{\gamma}$. The marginalized two dimensional likelihood for Ω_m and γ is shown in Figure 2.13. The grey contour is combined constraint from Planck and eCMASS ($\gamma = 0.477 \pm 0.096$). The red contours show the constraint obtained using Planck and $f\sigma_8(z)$ measurement($\gamma = 0.595 \pm 0.079$) and the blue contours are for combined data set of Planck with $f\sigma_8(z)$ and eCMASS ($\gamma = 0.612 \pm 0.072$). We have obtained $\gamma = 0.612 \pm 0.072$ (11.7% measurement) completely consistent with the general relativity prediction.
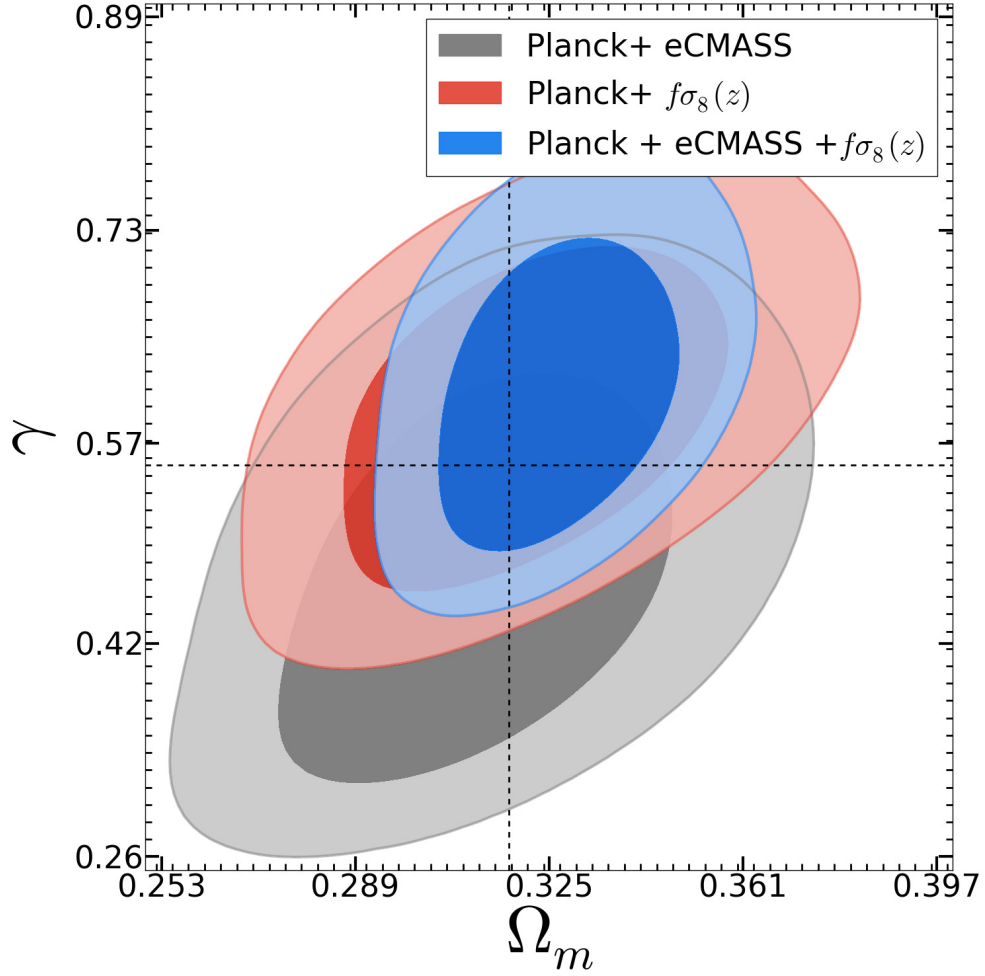
Figure 2.13: **Growth index (γ):** The two dimensional posterior likelihood of γ and Ω_m for growth index parametrization. The grey contour is the combined constraint from Planck and eCMASS ($\gamma = 0.477 \pm 0.096$). The red contour is the combined constraint from Planck and $f\sigma_8(z)$ ($\gamma = 0.595 \pm 0.079$). The blue contour represents results from the combination of Planck, $f\sigma_8(z)$ and eCMASS ($\gamma = 0.612 \pm 0.072$)

2.8 Discussion

We have constrained the parameters of the standard cosmological model, ΛCDM, as well as those of various extensions using the current measurements of growth rate between redshift 0.06 and 0.83 (Figure 2.4), eCMASS and Planck 2013. We have been careful with several important details while combining results from various surveys and different cosmologies of measurements. We have first showed that the standard ΛCDM parameter space has a consistent posterior, independent of the model considered except for Chameleon gravity. Next, we focused on each model and analyzed the constraint on its extension parameters. As for the standard model, ΛCDM, using the growth factor we do not improve constraints on any of its parameters because the growth rate is already highly constrained with Planck measurement for the standard model of cosmology. It is impressive to notice that ΛCDM, without any extra parameter, is completely consistent with the measurements of $f\sigma_8$ from very different galaxy types and redshifts. In the case of the extension where the dark energy equation of state is constant but free to vary, wCDM, we obtain $w_0 = -0.87 \pm 0.077$ (8.8% measurement). This is a 3.7 times improvement on the precision compared to Planck only measurement $w = -1.27 \pm 0.42$ (33% measurement) and comparable to the 8% measurement of Samushia et al. [323]. Our measurement prefers $w < -1$ at 1σ level. We have also noticed that the growth rate and BAO have slightly different degeneracy for wCDM. This shows the potential to improve the constraint on w by combining the growth rate and BAO measurements from a range of galaxy redshift surveys. However, one difficulty in doing so, is to model the correlation between the measurement of growth rate and BAO.

We also report one of the best measurements on the parameters of the model with a time-dependent equation of state, $w_0 w_a$CDM. We have measured $w_0 = -0.94 \pm 0.17$ (18% measurement) and $1 + w_a = 1.16 \pm 0.36$ (31% measurement). This represents a significant

improvement on w_a compared to all other measurements [267, 27]. The measurements of $f\sigma_8$, H and D_A in eCMASS help to constrain ΛCDM parameters, while the evolution of the growth rate over a large redshift range, obtained through measurements of $f\sigma_8(z)$ at multiple redshifts, improves the constrain on evolving dark energy. This hints at the potential of using combined growth rate and anisotropic BAO as function of redshifts, when future surveys like eBOSS and Euclid [196] will provide much stronger growth rate and BAO constraints at much higher redshifts. We have also looked at the possibility of a non-zero curvature for the universe, $o\Lambda$CDM, finding $1 + \Omega_k = 0.9976 \pm 0.0032$ (0.3% measurement), which is same as the best constraint reported in [323]. We notice that the optical depth (τ) and amplitude of scalar power spectrum (A_s) is relatively low for $o\Lambda$CDM, which predicts smaller redshift of reionization ($z_{re} = 7.20 \pm 2.81$) but it is above the lower limit observed through Lymanα Forest observations ([36]).

We have also looked at some of the popular modifications of gravity and found no significant deviations from GR using growth rate and Planck 2013 measurement. We have investigated general scalar-tensor theories under the parametrization introduced in [46], constraining the corresponding five parameters. We have found constraints on the two coupling parameters ($\beta_1 = 1.23 \pm 0.29$, $\beta_2 = 0.93 \pm 0.44$) while the posterior of other three parameters were largely non-constraining. We then restricted to the subset of Chameleon theories, for which only three parameters are needed. While imposing a theoretical bound of $\beta_1 > 1$, we constrained the coupling of Chameleon theories to $\beta_1 < 1.008$ (1 σ C.L.), while jointly varying the remaining two free parameters that describe the lengthscale of the scalar degree of freedom, $\{B_0, s\}$. While the latter are loosely constrained by data, the constraint on the coupling is quite stringent. We explored also an extension of Chameleon models, that we dubbed eChameleon, where we let the coupling β_1 vary within the range $[0, 2]$. Also in this case, data place a stringent bound on the coupling, while loosely constraining $\{B_0, s\}$. Interestingly, for this case data select a region where $\beta_1 < 1$, with the

bound $\beta_1 = 0.932 \pm 0.031$; the latter corresponds to a region of the parameter space for which growth is suppressed. This improves significantly over previous analysis, e.g. the bound $\beta_1 = 1.3 \pm 0.25$ (19.2 % measurement) obtained in [157] using WMAP CMB, SNe and ISW dataset. This excludes standard Chameleon models, including $f(R)$ theories, for which $\beta_1 > 1$ and the growth is enhanced. After all, the same data place very stringent constraints on the latter models, forcing them to be very close to ΛCDM (see Figure 2.11 and 2.12). We also notice that the optical depth (τ) and amplitude of scalar power spectrum (A_s) is higher for eChameleon gravity. This predicts higher redshift of reionization ($z_{re} = 14.43 \pm 3.77$) and higher growth. In such a situation the only way in which the model can align itself with the measured $f\sigma_8$ is by choosing a smaller coupling parameter (β_1). We have placed very stringent bounds on $f(R)$ models with a ΛCDM bacgkround, constraining their only free parameter to be $B_0 < 1.36 \times 10^{-5}$ (1 σ C.L.). This is competitive with the constraint from solar system tests and clusters [163, 331, 75] and other cosmological measurements [401, 105, 296, 285].

Finally, we have analyzed the growth index parametrization of the growth rate, measuring $\gamma = 0.612 \pm 0.072$ (11.7% measurement), which is completely consistent with the general relativity prediction. This is a slight improvement on the 16% measurement of Samushia et al. [325]. We also note that our measurement of growth index is slightly less precise than current best measurement $\gamma = 0.665 \pm 0.0669$ (10% measurement) [176] using combination of galaxy power spectrum, velocity power spectrum, Type Ia SNe, the cosmic microwave background (CMB), CMB lensing, and the temperature-galaxy cross correlation.

It is remarkable to notice that even after allowing many different kind of degree of freedom. our analysis shows that everything is consistent with vanilla ΛCDM cosmology and General theory of relativity.

Acknowledgement

Chapter 3

Probing Gravity at Large Scales through CMB Lensing

Anthony R. Pullen, Shadab Alam, and Shirley Ho

3.1   Abstract

We describe a methodology to probe gravity with the cosmic microwave background (CMB) lensing convergence κ, specifically by measuring E_G, the ratio of the Laplacian of the gravitational scalar potential difference with the velocity divergence. Using CMB lensing instead of galaxy-galaxy lensing avoids intrinsic alignments while also lacking a hard limit on the lens redshift and significant uncertainties in the source plane. We model E_G for general relativity and modified gravity, finding that E_G for $f(R)$ gravity should be scale-dependent due to the scale-dependence of the growth rate f. Next, we construct an estimator for E_G in terms of the galaxy-CMB lensing and galaxy clustering angular power spectra, along with the RSD parameter β. We also forecast statistical errors for E_G from the current *Planck*

CMB lensing map and the spectroscopic galaxy and quasar samples from the Sloan Digital Sky Survey Data Release 11, being 9% with galaxies and 8% when quasars are included. We also find that upcoming spectroscopic and photometric surveys, combined with the final *Planck* lensing map, can measure precisely the redshift- and scale-dependence of E_G out to redshifts $z = 2$ and higher, with photometric surveys having an advantage due to their high number densities. Advanced ACTPol's lensing map will increase the E_G sensitivity even further. Finally, we find that Advanced ACTPol cross-correlated with spectroscopic (photometric) surveys can differentiate between general relativity and $f(R)$ gravity at the level of 3σ (13σ). Performing a $< 1\%$ measurement of E_G requires a 10% precision in β from *Euclid* or LSST, currently achievable with a spectroscopic survey but difficult with only a photometric survey.

3.2   Introduction

The discovery of cosmic acceleration [307, 263] has inspired numerous theoretical explanations for its existence. On one hand, the acceleration can be caused by a new, unknown force that exhibits negative pressure called *dark energy* [253]. The cosmological constant, a special case of dark energy, is a major component of the ΛCDM framework that explains the expansion history and the growth history of the Universe [22] and the cosmic microwave background (CMB) [40, 266]. On the other hand, it is possible that the dynamics of gravity deviate from general relativity (GR) on cosmological scales [107, 74], a concept called *modified gravity*. In observations of the universe's expansion history, these two effects are degenerate with one another. However, we expect the growth of structure to differ between dark energy and modified gravity models such that the degeneracy is broken.

An observable that probes the expansion history and growth of structure simultaneously is E_G [409], which is related to the ratio of the Laplacian of the difference between

the two scalar potentials $\nabla^2(\psi - \phi)$ to the peculiar velocity perturbation field θ. The value of E_G depends on how gravity behaves on large scales. Traditionally, when measuring E_G, $\nabla^2(\psi - \phi)$ is probed by a galaxy lensing correlation with a tracer of large-scale structure (LSS), while the peculiar velocity field is probed by either a galaxy-velocity cross-correlation or, equivalently, a galaxy autocorrelation times the redshift-space distortion (RSD) parameter $\beta = f/b$, where f is the growth rate and b is the clustering bias of the galaxies. A major advantage of E_G over other observables is that it is independent of clustering bias on linear scales, reducing the model uncertainty. E_G was first measured in Reyes et al. [303], using galaxy-galaxy lensing exhibited by Sloan Digital Sky Survey (SDSS) [408] Luminous Red Galaxies (LRGs) [112] to find $E_G(z = 0.32) = 0.392 \pm 0.065$, consistent with ΛCDM.

In this analysis we assess the possibility of using CMB lensing [57, 207, 82] cross correlated with galaxies [148, 353, 150, 271] as a probe of $\nabla^2(\psi - \phi)$ instead of the traditional method of using galaxy lensing. One advantage of using CMB lensing over galaxy lensing is that the CMB lensing kernel is very broad over redshift, allowing probes of E_G at much higher redshifts than with galaxy lensing. At these higher redshifts, CMB lensing also has the added bonus of probing more linear scales, reducing systematic effects due to nonlinear clustering. Also, since the CMB propagates throughout all of space, all of LSS sampled by the survey lenses the CMB, allowing us to measure the lensing part of E_G at much higher redshifts. We also do not have to worry about complex astrophysical uncertainties of the source galaxies, *i.e.* intrinsic alignments, since the CMB is simple. Finally, we know the CMB redshift, so we can avoid determining the photometric redshift distribution of the sources. We construct an estimator for E_G in terms of the angular cross-power spectrum between the CMB lensing convergence κ and galaxies, the angular auto-power spectrum of the same galaxies, and the RSD parameter β.

Next, we derive E_G for general relativity (GR), as well as modified gravity using the $\mu\gamma$

77

formalism from Hojjati et al. [156]. While $E_G(z)$ can be written as $\Omega_{m,0}/f(z)$ for ΛCDM, where $\Omega_{m,0}$ is the matter density today relative to the critical density and $f(z)$ is the growth rate at redshift z, E_G for modified gravity models is expected to differ from this value. We also found that E_G for $f(R)$ gravity [74] and chameleon gravity [186] can exhibit scale-dependence through f, which could potentially help differentiate between these gravity models and GR.

Next, we consider the prospect of measuring E_G with CMB lensing by forecasting errors for an E_G measurement using the current *Planck* CMB lensing map [271] along with the CMASS galaxy ($z = 0.57$), LOWZ galaxy ($z = 0.32$), and BOSS quasar [250] spectroscopic samples from Data Release 11 (DR11) [22] of the SDSS-III [114] Baryon Oscillations Spectroscopic Survey (BOSS) [97]. We also consider possibilities with upcoming surveys. First, we consider the final *Planck* lensing map cross-correlated with spectroscopic surveys, specifically the Dark Energy Spectroscopic Instrument (DESI) [200], *Euclid* [195], and the Wide Field InfraRed Survey Telescope (WFIRST) [356]. We find, however, that an E_G measurement using the *Planck* CMB lensing map and upcoming spectroscopic surveys is not sensitive enough to differentiate between GR and $f(R)$ gravity at current limits, and that the new limits on chameleon gravity would be modest. We find that spectroscopic surveys with Advanced ACTPol can differentiate between GR and $f(R)$ gravity at the level of 3σ, with higher significances for the chameleon gravity model.

We also consider the CMB lensing maps cross-correlated with photometric surveys, specifically the Dark Energy Survey (DES) [371], the Large Synoptic Survey Telescope (LSST) [216], and *Euclid*. We find that for the scales which E_G dominates, being small but still only quasi-linear, the lensing measurement dominates the error in E_G as opposed to the RSD. Thus, reducing the shot noise by increasing the survey number density is more important than having more precise redshifts for RSD. We find DES is comparable in power to DESI, and LSST and photometric *Euclid* can discriminate between GR and $f(R)$

gravity at very high significance using lensing from Adv. ACTPol. However, this will require an RSD precision on the order of 10%, which is difficult but possible for *Euclid* and LSST. Photometric surveys combined with CMB lensing experiments can produce significant constraints to E_G that could help uncover the true nature of gravity.

The plan of the paper is as follows: in Section 3.3, we write the theoretical E_G for modified gravity, while Section 3.4 gives the estimator for E_G in terms of CMB lensing. In Section 3.5 we construct forecasts for various experiment configurations, and in Section 3.6 we present conclusions. We assume the combined CMASS/*Planck* cosmology [266, 22] with $\Omega_m h^2 = 0.1418$, $h = 0.676$, $\Omega_b h^2 = 0.0224$, $n_s = 0.96$, and $\sigma_8 = 0.8$.

3.3 Theory

We begin with the definition of E_G in Fourier space from Zhang et al. [409], given by

$$
\begin{aligned}
E_G(k, z) &= \frac{c^2 [\nabla^2 (\psi - \phi)]_k}{3H_0^2 (1+z)\theta(k)} \\
&= \frac{c^2 k^2 (\phi - \psi)}{3H_0^2 (1+z)\theta(k)},
\end{aligned}
\tag{3.1}
$$

where H_0 is the Hubble parameter today and $\theta(k)$ is the perturbation in the matter velocity field. Assuming a flat universe described by a Friedmann-Robertson-Walker (FRW) metric with perturbation fields ψ in the time component and ϕ in the spatial component, as well as negligible anisotropic stress and non-relativistic matter species, the time-time and momentum Einstein field equations in general relativity (GR) can be written in Fourier space as [156]

$$
\begin{aligned}
k^2 \psi &= -4\pi G a^2 \rho(a) \delta \\
\phi &= -\psi,
\end{aligned}
\tag{3.2}
$$

79

where a is the scale factor, ρ is the background matter density, and δ is the matter density perturbation. These equations are generalized to a modified gravity (MG) model such that

$$
\begin{aligned}
k^2\psi &= -4\pi G a^2 \mu(k,a)\rho(a)\delta \\
\phi &= -\gamma(k,a)\psi\,,
\end{aligned}
\tag{3.3}
$$

where $\mu(k,a)$ and $\gamma(k,a)$ are arbitrary functions of k and a, and $\mu = \gamma = 1$ for GR.

Using this formalism, we can write the numerator of E_G in Eq. 3.1 as

$$
\begin{aligned}
k^2(\phi - \psi) &= -k^2[1 + \gamma(k,a)]\psi \\
&= 4\pi G a^2 \rho(a)\mu(k,a)[1 + \gamma(k,a)]\delta\,.
\end{aligned}
\tag{3.4}
$$

Substituting $\rho(a) = \rho_0 a^{-3}$ and $\Omega_{m,0} = 8\pi G\rho_0/3H_0^2$, we find

$$
k^2(\phi - \psi) = \frac{3}{2}H_0^2\Omega_{m,0}(1 + z)\mu(k,a)[\gamma(k,a) + 1]\delta
\tag{3.5}
$$

The velocity perturbation θ can be written as $\theta = f\delta$ on linear scales. Combining this expression and Eq. 3.5 gives E_G from Eq. 3.1 as

$$
E_G(k,z) = \frac{\Omega_{m,0}\mu(k,a)[\gamma(k,a) + 1]}{2f}\,.
\tag{3.6}
$$

This expression gives us the correct value in the GR limit, namely $E_G = \Omega_{m,0}/f(z)$.

For $f(R)$ gravity [74] using the parametrization in Song et al. [354], μ and γ are given

by [376, 156]

$$\mu^{\text{fR}}(k, a,) = \frac{1}{1 - B_0 a^{s-1}/6} \left[\frac{1 + (2/3) B_0 \bar{k}^2 a^s}{1 + (1/2) B_0 \bar{k}^2 a^s} \right]$$

$$\gamma^{\text{fR}}(k, a) = \frac{1 + (1/3) B_0 \bar{k}^2 a^s}{1 + (2/3) B_0 \bar{k}^2 a^s} , \tag{3.7}$$

where $\bar{k} = k[2997.9 \, \text{Mpc}/h]$, $h = H_0/[100 \, \text{km/s/Mpc}]$, $s=4$ for models that follow the ΛCDM expansion history, and B_0 is a free parameter which is related to the Compton wavelength of an extra scalar degree of freedom and is proportional to the curvature of $f(R)$ today. Current measurements limit $B_0 < 5.6 \times 10^{-5}$ (1σ) [400, 37]. For this gravity model, E_G is given by

$$E_G^{\text{BZ}}(k, z) = \frac{1}{1 - B_0 a^{s-1}/6} \frac{\Omega_{m,0}}{f^{\text{BZ}}(k, z)} , \tag{3.8}$$

where $f^{\text{BZ}}(k, z)$ is the BZ growth rate, which is scale-dependent since μ is scale-dependent [156].

Chameleon gravity [186] is a Yukawa-type dark matter interaction equivalent to a class of scalar-tensor theories with a scalar field non-minimally coupled to the metric. For chameleon gravity, using the Bertschinger and Zukin (BZ) parametrization [45], μ and γ are given by [156]

$$\mu^{\text{Ch}}(k, a) = \frac{1 + \beta_1 \lambda_1^2 k^2 a^s}{1 + \lambda_1^2 k^2 a^s}$$

$$\gamma^{\text{Ch}}(k, a) = \frac{1 + \beta_2 \lambda_2^2 k^2 a^s}{1 + \lambda_2^2 k^2 a^s}$$

$$\lambda_2^2 = \beta_1 \lambda_1^2$$

$$\beta_2 = \frac{2}{\beta_1} - 1 , \tag{3.9}$$

where the typical ranges for β_1 and s are $0 < \beta_1 < 2$ and $1 \leq s \leq 4$. We will relate λ_1

81
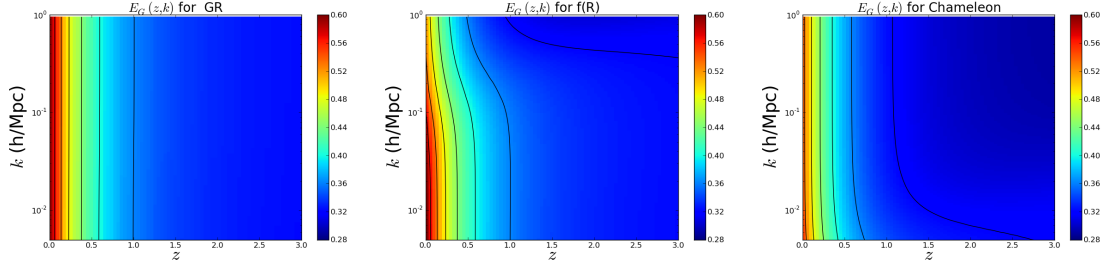
Figure 3.1: E_G as a function of redshift z and wavenumber k for GR (top), $f(R)$ gravity ($B_0 = 5.6 \times 10^{-5}$) (middle), and chameleon gravity ($\beta_1 = 1.2$, $B_0 = 0.4$, $s = 4$) (bottom). E_G for $f(R)$ gravity exhibits strong scale dependence, decreasing by $\sim 10\%$ at small scales.

to B_0, a parameter similar to that for $f(R)$ gravity but much less constrained due to the extra degree of freedom in the model. The typical range for B_0 in this model is [0,1] and is related to λ_1 by

$$B_0 = \frac{2\lambda_1^2 H_0^2}{c^2} \, . \tag{3.10}$$

We calculate $E_G(k, z)$ for GR, $f(R)$ gravity, and chameleon gravity using MGCAMB [203, 156], which we plot in Fig. 3.1. In GR, E_G is scale-independent. However, in $f(R)$ gravity E_G decreases at small scales by $\sim 10\%$, with the decrease being more pronounced at higher redshifts and smaller scales. On the other hand, chameleon gravity shifts E_G to lower values with respect to GR. These results show that the ability to measure the scale-dependence of E_G will be advantageous for constraining MG models, particularly for $f(R)$ gravity.

3.4 Estimator

Here we derive an estimator for E_G in terms of the galaxy-convergence cross-power spectrum $C_\ell^{g\kappa}$, the galaxy auto-power spectrum C_ℓ^{gg}, and the RSD parameter β. The estimator is

similar to the expression in Reyes et al. [303] using the galaxy-galaxy lensing cross-power spectrum.

Starting with Eq. 3.1, E_G can be estimated in terms of power spectra as

$$\hat{E}_G(k, z) = \frac{c^2 \hat{P}_{\nabla^2(\psi - \phi)g}(k)}{3H_0^2(1 + z)\hat{P}_{\theta g}(k)} \, , \tag{3.11}$$

where $P_{\nabla^2(\psi - \phi)g}$ is the galaxy-$\nabla^2(\psi - \phi)$ cross-power spectrum and $P_{\theta g}$ is the galaxy-peculiar velocity cross-power spectrum. Projecting 3D power spectra into angular quantities, we can estimate E_G as

$$\hat{E}_G(\ell, \bar{z}) = \frac{c^2 \hat{C}_\ell^{\kappa g}}{3H_0^2 \hat{C}_\ell^{\theta g}} \, . \tag{3.12}$$

$C_\ell^{\kappa g}$ is the galaxy-convergence angular cross-power spectrum, given on small scales using the Limber approximation[1] by

$$C_\ell^{\kappa g} = \frac{1}{2} \int_{\chi_1}^{\chi_2} d\chi \, W(\chi) f_g(\chi) \chi^{-2} P_{\nabla^2(\psi - \phi)g} \left(\frac{\ell}{\chi}, z \right) \, , \tag{3.13}$$

where f_g is the galaxy redshift distribution, χ_1 and χ_2 are the limits of the redshift distribution, and $W(\chi) = \chi(1 - \chi/\chi_{\text{CMB}})$ is the CMB lensing kernel. In order to match the kernel in the galaxy-convergence power spectrum, we define $C_\ell^{\theta g}$, the velocity-galaxy angular cross-power spectrum, to be

$$C_\ell^{\theta g} = \frac{1}{2} \int_{\chi_1}^{\chi_2} d\chi \, W(\chi) f_g(\chi) \chi^{-2} (1 + z) P_{\theta g} \left(\frac{\ell}{\chi}, z \right) \, . \tag{3.14}$$

This cross-power spectrum is a construct used to measure E_G without multiplicative bias, and is not equivalent to the RSD angular power spectrum derived in Padmanabhan et al.

---

[1]Since we are mainly interested in small scales ($\ell \gtrsim 100$), the Limber approximation is valid for most of the cases we consider (see Sec. 3.5.2)

[247].

In our analysis, as in Reyes et al. [303], we assume that the RSD parameter β will be measured separately, and we approximate the lensing kernel and β as constants over redshift within the integral, and we approximate $f_g(\chi) \simeq f_g^2(\chi)/f_g(\bar{\chi})$ within the redshift range. This approximation works well when the galaxy redshift distribution is highly peaked, which is especially true when we use small redshift bins in forecasts for upcoming surveys. Also, we assume from linear theory $\theta = f\delta$. In that case, Eq. 3.14 can be written as

$$
\begin{aligned}
C_\ell^{\theta g} &\simeq \frac{W(\bar{\chi})(1+\bar{z})}{2f_g(\bar{\chi})} \int_{\chi_1}^{\chi_2} d\chi\, f_g^2(\chi)\chi^{-2}\beta(z)P_{gg}\left(\frac{\ell}{\chi}, z\right) \\
&\simeq \frac{W(\bar{\chi})\beta(\bar{z})(1+\bar{z})}{2f_g(\bar{\chi})}C_\ell^{gg} ,
\end{aligned}
\tag{3.15}
$$

where C_ℓ^{gg} is the galaxy angular auto-power spectrum. Note that β could exhibit scale-dependence due to modified gravity through the growth rate. Thus, E_G in this case can be written as

$$
\hat{E}_G(\ell, \bar{z}) = \frac{2c^2\hat{C}_\ell^{\kappa g}}{3H_0^2(1+\bar{z})W(\bar{\chi})\Delta\chi\beta(\bar{z})\hat{C}_\ell^{gg}} ,
\tag{3.16}
$$

and we can write the error of E_G in terms of the errors of β and C_ℓ^{gg} as

$$
\frac{\sigma^2[E_G(\ell, \bar{z})]}{E_G^2} = \left[\left(\frac{\sigma(C_\ell^{\kappa g})}{C_\ell^{\kappa g}}\right)^2 + \left(\frac{\sigma(\beta)}{\beta}\right)^2 + \left(\frac{\sigma(C_\ell^{gg})}{C_\ell^{gg}}\right)^2\right] ,
\tag{3.17}
$$

which is strictly true if β and C_ℓ^{gg} are measured from separate surveys. This approximation does underestimate the error if β and C_ℓ^{gg} are measured from the same survey. However, it should not be much of a concern for us. For current surveys and upcoming spectroscopic surveys, the error is mainly dominated by the CMB lensing, which is a measure

independent of β and C_ℓ^{gg}. For example, switching between independent to dependent measures of β and C_ℓ^{gg} for BOSS reduces the signal-to-noise ratio for E_G by 1%. For upcoming photometric surveys when the lensing error is competitive with the error in β, the error in the galaxy clustering due to shot noise should be small enough such that it can be neglected, making the βC_ℓ^{gg} error independent of this concern. For example, switching between independent to dependent measures of β and C_ℓ^{gg} for *Euclid* photometric survey with Adv. ACTPol reduces the signal-to-noise ratio for E_G by 5%. The uncertainty in $C_\ell^{\kappa g}$ can be written as

$$\sigma^2(C_\ell^{\kappa g}) = \frac{(C_\ell^{\kappa g})^2 + (C_\ell^{\kappa\kappa} + N_\ell^{\kappa\kappa})(C_\ell^{gg} + N^{gg})}{(2\ell + 1)f_{\text{sky}}}\,, \tag{3.18}$$

where $C_\ell^{\kappa\kappa}$, the convergence auto-power spectrum, is computed from CAMB [203], $N_\ell^{\kappa\kappa}$ is the noise in the convergence power spectrum computed using the formalism in Hu and Okamoto [162], and N^{gg} is the shot noise.

A precise measurement of E_G will be slightly biased from the true value due to several reasons similar to those outlined in the Appendix of Reyes et al. [303]. For one, galaxy redshift distributions can exhibit a spread and skewness, causing the approximation in Eq. 3.15 to break down. However, we can characterize this deviation analytically as a function of angular scale. Also, in order to extend our measurement of E_G to small scales, we must correct for the scale-dependence of the bias due to clustering at nonlinear scales. We may also need to consider scale-dependent β due to nonlinear density and velocity perturbations, although velocity perturbations tend to stay linear at smaller scales than for density perturbations. In addition, constraints on modified gravity parameters will have to account for the scale dependence of β due to the growth rate. We expect these effects to be small and will neglect them in our forecasts.

3.5 Forecasts

In this section we will predict the ability of current and future surveys to measure E_G and differentiate between GR and MG models. In all our forecasts we will assume GR when calculating uncertainties. We describe the sensitivity of the measured E_G with the signal-to-noise ratio (SNR) of E_G marginalized over angular scale and redshift, given by

$$\mathrm{SNR}^2(E_G) = \sum_{\ell, z_i} \frac{[E_G^{\mathrm{GR}}(z_i)]^2}{\sigma^2[E_G(\ell, z_i)]} , \tag{3.19}$$

where z_i denotes redshift bins. We also calculate the χ^2 value between GR and MG models to determine if a particular E_G measurement could distinguish between GR and a given MG model. We write χ^2 as

$$\chi^2(E_G) = \sum_{\ell, z_i} \frac{[E_G^{\mathrm{MG}}(\ell, z_i) - E_G^{\mathrm{GR}}(z_i)]^2}{\sigma^2[E_G(\ell, z_i)]} , \tag{3.20}$$

where $E_G^{\mathrm{MG}}(\ell, z_i)$ is the E_G estimate for a given MG model, which is generally ℓ-dependent. This χ^2 is related to the likelihood ratio between GR and modified gravity, assuming modified gravity is the true theory, and $\chi^2 \gg 1$ means the two theories can be differentiated at high significance. Throughout the section we quote $\chi_{\mathrm{rms}} = \sqrt{\chi^2}$. Note that for the following limits, $f(R)$ gravity is set to its upper limit value $B_0 = 5.6 \times 10^{-5}$, and that chameleon gravity's base set of parameters is $B_0 = 0.4$, $\beta_1 = 1.2$, and $s = 4$, unless otherwise stated.

3.5.1 Current Surveys

We begin with forecasts of E_G measurements from the publicly available *Planck* CMB lensing map [271] and the CMASS and LOWZ spectroscopic galaxy samples from BOSS DR11 [22], as well as the spectroscopic quasar (QSO) sample [250] from DR11. We use

Table 3.1: Properties of the various spectroscopic surveys considered in our analysis.

Survey	z	Area (deg^2)	N_{gal}
BOSS CMASS	0.43–0.7	7900	704,000
BOSS LOWZ	0.15–0.43	6900	306,000
BOSS QSOs	2.1–3.5	10,200	175,000
DESI ELGs	0.6–1.7	14,000	1.8×10^7
DESI LRGs	0.6–1.2	14,000	4.1×10^6
DESI QSOs	0.6–1.9	14,000	1.9×10^6
Euclid	0.5–2.0	20,000	1.7×10^7
WFIRST	1.05-2.9	2000	3.0×10^7

the noise estimate given in the public *Planck* CMB lensing map. The total number of galaxies (or quasars) within each sample along with the survey area are listed in Table 3.1. For CMASS, we use the measurements of $b\sigma_8$ and $f\sigma_8$ from Samushia et al. [326] to set b[CMASS]=2.16 and $\sigma(\beta)/\beta \sim 10\%$ for the entire redshift range. The corresponding values for the LOWZ sample have not been measured model-independently for DR11, so we assume a 10% measurement of β for the entire redshift range and, as in Tojeiro et al. [374], we assume b[LOWZ]=1.85. We use Eq. 3.17 to calculate the E_G uncertainty for these samples. For the BOSS quasar sample, we use the BOSS DR9 bias measurements from White et al. [396], assuming the average value $b_{\mathrm{QSO}} = 3.83$. We also assume a 15% β measurement in each of two redshift bins for the BOSS quasars. This is a bit optimistic, considering there are systematic issues on linear scales with measuring RSD from BOSS quasars. However, we confirm that even a measurement error of 100% $[\sigma(\beta)/\beta = 1]$ only increases the errors on E_G by 5%.

We plot the signal-to-noise ratio (SNR) for $10 < \ell < 1000$ for the CMASS, LOWZ, and quasar samples in Fig. 3.2. The peaks of all three plots vary due to the redshift of each sample. We find that most of the signal for E_G comes from linear to quasi-linear scales. We set the maximum wavenumber within quasi-linear scales to k_{NL}, where $\Delta(k_{\mathrm{NL}}, z) = k_{\mathrm{NL}}^3 P(k_{\mathrm{NL}}, z)/(2\pi^2) = 1$. We find k_{NL}[LOWZ,CMASS]=[0.354,0.466]

h/Mpc. For the following forecasts, we limit the angular scales used to $\ell > 100$ to avoid large-scale systematic effects. In Fig. 3.2 we also show how the SNR increases with ℓ_{max} for CMASS and LOWZ. We see that most of the sensitivity is obtained by $\ell \sim 500$ for CMASS and $\ell \sim 300$ for LOWZ. We set these as our limits in ℓ for CMASS and LOWZ, while for quasars we will use all scales $\ell < 1000$.

We also consider how our forecasts for E_G are affected if we restrict the scales used to measure E_G to only linear scales for CMASS and LOWZ. Note we define linear scales $k < k_{\mathrm{lin}}$ as those for which the matter power spectrum $P(k)$ computed from N-body simulations differs from the linear $P(k)$ by less than a few percent. We determine which scales are linear using the linear and N-body $P(k)$ predictions from Fig. 2 of Vlah et al. [384]. We find that the purely linear scales for CMASS and LOWZ are limited to $k \lesssim 0.1h$/Mpc, which is significantly less than k_{NL} determined above for these surveys. As can be seen in Fig. 3.2, the surveys each lose about half their signal to noise if the measurements are restricted to linear scales.[2] Note that as the redshift of the survey increases, the more scales are linear. However, E_G estimates for modified gravity, particularly for $f(R)$ gravity, tend to differ from GR mainly at low redshifts. Thus, differentiating MG models from GR requires measuring E_G at quasi-linear scales.

Next we forecast constraints on E_G from BOSS surveys cross-correlated with the *Planck* CMB lensing map. We find promising results, listed in Table 3.2. Specifically, we predict SNRs of 9.3, 5.2, and 6.8 for the CMASS, LOWZ, and QSO surveys, respectively. We translate these into E_G values in Fig. 3.3. We see that our LOWZ measurement would be comparable to that from Reyes et al. [303], although this may be somewhat optimistic considering LOWZ may exhibit unforeseen systematics. However, combining all three measurements would give a SNR of 13, or an 8% measurement. This assumes we can measure RSD from quasars, which is very optimistic considering systematic errors that exist in

---

[2] ℓ_{lin}[LOWZ] < 100, so we set ℓ_{min}[LOWZ] $= 50$ when considering the total signal.
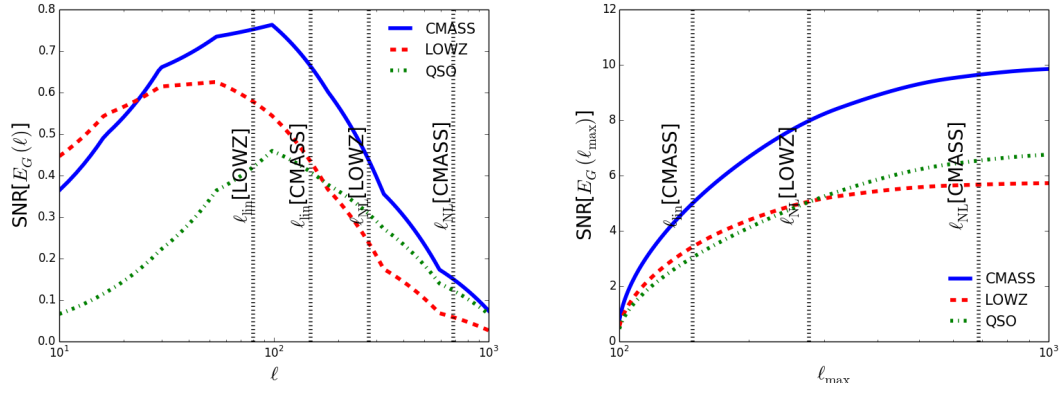
Figure 3.2: (*Top*): The SNR of E_G as a function of ℓ for the *Planck* CMB lensing map cross-correlated with various BOSS DR11 surveys. We also mark with vertical lines where the angular modes correspond to nonlinear scales. We see that most of the sensitivity will come from linear scales, although our chosen cuts in ℓ listed in the text will lose some sensitivity. (*Bottom*): The relation of the SNR of E_G with an increasing $\ell_{\max}$ for the BOSS DR11 samples with the *Planck* CMB lensing map. We see that most of the sensitivity is gained using $\ell_{\max} \sim 300\,(500)$ for LOWZ (CMASS), while the sensitivity for the QSO sample is still increasing at $\ell_{\max} = 1000$.

quasars at large scales [292]. We also consider our fiducial model of $f(R)$ gravity corresponding to the upper limit on the BZ parameter B_0. We see that the $f(R)$ prediction differs from GR only at lower redshifts, greatly suppressing the utility of the quasar measurement and slightly increasing the utility of the LOWZ measurement. $\chi_{\rm rms} = \sqrt{\chi^2}$ for CMASS and LOWZ are both less than unity, implying that these surveys are not able to significantly tighten constraints on B_0. The sensitivity to chameleon gravity is only slightly better, in that CMASS, LOWZ, and BOSS QSOs together could differentiate models with very high (or low) values of β_1 from GR due to the rapid evolution of E_G with β_1.

3.5.2 Upcoming Spectroscopic Surveys

We now consider upcoming spectroscopic surveys. We consider two cases for the CMB lensing map, including (1) the full Planck CMB lensing map and (2) the Advanced ACT-Pol[3] CMB lensing map. In both cases, we assume the CMB lensing maps will be estimated using the temperature map and both E and B polarization maps, and we assume the B map only contains noise. We predict the noise in the *Planck* lensing map assuming the detector sensitivity and beam sizes listed in the *Planck* Bluebook [372]. Advanced ACTPol will survey 20,000 deg^2, and its increased temperature and polarization sensitivity will create a CMB lensing map that is an order of magnitude more sensitive than *Planck*. The specifications we use for Adv. ACTPol are listed in Table 3.3. For spectroscopic surveys, we consider the DESI emission line galaxy (ELG), luminous red galaxy (LRG), and quasar surveys, as well as the *Euclid* Hα survey and the WFIRST Hα and OIII combined survey. The properties of the surveys are listed in Table 3.1. For DESI, we assume the same values as in the DESI Conceptual Design Report[4]: $b_{\rm LRG}D(z) = 1.7$, $b_{\rm ELG}D(z) = 0.84$, $b_{\rm QSO}D(z) = 1.2$, where $D(z)$ is the growth factor. We also assume a 4% error in β within

---

[3]private communication with Advanced ACTPol team
[4]http://desi.lbl.gov/cdr/
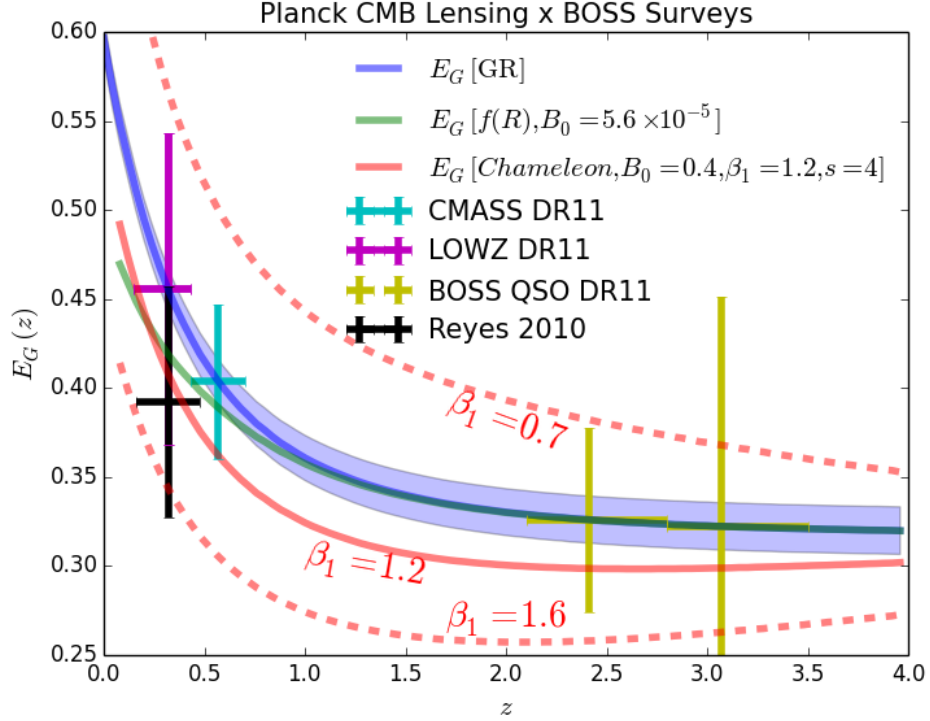
Figure 3.3: E_G forecasts for BOSS galaxy surveys cross-correlated with the current *Planck* CMB lensing map, in comparison with the latest measurement of E_G using galaxy-galaxy lensing [303]. Note that we do not translate their E_G measurement from the WMAP3 cosmology [358] to the cosmology we assume. The band around the GR prediction corresponds to the likelihood function of E_G based on *Planck* and BOSS constraints on cosmological parameters. The E_G predictions for $f(R)$ gravity and chameleon gravity are averaged over the wavenumber range at every redshift corresponding to $100 < \ell < 500$, the range used for CMASS. The dashed lines show chameleon gravity predictions for higher and lower values of β_1. These surveys are not sensitive enough to tighten constraints on $f(R)$ gravity set by current measurements.

$\Delta z = 0.1$ bins. Note that Adv. ACTPol's survey area overlaps with only $\sim$75% of DESI's area; we take this into account in our DESI forecasts. For *Euclid* and WFIRST ELGs, we assume $b(z) = 0.9 + 0.4z$, a fit [367] to semi-analytic models [244] that compares well with data. We determine the redshift distribution of *Euclid* Hα galaxies using the Hα luminosity function from Colbert et al. [81] and assume a flux limit of 4×10^{-16}. This flux limit is in the middle of the range being considered, so the following *Euclid* forecasts can change accordingly. We also assume a 3% error in β within $\Delta z = 0.1$ bins for *Euclid* and WFIRST [17]. For all subsequent forecasts, we assume E_G measurements over angular scales $100 \leq \ell \leq 500$.

The forecasts are listed in Table 3.2, but here we list some highlights. Figs. 3.4 and 3.5 show that DESI and *Euclid* combined with *Planck* can each measure E_G almost at the 2% level, unlike WFIRST which is limited by its small survey area. This should allow DESI and *Euclid* combined with *Planck* to produce constraints of some models, and β_1 constraints should get tighter than those from BOSS. For Adv. ACTPol, DESI should reach a 1% measurement of E_G, allowing it to differentiate GR and chameleon gravity with $\beta_1 > 1.1$ at the 5σ level. DESI produces tighter constraints than *Euclid* due to its higher number density at low redshifts. Note that we use a moderate number of redshift slices for each survey, as seen in Figs. 3.4 and 3.5. The redshift accuracy of these spectroscopic surveys would allow us to use much smaller redshift bins in an attempt to decrease errors in E_G. This does not work, however, because each of these surveys are shot-noise dominated on the scales where the E_G signal dominates, increasing the errors in the galaxy-CMB lensing cross-correlation.[5] We also considered more pessimistic errors in β, finding that increasing the error in β by a factor of 3 did not noticeably increase E_G errors from *Planck*, while it increased E_G errors from Adv. ACTPol by less than 2%.

---

[5]Using the formalism in Loverde and Afshordi [215], the Limber approximation breaks down slightly for *Euclid* with Adv. ACTPol at some of the larger redshifts, where $\chi/\Delta\chi \gtrsim 100$. This should not affect the results significantly.
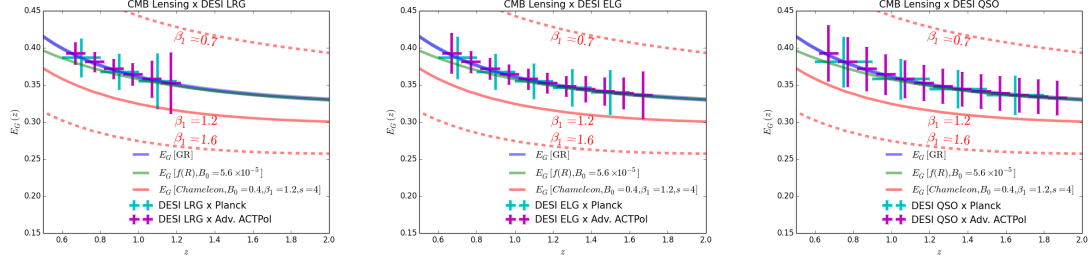
Figure 3.4: E_G forecasts for DESI galaxy surveys cross-correlated with the final *Planck* CMB lensing map and with the Advanced ACTPol lensing map. The points for Adv. ACT-Pol are shifted rightward by 0.02 for clarity. The E_G predictions for $f(R)$ and chameleon gravity are averaged over the wavenumber range at every redshift corresponding to $100 < \ell < 500$. The dashed lines show chameleon gravity predictions for higher and lower values of β_1.
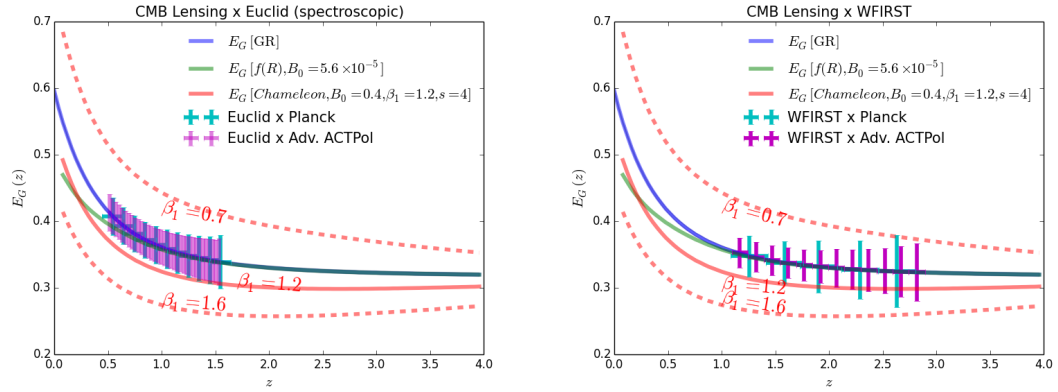
Figure 3.5: E_G forecasts for Euclid and WFIRST galaxy surveys cross-correlated with the final *Planck* CMB lensing map and with the Advanced ACTPol lensing map. The points for WFIRST and Adv. ACTPol are shifted rightward by 0.02 for clarity. Note the *Euclid*-Adv. ACTPol forecasts contain 50 bins in redshift.

Table 3.2: Forecasts of the signal-to-noise ratio (SNR) and $\chi_{\rm rms} = \sqrt{\chi^2}$ between GR and $f(R)$ or chameleon gravity for E_G measurements from various current and upcoming surveys. For $f(R)$ gravity, we assume $B_0 = 5.65 \times 10^{-5}$. For chameleon gravity, the first column assumes $B_0 = 3.2 \times 10^{-4}$ with β_1 and s set to the base model, and the second column assumes $\beta_1 = 1.1$ with B_0 and s set to the base model (see the beginning of Sec. 3.5).

Survey (Galaxy $\times$ CMB lensing)	z	SNR	$\chi_{\rm rms}[f(R)]$	$\chi_{\rm rms}[Cham, B_0]$	$\chi_{\rm rms}[Cham, \beta_1]$
BOSS CMASS $\times$ *Planck* (current)	0.43–0.7	9.3	0.40	0.53	0.52
BOSS LOWZ $\times$ *Planck* (current)	0.15–0.43	5.2	0.42	0.42	0.30
BOSS QSOs $\times$ *Planck* (current)	2.1–3.5	6.8	0.051	0.042	0.26
BOSS (CMASS+LOWZ+QSOs) $\times$ *Planck* (current)	–	13	0.58	0.68	0.65
DESI ELGs $\times$ *Planck* (full)	0.6–1.7	31	0.51	0.84	1.5
DESI LRGs $\times$ *Planck* (full)	0.6–1.2	23	0.55	0.83	1.1
DESI QSOs $\times$ *Planck* (full)	0.6–1.9	25	0.29	0.52	1.2
DESI (ELG+LRG+QSO) $\times$ *Planck* (full)	–	46	0.80	1.3	2.2
DESI ELGs $\times$ Adv. ACTPol	0.6–1.7	73	1.4	2.3	3.6
DESI LRGs $\times$ Adv. ACTPol	0.6–1.2	56	1.8	2.5	2.9
DESI QSOs $\times$ Adv. ACTPol	0.6–1.9	50	0.66	1.1	2.4
DESI (ELG+LRG+QSO) $\times$ Adv. ACTPol	–	105	2.4	3.6	5.2
Euclid (spectro) $\times$ *Planck* (full)	0.5–2.0	41	0.96	1.4	2.1
Euclid (spectro) $\times$ Adv. ACTPol	0.5–2.0	83	2.4	3.2	4.1
WFIRST $\times$ *Planck* (full)	1.05-2.9	20	0.12	0.21	0.91
WFIRST $\times$ Adv. ACTPol	1.05-2.9	44	0.28	0.55	2.0
DES $\times$ *Planck* (full)	0.0–2.0	35	1.2	1.3	1.7
DES $\times$ Adv. ACTPol	0.0–2.0	78	3.0	3.3	3.9
LSST $\times$ *Planck* (full)	0.0–2.5	84	5.1	5.2	6.0
LSST $\times$ Adv. ACTPol	0.0–2.5	189	15	15	16
Euclid (photo) $\times$ *Planck* (full)	0.0–3.7	90	4.9	5.1	5.9
Euclid (photo) $\times$ Adv. ACTPol	0.0–3.7	205	15	15	16

Table 3.3: Properties of the Advanced ACTPol CMB survey. Note that the area of the survey is 20,000 deg^2 and we assume $\Delta_P = \Delta_T \sqrt{2}$.

Center Freq.	Δ_T (μK-arcmin)[6]	$\theta_{\rm res}$ (arcmin)
90 GHz	7.8	2.2
150 GHz	6.9	1.3
230 GHz	25	0.9

3.5.3 Upcoming Photometric Surveys

In this section we consider measuring E_G from upcoming photometric galaxy surveys. These surveys, which measure less precise redshifts than spectroscopic surveys, are tailored for measuring weak lensing and not RSD. However, the errors in E_G are dominated by the CMB lensing at lower redshifts where the E_G signal is highest, meaning that reducing shot noise in the lensing-galaxy cross-correlation through attaining higher number densities is be more important than having precise redshifts. Also, upcoming photometric surveys plan to approach redshift precisions of $\sigma_z/(1 + z) \sim 0.05$. Recent work has shown that upcoming photometric surveys could measure RSD [311, 93, 26]. This may cause photometric surveys to produce competitive E_G measurements. It should be noted that Adv. ACTPol gets close to the lensing noise limit where errors in RSD could begin to matter. An E_G measurement from a future CMB experiment that surpasses Adv. ACTPol may reach the limit such that RSD errors may begin to dominate. Also, the photometric redshift errors and systematic errors within photometric surveys will make measuring RSD with photometric surveys more difficult than with spectroscopic surveys [152].

We will construct forecasts for photometric surveys of DES, LSST, and *Euclid*. The properties of these surveys are listed in Table 3.4. For DES and LSST, we model the normalized redshift distribution in the same manner as Font-Ribera et al. [120] as

$$f_g(z) = \frac{\eta}{\Gamma\left(\frac{\alpha+1}{\eta}\right) z_0} \left(\frac{z}{z_0}\right)^\alpha \exp^{-(z/z_0)^\eta}, \tag{3.21}$$

where $\alpha = 1.25\,(2.0)$, $\eta = 2.29\,(1.0)$, and $z_0 = 0.88\,(0.3)$ for DES (LSST). For *Euclid* we use estimates of the redshift distribution based on the CANDELS GOODS-S catalog [137, 160]. For all three surveys we assume $b(z) = 0.9 + 0.4z$ [367, 244], as in the spectroscopic case. For RSD, we assume a 17% error in β over $\Delta z = 0.1(1 + z)$ bins for

Table 3.4: Properties of various galaxy photometric surveys included in our analysis.

Survey	z	Area (deg^2)	N_{gal}	$\sigma_z/(1+z)$
DES	0.0–2.0	5000	2.16×10^8	0.07
LSST	0.0–2.5	20,000	3.6×10^9	0.05
Euclid	0.0–3.7	20,000	1.86×10^9	0.05

DES [311]. Since *Euclid* and LSST will cover about 4 times the volume of DES, we expect the errors on β to decrease by a factor of 2.

We find that photometric surveys can discriminate between gravity models more effectively than spectroscopic surveys, as can be seen in Fig. 3.6 and Table 3.2. DES, with its higher number density, has constraining power comparable to DESI and *Euclid* with their larger survey areas. LSST and photometric *Euclid* combined with *Planck* approach 1% measurements, while substituting *Planck* for Adv. ACTPol exceeds that level. In Fig. 3.7, we display constraints on E_G in individual k-bins at $z = 1 \pm 0.05$ from LSST with both CMB surveys, finding that at this redshift the constraining power between gravity models mainly appears at smaller scales. These two photometric surveys combined with Adv. ACTPol could differentiate $f(R)$ gravity and GR at the 13σ level for $B_0 > 10^{-7}$, severely testing $f(R)$ as a viable theory. These surveys also would place significant tests on chameleon gravity, although the value of χ^2 decreases when smaller values of B_0 are assumed. Also, catastrophically increasing the errors in β by a factor of 3 in DES increases the errors in E_G using *Planck* by only 5%. Similar increases also apply to *Euclid* and WFIRST. For Adv. ACTPol, E_G is more sensitive to this effect, in that increasing β errors by a factor of 3 increases E_G errors by 20%. This suggests that in this regime, RSD errors must remain low to take advantage of the power of photometric surveys to measure E_G, on the order of 10% for *Euclid* or LSST.
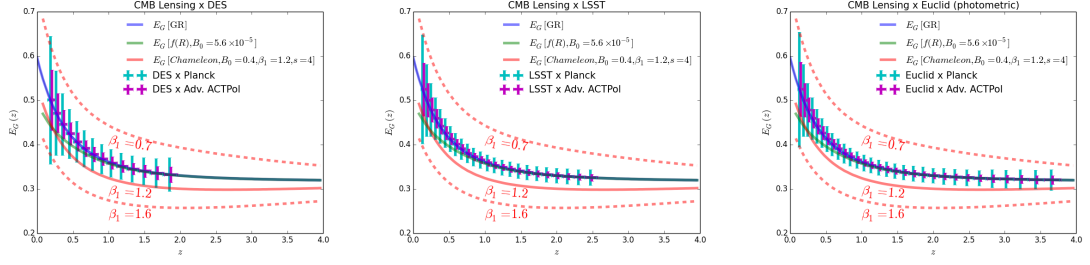
Figure 3.6: E_G forecasts for DES, LSST, and Euclid photometric galaxy surveys cross-correlated with the final *Planck* CMB lensing map and with the Advanced ACTPol lensing map. The points for Adv. ACTPol are shifted rightward by 0.02 for clarity. Note that the forecasts involving Adv. ACTPol require a precision in the RSD parameter β of 10%, which may need to be obtained from a spectroscopic survey.
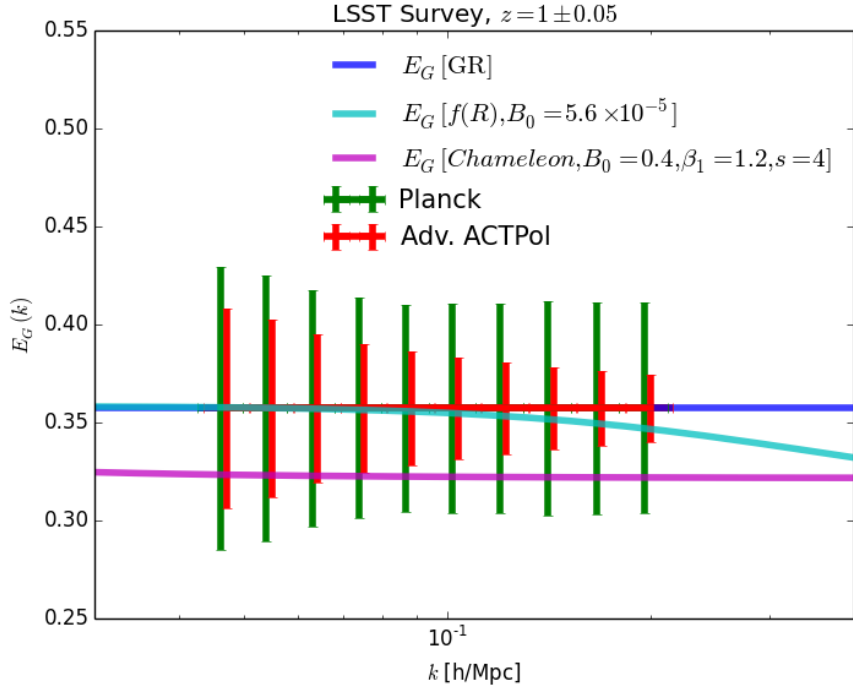
Figure 3.7: $E_G(k)$ forecasts for the LSST photometric galaxy survey in the redshift bin $z = 1 \pm 0.05$ cross-correlated with the final *Planck* CMB lensing map and with the Advanced ACTPol lensing map. The points for Adv. ACTPol are shifted rightward by 2% for clarity. We also plot E_G predictions for $f(R)$ gravity and chameleon gravity.

97

3.6 Conclusions

In this work we consider CMB lensing as a probe of E_G, a statistic that differentiates between gravity models on cosmological scales. We derive E_G for the general MG parametrization described by $\mu(k, z)$ and $\gamma(k, z)$, as well as for the specific MG models of $f(R)$ gravity and chameleon gravity. We show that generally, E_G for these models are scale-dependent, causing the scale-dependent E_G to be useful for differentiating between MG models and GR.

We produce forecasts for current surveys, showing that BOSS spectroscopic galaxies and quasars combined with *Planck* CMB lensing each measure E_G at the 8% level. Our results suggest that CMB lensing contributes most of the error, and that measuring E_G on quasi-linear scales is required to produce significant constraints.

For upcoming surveys, we find that upcoming photometric surveys will outperform spectroscopic surveys due to their higher number densities, even at the expense of having less precise redshifts. Specifically, LSST and photometric *Euclid* should produce errors on E_G less than 1%, and place very tight constraints on $f(R)$ and chameleon gravity, assuming these surveys can measure RSD with a precision of around 10%. However, these measurements will be limited by how well these photometric surveys can identify and remove systematic errors. Also, since it is necessary to use E_G from quasi-linear scales, measuring RSD effects at these scales will be challenging. Finally, it is possible that more precise estimates of E_G and more precise measurements of cosmological parameters may change the underlying E_G errors slightly. However, CMB lensing has the potential to probe E_G with very high sensitivities without the astrophysical contaminants of galaxy-galaxy lensing, and reveal the nature of gravity.

Acknowledgments

Chapter 4

Constraining Gravity at the Largest Scales through CMB Lensing and Galaxy Velocities

Anthony R. Pullen, Shadab Alam, Siyu He, and Shirley Ho

4.1 Abstract

We demonstrate a new method to constrain gravity on the largest cosmological scales by combining measurements of cosmic microwave background (CMB) lensing and the galaxy velocity field. E_G is a statistic, constructed from a gravitational lensing tracer and a measure of velocities such as redshift-space distortions (RSD), that can discriminate between gravity models while being independent of clustering bias and σ_8. While traditionally, the lensing field for E_G has been probed through galaxy lensing, CMB lensing has been proposed as a more robust tracer of the lensing field for E_G at higher redshifts

while avoiding intrinsic alignments. We perform the largest-scale measurement of E_G ever, up to 150 Mpc/h, by cross-correlating the *Planck* CMB lensing map with the Sloan Digital Sky Survey III (SDSS-III) CMASS galaxy sample and combining this with our measurement of the CMASS auto-power spectrum and the RSD parameter β. We report $E_G(z = 0.57) = 0.243 \pm 0.060\,(\text{stat}) \pm 0.013\,(\text{sys})$, a measurement in tension with the general relativity (GR) prediction at a level of 2.6σ. Note that our E_G measurement deviates from GR only at scales greater than 80 Mpc/h, scales which have not been probed by previous E_G tests. Upcoming surveys, which will provide an order-of-magnitude reduction in statistical errors, can significantly constrain alternative gravity models when combined with better control of systematics.

4.2 Introduction

Since cosmic acceleration was first discovered [307, 263], there have been many investigations seeking to determine its cause. The cosmological constant, a form of dark energy [253] that exhibits a negative pressure $p = -\rho$, can explain the cosmic acceleration and is consistent with measurements of the cosmic microwave background (CMB) [40, 280, 283] and large-scale structure (LSS) [22]. However, if gravity were weaker than predicted by general relativity (GR) on cosmological scales, then this could also cause the cosmic expansion to accelerate. This concept, called *modified gravity*, cannot be distinguished from dark energy by measuring the cosmic expansion, *i.e.* through supernova [363] or baryon acoustic oscillations [22], alone, requiring a measurement of the growth of structure, *e.g.* through redshift-space distortions (RSD) [179, 139, 47, 326, 11, 10], to break this degeneracy. Several upcoming observatories hope to test general relativity on cosmological length scales using these methods.

E_G [409] is a statistic that probes gravity by measuring the ratio between curvature and

velocity perturbations using measurements of gravitational lensing, galaxy clustering, and growth of structure. This quantity is a member of a general class of parametrized deviations from GR [*e.g.* see Hojjati et al. [156], Di Valentino et al. [102], and references therein]. E_G is related to the Poisson field equation which is modified between various gravity models, breaking the degeneracy and model dependence in current cosmological probes of gravity and dark energy. It is also independent of clustering bias on linear scales; thus unlike probes of gravity using measurements of structure growth directly, the clustering bias does not have to be modeled or marginalized in E_G measurements. The lensing signal within E_G has traditionally been probed with galaxy-galaxy lensing [221], or lensing of galaxies by foreground galaxies. In Reyes et al. [303], E_G was measured at $z = 0.32$ over scales 10–50 Mpc/h to be 0.39±0.06. Recently, a measurement of E_G from galaxy lensing was performed using several datasets [55], finding, over scales 10–50 Mpc/h, to be 0.48±0.10 at $z = 0.32$ and 0.30±0.07 at $z = 0.57$. All these measurements are consistent within 1σ with predicted GR values. In other work, constraints for future galaxy lensing surveys were forecasted [198].

It has recently been proposed [294] to measure E_G using galaxy-CMB lensing [281], a more robust lensing tracer that can probe E_G at earlier times and larger scales than is currently possible with galaxy lensing. In addition, measuring E_G using CMB lensing has advantages over galaxy-galaxy lensing. Source galaxies in galaxy-galaxy lensing are usually assigned photometric redshifts with non-negligible uncertainties and can only be lensed by foreground galaxies at low redshifts. For CMB lensing, the source redshift, $z = 1100$ is well known and extremely high relative to galaxies ($z \sim 1$), allowing probes of E_G at much higher redshifts. Also, the intrinsic distribution of CMB photons is nearly Gaussian [278] and is not affected by complex astrophysical effects, such as intrinsic alignments in galaxy lensing. It was shown in Pullen et al. [294] that Advanced ACTPol [141], an upcoming CMB survey, combined with a spectroscopic galaxy survey, *e.g.* the Dark Energy

Spectroscopic Instrument (DESI) [200], would measure E_G at 2% precision, or $< 1\%$ precision with a photometric survey, *e.g.* the Large Synoptic Survey Telescope (LSST) [216]. Recently, Giannantonio et al. [126] proposed a bias-independent statistic D_G, an alternative to E_G that does not include growth information. This work was also able to measure D_G using the *Planck* CMB lensing map and the Dark Energy Survey (DES) [371] with photometric redshifts. However, unlike E_G, D_G cannot be directly related to modified gravity models.

In this analysis, we measure E_G by combining measurements of the CMB lensing convergence map [281] from the latest *Planck* data release [276] with the galaxy distribution from the CMASS galaxy sample [22] from the Sloan Digital Sky Survey (SDSS) III [114]. We also test for various systematic effects in both the CMASS galaxy map and the *Planck* CMB lensing convergence map. We find $E_G(z = 0.57) = 0.243 \pm 0.060\,(\text{stat}) \pm 0.013\,(\text{sys})$, which is in tension with the expected ΛCDM value of $E_G(z = 0.57|\text{GR}) = 0.402 \pm 0.012$. This tension appears at scales greater than 80 Mpc/h, scales which have not been probed by previous E_G measurements. By probing gravity over the scales 23–150 Mpc/h, this is the largest-scale measurement of E_G ever performed, and only next-generation surveys, *e.g. Euclid* [195], will be able to probe these scales with E_G using galaxy lensing.

The plan of our paper is as follows: in Section 4.3 we review the expression for E_G and how we estimate it, and we describe the *Planck* and CMASS data products we use in Section 4.4. In Section 4.5 we describe how our angular power spectrum models are constructed. We describe our estimators for the angular power spectra and β in Section 4.6, and we present our results in Section 4.7 and estimates of systematic errors in Section 4.8. We conclude in Section 4.9.

4.3 E_G Formalism

Here we present a brief review of the expression for E_G and how it is measured. For a more comprehensive presentation, see Zhang et al. [409] and Pullen et al. [294].

The quantity E_G is given by the expression (in Fourier space)

$$E_G(k) = \frac{c^2 k^2 (\phi - \psi)}{3H_0^2 (1 + z)\theta(k)} \, , \tag{4.1}$$

assuming a flat universe described by a Friedmann-Robertson-Walker (FRW) metric, where H_0 is Hubble's constant, $\theta(k)$ is the perturbation in the divergence of the velocity field, and ψ and ϕ are the time and space perturbations in the FRW metric. On linear scales, $\theta(k) = f(z)\delta(k)$, where δ is the matter field perturbation, and $f(z)$ is the logarithmic rate of structure growth, also known as the growth rate. By assuming GR, non-relativistic matter species, and no anisotropic stress, it can be shown using the Poisson equation from GR that Eq. 4.1 simplifies to

$$E_G = \frac{\Omega_{m,0}}{f(z)} \, , \tag{4.2}$$

where $\Omega_{m,0}$ is the relative matter density today and $f(z) \simeq [\Omega_m(z)]^{0.55}$ is the growth rate for GR. Note that E_G for ΛCDM with GR is scale-independent. For modified gravity theories, the expressions for $E_G(z)$ and $f(z)$ can be altered, producing values for E_G that are distinct from GR and possibly scale-dependent.

E_G can be estimated as

$$E_G(\ell) = \Gamma \frac{C_\ell^{\kappa g}}{\beta C_\ell^{gg}} \, , \tag{4.3}$$

where Γ is a prefactor depending on Hubble parameter $H(z)$, the CMB lensing kernel

$W(z)$, and the galaxy redshift distribution $f_g(z)$ (see Eq. 4.15), $C_\ell^{\kappa g}$ is the CMB lensing convergence-galaxy angular cross-power spectrum, C_ℓ^{gg} is the galaxy angular auto-power spectrum, and β is the redshift space distortion parameter. In the linear perturbation regime, $\beta = f/b_g$ where f is the growth rate and b_g is the clustering bias of galaxies relative to matter perturbations. Note that κ is the lensing convergence, which is a line-of-sight integral of $\nabla^2(\psi - \phi)$ over the lensing kernel. As in previous measurements using galaxy-galaxy lensing, E_G measured using CMB lensing is independent of clustering bias and the amplitude of matter perturbations parametrized by σ_8, eliminating the need for measurements of (or marginalizing over) b_g and σ_8 as in other gravity probes.

4.4 Data

4.4.1 Cosmic Microwave Background Lensing Map

The cosmic microwave background (CMB) lensing map was provided by the Planck Collaboration [276]. The *Planck* satellite observed the intensity and polarization fields of the cosmic background radiation (CBR) over the whole sky. The CBR was measured between August 2009 and August 2013 using an array of 74 detectors consisting of two instruments. The Low-Frequency Instrument (LFI) [44, 227] consists of pseudo-correlation radiometers and contains 3 channels with frequencies 30, 40 and 70 GHz. The High-Frequency Instrument (HFI) [193, 288] consists of bolometers and contains 6 channels with frequencies 100, 143, 217, 353, 545, and 857 GHz. These maps were combined and foreground-cleaned using the SMICA code [277] to produce temperature and E and B polarization maps of the CMB with HEALPix [130] pixelization with $N_{\mathrm{side}} = 2048$ over approximately 70% of the sky. The temperature and polarization maps over all available frequencies are combined to reconstruct the minimum-variance CMB lensing field [281]; however, most of the lensing

information comes from the 143 GHz and 217 GHz maps. These channels have Gaussian beams with full-width-at-half-maxima (FWHMs) of 7' and 5', respectively, and temperature (polarization) noise levels of 30 μK-arcmin (60 μK-arcmin) and 40 μK-arcmin (95 μK-arcmin), respectively. The lensing map was checked for systematic effects from the Galaxy, point sources, dust, and instrumental noise bias [281], which were found to be mostly sub-dominant to the statistical errors.

4.4.2   Galaxy Survey Maps

We use the CMASS spectroscopic sample from the Sloan Digital Sky Survey (SDSS) III [114] Baryon Oscillations Spectroscopic Survey (BOSS) [97] Data Release 11 (DR11) [22, 8], which was publicly released with the final BOSS data set. SDSS-III, like SDSS I and II [408], consists of a 2.5 m telescope [135] with a five-filter ($ugriz$) [121, 352, 103] imaging camera [133], designed to image over one-third of the sky. Automated pipelines are responsible for astrometric calibration [264], photometric reduction [217], and photometric calibration [249]. Bright galaxies, luminous red galaxies (LRGs), and quasars are selected for follow-up spectroscopy [362, 112, 305, 59, 350]. The data used in this survey were acquired between August 1998 and May 2013.

CMASS [22] ($z = 0.43 - 0.7$) consists of 690,826 galaxies over an area of 8498 deg^2, has a mean redshift of 0.57, and is designed to be stellar-mass-limited at $z > 0.45$. Each spectroscopic sector, or region covered by a unique set of spectroscopic tiles [7], was required to have an overall completeness (the fraction of spectroscopic targets that were observed) over 70% and a redshift completeness (the fraction of observed galaxies with good spectra) over 80%. We use these galaxies to construct an overdensity map $\delta_i = (n_i - \bar{n})/\bar{n}$, where i denotes the pixel on the sky. $n_i = \sum_{j \in \text{pixel } i} w_j$, where w_j is the systematic weight [22] of galaxy j. The map is given a HEALPix pixelization with $N_{\text{side}} = 1024$. Note that

we do not weigh the pixels by their observed area because the HEALPix pixels are much smaller than the observed sectors for which the completeness is computed, and we did not want to introduce extra power due to possible errors in the completeness on small scales. We also confirm (see Section 4.8) that including pixel weights have only a small effect on the final result.

4.5   Angular Power Spectra

4.5.1   Theory

We model the theoretical galaxy-CMB lensing convergence angular cross-power spectrum and the galaxy clustering angular auto-power spectrum using standard methods. We assume ΛCDM with parameters consistent with *Planck* 2013 [270] and BOSS Data Release 11 [22]. We use these models to estimate statistical errors from mocks and systematic corrections to E_G (see Section 4.6). However, our measurement of E_G along with errors from jackknife resampling, which we use in our final result, does not use our power spectrum models and is independent of ΛCDM. In addition, the corrections we determine from these models are well within statistical error bars.

Using the Limber approximation for small scales ($\ell \gtrsim 10$) and assuming the ΛCDM model, the galaxy-CMB lensing convergence angular cross-power spectrum can be written as

$$
\begin{aligned}
C_\ell^{\kappa g} &= \frac{3H_0^2\Omega_{m,0}}{2c^2} \int_{z_1}^{z_2} dz\, W(z) f_g(z) \chi^{-2}(z)(1+z) \\
&\quad \times P_{mg}\left[\frac{\ell}{\chi(z)}, z\right],
\end{aligned}
\tag{4.4}
$$

where $f_g(z)$ is the galaxy redshift distribution, $W(z) = \chi(1 - \chi(z)/\chi_{\text{CMB}})$ is the CMB

lensing kernel, $\chi(z)$ (χ_{CMB}) is the comoving distance out to redshift z (the CMB surface-of-last-scattering redshift $z_{\mathrm{CMB}} = 1100$), and $P_{mg}(k, z)$ is the matter-galaxy 3D cross-power spectrum as a function of z and wavenumber k [148]. The cosmological parameters present are the Hubble parameter today H_0 and the current matter density parameter $\Omega_{m,0}$. The galaxy redshift distribution for CMASS is shown in Fig. 1 of Anderson et al. [22]. The galaxy clustering angular auto-power spectrum can be written as

$$C_\ell^{gg} = \int_{z_1}^{z_2} dz \, \frac{H(z)}{c} f_g^2(z) \chi^{-2}(z) P_{gg} \left[\frac{\ell}{\chi(z)}, z \right] , \qquad (4.5)$$

where $H(z)$ is the Hubble parameter at redshift z and $P_{gg}(k, z)$ is the galaxy 3D auto-power spectrum.

4.5.2 Mock Galaxy Catalogues from N-body Simulations

We compute the power spectra $P_{mg}(k, z)$ and $P_{gg}(k, z)$ using N-body simulations in order to model both nonlinearities and the occupation of halos with galaxies. The N-body simulation runs using the TreePM method [29, 394, 302]. We use 10 realizations of this simulation based on the ΛCDM model with $\Omega_m = 0.292$ and $h = 0.69$. Although these parameters differ from those from the joint Planck/BOSS analysis, this should not affect the results because $P(k)$ is not so sensitive to the cosmic parameters relative to C_ℓ. These simulations are in a periodic box of side length $1380h^{-1}$Mpc and 2048^3 particles. A friend-of-friend halo catalogue was constructed at an effective redshift of $z = 0.55$. This is appropriate for our measurement since the galaxy sample used has effective redshift of 0.57. We use a Halo Occupation Distribution (HOD) [251, 338, 41, 393, 42, 90] to relate the observed clustering of galaxies with halos measured in the N-body simulation. We have used the HOD model proposed in Beutler et al. [49] to populate the halo catalogue with

galaxies.

$$\begin{aligned}
\langle N_{\text{cen}} \rangle_M &= \frac{1}{2} \left[1 + \text{erf} \left(\frac{\log M - \log M_{\text{min}}}{\sigma_{\log M}} \right) \right] \\
\langle N_{\text{sat}} \rangle_M &= \langle N_{\text{cen}} \rangle_M \left(\frac{M}{M_{\text{sat}}} \right)^{\alpha} \exp \left(\frac{-M_{\text{cut}}}{M} \right) ,
\end{aligned} \tag{4.6}$$

where $\langle N_{\text{cen}} \rangle_M$ is the average number of central galaxies for a given halo mass M and $\langle N_{\text{sat}} \rangle_M$ is the average number of satellites galaxies. We use the HOD parameter set $(M_{\text{min}} = 9.319 \times 10^{13} M_{\odot}/h, M_{\text{sat}} = 6.729 \times 10^{13} M_{\odot}/h, \sigma_{\log M} = 0.2, \alpha = 1.1, M_{\text{cut}} = 4.749 \times 10^{13} M_{\odot}/h)$ from Beutler et al. [49]. We have populated central galaxies at the center of our halo. The satellite galaxies are populated with radius (distance from central galaxy) distributed as per the NFW profile out to r_{200} and the direction is chosen randomly with a uniform distribution.

4.6 Estimators

We estimate $C_{\ell}^{\kappa g}$ and C_{ℓ}^{gg} along with errors using the *Planck* CMB lensing map and CMASS galaxy map. We estimate both angular power spectra in 11 flat band-powers that comprise the range $62 \leq \ell \leq 400$, with each band containing the minimum-variance estimate of the power spectrum over that band. Note that this angular scale range is equivalent to the range 23 Mpc/$h < R_{\perp} < 150$ Mpc/h, where $R_{\perp} = 2\pi \chi(z)/\ell$ is the linear scale on the sky corresponding to the angular scale ℓ at redshift z. We do not use angular scales $\ell > 400$ ($R_{\perp} < 23$ Mpc/h) because the CMB lensing convergence at these scales is likely to be contaminated by Gaussian and point-source bias corrections in the lensing estimator [271]. We do not use angular scales $\ell < 62$ ($R_{\perp} > 150$ Mpc/h) because measurements by the BOSS collaboration of $P_{gg}(k)$ at larger scales were shown to be inconsistent between the north and south Galactic caps [313], suggesting the larger-scale measurement could be plagued

by systematics.

We estimate use a pseudo-C_ℓ estimator of the form [205, 271]

$$\hat{C}_\ell^{\kappa g} = \frac{1}{(2\ell+1)f_{\rm sky}^{\kappa g}} \sum_{m=-\ell}^{\ell} g_{\ell m} \kappa_{\ell m}^* , \tag{4.7}$$

where $f_{\rm sky}^{\kappa g}$ is the sky fraction common to the galaxy catalog and the CMB lensing conver-gence map, $\kappa_{\ell m}$ is the spherical harmonic transform of the CMB lensing convergence field, and $g_{\ell m}$ is the spherical harmonic transform of the galaxy overdensity field. The error in $\hat{C}_\ell^{\kappa g}$ is estimated as

$$\sigma^2(\hat{C}_\ell^{\kappa g}) = \frac{1}{(2\ell+1)f_{\rm sky}^{\kappa g}} \left[(\hat{C}_\ell^{\kappa g})^2 + \hat{D}_\ell^{\kappa\kappa} \hat{D}_\ell^{gg} \right] , \tag{4.8}$$

where $\hat{D}_\ell^{\kappa\kappa}$ and $\hat{D}_\ell^{gg}$ are estimators of the κ and galaxy angular auto-power spectra with statistical noise included, given by

$$\hat{D}_\ell^{\kappa\kappa} = \frac{1}{(2\ell+1)f_{\rm sky}^{\kappa}} \sum_{m=-\ell}^{\ell} |\kappa_{\ell m}|^2 , \tag{4.9}$$

and

$$\hat{D}_\ell^{gg} = \frac{1}{(2\ell+1)f_{\rm sky}^{g}} \sum_{m=-\ell}^{\ell} |g_{\ell m}|^2 , \tag{4.10}$$

where $f_{\rm sky}^{\kappa}$ and $f_{\rm sky}^{g}$ are the sky fractions for the CMB lensing convergence map and galaxy catalog, respectively. We can then use $\hat{C}_\ell^{\kappa g}$ and $\sigma(\hat{C}_\ell^{\kappa g})$ to bin the angular cross-power spectrum. Note since the lensing field is not Gaussian, least-squares estimates of $C_\ell^{\kappa g}$ will be slightly biased, but not significantly compared to our measurement errors.

We estimate C_ℓ^{gg} using a quadratic minimum-variance estimator, a method which has been used in previous estimates [370, 246, 151]. Note we do not estimate $C_\ell^{\kappa g}$ using this

method because the required covariance matrix for the CMB lensing convergence is not well-defined. We estimate C_ℓ^{gg} in the same 11 ℓ-bins used for $C_\ell^{\kappa g}$. We construct a parameter vector $\mathbf{p}$ that contains all the band-powers for C_ℓ^{gg}, whose minimum-variance estimator is given by $\hat{\mathbf{p}} = \mathbf{F}^{-1}\mathbf{q}$, where

$$F_{ij} = \frac{1}{2}\mathrm{tr}\left[\mathbf{C}_{,i}\,\mathbf{C}^{-1}\mathbf{C}_{,j}\,\mathbf{C}^{-1}\right],\qquad(4.11)$$

and

$$q_i = \frac{1}{2}\mathbf{x}^T\mathbf{C}^{-1}\mathbf{C}_{,i}\,\mathbf{C}^{-1}\mathbf{x},\qquad(4.12)$$

are the Fisher matrix and quadratic estimator vector, respectively, $\mathbf{x}$ is the galaxy overdensity map, $\mathbf{C} = \langle\mathbf{x}\mathbf{x}^T\rangle$ is the covariance matrix, and $\mathbf{C}_{,i} = \partial\mathbf{C}/\partial p_i$. Note that $\mathbf{x}$ and $\mathbf{C}$ are given in pixel space. The iterative and stochastic methods used for matrix inversion and trace estimation are described in Hirata et al. [148], Padmanabhan et al. [247].

The measurement of the redshift space distortions (RSD) parameter β is one of the key requirements to measure E_G. We estimate β by fitting the monopole and quadruple moments of the galaxy auto-correlation function. We use the Landy-Szalay estimator [194] to compute a two-dimensional galaxy auto-correlation. We project the galaxy auto-correlation onto the Legendre basis in order to obtain the monopole and quadrupole moments. We fit the monopole and quadrupole moments of the correlation function using Convolution Lagrangian Perturbation Theory (CLPT) and the Gaussian Streaming Model (GSM) [72, 386]. We measure $f\sigma_8$ and $b\sigma_8$ using scales between 30 h^{-1}Mpc to 126 h^{-1}Mpc following [11], where f is the logarithmic derivative of the growth factor and b is linear galaxy bias. We tested our RSD model against various systematics and mocks as described in [11]. We run a Markov Chain Monte Carlo(MCMC) to fit for the galaxy auto-correlation function using

COSMOMC [201]. We obtain the likelihood of RSD parameter β for each jackknife region by taking the ratio of the measured growth rate and bias $\beta = f/b$. The mean β from each jackknife region is then combined to get the final measurement of β. Although we do not use scales $126 < R_\perp < 150$ Mpc/h in our β measurement, the information in these scales is relatively low due to cosmic variance, and we expect β to not be significantly different at these scales. We do not fit β at scales $R_\perp < 30$ Mpc/h as we do not have mocks that can validate the theory model (GSM) at these scales.

4.6.1 Error Estimates

We use two methods to determine the errors in $\hat{C}_\ell^{\kappa g}$, $\hat{C}_\ell^{gg}$, and $\hat{\beta}$, namely jackknife resampling and mocks. Jackknife resampling includes systematics effects naturally; however, the jackknife regions we use, which are all more than 250 Mpc/h, may introduce errors in the covariance matrix at the largest scales we sample. Thus, we also perform a separate error analysis using CMASS mock galaxy catalogs with simulated lensing convergence maps as a check at large scales.

For the first method, we perform jackknife resampling of 37 equal-weight regions of the CMASS survey area, where weight is defined as the effective observed area calculated using the number of random galaxies in CMASS random galaxy maps. Note that this is not necessarily given by the sky area. We plot the 37 regions in Fig. 4.1. Each jackknife region is at least 250 Mpc/h on a side, total weights for regions in the CMASS north galactic cap differ from the CMASS south galactic cap by less than 2%, and the total weights of each jackknife region differ within a galactic cap by less than 0.8% (less than 0.1% for most regions). We use jackknife resampling to compute expectation values for $\hat{C}_\ell^{\kappa g}$, $\hat{C}_\ell^{gg}$, and $\hat{\beta}$, as well as $\hat{E}_G(\ell)$ and the covariance matrix $\mathrm{Cov}(E_G)$ for $E_G(\ell)$.

The second method computes $\hat{C}_\ell^{\kappa g}$, $\hat{C}_\ell^{gg}$, $\hat{\beta}$, and $\hat{E}_G(\ell)$ using the full *Planck* and CMASS
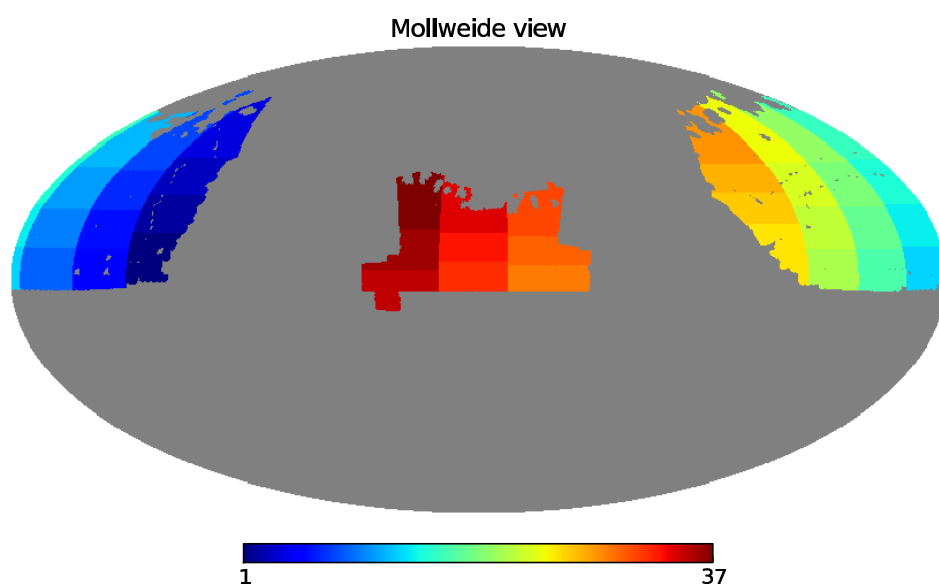
Figure 4.1: An equatorial map of the CMASS survey divided into 37 regions used for jackknife resampling.

surveys, and the covariances for all four quantities are determined using simulations and mocks. For the CMB lensing field, we simulate 100 convergence maps, in which each map is a Gaussian field with the correct signal and noise power spectra and mask provided by *Planck*. For the galaxies, we use 100 CMASS mock catalogs [223]. The halo occupation density used to construct these mocks, presented in Manera et al. [223], was significantly updated recently [49]. This is reflected in that C_ℓ^{gg} for the mocks from Manera et al. [223] are significantly lower than the data on small scales, the data which was fitted to determine the HOD in Beutler et al. [49]. We remedy this by rescaling C_ℓ^{gg} for all the mocks equally such that the average C_ℓ^{gg} of the mocks matches C_ℓ^{gg} from the data. Also, the lensing simulations were not constructed to be correlated with the mocks, but we do not expect this to be important because the CMB lensing-galaxy correlation should only contribute 1-2% of the errors in $C_\ell^{\kappa g}$. Also, since the galaxy mocks are not correlated with the κ simulations, there is no need to rescale $C_\ell^{\kappa g}$.

Assuming the GR case where E_G is independent of ℓ, we construct a likelihood function given by

$$\mathcal{L}(E_G) \quad \propto \quad \exp\left\{-\frac{1}{2}\sum_{\ell,\ell'}[\hat{E}_G(\ell) - E_G][\mathrm{Cov}(E_G)]_{\ell,\ell'}^{-1}[\hat{E}_G(\ell') - E_G]\right\}, \quad (4.13)$$

from which we determine the maximum likelihood value for E_G along with statistical errors. In order to correct the bias to $[\mathrm{Cov}]^{-1}$ due to using a finite number of jackknives/mocks, we multiply $[\mathrm{Cov}]^{-1}$ by $(1 - D)$, in which

$$D = \frac{n_b + 1}{n_s - 1}, \quad (4.14)$$

where n_b is the number of bins for which we estimate the covariance matrix, and n_s is the number of samples [256, 173]. Thus, $D = 7/36$ for the jackknives and $D = 7/99$ for the

simulations/mocks, although we acknowledge that the scaling for the jackknives could be inaccurate at larger scales due to the size of the jackknife regions. However, this does not appear to make the jackknife results much different from that of the simulations/mocks.

4.6.2   Systematic Corrections to E_G

Our estimator for E_G in Eq. 4.3 is not unbiased due to scale-dependent clustering bias as well as a mismatch between the CMB lensing kernel and the redshift distribution of CMASS galaxies. We apply systematic corrections to our E_G estimator to debias our result, which we outline in this subsection. These correction factors are similar in purpose to those applied to the first E_G estimate in Reyes et al. [303], although their kernel and effective redshift corrections are combined in our the kernel mismatch correction.

We derive Γ in Eq. 4.3 by relating $C_\ell^{\kappa g}$ and C_ℓ^{gg} in Eqs. 4.4 and 4.5 and then setting Γ such that the expectation value of the resulting expression for E_G is consistent with Eq. 4.1. It can be shown that by removing the appropriate functions from the integrands which are slowly varying compared to $f_g^2(z)$, the correct expression for Γ is

$$\Gamma = \frac{2c}{3H_0} \left[\frac{E(z)f_g(z)}{W(z)(1+z)} \right] , \qquad (4.15)$$

where $E(z) = H(z)/H_0$. The approximations required to produce this expression are not perfect, causing E_G measured using Eq. 4.3 to slightly deviate from the true value of E_G. We correct this systematic effect by multiplying Γ by C_Γ, given by

$$C_\Gamma(\ell) = \frac{W(z)(1+z)}{2f_g(z)} \left[\frac{c}{H(z)} \right] \frac{C_\ell^{mg}}{Q_\ell^{mg}} , \qquad (4.16)$$

where Q_ℓ^{mg} and C_ℓ^{mg} are defined as

$$
\begin{aligned}
Q_\ell^{mg} &\equiv \frac{1}{2} \int_{z_1}^{z_2} dz\, W(z) f_g(z) \chi^{-2}(z)(1+z) \\
&\quad \times P_{mg}\left[\frac{\ell}{\chi(z)}, z\right],
\end{aligned}
\tag{4.17}
$$

and

$$
C_\ell^{mg} \equiv \int_{z_1}^{z_2} dz\, \frac{H(z)}{c} f_g^2(z) \chi^{-2}(z) P_{mg}\left[\frac{\ell}{\chi(z)}, z\right].
\tag{4.18}
$$

Another systematic correction concerns the clustering bias. Specifically, while β is computed using the linear bias, the angular power spectra are computed over a range of scales, including small, non-linear scales where the clustering bias is scale-dependent. This causes the clustering bias factors in E_G to not fully cancel. This systematic effect is corrected by multiplying E_G by C_b, where

$$
C_b(\ell) = \frac{C_\ell^{gg}}{b_{\text{lin}} C_\ell^{mg}}.
\tag{4.19}
$$

We plot these corrections to E_G in Fig. 4.2 for the same 11 ℓ-bins used to compute E_G in section 4.6. We see that the Γ correction is approximately 6% from unity with $\pm 1\%$ variation, while the bias correction is only 1% from unity with little variation. The errors are due to the fluctuations in the 10 N-body simulations used to calculate the power spectra. The size of C_Γ is due to the kernels of Q_ℓ^{mg} and C_ℓ^{mg} peaking at different redshifts, and the wiggles are due to baryonic acoustic oscillations. Note that we did not include uncertainties in cosmological parameters into the errors. By combining the errors for these corrections over the scale range, we estimate a systematic error of 1.2%.

We test our corrections by computing $E_G(\ell)$, both with and without corrections, based
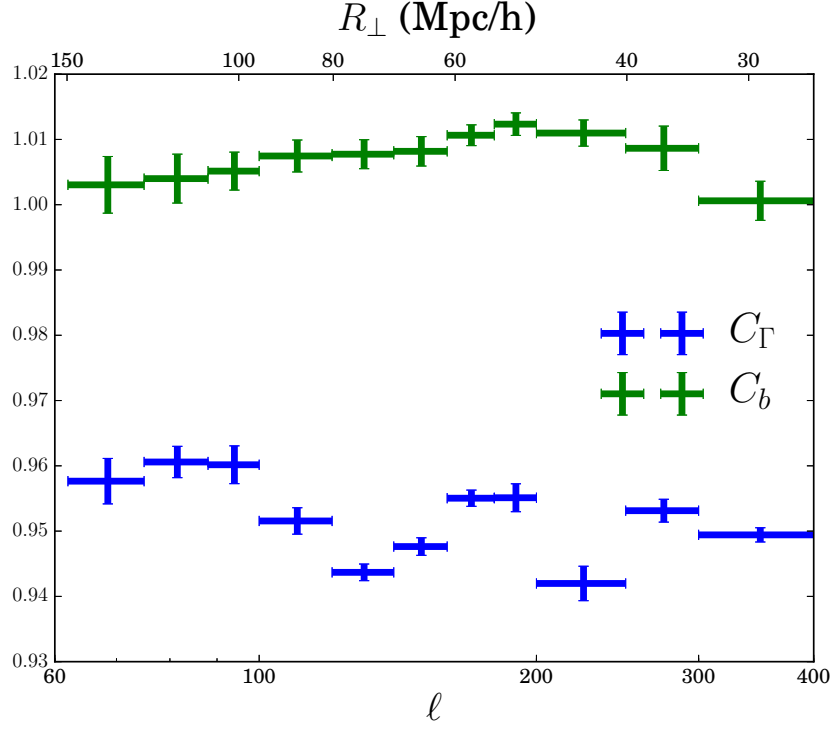
Figure 4.2: Correction factors applied to E_G due to Γ (solid) and bias (dashed). These correction factors were determined from N-body simulations.

on the N-body simulations and comparing them with the fiducial value. In Fig. 4.3, we see that the result matches well with the fiducial value. It is possible that the modeling of the clustering in the N-body simulations and the HOD could affect the corrections, particularly C_b. Incorrect modeling of the redshift distribution could also affect the corrections, particularly C_Γ. The statistical error on our final E_G estimate is large enough such that this should not be an issue, but this could affect upcoming E_G measurements that are more precise, requiring more precise modeling of the corrections using simulations.
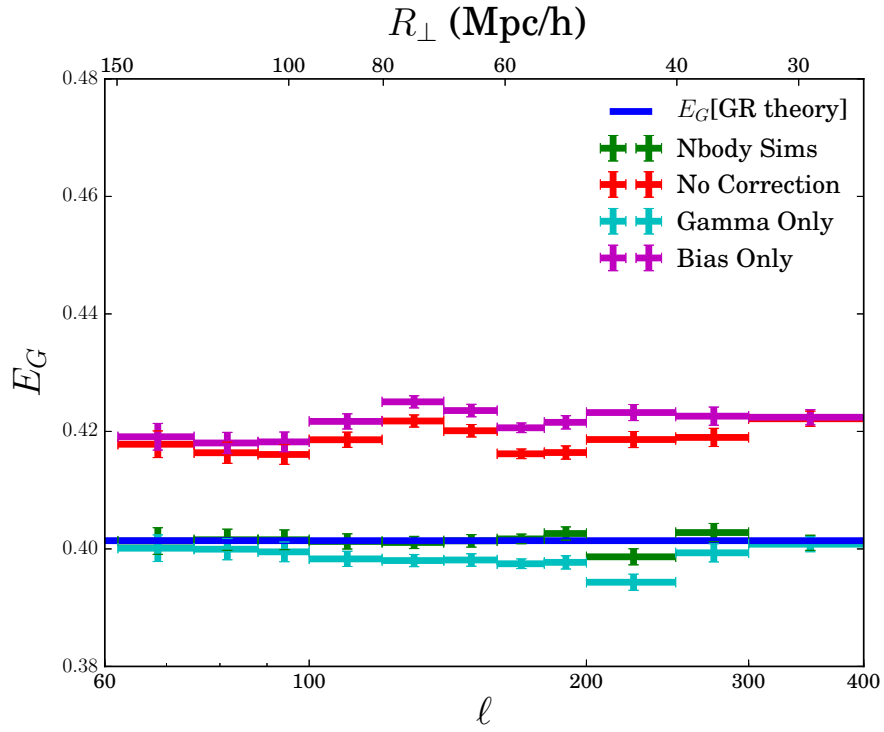
Figure 4.3: Test of E_G correction factors C_Γ and C_b on N-body simulations (green crosses) compared to the fiducial value of E_G (solid). We also show E_G without corrections (red crosses) and with only the Γ correction (cyan crosses) or the scale-dependent bias correction (magenta crosses).

4.7 Results

We show in Fig. 4.4 the angular power spectra for galaxy-CMB lensing, $C_\ell^{\kappa g}$, and galaxy clustering, C_ℓ^{gg}, which we estimate from the *Planck* CMB lensing map and the CMASS galaxy number density maps using jackknife resampling. It is evident that the measured C_ℓ^{gg} is consistent with the theoretical prediction from ΛCDM combined with the HOD model. However, the measured $C_\ell^{\kappa g}$ is a bit lower at large scales than the theoretical prediction. Specifically, we find a cross-correlation amplitude of $A = 0.754 \pm 0.097$, which is low but consistent with the value reported in Kuntz [191], $A = 0.85^{+0.15}_{-0.16}$, for *Planck* cross-correlated with the CFHTLens[1] galaxy sample. Note that this low value of A is also inconsistent with values of $A > 1$ favored by the *Planck* CMB temperature and polarization maps alone [280, 287]. We also perform jackknife resampling for the RSD parameter, finding $\beta = 0.368 \pm 0.046$. The full results for β, including the likelihood and the measurements of $b\sigma_8$ and $f\sigma_8$, are shown in Fig. 4.5.

We considered whether the deficit in $C_\ell^{\kappa g}$ at large scales could be due to a systematic effect introduced in the latest lensing map. Recent work has suggested there may be tension between the *Planck* CMB lensing maps from 2013 and 2015 [243, 212, 191]. In particular, the galaxy cross-correlation with the *Planck* 2015 CMB lensing map appears to measure a smaller clustering bias than the 2013 map, suggesting that the 2013 CMB lensing map may have produced a cross-correlation more consistent with our $C_\ell^{\kappa g}$ model on these scales. We test this by taking the difference map between the *Planck* 2015 and 2013 CMB lensing maps and cross-correlating with the CMASS map, the *Planck* 545 GHz map (dust-dominated), and the Sunyaev-Zeldovich (SZ) Compton-y map [286]. In all three cases (see Figs. 4.6-4.8) we find the cross-correlations are consistent with zero, suggesting that the *Planck* 2015 and 2013 CMB lensing maps are equivalent, and that any contam-

---

[1]http://cfhtlens.org
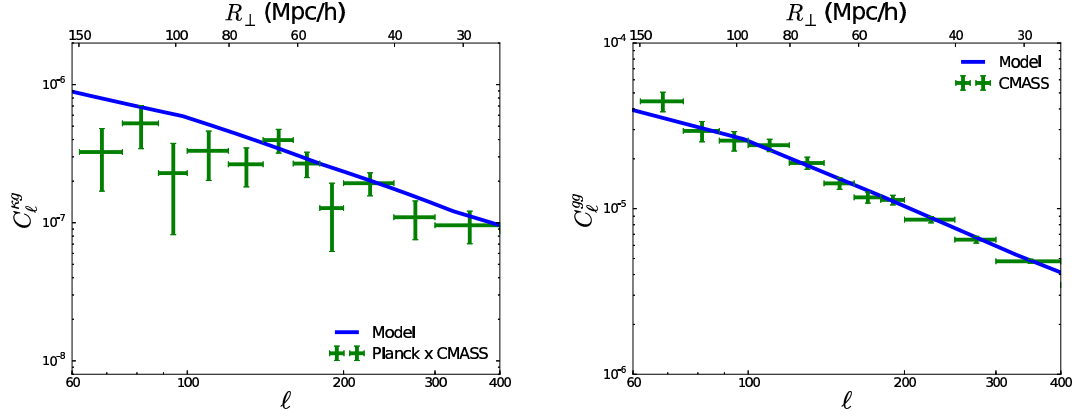
Figure 4.4: Observed angular power spectra (crosses) for galaxy-CMB lensing (*top*) and galaxy clustering (*bottom*) with 1σ errors using the CMASS galaxy sample and the *Planck* CMB lensing map. In both panels, we show ℓ on the lower horizontal axis and $R_\perp$, the corresponding linear scale projected onto the sky, on the upper horizontal axis. The errors were derived using jackknife resampling of 37 equally weighted regions in the CMASS survey. Our galaxy angular power spectrum measurement is consistent with theoretical models (solid lines) derived from N-body simulations, while our galaxy-CMB lensing angular cross-power spectrum is low yet consistent with other measurements, *e.g.* Kuntz [191]. We discuss possible causes for this deficit in Sec. 4.7.
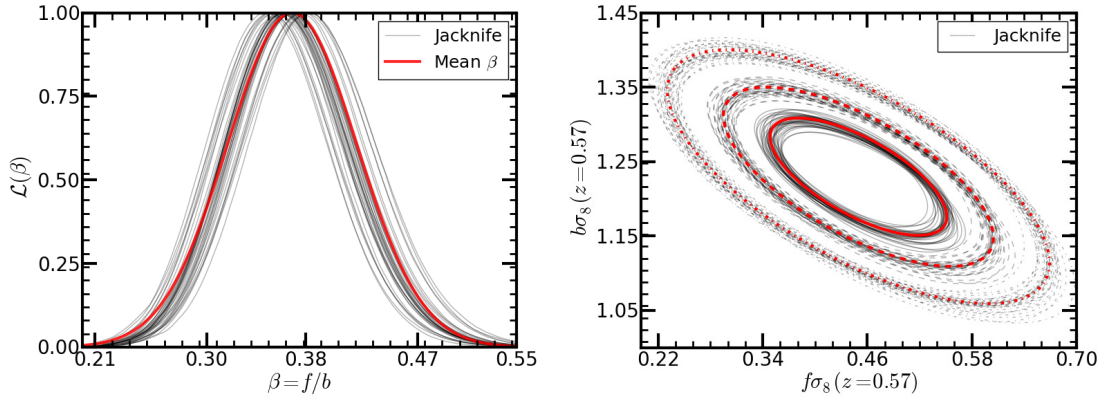
Figure 4.5: The top plot shows the likelihood of β and the bottom plot shows our constraint in the $b\sigma_8 - f\sigma_8$ plane. The black lines are the likelihood obtained for individual jackknife regions and the red lines are our likelihood obtained by combining the mean of individual jackknife region. These plots also shows that our jackknife sampling is unbiased in estimating the parameters.
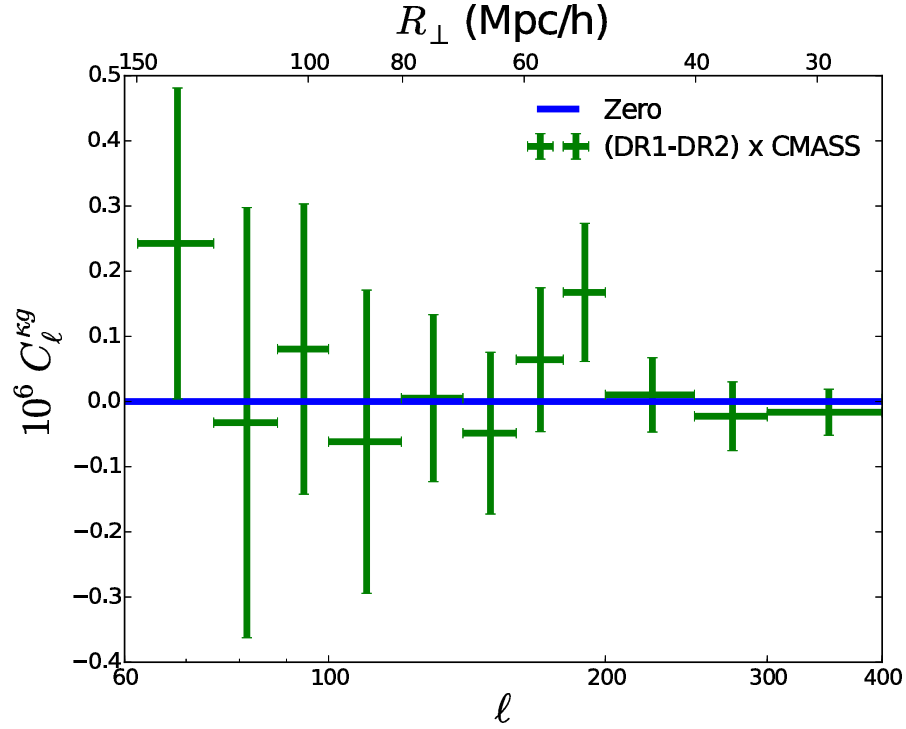
Figure 4.6: Observed angular cross-power spectrum (crosses) with 1σ errors between the CMASS galaxy sample and the difference map between the *Planck* 2013 (DR1) and 2015 (DR2) CMB lensing maps. We show ℓ on the lower horizontal axis and $R_\perp$, the corresponding linear scale projected onto the sky, on the upper horizontal axis. The angular cross-power spectrum measurements is consistent with a null result (solid line).

ination must be common to both maps. It is possible that $C_\ell^{\kappa g}$ could be correlated with the scanning direction, and that lensing convergence maps for separate surveys with different scanning strategies could reveal a discrepancy. Testing this would require constructing lensing convergence maps for partial surveys, which we leave for future work.

Previous work has also shown [126] that the large-scale $C_\ell^{\kappa g}$ deficit is also present in the cross-correlation between the Dark Energy Survey [371] Science Verification galaxy sample and the South Pole Telescope CMB lensing map [361], which suggests the source of this deficit is not unique to the *Planck* CMB maps. Thus, it appears that the source of this deficit may very well be astrophysical or cosmological. The deficit could be caused
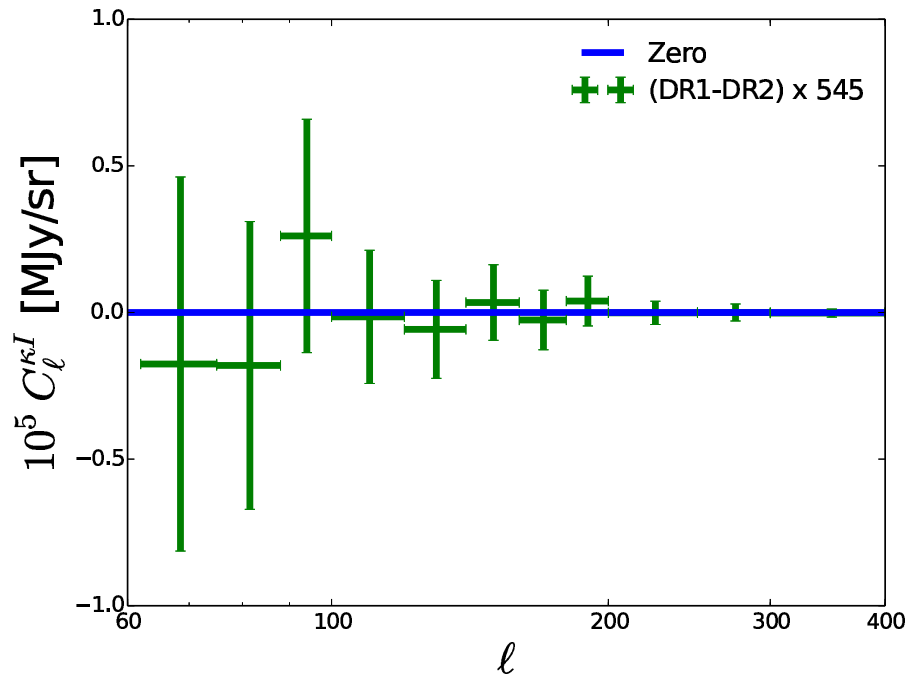
Figure 4.7: Observed angular cross-power spectrum (crosses) with 1σ errors between the *Planck* 545 GHz map (dust-dominated) and the difference map between the *Planck* 2013 (DR1) and 2015 (DR2) CMB lensing maps. The format is similar to Fig. 4.6. The angular cross-power spectrum measurements is consistent with a null result (solid line).
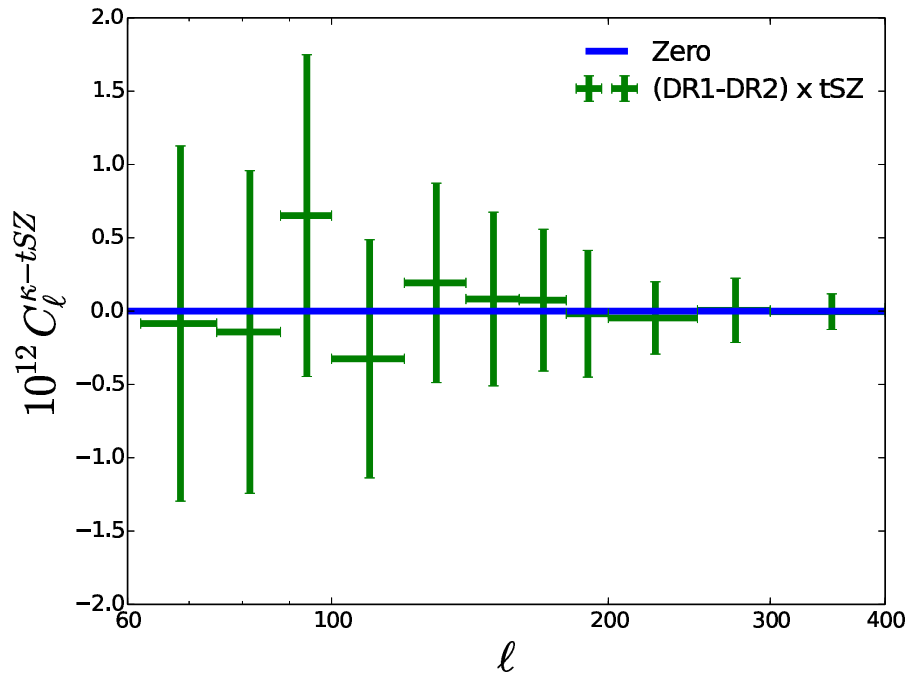
Figure 4.8: Observed angular cross-power spectrum (crosses) with 1σ errors between the *Planck* SZ y map and the difference map between the *Planck* 2013 (DR1) and 2015 (DR2) CMB lensing maps. The format is similar to Fig. 4.6. The angular cross-power spectrum measurements is consistent with a null result (solid line).

by thermal SZ contamination, in that the SZ increases the variance a CMB map, which the lensing estimator interprets as an "anti-lens." Unfortunately, thermal SZ was not removed from the *Planck* SMICA maps [277]. Recent work [379] showed that the CMB lensing-galaxy cross-correlation could be biased due to contamination from thermal SZ and the cosmic infrared background (CIB), though the predicted magnitudes of the biases ($\sim 4 - 6\%$) are too small to explain the deficit. Also, the lack of evidence for contamination could be due to a lack of power spectrum sensitivity instead of a lack of contamination. Of course, a combination of causes could also explain the discrepancy. In addition, other analyses have claimed an excess ($A > 1$) galaxy-CMB lensing correlation [51, 52] in contradiction to the deficit seen in the previously mentioned claims. More research is needed to determine the nature of this deficit; however, we consider this beyond the scope of our investigation and leave this for future work.

The power spectra, $C_\ell^{\kappa g}$ and C_ℓ^{gg}, and β are combined using Eq. 4.3 to compute $E_G(\ell)$ within 11 ℓ-bins comprising the angular modes $\ell = 62 - 400$ ($23 < R_\perp < 150$ Mpc/h), which we present in Fig. 4.9. Note that we probe scales much larger than the previous measurements using galaxy lensing [303, 55]. The range in ℓ was chosen to avoid observational systematic effects on large scales [152, 313, 315] and lensing noise bias on small scales [271]. The low values of E_G are attributable to the deficit in $C_\ell^{\kappa g}$, while E_G in the first ℓ-bin is even lower due to its excess C_ℓ^{gg}. The covariance matrix for $E_G(\ell)$ over the 11 ℓ-bins was computed using jackknife resampling. Taking the average of $E_G(\ell)$ over ℓ, while accounting for the covariance matrix, we find $E_G = 0.243 \pm 0.060$ (1σ). This is a measurement with 25% statistical errors, over two times larger than forecasts [294] mainly due to the low expectation value we find relative to GR and correlations between E_G estimates at different angular scales, possibly due to systematic foregrounds. Repeating the E_G estimation using the full CMB lensing and galaxy maps with an E_G covariance matrix produced from the CMASS mock galaxy catalogues [223] and Gaussian simula-
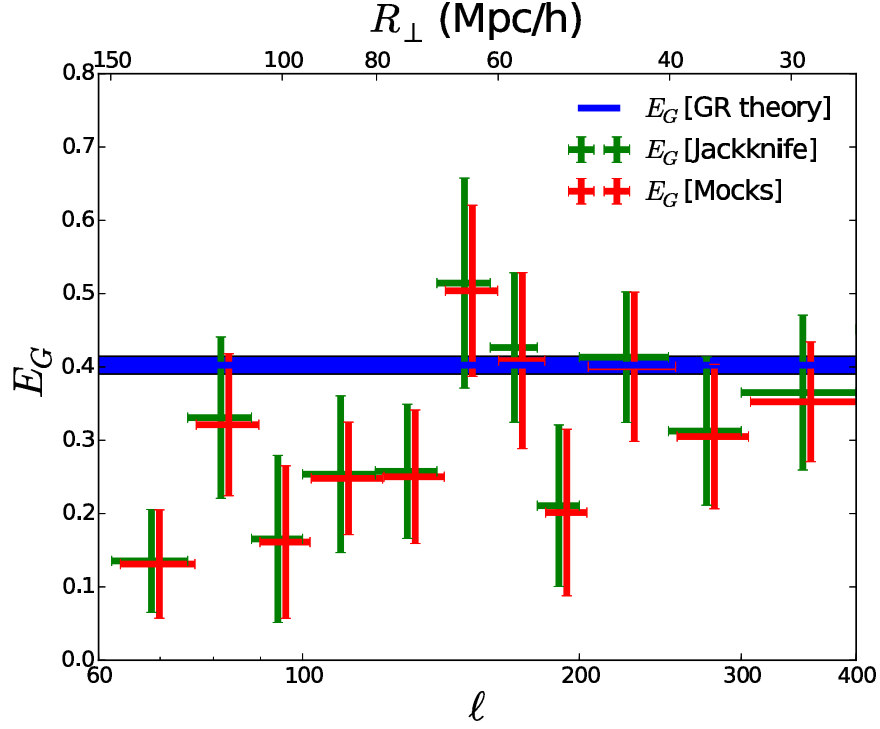
Figure 4.9: E_G measurements with 1σ errors using the CMASS galaxy sample and the *Planck* CMB lensing map. The horizontal axes are described in the caption for Fig. 4.4. We show estimates using jackknife resampling of the full sample [green crosses; see Fig. 4.4] and estimates using the full sample with errors computed from 100 CMASS mock galaxy catalogues and Gaussian simulations of the lensing convergence field (red crosses). The blue region shows the GR prediction $E_G = 0.402 \pm 0.012$ with the error determined from the likelihood from *Planck* and BOSS measurements. Averaging the E_G values from jackknife resampling over all scales, we find $E_G = 0.243 \pm 0.060$ (1σ), a 2.6σ deviation from GR.

tions of the lensing convergence field gives us a similar result $E_G = 0.269 \pm 0.047$, which is consistent with the result from jackknife resampling. Since the results using jackknife resampling have larger errors than those using mocks, we choose the more conservative jackknife results as our main GR constraint.

The general relativistic prediction for E_G is given by $\Omega_{m,0}/f(z) = 0.402 \pm 0.012$ at redshift $z = 0.57$, based on estimates of the cosmological parameters [270] by the *Planck* satellite and the BOSS measurements of the baryon acoustic oscillations (BAO)

125

scale. There is tension between the value from general relativity and our measurement, on the order of 2.6σ. We test GR at scales three times as large as those probed in the previous E_G measurements using galaxy-galaxy lensing [303, 55], and it is at these larger scales that this deviation appears. Specifically, our averaged E_G measurement deviates from the GR value by more than 1σ when scales greater than 80 Mpc/h ($\ell < 150$) are included. However, there are still unanswered questions regarding the nature of the deficit in $C_\ell^{\prime\kappa g}$. Thus, we do not claim significant evidence for a departure from general relativity.

In Pullen et al. [294], the authors derive E_G for $f(R)$ gravity [74], which is given by

$$E_G^{\mathrm{fR}}(k,z) = \frac{1}{1 - B_0 a^{s-1}/6} \frac{\Omega_{m,0}}{f^{\mathrm{fR}}(k,z)}, \qquad (4.20)$$

where B_0 [354, 45] is a free parameter which is related to the Compton wavelength of an extra scalar degree of freedom and is proportional to the curvature of $f(R)$ today, s=4 for models that follow ΛCDM, and $f^{\mathrm{fR}}(k,z)$ is the $f(R)$ growth rate, which is scale-dependent [156]. Current measurements limit $B_0 < 1.36 \times 10^{-5}$ (1σ) [400, 37, 10]. $f(R)$ gravity would be indistinguishable by eye from the GR curve in Fig. 4.9, suggesting that we cannot constrain it further using our measurement. The relative constraining power of the RSD measurement alone [10] compared to our measurement is partially due to the use of 6 LSS surveys in the growth rate analysis as compared to our use of one survey in our E_G analysis. In addition, most of our constraining power is degraded because of the relatively low signal-to-noise ratio of the lensing measurement. Future CMB surveys such as Advanced ACTPol [141] or possibly the Primordial Inflation Explorer (PIXIE) [188] with high sensitivities and angular resolution combined with upcoming large-area galaxy surveys with high number densities and moderate redshift precision, along with better control of systematics, should be much more competitive with growth rate measurements without the clustering-bias degeneracy that the growth rate exhibits [294]. These upcoming

E_G measurements should also be capable of differentiating between GR and other gravity models.

4.8 CMB Lensing and Galaxy Systematics

We consider contamination from dust emission and point sources, which could correlate with both the CMB lensing map and our galaxy sample, thus biasing $C_\ell^{\kappa g}$. Specifically, for both the CMB lensing map and our galaxy sample we construct 6 cross-correlations, one with a dust map and 5 with point-source maps from *Planck*, using a pseudo-C_ℓ estimator similar to Eqs. 4.7 and 4.8. To trace dust emission, we use the Schlegel et al. [329] galactic extinction map using infrared emission data from the Infrared Astronomy Satellite (IRAS) and the Diffuse Infrared Background Experiment (DIRBE). Three point-source overdensity maps are constructed from the *Planck* Catalog of Compact Sources [269] at frequencies 100, 143, and 217 GHz. We also consider the *Planck* SZ Catalog [279] of sources detected through the SZ effect [364], as well as the *Planck* Catalog of Galactic Cold Clumps [284].

We use the cross-correlations to estimate the bias to $C_\ell^{\kappa g}$ due to each systematic. Assuming the formalism in Ross et al. [310] and Ho et al. [152], where the total measured perturbation in κ or the galaxies is a linear combination of the true perturbation and templates for the systematics, it has been shown [126] that the bias and error for one systematic is given by

$$
\begin{aligned}
\Delta C_{\ell,i}^{\kappa g} &= \frac{C_\ell^{\kappa M_i} C_\ell^{g M_i}}{C_\ell^{M_i M_i}} \\
\sigma^2\left(\Delta C_{\ell,i}^{\kappa g}\right) &= \left(\Delta C_{\ell,i}^{\kappa g}\right)^2 \left[\left(\frac{\sigma(C_\ell^{\kappa M_i})}{C_\ell^{\kappa M_i}}\right)^2 + \left(\frac{\sigma(C_\ell^{g M_i})}{C_\ell^{g M_i}}\right)^2\right],
\end{aligned} \qquad (4.21)
$$

where i denotes one of the 6 dust/point source maps we consider and $C_\ell^{M_i M_i}$ is the auto-

correlation for the systematic map M_i. This formalism can be easily extended to find the total bias including all the systematics; however, we do not attempt this because the error on the bias becomes comparable to the magnitude of $C_\ell^{\kappa g}$. In Fig. 4.10 we plot $\Delta C_{\ell,i}^{\kappa g}$ for each systematic. We find that most of the bias measurements are less than 1σ error from a null result, even more than expected from a normal distribution. In addition, all biases are less than 2σ error from the null result. Therefore, we do not report from this calculation any evidence for significant bias due to any of the tested systematic templates in our $C_\ell^{\kappa g}$ measurement.

We then consider the bias from each systematic as an estimate of the bias for $C_\ell^{\kappa g}$, and we estimate the systematic error due to these contaminants by calculating the spread of the biases at each angular scale, which are then added in quadrature to estimate the full systematic error. We define the spread in bias values as the average absolute value of $\Delta C_{\ell,i}^{\kappa g}$, weighted by $1/\sigma^2 \left(\Delta C_{\ell,i}^{\kappa g} \right)$. This procedure gives an estimate of 2.7% for the systematic error.

Redshift space distortions can also systematically reduce E_G by introducing an extra correlation [247] in the galaxy angular power spectrum on large scales. We find a 1.4% effect based on the largest angular scale we use ($\ell = 62$). At smaller scales this effect's magnitude decreases, and we estimate that the effect on E_G marginalized over scale is approximately 0.7% of E_G.

We test the effects of the systematic weights for the galaxy sample by estimating E_G (see section 4.6) with various weights turned off. We also estimate E_G with pixels weighted by observed area. Note that for the systematic weights, the shift in E_G includes shifts in $C_\ell^{\kappa g}$, C_ℓ^{gg}, and β, while for the pixel weighting we do not include a shift in β because it is fitted from a 3D correlation function in which the completeness is already included. In the results shown in Fig. 4.11, we see that removing weights does not change our result by more than 1σ. We also see that weighting the pixels by the observed area (or completeness)
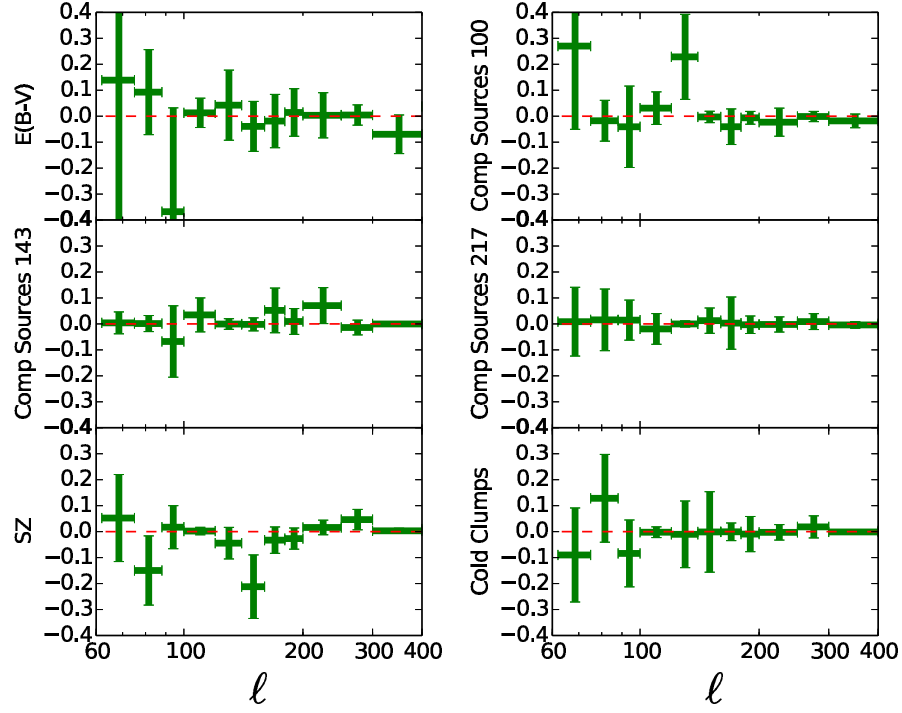
Figure 4.10: The estimated bias to $C_\ell^{\kappa g}$ due to each systematic template with 1σ error bars. The panel for dust is labeled "E(B-V)", compact sources are labeled "Comp Sources" with a given frequency, and the last two panels are for SZ and Cold Clumps. It appears that the biases from compact sources and SZ are significantly deviant from null at some scales, but overall our $C_\ell^{\kappa g}$ measurement does not appear to be biased from these systematic templates.
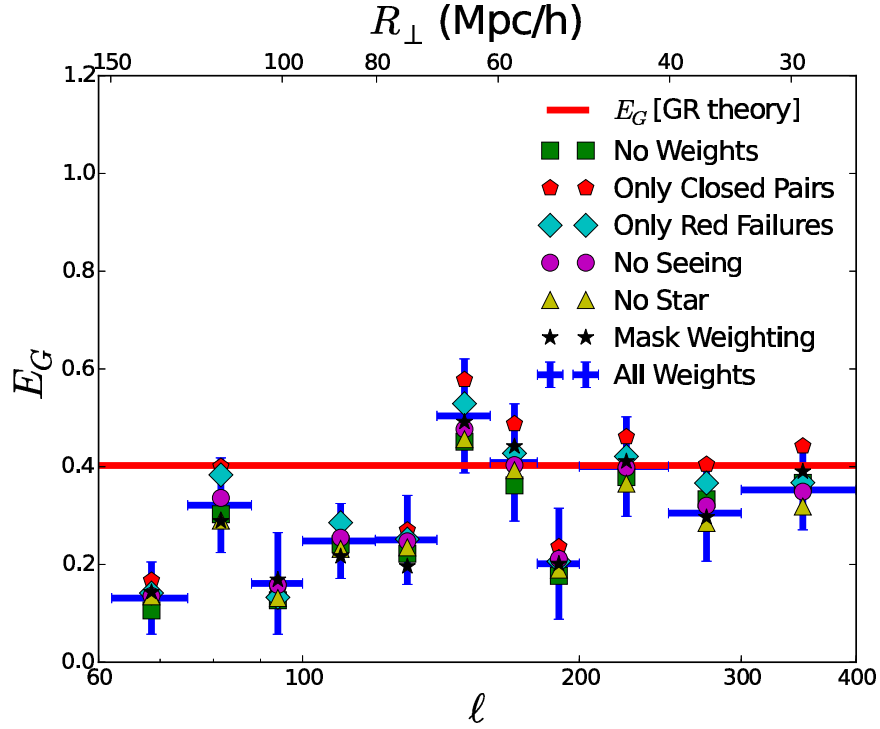
Figure 4.11: The observed E_G results from mock/simulations using systematic weights [blue crosses; see Fig. 4.9] along with markers denoting the E_G estimates with various systematic weights turned off, as well as an E_G with pixel mask weighting turned on. Most of these scenarios do not shift the E_G measurement significantly. Removing stellar and seeing weightings does shift the measurement, but not when all weights are removed.

would not shift the results significantly either.

We also consider the galaxy weights (see section 4.8) as a source of systematic error. The scatter in E_G among all the combinations of weights we consider implies a systematic error that is $\sim 11\%$ of E_G. However, this includes the two E_G values assuming only close pair weights and only redshift failure weights, which appear to be systematically higher than the other E_G values. It has been shown [22] that stellar and seeing weights are necessary to produce unbiased estimates of the power spectrum, thus we will not consider the two systematically high E_G values in our error estimate. Under this assumption, the systematic error due to galaxy weights is approximately 4.5% of E_G. Note that this estimate

properly combines the individual systematic errors in the angular power spectra and β into an error for E_G. This error is much greater than all the other sources of error, including from systematic corrections to E_G, $C_\ell^{\kappa g}$ bias, and the RSD bias in C_ℓ^{gg}; adding all the effects together in quadrature, we find a full systematic error estimate of 5.4%, which is much less than the statistical errors in E_G.

4.9 Conclusions

E_G is a bias-independent probe of gravity on large cosmological scales, and we provide the first measurement of this quantity using CMB lensing. We construct our measurement using data from the *Planck* CMB lensing map and the CMASS galaxy sample. By using the CMB to trace the gravitational lensing field, ours is the largest-scale measurement of E_G attempted. While our measurement was not precise enough to confirm or rule out alternatives to GR, such as $f(R)$ gravity, our measurement serves as a "first step" towards much more precise measurements of E_G from upcoming galaxy surveys, such as the Dark Energy Spectroscopic Instrument (DESI) [200], the Large Synoptic Survey Telescope (LSST) [216], and *Euclid* [195] combined with next-generation CMB surveys such as Advanced ACTPol [141].

A major forthcoming challenge will be mitigating systematics in upcoming measurements. The statistical errors in our measurements were much larger than our systematic errors, but this will not be the case with percent-level statistical errors from upcoming surveys. Specifically, foregrounds like stellar contamination for galaxies and point sources will have to be better identified and controlled in future E_G measurements. One thing to note, however, is that E_G is particularly robust to systematics in the CMB map in that those same systematics would also have to contaminate the galaxy map in order to bias E_G.

Finally, this work should spur future work in new probes of E_G. For example, intensity

mapping [383] of 21-cm line emission will produce low-angular-resolution maps of large-scale structure (LSS). Since E_G probes gravity on large scales, high angular resolution is not necessary, allowing intensity mapping to replace the galaxy map in the E_G estimator with advantages of high redshift precision and high LSS sampling. In addition, it has been predicted [291] that the Square Kilometer Array[2] could measure the galaxy-lensing cross-correlation from intensity mapping with high precision and at multiple source redshifts. Thus, measurements of E_G using intensity mapping could serve as the supreme modified gravity probe.

Acknowledgments

---

[2]www.skatelescope.org

Chapter 5

Testing gravity at large scales by combining galaxy-galaxy lensing with redshift space clustering

Shadab Alam, Hironao Miyatake, Surhud More, Shirley Ho, Rachel Mandelbaum

5.1   Abstract

We measure a combination of gravitational lensing, galaxy clustering, and redshift-space distortions called E_G. The quantity E_G probes both parts of metric potential and is insensitive to galaxy bias and σ_8. These properties make it an attractive statistic to test ΛCDM, General Relativity and its alternate theories. We have combined CMASS DR11 with CFHTLenS and recent measurements of β from RSD analysis, and find $E_G(z = 0.57) = 0.41 \pm 0.047$, an 11% measurement in agreement with the prediction of general relativity $E_G(z = 0.57) = 0.396 \pm 0.011$ using the Planck 2015 cosmological parameters.

We have corrected our measurement for various observational and theoretical systematics. Our measurement is consistent with the first measurement of E_G using CMB lensing in place of galaxy lensing [293] at small scales, but shows 2.8σ tension when compared with their final results including large scales. This analysis with future surveys will provide improved statistical error and better control over systematics to test General Relativity and its alternate theories.

5.2 Introduction

The theory of General Relativity (GR) is the most successful theory of the gravity. The GR was first proposed by Einstein [110]. GR has passed the most stringent tests at solar system scales [319]. But it is still an ongoing pursuit to test the predictions of GR at cosmological scale before we finally declare that it is the ultimate theory of gravity. There are some observational mysteries like dark matter [417, 178, 316] and dark energy [306, 262] which cannot be explained with the current models. But if one ignores the questions about origin of dark matter and dark energy, then ΛCDM-GR is in good agreement with Cosmic Microwave Background (CMB) [39, 268], Baryon Acoustic Oscillation (BAO) [113, 85, 167, 184, 259, 23, 21] and Hubble constant [308]. One of the fundamental theoretical mysteries is the incompatible nature of quantum mechanics and GR. The nature of time in the two theories is so different that it is difficult to combine them in a single framework [377, 19]. In order to further the understanding of these mysteries and develop consistent theories, it is important to test the predictions of these theories in various regimes. A fundamental difficulty of testing modifications to GR is the ability to absorb these modifications in dark energy. Fortunately, modified gravity predicts large scale structures different from those predicted by Einstein's theory of gravity [190].

GR predicts many signatures of structure formation which can be observed in a wide

variety of surveys. Two complimentary signals measured are weak gravitational lensing and redshift space distortions (RSD). Gravitational lensing was first proposed by Einstein in Einstein [111]. Weak gravitational lensing is a statistical measurement of deflection of photons due to gravitational interaction with the matter density [for a review, see 33, 297, 334, 153, 224, 387]. Its signal is imprinted in the cross-correlation of background galaxy shapes with foreground galaxy positions [e.g., 197, 221, 382, 140, 164, 415], and can be measured as "cosmic shear" (the auto- and cross-correlation of pairs of galaxy shapes; e.g., Heymans et al. 144, Jee et al. 169). The redshift space distortion is the measurement of anisotropy produced in the galaxy auto-correlation function due to the peculiar velocity component in the galaxy redshift. This anisotropy allows us to measure the growth rate ($f = d \ln D/d \ln a$) of cosmic structure formation. It was first introduced by [180] and then further developed by others [138, 336]. It has been measured by various galaxy redshift surveys using different modeling schemes [258, 54, 47, 99, 77, 327, 48, 12].

The larger surveys and novel combinations of probes will test the predictions of GR with unprecedented precision. One such combination of redshift space distortion and weak gravitational lensing was proposed by [410]. It is important to test the relative amplitude of the effect of RSD and weak gravitational lensing as it probes space and time both parts of the metric. They have constructed a quantity E_G which can be measured by combining the signal from these two complimentary measurements. It has been proposed that E_G has the potential to serve as the most precise signal to test the nature of gravity [410]. E_G is independent of linear bias and the amplitude of matter fluctuations (σ_8). [304] has measured the first signal of E_G using a lower redshift sample from the Sloan Digital Sky Survey at an effective redshift of 0.32. Recently [56] reported the measurement of E_G at two different redshifts, 0.32 and 0.57. A number of possible theoretical systematics of E_G is discussed in [199].

In this paper we measure E_G by combining the measurement of the weak gravitational

lensing [230] from the Canada-France-Hawaii Lensing Survey [143], hereafter referred to as CFHTLenS, with the measurement of redshift-space galaxy clustering from the Data Release 11 (DR11) CMASS sample [9] of Baryon Oscillation Spectroscopic Survey (BOSS; Ahn et al. 4), which is part of Sloan Digital Sky Survey III (SDSS-III; Eisenstein et al. 115).

We have organized this paper in the following manner. In section 7.3, we provide some brief theoretical background of the E_G. Section 6.4 describes the samples of data used in our measurements. Section 6.5 describes the measurement of different components of E_G in detail with some systematic corrections. Section 5.6 provides the details of N-body simulation used in our analysis. The list of possible systematics affecting our E_G measurement with possible corrections is discussed in section 5.7. Finaly, we provide our main measurement and estimate of uncertainity on the measurement in section 5.8. We end our paper with the discussion of the main points of our analysis and the implications of our results, along with some future directions, in section 6.7. Our fiducial cosmology is flat ΛCDM with $\Omega_m = 0.31$ and $h = 0.67$ all throughout the paper unless mentioned otherwise.

5.3   Theory

The combination of galaxy-galaxy clustering, redshift space distortions and galaxy-galaxy lensing provides E_G. The measurements of lensing and clustering signals have been transformed to new quantities called Υ in order to reduce the impact of theoretical uncertainties and failures of certain approximations on small scales (as discussed later). The combined probe E_G has been operationally defined in Reyes et al. [304] as follows:

$$E_G(r_p) = \frac{\Upsilon_{gm}(r_p)}{\beta \Upsilon_{gg}(r_p)} \tag{5.1}$$

137

where $\beta = f/b$ is the redshift space distortion parameter with f being logarithmic deriva-tive of growth with respect to scale factor and b is the linear bias. The quantities Υ_{gm} and Υ_{gg} are called galaxy-matter and galaxy-galaxy annular differential surface densities respectively [ADSDs; 31]. Υ_{gm} is defined as

$$
\begin{aligned}
\Upsilon_{gm}(r_p) &= \Delta\Sigma_{gm}(r_p) - \left(\frac{R_0}{r_p}\right)^2 \Delta\Sigma_{gm}(R_0) \\
&= \frac{2}{r_p^2} \int_{R_0}^{r_p} dR' R' \Sigma_{gm}(R') - \Sigma_{gm}(r_p) + \left(\frac{R_0}{r_p}\right)^2 \Sigma_{gm}(R_0).
\end{aligned}
$$

(5.2)

The observable for the weak gravitational lensing is the sum of the tangential shear from lensing (γ_t^G) and galaxy intrinsic shear (γ^I). Assuming galaxy intrinsic shear is negligible, lensing observation is proportional to $\Delta\Sigma(r_p) = \bar{\Sigma}(< r_p) - \Sigma(r_p)$, which is a measure of excess surface mass density. The value of $\Delta\Sigma(r_p)$ depends on all scales below r_p, which is not quite well described by linear theory. Υ_{gm}, shown in Eq. (5.2), is an attempt to cast the lensing observable $\Delta\Sigma(r_p)$ in such a way that it becomes independent of information below a certain scale R_0. Υ_{gg} is defined as

$$
\Upsilon_{gg}(r_p) = \rho_{crit} \left[\frac{2}{r_p^2} \int_{R_0}^{r_p} dR' R' w_{gg}(R') - \right.
$$

$$
\left. w_{gg}(r_p) + \left(\frac{R_0}{r_p}\right)^2 w_{gg}(R_0) \right] \quad (5.3)
$$

Here w_{gg} represents the projected galaxy-galaxy correlation function. These definitions ensure that despite measuring slightly different observables for the lensing and clustering, they are transformed to the same statistic of the correlation function, so that the theoretical prediction of E_G is equivalent to the measurement. Theoretically E_G can be defined in

terms of metric perturbations:

$$E_G = \frac{\nabla^2(\Psi(r) - \Phi(r))}{3H_o^2 a^{-1}\theta}\,, \tag{5.4}$$

where θ is the perturbation in matter velocity field, H_0 is the Hubble parameter today and a is the scale factor. The ψ and ϕ represent metric perturbations to the time and space components, respectively, assuming a Friedmann-Robertson-Walker (FRW) metric with a flat universe. The numerator $\nabla^2(\Psi(r) - \Phi(r))$ probes the lensing convergence and the θ in denominator probes the redshift space distortions. As shown in [157], the time-time and momentum Einstein field equation in GR, under the assumption of negligible anisotropic stress and non-relativistic matter species, becomes the simple algebraic equation,

$$k^2\Psi = -4\pi Ga^2\rho(a)\delta\,, \tag{5.5}$$

$$\Phi = -\Psi\,, \tag{5.6}$$

where ρ is the background matter density and δ is the matter density perturbation. In modified theories of gravity these relations are different, which requires two extra functions $\mu(k,a)$ and $\gamma(k,a)$ to account for departure from GR [157].

$$k^2\Phi = -4\pi Ga^2\mu(k,a)\rho\Delta \tag{5.7}$$

$$\Phi = -\gamma(k,a)\Psi\,, \tag{5.8}$$

The perturbation equations in Ψ and Φ are in fourier space which should be related to its real space counter part $\Psi'(r) = \Psi(k)e^{-ikr}$, $\Phi'(r) = \Phi(k)e^{-ikr}$. This gives us the relation $\nabla^2(\Psi'(r) - \Phi'(r)) = -k^2(\Psi(k) - \Phi(k))$. We combine the perturbation equation and the definition of E_G with $\Omega_M(z=0) = \frac{8\pi G\rho_o}{3H_o^2}$, $\rho = \rho_o a^{-3}$ and $\theta = -f\delta$ to get our theoretical

prediction of $E_G = -\Omega_M(z=0)\mu(k,a)(\gamma(k,a)+1)/2f$. The $E_G = \Omega_M(z=0)/f$ can be recovered for GR by substituting $\mu = -1$ and $\gamma = 1$.

It is non-trivial to see the connection between our theoretical definition (Eq. 5.4) and the observational definition (Eq. 5.1). We provide a brief outline to make this connection a little bit easier. Please refer to Reyes et al. [304] and Baldauf et al. [31] for more details. The statistics Υ for galaxy-matter and galaxy-galaxy can be written in terms of their corresponding power spectrum as follows.

$$\Upsilon_{gg,gm}(r_p; R_0) = \int P_{gg,gm} W_\Upsilon(k; r_p, R_0) dk \,, \tag{5.9}$$

where $W_\Upsilon(k; r_p, R_0)$ is the window function for Υ given in equation 17 of Baldauf et al. [31]. We know that galaxy-matter power spectrum is proportional to the cross power of convergence ($\nabla^2(\Psi - \Phi)$) and galaxy. This implies that $P_{gm} \equiv \langle \nabla^2(\Psi - \Phi)\delta_g \rangle$. We also know that galaxy-galaxy power spectrum can be written as follows,

$$P_{gg} \equiv \langle \delta_g \delta_g \rangle = -\frac{1}{\beta} \langle \theta \delta_g \rangle \tag{5.10}$$

The first equivalence is the definition of the galaxy-galaxy power spectrum. The second equality results from the fact that for linear regime, matter conservation relates velocity perturbations (θ) to matter perturbations (δ) by $\theta = -f\delta$ and, linear bias model relates δ to δ_g by $\delta_g = b\delta$. Now, the ratio of Υ_{gm} and $\beta\Upsilon_{gg}$ gives the ratio of power spectrum, which will be proportional to $(\nabla^2(\Psi - \Phi)\delta_g)/\theta\delta_g$. Therefore our observational definition given by Eq. (5.1) is same as the theoretical definition given by Eq. (5.4).

5.4 DATA

We use the SDSS-III BOSS CMASS sample and shape measurements from CFHTLenS data to measure the galaxy-galaxy clustering, galaxy matter cross-correlation and redshift space distortions parameter. We describe the data sets used in our analysis in the following sections.

5.4.1 BOSS CMASS

We use data included in data release 11 (DR11; Alam et al. 9) of the Sloan Digital Sky Survey (SDSS; York et al. 407). Together, SDSS I, II [1] and III [115] used a drift-scanning mosaic CCD camera [132] to image over one-third of the sky (14555 square degrees) in five photometric bandpasses [122, 351, 104] to a limiting magnitude of $r < 22.5$ using the dedicated 2.5-m Sloan Telescope [134] located at the Apache Point Observatory in New Mexico. The imaging data were processed through a series of pipelines that perform astrometric calibration [265], photometric reduction [218], and photometric calibration [248]. All of the imaging was reprocessed as part of SDSS Data Release 8 (DR8; Aihara et al. 6). BOSS [96] is designed to obtain spectra and redshifts for 1.35 million galaxies over a footprint covering 10,000 square degrees. These galaxies are selected from the SDSS DR8 imaging and are being observed together with 160,000 quasars and approximately 100,000 ancillary targets. The targets are assigned to tiles using a tiling algorithm that is adaptive to the density of targets on the sky [60]. Spectra are obtained using the double-armed BOSS spectrographs [349]. Each observation is performed in a series of 900-second exposures, integrating until a minimum signal-to-noise ratio is achieved for the faint galaxy targets. This ensures a homogeneous data set with a high redshift completeness of more than 97% over the full survey footprint. Redshifts are extracted from the spectra using the methods described in Bolton et al. [65]. A summary of the survey design appears in Eisenstein et al.

[115], and a full description is provided in Dawson et al. [96].

We use the CMASS sample of galaxies [65] from Data Release 11. The CMASS sample has 690,826 massive galaxies covering 8498 square degrees in the redshift range $0.43 < z < 0.70$, which correspond to an effective volume of 6 Gpc^3.

5.4.2   CFHTLENS

For the galaxy-galaxy lensing measurements, we use the deeper and better quality imaging data from the Canada France Hawaii Telescope Legacy survey (CFHTLS). This data allows us to measure the tangential distortion of background galaxies around our sample of CMASS galaxies. We use the photometric reduction and image shape determinations in the publicly available CFHTLenS catalog[1]. The quantities needed for each galaxy, namely its shear estimate, shear calibration factors, weight, and the posterior distribution of its photometric redshift distribution are provided in the catalog [143, 116, 228, 145]. We use the same quality cuts on the data as were applied in Miyatake et al. [231]. Finally we note that the overlap between the CFHTLS and the DR11 BOSS fields is limited to an area of about 105 deg^2. The number of CMASS galaxies that lie within the CFHTLS footprint is 8899.

5.5   Measurements

The quantity E_G is a combination of galaxy-galaxy annular differential surface density (Υ_{gg}), galaxy-matter annular differential surface density (Υ_{gm}) and the redshift space distortion parameter (β). In the following section we describe the procedure to obtain each of these signals.

---

[1]http://www.cfhtlens.org/astronomers/data-store

5.5.1 Galaxy-Galaxy annular surface density (Υ_{gg})

The data from SDSS-III BOSS includes the three-dimensional positional information of CMASS galaxies, which enables us to perform a high signal-to-noise measurement of the projected correlation function, w_p, and the associated Galaxy-Galaxy annular surface density, Υ_{gg}. We account for a number of subtle selection effects in order to obtain a precise measurement of clustering [314]. The spectroscopic target sample is obtained from the SDSS imaging observations after the application of a variety of colour and photometric selection cuts [96, 298]. However, due to the limited number of fibers available, not all galaxies from this target sample can be allocated a fiber while performing spectroscopic observations to determine their redshifts. This could also happen if two targets are within $62''$ of each other and hence cannot be simultaneously observed due to the finite size of fibers. If such fiber-collided galaxies lie in a region of the sky which is visited multiple times (due to overlaps in the target tiling) then they may have redshift measurements. There are also instances where a galaxy is assigned to a fiber, but its redshift could not be obtained. Finally, there are also instances where it is difficult to perform star-galaxy separation, especially in fields with a high number density of stars. These effects have been quantified in the parent DR11 catalog of CMASS galaxies by assigning a weight to each galaxy such that

$$w_\mathrm{l} = w_* \left(w_\mathrm{noz} + w_\mathrm{cp} - 1 \right), \tag{5.11}$$

where w_noz is the weight assigned to a galaxy if it is the nearest neighbour (in the plane of the sky) of a redshift failure galaxy, w_cp is similarly assigned to account for the nearest neighbours of fiber collided galaxies[2], and w_* accounts for the systematic relationship be-

---

[2]Nearest neighbour corrections have been shown to accurately correct for fiber collisions above the fiber collision scale ($\sim 0.4 h^{-1}$ Mpc) by Guo et al. [136]. Both w_noz and w_cp are equal to unity by default for all galaxies. Their values are incremented for the nearest neighbours of every redshift failure or fiber collided galaxy.

tween density of stars and density of BOSS target galaxies [for details, see 21]. The BOSS parent catalog contains an additional weight, w_{FKP}, for each galaxy which depends upon the number density of galaxies in the sample at its redshift [118]. The total weight for each galaxy that we use is given by

$$w_{\mathrm{tot}} = w_{\mathrm{l}} w_{\mathrm{fkp}} \,. \tag{5.12}$$

We use catalogues of random points with the same angular and redshift selection as our galaxy subsample. These random catalogs consist of about 50 times more points than the number of galaxies in each of our subsamples. We assign each random point a weight of $N_{\mathrm{gal}}/N_{\mathrm{ran}}$ to account for this difference. In practice, we use the random catalogs provided with SDSS DR11 [298].

We measure the correlation function of galaxies, $\xi(r_p, \Pi)$, where r_p is the projected separation of galaxies, and Π, their line-of-sight separation, using the estimator proposed by Landy and Szalay [194],

$$\xi(r_p, \Pi) = \frac{DD - 2DR + RR}{RR} \,. \tag{5.13}$$

Here, DD, RR and DR represent the number of appropriately weighted pairs of galaxies with a given separation (r_p, Π), where both galaxies lie either in the galaxy catalog or the random catalog or one in each of the catalogs, respectively. The projected correlation function is obtained by integrating $\xi(r_p, \Pi)$ along the line of sight,

$$w_{\mathrm{p}}(r_p) = 2 \int_0^{\Pi_{\mathrm{max}}} \xi(r_p, \Pi) \, d\Pi \,, \tag{5.14}$$

where we adopt $\Pi_{\mathrm{max}} = 100 h^{-1}\mathrm{Mpc}$. We then convert the projected correlation function into galaxy-galaxy annular differential surface density following Eq. (5.1), where we adopt $R_0 = 1.49 h^{-1}\mathrm{Mpc}$. Figure 5.2 shows the projected correlation function and galaxy-

galaxy ADSDs measured from data and simulation. We carry out this measurement at $1.5 \lesssim r_p \lesssim 40\ h^{-1}\mathrm{Mpc}$ divided into 9 bins.

5.5.2 Galaxy-Matter annular surface density (Υ_{gm})

For the weak lensing measurement, we followed the procedure described in [231]. In this paper we summarize the procedure; we encourage those who are interested in details to read reference. The tangential shear caused by lensing is related to the excess surface mass density as

$$\gamma_t^G = \frac{\Delta\Sigma(r_p)}{\Sigma_{\mathrm{cr}}}, \tag{5.15}$$

where Σ_{cr} is defined as

$$\Sigma_{\mathrm{cr}}(z_l, z_s) = \frac{c^2}{4\pi G}\frac{d_A(z_s)}{d_A(z_l)d_A(z_l, z_s)(1 + z_l)^2}. \tag{5.16}$$

Here, $d_A(z_l)$, $d_A(z_s)$, and $d_A(z_l, z_s)$ are the angular diameter distance to lens, source and between lens and source. The factor of $(1+z_l)^{-2}$ is due to our use of comoving coordinates. Using lens-source pairs, the excess surface mass density is calculated as

$$\Delta\Sigma(r_p) = \frac{\sum_{ls} w_{ls} e_t^{ls} \Sigma_{\mathrm{cr}}^{ls}}{(1 + K(r_p))\sum_{ls} w_{ls}}, \tag{5.17}$$

where e_t is the ellipticity of a source galaxy given by the CFHTLenS catalog[3]. When calculating $\Sigma_{\mathrm{cr}}^{ls}$, we use the probability distribution function of photometric redshift (photo-z). We use the weight $w_{ls} = w_{\mathrm{tot},l} w_s \Sigma_{\mathrm{cr}}^{-2}$, where $w_{\mathrm{tot},l}$ is the weight of each lens galaxy given by Eq. (5.12) and w_s is the weight of each galaxy given by the CFHTLenS catalog. The factor of $(1 + K(r_p))^{-1}$ is calculated using the multiplicative bias correction factor

---

[3]The ellipticity in the CFHTLenS catalog is defined by $|e| = (a - b)/(a + b)$, where a and b are the semi-major and semi-minor axes of the ellipse. The ensemble expectation value of this ellipticity definition is equal to the lensing shear.

given by the CFHTLenS catalog. We use the same r_p binning as the clustering measurement (Υ_{gg}).

We perform two systematic tests for the lensing measurement. The first is a test for contamination from galaxies that are physically associated with lens galaxies, and therefore not lensed. If we wrongly select those galaxies as sources, the lensing signal is diluted. This effect can be diagnosed using the so-called "boost factor" which is a ratio of the sum of the weight of galaxies behind lens galaxies to that behind random points [342]. If the lensing signal is diluted, the boost factor is larger than unity. In our measurement, we find the boost factor is consistent with unity within 1.6% at $r_p \gtrsim 1.5\ h^{-1}\mathrm{Mpc}$, the scales used for this study. The statistical error in the boost factor is subdominant compared to the statistical error coming from the shape noise. The second systematic test is for the effect of imperfect PSF correction. This can be diagnosed by measuring the lensing signal around random points, which exhibits a spurious signal for certain types of imperfection in the PSF correction. In our measurement, the lensing signal around random points deviates from zero at $r_p \gtrsim 5\ h^{-1}\mathrm{Mpc}$. We find that the 45-degree rotated signal, which should be consistent with zero around galaxies, deviates from zero at these scales. After subtracting the signal around random points, the 45-degree rotated signal becomes consistent with zero except for the outermost bin at $r_p \sim 40\ h^{-1}\mathrm{Mpc}$. Thus we apply the same correction to the lensing signal, and discard the outermost bin. The correction ranges from 5% to 14% of the lensing signal before correction. The statistical uncertainty on this correction is very small since the number of random points is much larger than the number of real lenses. This correction is a valid way to correct for shear systematics that were not fully removed by the PSF correction routine, provided that the source of the systematics does not correlate with the lens number density. Since the lenses are selected in one survey and the shears measured in another, there is no reason for such a correlation to exist, so the correction is valid and we do not associate a systematic uncertainty with this correction [220].

The covariance matrix of the lensing signal is estimated by using 50 realizations of the lensing signal around random lens samples. This naturally accounts for correlated shape noise at large radii, which is caused by the use of the same source galaxies multiple times as the stacking annuli overlap for different lens galaxies, and projection effect due to the large-scale structure along the line of sight.

We then convert the excess surface mass density into galaxy-matter annular differential surface density following Eq. (5.1). Figure 5.1 shows our measured galaxy-matter annular differential surface density, including the size of the systematic correction for imperfect PSF correction.

5.5.3 Redshift Space Distortions parameter (β)

We measure the two-dimensional auto-correlation function of the BOSS CMASS galaxies using the Landy-Szalay [194] estimator. The correlation function is first binned in (r, μ), where r is the three-dimensional galaxy pair separation and $\mu = \cos(\theta)$ with θ being the angle made by the pair of galaxies from the line of sight. The galaxy-galaxy auto-correlation is projected onto the Legendre basis in order to obtain the monopole (ξ_0) and quadruple (ξ_2) moments. The monopole and quadruple moments of the correlation function are evaluated between 6 to 198 h^{-1}Mpc in linear bins of width 8 h^{-1}Mpc. The bin size of 8 h^{-1}Mpc is chosen to optimize signal-to-noise without smoothing out the important physics. We have used 600 PTHalo mocks [222] to generate an estimate of the covariance matrix for the measured correlation function. The fit to the monopole and quadruple moments of the correlation function is obtained using Convolution Lagrangian Perturbation Theory (CLPT) and Gaussian Streaming Model (GSM) [72, 386].

The theoretical model has been tested using PTHalo mocks. It was shown that our model gives accurate prediction of $\xi_{0,2}$ at scales ranging from 30 h^{-1}Mpc to 126 h^{-1}Mpc
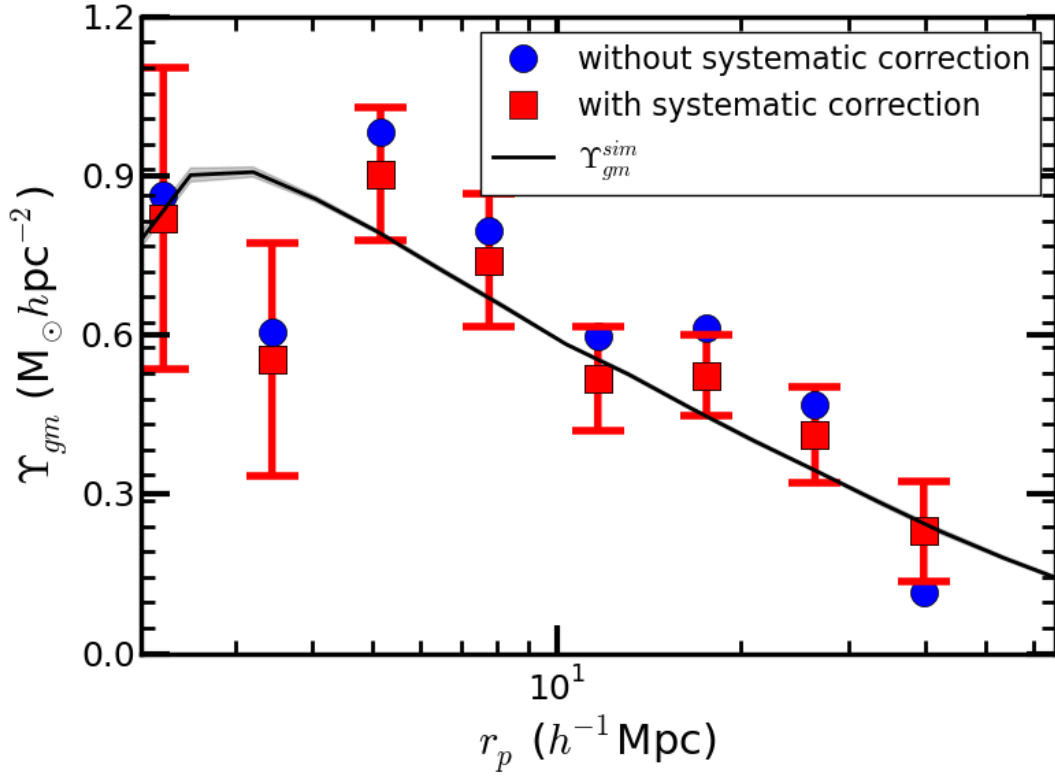
Figure 5.1: The plot shows the galaxy-matter annular surface density (Υ_{gm}) measured from CFHTLenS and CMASS catalogues. The blue points are measurements before and red points are after applying an additional systematic correction for imperfect PSF correction resulting in additive shear systematics. The black line and shaded region shows the measurement of Υ_{gm} and 1σ error from an N-body simulation.

with 8 h^{-1}Mpc bin width. The measured $f\sigma_8(z = 0.57) = 0.462 \pm 0.041$ and $b\sigma_8(z = 0.57) = 1.194 \pm 0.032$, as reported in [12] .The RSD parameter β is computed by taking the ratio of the measured growth rate f and bias b, i.e., $\beta = f/b$. This gives us $\beta(z = 0.57) = 0.387 \pm 0.042$, while accounting for the correlation between growth rate and bias. The complete redshift space distortion analysis is reported in [12], including the list of parameters marginalized and prior used on those parameters in table 2 of that work. A comparison of this measurement with other similar measurements is shown in Figure 6 of [12].

5.6 N-body Simulations

We use N-body simulations in order to investigate systematic effects and estimate various possible systematic corrections. We use an N-body simulation run using the TreePM method [30, 394, 302], provided by Martin White. We are using 10 realizations of this simulation based on the ΛCDM model with $\Omega_m = 0.292$ and $h = 0.69$. These simulations are in a periodic box of side length $1380h^{-1}$Mpc and 2048^3 particles. A friend-of-friend halo catalogue was constructed at effective redshift of $z = 0.55$. This is appropriate for our measurements since the galaxy sample used has effective redshift of 0.57. Miyatake et al. [231] found weak redshift evolution of the clustering and lensing signal. Therefore our simulations should provide a good approximation to the original data. The Halo Occupation Distribution [HOD; 251, 338, 41, 393, 42, 91] is used to relate the observed clustering of galaxies with halos measured in the N-body simulation. The HOD model used was proposed in [395] to populate the halo catalogue with galaxies. The number of galaxies hosted in each halo is a function of halo mass; halos can host central and satellite galaxies. The

occupation distributions are

$$\langle N_{\mathrm{cen}}\rangle_M = \tfrac{1}{2}\mathrm{erfc}\left(\frac{\ln(M_{cut}/M)}{\sqrt{2}\sigma}\right),$$
$$\langle N_{\mathrm{sat}}\rangle_M = \langle N_{\mathrm{cen}}\rangle_M \left(\frac{M-\kappa M_{cut}}{M_1}\right)^\alpha, \tag{5.18}$$

where $\langle N_{\mathrm{cen}}\rangle_M$ is the average number of central galaxies for a given halo mass M and $\langle N_{\mathrm{sat}}\rangle_M$ is the average number of satellites galaxies. The HOD parameters we used[4] are $(M_{cut} = 1.77 \times 10^{13} M_\odot/h, M_1 = 1.51 \times 10^{14} M_\odot/h, \sigma = 0.897, \kappa = 0.137, \alpha = 1.151)$. We have populated central galaxies at the center of the halos. The satellite galaxies are populated with radius (distance from central galaxy) distributed as per the NFW profile out to r_{200} and the direction is chosen randomly with a uniform distribution assuming satellites are spherically distributed. It is a good approximation because only $\sim 10\%$ of the galaxies are satellites. The central galaxies are each assigned the same velocity as their halo. The satellite galaxies are assigned velocities which are normally distributed, with mean as the halo velocity and dispersion the same as the halo velocity dispersion.

We find that the clustering measurement between our N-body simulation and measurement agrees within 1σ. The top panel of Figure 5.2 shows the projected galaxy-galaxy (red) and galaxy-matter (blue) correlation functions. The shaded regions are the standard deviation of 10 N-body mocks. The galaxy-galaxy projected correlation function measured from data shown in black points agrees quite well with the one measured from N-body simulation. The projected galaxy-galaxy correlation is used to measure Υ_{gg}, which is shown in the middle panel of Figure 5.2. The projected galaxy-matter cross-correlation function is

---

[4]These HOD parameters were obtained by carrying out a fit to the projected clustering signal, w_{p} measured in Section 5.5.1, and the CMASS galaxy abundance using the analytical halo model framework [378, 234, 70]. The analytical halo model developed in these papers accounts for halo exclusion, radial dependence of halo bias, and the residual redshift space distortions due to finite extent of the line-of-sight integration used to compute w_{p}. We refer the reader to these papers and to More et al. [236] for the details of the modelling procedure. **We have to be careful because the halo masses are $M_{200\mathrm{m}}$ in the model while the halos are FOF.**

used to compute Υ_{gm}, which is shown in Figure 5.1. The measurement of Υ_{gm} from the N-body simulation (using the w_p-based HOD parameters) and data agrees very well.

5.7   Potential Systematics

We investigate various possible systematic effects which can affect our measurement of E_G. We will show that some of them are negligible and have computed corrections for others. These corrections are small compared to the statistical uncertainty on the measurement. We have applied these systematic corrections to our final measurement. An alternative approach to account for these systematic shifts is to apply them to the theoretical prediction as shown in [199].

5.7.1   Scale dependence of bias

Galaxies are formed in dark matter halos, which makes the clustering amplitude of galaxies biased compared to that of dark matter. The massive galaxies used in our analysis are a highly biased sample. It has been shown that a linear bias model fails to match the observations and simulations at small scales [318]. E_G is constructed in such a way that it is independent of linear bias. However, the redshift space distortion parameter β is computed using the linear bias whereas the projected correlation function is calculated at smaller scales, where the bias is scale-dependent, the causing bias factor in E_G to not completely cancel. To correct for this factor, we compute the correction factor $C_b(r_p) = \Upsilon_{gg}(r_p)/b\Upsilon_{gm}(r_p)$ the from mock catalogs in Section 5.6, as proposed by [304]. The correction factor $C_b(r_p)$ is shown in Figure 5.3, where linear bias $b = 1.95$ was measured in RSD analysis of our N-body simulation using RSD model of [12]. The Υ_{gg} and Υ_{gm} for this correction is computed using 10 N-body simulations shown in Figure 5.2. The scale-dependent bias correction C_b has maximum value of 8% at 8 h^{-1}Mpc. It is important to note that our
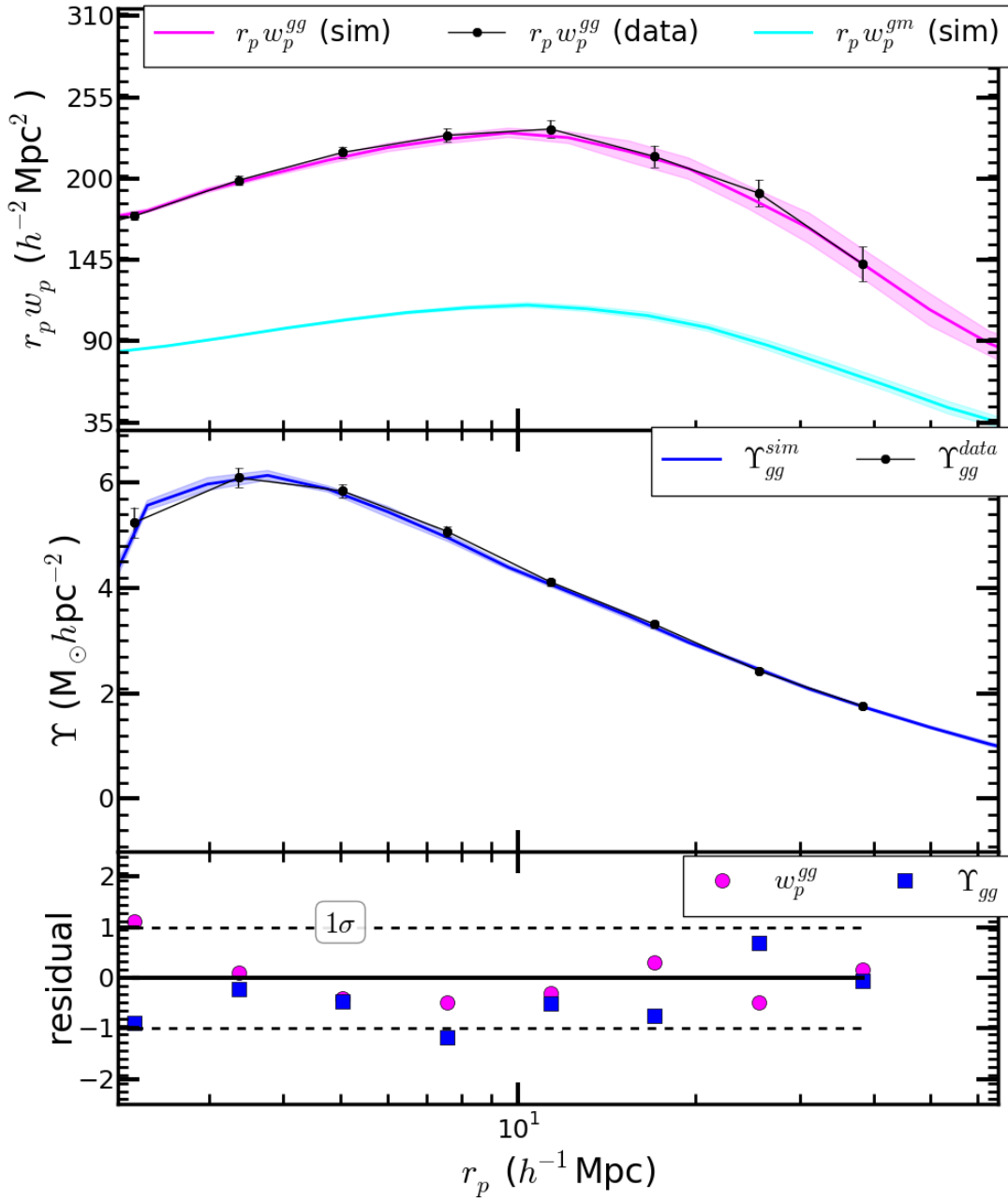
Figure 5.2: The top panel shows the projected correlation function, middle panel shows ADSDs and the bottom panel shows the residual between data and simulation as the function of r_p. The black dots are measurement from the BOSS CMASS sample. The red and blue line represents measurements of galaxy-galaxy and galaxy-matter clustering from N-body simulations. The shaded regions are standard deviation of 10 N-body simulations. The red and blue points in the bottom panel shows that the residuals (normalized by statistical uncertainties) are within 1σ for both w_p^{gg} and Υ_{gg} respectively. This shows that our simulations and observations gives consistent results.

scale-dependent bias correction does not approach 1 at the large scales used for this analysis, contrary to our naive expectations. This is because the linear bias is measured from monopole of two point correlation function in redshift space, whereas the bias correction uses projected clustering using Υ, and hence looking at a different projection of two point clustering leads to a different large scale bias.

5.7.2 Difference in Lensing and Clustering Window

E_G includes the ratio of the galaxy-galaxy auto-correlation with galaxy-matter cross-correlation measured from lensing. The galaxy-galaxy auto-correlation is measured in redshift space with a top-hat window. The galaxy-matter cross-correlation, on the other hand, is measured with very broad lensing window that washes out the effect of redshift space distortions and behaves differently with line of sight separation compared to a top-hat. To correct both of these effects, we use the window function correction (C_{win}). The window function correction consists of two parts $C_{win} = C_{RSD}C_{integration}$, where the C_{RSD} is the ratio of Υ_{gg} in redshift and in real space. We compute this correction by evaluating the clustering in real and in redshift space from 10 N-body simulations.

The motivation for the $C_{integration}$ correction is as follows. When making our theoretical predictions for E_G, we begin from a 3D model that we assume is projected to 2D in the same way for both galaxy-galaxy and galaxy-matter correlations, using $\int_{-\Pi_{\max}}^{\Pi_{\max}} \xi_{gg,gm}(r_p, \pi) \, d\Pi$. This is a top-hat window with a hard cutoff at $\Pi_{\max}$. However, reality provides us with a lensing shear signal that is projected using a non-top-hat window. It is not truncated at $\Pi_{\max}$, and it is not flat like a top-hat. We must consider a more generalized situation with some window function $W(\Pi)$ using $\int_{-\Pi_{\max}}^{\Pi_{\max}} \xi_{gm}(r_p, \Pi) W(\Pi) \, d\Pi$. Thus, the ratio of quantities used to construct E_G should differ slightly from the theory prediction that assumes a top-hat window for both. The correction factor by which we should multiply our observed

153

E_G (before comparing with theory) is $C_{integration}$, the ratio of $\Upsilon_{gm}^{(top)}$ with a top-hat window and $\Upsilon_{gm}^{(win)}$ with the lensing window as determined by the source and lens redshift distribution ($C_{integration} = \Upsilon_{gm}^{(top)}(r_p)/\Upsilon_{gm}^{(win)}(r_p)$). The "top" version is in the numerator because we construct E_G with the real lensing data, i.e., we implicitly computed and used the "win" version in the data. We want to divide that out and replace it with the "top" version when comparing with the theory. The lensing window can be written as follows:

$$W(\Pi = \chi(z_m) - \chi(z_l)) = \frac{1}{N} \int dz_l P_{lens}(z_l) \tag{5.19}$$
$$\int_{z_m}^{\infty} dz_s P_{src}(z_s) \Sigma_{cr}^{-2}(z_l, z_s) \frac{\Sigma_{cr}(z_l, z_s)}{\Sigma_{cr}(z_m, z_s)}$$
$$N = \int dz_l P_{lens}(z_l) \int_{z_m}^{\infty} dz_s P_{src}(z_s) \Sigma_{cr}^{-2}(z_l, z_s) \tag{5.20}$$

where the $\Sigma_{cr}(z_1, z_2)$ is given in Eq. (5.16). Currently our theory assumes that we simply take the galaxy matter cross-correlation ξ_{gm}, which is the correlation function between matter at that lens redshift and the lens galaxy position, and projected along the line of sight with a top-hat window. But in practice, if you have matter that is correlated with the lens but not exactly at the lens redshift, then the shear for that source is determined by $\Sigma_{cr}(z_m, z_s)$, which varies along the line of sight as z_m is closer to or farther away from the lens. The (z_l, z_m, z_s) are the redshifts of lens, matter and source respectively. The innermost integral is to account for the fact that matter at z_m will lens all the sources behind matter ($z_s > z_m$) and $P_{src}(z_s)$ is the redshift distribution of source in our sample. The outer integral is to account for the fact that we have a distribution of lens given by $P_{lens}(z_l)$ which should be integrated over. The lens redshift sets the zero point of the line-of-sight separation (Π) for the galaxy-matter cross-correlation. Π is the comoving distance between matter and lens ($\Pi = \chi(z_m) - \chi(z_l)$). Here $\chi(z)$ is the comoving distance to the redshift z. We compute $W(\Pi)$ with the CFHTLenS source redshift distribution and CMASS lens redshift

distribution. We use the N-body simulation to estimate the galaxy-matter cross-correlation and apply $W(\Pi)$ in order to compute the projected correlation function with the lensing window. Figure 5.3 shows the C_{win} correction we have computed for our sample. It is below 8% at the scales of interest.

5.7.3 Different redshift weighting of lensing and clustering

The lensing signal depends on the number of source galaxies behind a lens galaxy. Within an annulus of fixed transverse separation, the galaxies at lower redshift have a higher number of sources behind them compared to galaxies at higher redshift. This makes the effective redshift of the lensing measurement smaller than the effective redshift of clustering measurement. In order to correct for this difference in redshift, we compute the multiplication factor $C_z = \Upsilon_{gg}^{clust}/\Upsilon_{gg}^{lens}$. Here Υ_{gg}^{lens} is galaxy-galaxy clustering signal obtained with lensing weight as the function of redshift and Υ_{gg}^{clust} is galaxy-galaxy clustering signal obtained without lensing weight. This shifts the effective redshift of the clustering signal to the effective redshift of lensing signal. Figure 5.3 shows the C_z correction we have computed for our sample. It is less than 1% at the scales of our interest.

5.7.4 Effects of Intrinsic Alignments

When photometric redshift errors cause galaxies that are at the lens redshift to be included in the source sample for the lensing meausurement, the lensing measurement can be contaminated by intrinsic alignments [for reviews, see 375, 175] of the false sources towards the lenses. The majority of the large-scale intrinsic alignment signal is carried by red galaxies [e.g., 149], for which the linear tidal alignment model [e.g., 147] provides a reasonable large-scale description that matches observations of this effect [e.g., 174], and for which there are various descriptions on small scales [e.g., 63]. In brief, pressure-supported galax-
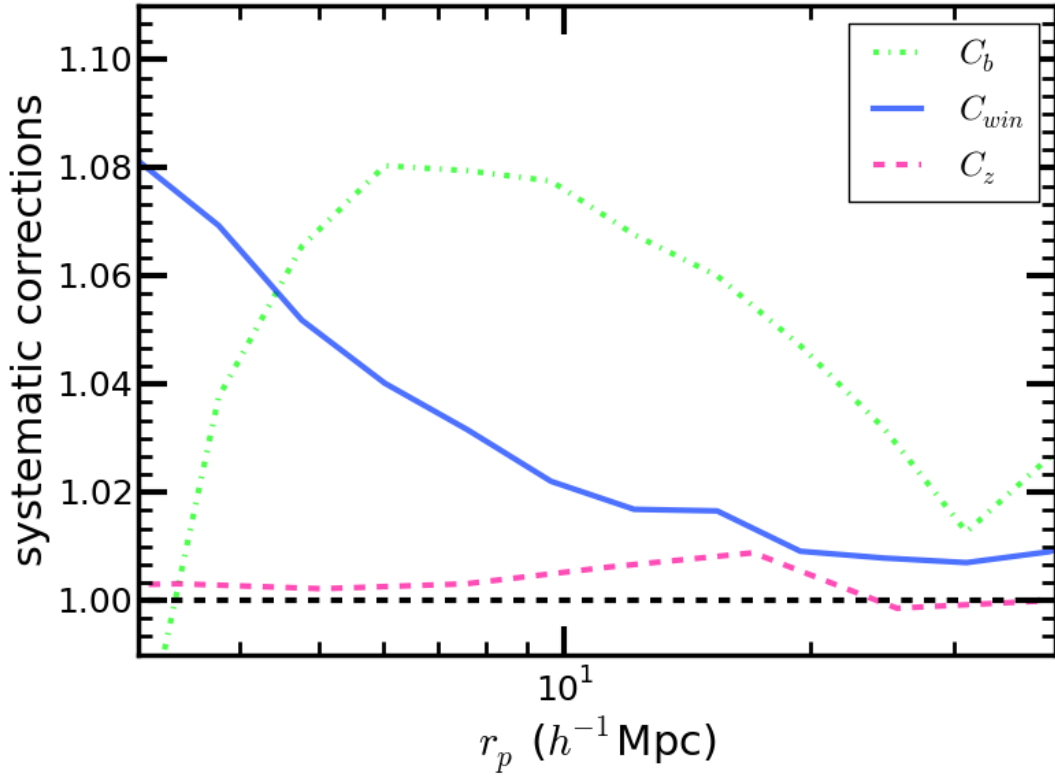
Figure 5.3: Figure shows the systematic corrections estimated for E_G . The green dashed-dotted line is the correction for the scale dependent bias (C_b; see section 5.7.1). The blue solid line is for the correction due to difference in the clustering and lensing radial windows (C_{win}; see section 5.7.2). The magenta dashed line is for the correction due to difference in redshift weighting of clustering and lensing (C_z; see section 5.7.3).

ies form in primordial tidal fields due to large-scale structure; these tidal fields have stretch-ing axes that point towards over-densities, and as a result the galaxies that form in those tidal fields also become radially aligned towards overdensities. This manifests as a negative galaxy-galaxy lensing signal, with intrinsically-aligned galaxies pointing radially towards the overdensities that our lens galaxies trace, reducing the measured $\Upsilon_{\rm gm}$. However, our removal of small-scale information partially mitigates the intrinsic alignment effect, which scales with separation roughly in the same way as the matter correlation function. Also, the photometric redshifts in CFHTLenS are good enough to reduce the contamination by physically-associated galaxies to a very low level.

To estimate the magnitude of possible intrinsic alignment contamination in the galaxy-galaxy lensing signal in this work, we need several pieces of information. The first is the average intrinsic shear for galaxies that are within $\sim 100h^{-1}$Mpc of the CMASS galax-ies in our source sample. To estimate this, we use the average intrinsic shear of LOWZ galaxies as a function of r_p, from [347]. We then use the redshift evolution of the linear alignment model to decrease this by a factor of 0.85 to go to the CMASS redshift, and by a factor of ten to account for the fact that the sources that are used here are on average about eight times fainter than LOWZ galaxies. The factor of 10 arises because intrinsic alignments are consistent with a slightly steeper than linear scaling with luminosity for red galaxies, as determined empirically in Joachimi et al. 174 and Singh et al. 347, though this is an extrapolation below the luminosity range in which measurements exist. This gives an estimate of $\langle \gamma_{\rm int} \rangle$ for the source sample in this work.

In cases where there are many satellite galaxies at the lens redshift included in the "source" sample, and thus a boost factor substantially in excess of 1, it is common practice to assume that only those excess galaxies are intrinsically aligned [e.g., 62]. In our case, there are essentially no "excess" galaxies, but we still must assume that non-excess galaxies near the lenses are intrinsically aligned. To account for this, we calculate the fraction of

sources that are within $100h^{-1}$Mpc along the line-of-sight from a typical CMASS galaxy, given the source $p(z)$. For example, for a fixed redshift z_{lens},

$$f_{\text{local}}(z_{\text{lens}}) = \int_{z_{\text{lower}}}^{z_{\text{upper}}} \mathrm{d}z\, p(z) \tag{5.21}$$

where the lower and upper limits of integration are defined by finding the redshift corresponding to $\pm 100h^{-1}$Mpc separations from the lens redshift, and we assume the source $p(z)$ are normalized to integrate to unity over all redshifts We average the $f_{\text{local}}(z_{\text{lens}})$ estimates over the lens redshift distribution. This average fraction $\langle f_{\text{local}} \rangle$ is approximately 0.05. Finally, we compare $\langle \gamma_{\text{int}} \rangle \langle f_{\text{local}} \rangle$, which is the total estimated intrinsic alignments contamination to the shear, with the measured shear. The estimated contamination has a maximum value (as a function of r_p) of 1 per cent of the measured shear, or at most 0.1σ. Even if some of the above assumptions are incorrect by a factor of two, we conclude that we can safely ignore intrinsic alignment contamination in our measurement, particularly given that (a) the estimates from [347] were for red galaxies, and many of the sources are blue galaxies; and (b) the redshift-dependent lens-weighting will suppress the contributions from these more "local" galaxies that may be intrinsically aligned.

5.7.5   Fingers of God in RSD β

Galaxies that are satellites orbiting within the same halo exhibit random motions due to the gravitational potential well of the halo. This can cause galaxies at the same line of sight distance to have different redshifts, so that they appear to be spread out into a very elongated structure along the line of sight. This effect is known as fingers of god. We have modeled the fingers of god by introducing a parameter σ_{FOG}, a scale-independent additive term in the velocity dispersion of the Gaussian Streaming Model (GSM) [299]. [12] shows that this model recovers the expected parameter for the PTHalo mocks [222] and

N-body mocks (Tinker et al. [373], in prep.). This means that our fingers of god modeling is accurate enough for scale used in our redshift space distortion analysis. The expected bias in the measurement of f should be below 2.6%, much smaller than uncertainty in other measurements, as shown in Figure 5.4. We do not expect any extra bias in our E_G measurement from β.

5.7.6   Cosmic Variance

The CFHTLenS is a relatively small area of sky covering 170 square degree. The overlap between CFHTLenS and BOSS is 105 square degree. This raises the question of our lensing measurement being limited by cosmic variance. We have estimated the cosmic variance from simulations by dividing our N-body simulation into roughly 100 square degree regions at $z = 0.57$. We created 25 such regions and compute Υ_{gm} for each of these regions. The variance of Υ_{gm} from these 25 regions should give us an estimate of cosmic variance in our analysis. We have found that the cosmic variance is much below our lensing statistical error due to shape noise. Figure 5.4 shows the percentage error in different component of our measurement. We can clearly see that the dashed blue line which represents cosmic variance on Υ_{gm} is below the solid blue line representing measurement error on Υ_{gm}.

5.7.7   Calibration Bias

Biases in the estimation of the ensemble lensing shear from the shape measurements of galaxies are one of the major systematics in galaxy lensing measurements. The inaccurate modeling of galaxy shape and PSF could leave both isotropic and anisotropic residuals in the ensemble shear. These residuals affect our shear measurements and can be parametrized as multiplicative and additive corrections [142]. The shape catalogue of CFHTLenS used in our analysis is corrected for these effects as described in [229].We have also shown that our
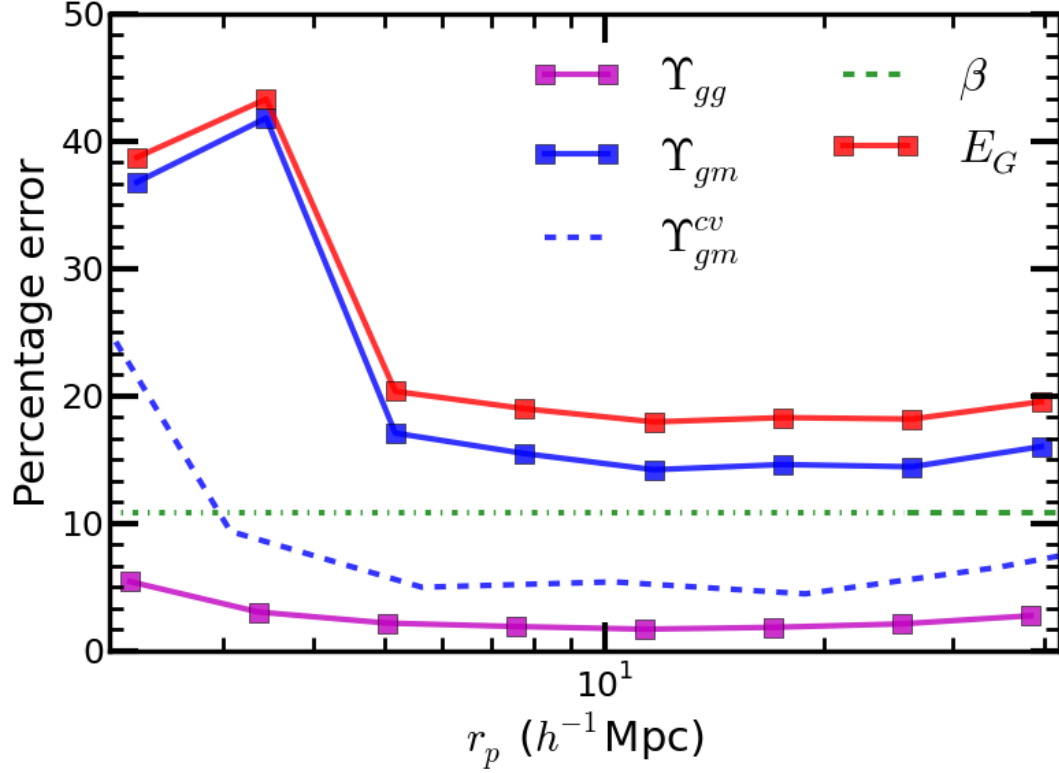
Figure 5.4: Figure shows the percentage error in different components of our measurement. The magenta line shows the error in Υ_{gg}, which is the lowest. The blue line represents the lensing error, and the dashed blue line is an estimate of the cosmic variance due to the finite size of the CFHTLenS fields. The green line is the error on the measurement of the RSD parameter β, and the red line is the combined error on our measurement of E_G. Note that β is measured only above $26 \, h^{-1}\text{Mpc}$, shown with a dashed line.

HOD tuned to match galaxy clustering also matches the lensing measurements without any tuning (see Figs. 5.1 and 5.2), indicating the absence of any statistically significant calibration bias. Although this is not a perfect test, as differences in cosmological parameters such as Ω_m between simulation and reality could potentially absorb such a bias. Note that [213] shows that a multiplicative bias could be detected in the faint subset of the CFHTLenS sample, but this could also be absorbed in many other unknowns and not necessarily hint towards a need for multiplicative bias correction.

Another possible systematic uncertainty in the lensing measurements is due to the bias in the photo-z estimates. In [231], they confirmed that the shift of the lensing signal is within a few percent for the possible range of the photo-z bias $\delta z = \pm 0.02$ [116], which is well below the statistical uncertainty in our lensing measurements.

5.8 Results

In this section we provide the details of our measurement of E_G and its covariance.

5.8.1 Measurement of $E_G(r_p)$

E_G is a combination of three different signals that is designed to be more sensitive to the modification of gravity. We have measured $\Upsilon_{gg}(r_p)$ and $\Upsilon_{gm}(r_p)$ for $2.28 < r_p < 40h^{-1}$Mpc in 8 logarithmic bins as described in Section 6.5. We combine our measured signal to get $E_G(r_p)$ as in Eq. (5.1), then multiply by $C_b C_{win} C_z$ as in Sec. 5.7 in order to correct for differences in how Υ_{gg} and Υ_{gm} are measured that result in deviation from theoretical predictions. Figure 5.5 shows our measurement of $E_G(r_p)$. The blue (red) points show the measurement before (after) systematic corrections. The black line shows the GR prediction and the shaded region is one sigma error according to Planck (2015; TT+lowP+lensing; Planck Collaboration et al. 275).

5.8.2 Covariance matrix of E_G

The covariance of Υ_{gm} has been computed as described in Section 6.5. The covariance on Υ_{gg} is obtained using jacknife. The error on measurement of β was obtained as part of the redshift space distortion analysis described in [12]. We compute the diagonal error on E_G by adding the errors from Υ_{gm}, Υ_{gg} and β in quadrature as

$$\sigma_{EG}(r_p) = E_G(r_p)\sqrt{\left(\frac{\sigma_{\Upsilon_{gm}}}{\Upsilon_{gm}}\right)^2 + \left(\frac{\sigma_{\Upsilon_{gg}}}{\Upsilon_{gg}}\right)^2 + \left(\frac{\sigma_\beta}{\beta}\right)^2} \tag{5.22}$$

We then compute the correlation matrix of Υ_{gm} given by

$$\Psi_{gm}(r_i, r_j) = \Sigma_{gm}(r_i, r_j)/\sqrt{(\Sigma_{gm}(r_i, r_i)\Sigma_{gm}(r_j, r_j))} \tag{5.23}$$

where $\Sigma_{gm}(r_i, r_j)$ represents the covariance matrix of Υ_{gm}. The covariance matrix for E_G is obtained by multiplying the σ_{EG} with the correlation matrix,

$$\Sigma_{EG}(r_i, r_j) = \sigma_{EG}(r_i)\sigma_{EG}(r_j)\Psi(r_i, r_j) \tag{5.24}$$

Figure 5.6 shows the correlation matrix of E_G we have measured. We have assumed that the different components of E_G are independent while estimating the covariance matrix. It is a reasonable assumption because the clustering signal Υ_{gg} and lensing signal Υ_{gm} are integrated along the line of sight and hence will not be correlated with the redshift space distortions parameter β. Also, the lensing measurement is dominated by shape noise with errors at the 20% level on all scales, whereas the statistical errors on the clustering measurements are below 5% at all scales. Moreover the lensing is measured in a very small fraction of the area used for the clustering measurement. For both reasons, the clustering and lensing are independent in our analysis, justifying the use of the Υ_{gm} correlation matrix
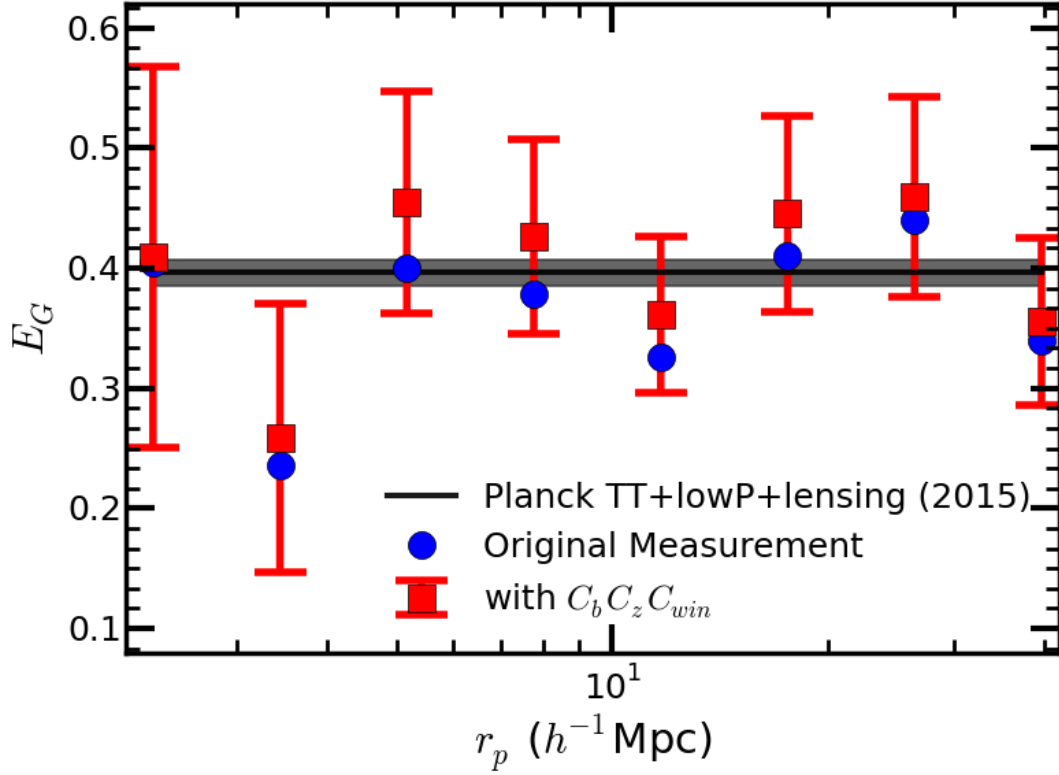
Figure 5.5: The plot shows E_G as a function of r_p. The blue points show the raw measurement (without any corrections) and the red points are the final measurement after multiplying by systematic corrections ($C_b C_z C_{win}$). The black line is the prediction of GR for Planck (2015; TT+lowP+lensing) cosmology with shaded region representing 1σ error.

to estimate the covariance matrix for E_G.

5.8.3 Constraint on E_G

We have shown our measurement of E_G in logarithmic bins of r_p in Figure 5.5. We can obtain a measurement of E_G at an effective average scale by combining the information from all scales. The constant E_G model can be used in order to obtain the constraint on E_G using our measurement. We have used measurements between r_p of $5.17h^{-1}$ Mpc and $26.4h^{-1}$ Mpc. The lower limit is to avoid small scales where systematic corrections become large and baryonic physics might start to become important [232]. The upper limit is
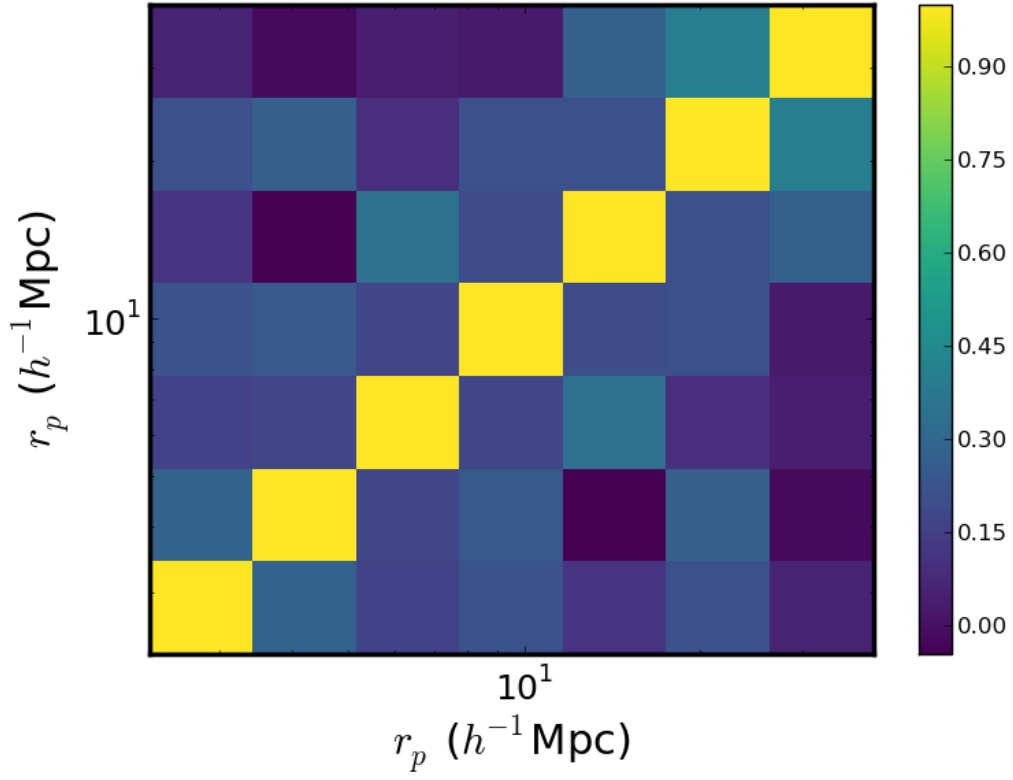
Figure 5.6: **Correlation matrix** (Ψ) **of** E_G**:** We have estimated covariance of Υ_{gm} from random points. This covariance is then used to compute the correlation matrix (see equation 5.23 for details).

determined by the scale at which the systematic correction for the lensing becomes substantial compared to the lensing signal itself. We fit our measurements of $E_G(r_p)$ with the full covariance matrix using the model of constant E_G, giving $E_G(z = 0.57) = 0.41 \pm 0.047$. Figure 5.7 shows our likelihood for E_G as a red solid line. The black line and the shaded region are the Planck (2015;TT+lowP+lensing) prediction. The magenta dashed line is the measurement of Blake et al. [56]. Our measurement is consistent with the Planck prediction and agrees with [56]. Our final measurement of E_G has an 11% statistical uncertainty, which is two times better than the previous best measurement at the same redshift [56]. Note that the Blake et al. [56] measurement is 1.4σ from the Planck 2015 cosmology but less than 1σ from the WMAP7 cosmology, which is closer to their assumed cosmology.

5.9 Discussion

We have analyzed data from CFHTLenS [143] and the SDSS-III BOSS DR11 CMASS sample [9]. We have measured tangential shear by cross-correlating the CFHTLenS galaxy shapes with the lens sample (CMASS). This produces a measure of the excess surface mass density $\Delta\Sigma$. We have also measured redshift space galaxy-galaxy clustering ($w_p(r_p)$) and the logarithmic derivative of growth rate (β). All of these measurements are tested for various systematics as described in Section 6.5. We then cast these measurements in terms of the annular differential surface densities [ADSDs; 31] to suppress the small scale information. The Υ_{gg} is defined to match the kernel with Υ_{gm}. These measurements are then combined to estimate $E_G(r_p)$ (see Figure 5.5). We have also estimated the covariance on our measurements by combining the covariance of Υ_{gm} with the diagonal error on Υ_{gg} and β in quadrature (see Figure 5.6). The scale-averaged measurement of E_G is obtained by fitting a constant E_G model. We have also considered potential systematic errors that can affect our measurements of E_G and computed possible corrections or provided upper
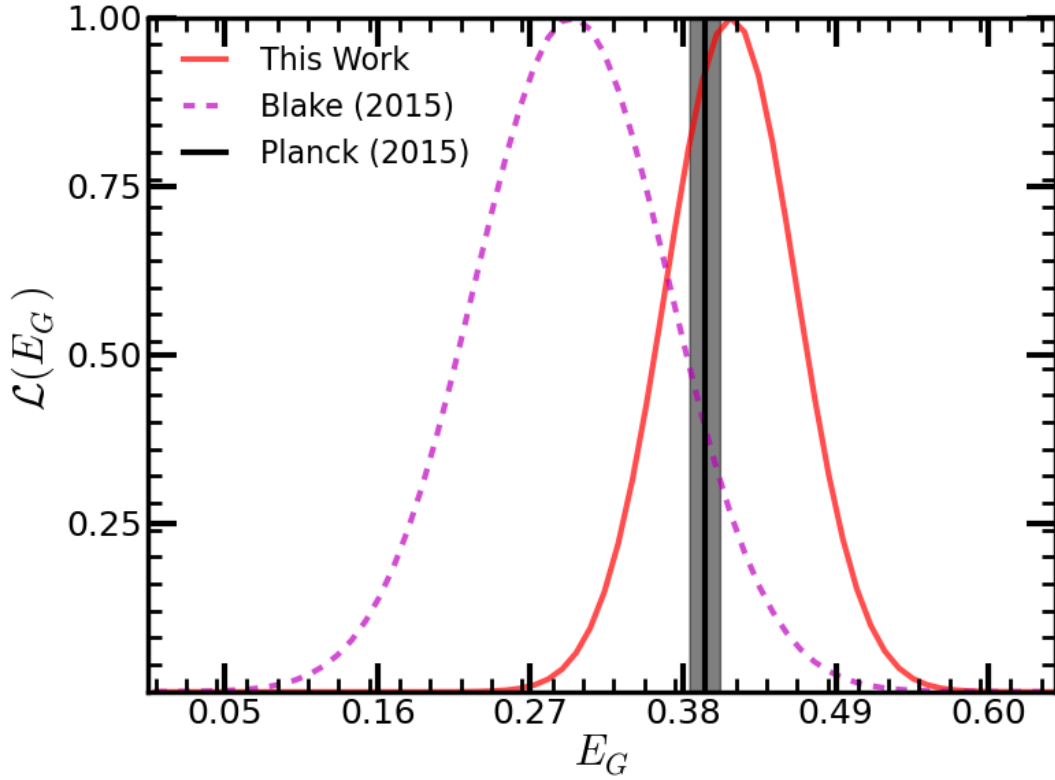
Figure 5.7: Figure shows the one-dimensional likelihood of E_G. The red solid line shows our measurement $E_G = 0.41 \pm 0.047$. The magenta dashed line is the measurement reported in Blake et al. [56], $E_G = 0.30 \pm 0.07$. The black shaded region is the GR prediction for Planck (2015; TT+lowP+lensing). Note that Blake et al. [56] assumes a cosmology with $\Omega_m = 0.27$ whereas we assume Planck 2015 cosmology.

limits (see Section 5.7). We finally report $E_G(z = 0.57) = 0.41 \pm 0.047$ (11% error) compared to the ΛCDM prediction of $E_G = 0.40$ using the [268] cosmology.

Our measurements are completely consistent with the prediction of ΛCDM, and provide a non-trivial test of GR at cosmological scales by virtue of probing both metric potentials. The first measurement of E_G, reported in Reyes et al. [304] at redshift of 0.32, was also consistent with ΛCDM. A more recent measurement was reported in Blake et al. [56] at redshifts 0.32 and 0.57. We improve on the measurement of Blake et al. [56] by a factor of 2 at redshift of 0.57. This improvement largely comes from the fact that we are using the BOSS DR11 sample, which has more data compared to the BOSS DR10 sample used by Blake et al. [56], and from the improved precision on β measurement, which we obtained using a different perturbation theory template. A similar measurement was first proposed in Pullen et al. [295] and measured in Pullen et al. [293] by replacing the gravitational lensing shear estimated using galaxies with CMB lensing. This is a complimentary measurement to ours by virtue of probing different scales with different systematics. Our measurement is consistent with the measurement of E_G using CMB lensing at small scales. But it shows 2.8σ tension when compared with their final results, which include large scales. This might indicate that these measurements have reached a limit where observational systematics are approaching the statistical uncertainty, and future surveys will require improved analysis methods.

We are entering the golden age of precision cosmology with much bigger and deeper surveys. For example, we have HSC, KIDS and DES taking data now, and LSST, WFIRST and Euclid happening in the next decade. The next generation surveys will provide an unprecedented handle on statistical errors, which necessitates a much better understanding of systematic errors. Using future surveys, we will be able to measure E_G much more precisely at multiple redshifts and over a wide range of scales. Such measurements will enable us to test the predictions of the ΛCDM model of structure formation as a function

of scale and time, which might provide key insights into dark energy, dark matter, and the theory of gravity.

Acknowledgments

Chapter 6

Relativistic distortions using the large-scale clustering of massive galaxies in SDSS-III BOSS CMASS sample

Shadab Alam, Hongyu Zhu, Rupert A. C. Croft, Shirley Ho and Elena Giusarma

6.1 Abstract

General relativistic effects have been long been predicted to subtly influence the observed large-scale clustering of galaxies. The current generation of galaxy redshift surveys have reached a size where detection of such effects is becoming feasible. In this paper, we make the first detection of the redshift asymmetry produced by relativistic effects on the cross-correlation function of two galaxy populations. The dataset we use is taken from the SDSS DR12 CMASS galaxy sample, and we detect the asymmetry at the 4.8σ level by applying a shell-averaged estimator to the cross-correlation function. Our measurement covers scales

from $\sim 3 - 20 \mathrm{h}^{-1}\mathrm{Mpc}$, larger than those over which the gravitational redshift profile has been recently measured in galaxy clusters, but smaller than scales for which linear perturbation theory is likely to be accurate. The detection significance varies by 1σ with the details of our measurement and tests for systematic effects. We have also devised two null tests to check for various survey systematics and show that results from them are consistent with the null hypothesis. Additionally we measure the dipole moment of the cross-correlation function, finding asymmetry to be detected at the 2.8σ level. The amplitude and scale-dependence of the clustering asymmetries we measure are approximately consistent with the expectations of General Relativity and a biased galaxy population, within large uncertainties. We explore theoretical predictions using numerical simulations in a companion paper.

6.2 Introduction

The General Theory of Relativity (GR; [111]) has been very successfully applied to the prediction of the structure of our Universe. As a theory it gives a complete account of the gravitational matter-matter and light-matter interactions. Einstein proposed three tests of general relativity, the perihelion precession of Mercury's orbit [78], the deflection of light by the Sun [108, 185] and the gravitational redshift of light [290].GR has been tested against many other observations over last century including post-Newtonian tests of gravity [242], the light travel time delay around massive objects, also known as Shapiro delay [340], constraints on the strong equivalence principle [240, 241], weak and strong gravitational lensing [333], cosmological tests using the growth rate of structure [180, 14] and the E_G parameter [410, 304, 295, 293], indirect detection of gravitational waves through pulsar timing [389] and recent direct detection through a binary black hole merger [2]. Recently several authors have studied relativistic effects on the large scale structure observed

in galaxy redshift surveys [226, 405, 171, 406, 94, 404, 66, 67]. These papers will hopefully mark the beginning of a new era testing general relativity by analyzing galaxy clustering with unprecedented precision (for a review see Yoo [402]).

The Universe is assumed to be isotropic and hence any statistical property (for example, distribution of galaxies) is expected to be isotropic. Galaxy redshift surveys have made measurements of millions of galaxies in certain parts of the Universe and analyzed their large-scale clustering properties [2dF: Colless et al. [86], 6dF: Jones et al. [177], SDSS-III: Eisenstein et al. [115], WiggleZ: Blake et al. [54], DEEP2: Newman et al. [238], VIPERS: Garilli et al. [123], GAMA: Liske et al. [211]]. The two point correlation functions (2PCF) of observed galaxies in these surveys are far from isotropic due to observational effects. The line-of-sight galaxy distances from the Earth are inferred from the redshift (z) of spectral features, assuming a cosmological model. As well as the distance, each redshift also contains information on the dynamics (peculiar velocity) and the environment (gravitational potential) of these galaxies. The redshift has three components: the Hubble recession velocity, the peculiar velocity of a galaxy and the local gravitational potential. The observed redshift (z_{obs}) is given by

$$z_{\mathrm{obs}} = H(z)r/c + v_{\mathrm{pec}}/c + z_g, \tag{6.1}$$

where $H(z)$ is the Hubble parameter, r is the true line-of-sight distance, v_{pec} is the peculiar velocity of galaxy, c is the speed of light, z_g is the gravitational redshift and the expression is valid for distances r where a linear Hubble relation is a good approximation. The peculiar velocity component of the observed redshift modifies the galaxy two-point correlation function, causing redshift space distortions (RSD). The effect of RSD is manifested in changes in the angle averaged 'even ordered multipoles' of the two point correlation function of galaxies, most prominently in the second order multipole (quadrupole) [138].

As the peculiar velocities of galaxies are isotropically oriented on average, only the even ordered multipoles of the 2PCF remain non-zero while the odd ordered multipoles vanish. Peebles [254] presented one of the first discussions of RSD affecting the large scale structure of the Universe. The first linear theory formalism to model RSD was developed by Kaiser [180]. Over the last few decades various galaxy redshift surveys have been analysed and they improve our understanding of large scale structure. The recent studies of RSD in this context include [258, 53, 47, 99, 321, 301, 327, 48, 302, 159, 12, 346]

The gravitational redshift component of the galaxy redshift is generated by the environment of the galaxy. Galaxies are known to occupy dark matter haloes which possess strong gravitational potentials (ϕ). The light emitted from a galaxy will experience a gravitational shift $z_g = -\phi/c^2$ as it climbs out of the potential well. This is one of the most fundamental predictions of GR. The manifestation of this phenomenon was first observed in a nuclear resonance experiment and reported by Pound and Rebka [290]. The gravitational redshift has also been measured in astrophysical systems, e.g. a red giant star sirius B [131], in the solar system [214, 368] and in galaxy clusters [399, 317, 172]. A formalism for measuring the gravitational redshift in individual galaxy clusters was presented by Cappi [71]. Later it was suggested that stacking large numbers of galaxies could be used to measuring the gravitational redshift profile of clusters as a function of scale [187].

In this paper, we present measurements of the relativistic distortions of galaxy clustering on scales larger than clusters. We use the cross-correlation of two galaxy populations with different masses. McDonald [226] provided the first linear theory formalism to predict the effect of gravitational redshift in the cross power spectrum of two different populations of galaxies. Croft [94] carried out N-body simulations of the effect of gravitational redshift on two population of haloes with different halo masses. It was found that allowing for measurements on non-linear scales, current galaxy redshift surveys should be able to detect such an effect and future surveys should be able to provide precise measurements.
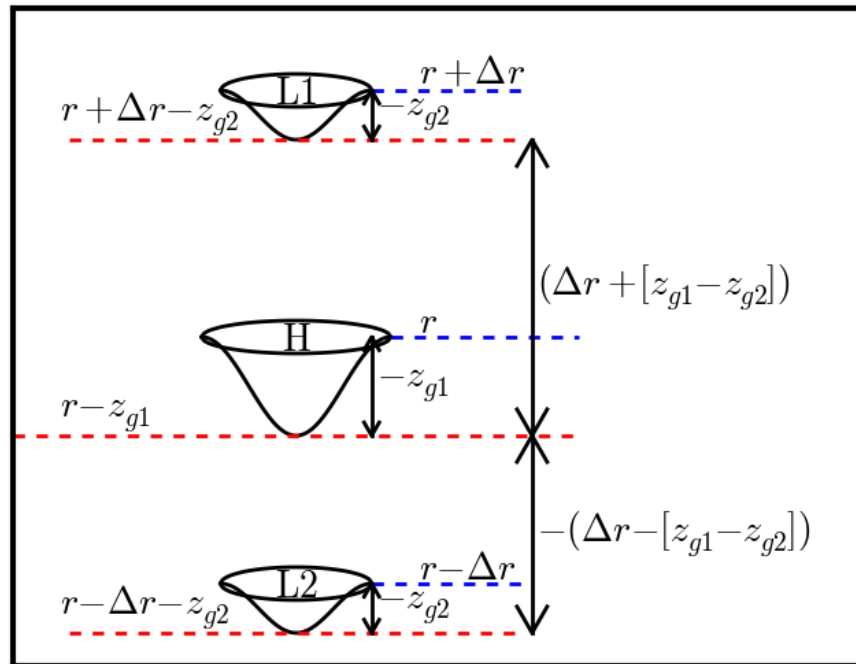
Figure 6.1: The diagram to illustrate symmetry breaking along line-of-sight due to gravitational potential.

Croft [94] also proposed an estimator to measure the line-of-sight asymmetry using the cross-correlation function of the two differently biased samples. Looking at galaxy cluster scales, Kaiser [181] and Zhao et al. [412] showed that gravitational redshift is the dominant of several relativistic distortions of non-linear clustering which should be considered together. Bonvin et al. [67] showed how gravitational redshift distortion is related to the full general relativistic asymmetry of the cross-correlation of two populations of galaxies. A measurement of the cross-correlation dipole (from datasets which included the SDSS CMASS sample) was made by [124]. This was on large $r > 20$ h^{-1}Mpc scales where the relativistic distortions were not measurable but a purely geometric distortion was seen.

Figure 6.1 illustrates how gravitational redshifts act to cause an asymmetry in clustering (alongside other relativistic effects). Consider a symmetric system of three galaxies where the central galaxy (H) is more massive than the other two galaxies (L1, L2). The distance of each of the smaller galaxies from the central galaxy is identically Δr. Imagine that each of these galaxies is hosted by a dark matter halo which adds extra gravitational components to the measured redshifts z_{g1} and z_{g2}. If we include these effects and then look at the redshift difference of each lower mass galaxy from the central galaxy, then we will find that L1 is $\Delta r + (z_{g1} - z_{g2})$ and L2 is $\Delta r - (z_{g1} - z_{g2})$ distance away from the central galaxy. The line of sight redshift-space distance of the two galaxies will be equal in the limit $z_{g1} = z_{g2}$. In the scenario when the galaxies are living in haloes of different masses (different gravitational potentials) the symmetry along the line of sight will break. This will produce odd ordered moments in the cross-correlations of galaxies and could be used to measure the different environments of the galaxies. It is important to note that in the autocorrelation function the pair counts are symmetric by construction and so no distortions of this type can be measured.

The line of sight asymmetry illustrated in Figure 6.1 can also be introduced by other observational effects ([67],[181]. We have studied some of the relativistic effects on target

selection (observational systematics) in a companion paper Alam et al. [13] . A study of all such relevant effects using N-body simulations is presented in another companion paper Zhu et al. [414]. We have also studied effects of baryons on the gravitational potential and velocities of galaxies and their impact of relativistic distortions using hydrodynamical simulations in a third companion paper Zhu et al. [413].

A outline of this paper is as follows. We provide a brief description of our theoretical model in Section 7.3. Section 6.4 describes our dataset and Section 6.5 describes the steps and methods used in our measurements. We next present our results in Section 6.6, which include a better than 3σ detection of the line of sight asymmetry using large scale structure. We also discuss several null tests and systematics. We end in section 6.7 with a summary and a discussion of our measurement.

6.3   Theory

The existence of gravitational redshift is one of the fundamental predictions of GR. As mentioned in Section 1, it has been studied theoretically and observed experimentally on various scales. We use N-body simulations to predict the measured signal from gravitational redshifts and other effects which distort the cross-correlation function. The perturbation theory approach (e.g., McDonald [226], Yoo et al. [405], Bonvin [66]) is valid on large-scales but we find that non-linear clustering (including the structure of the potential well on galactic and halo scales) is dominant on the scales which are accessible to current observations ([109], in prep.). We therefore use N-body simulations to make predictions for the gravitational potential and velocities of galaxies. We present the suite of N-body simulations and give details of how they were used to predict different components of the signal in a companion paper ([414], in prep.). Here, we briefly describe the simulations and effects included in our theoretical model.

We use N-body simulations produced by running the PGadget3 code [360, 359]. We use 8 realizations of a flat ΛCDM model with $\Omega_m = 0.3$ and $h = 0.7$. The simulations are dissipationless, in a periodic box of side length $1000h^{-1}\mathrm{Mpc}$ and contain 1024^3 particles. We use SubFind [360] to generate a catalog of subhalos which can be associated with galaxies. We then observed the subhalo catalog in the parallel line-of-sight approximation including various observational effects. We do not include "wide-angle" effects which [**?**] have shown become important on large, linear scales. The observed line-of-sight position is given as follows:

$$Z_{\mathrm{obs}} = Z_{\mathrm{real}} + Z_{\mathrm{pec}} + Z_g + Z_{\mathrm{TD}} + Z_{\mathrm{LC}} + Z_{\mathrm{galaxy}}, \qquad (6.2)$$

where Z_{obs} is the final observed distance from the observer in comoving units ($h^{-1}\mathrm{Mpc}$) including all the effects we study. From now on, v will denote velocity while β denotes the ratio v/c, where c is the speed of light. Also, $H = 100(km/s)/(h^{-1}Mpc)$. The cartesian components of velocity and β are indicated using subscripts (e.g., $v_{x,y,z}, \beta_{x,y,z}$). $Z_{\mathrm{pec}} = v_z/H$ gives the effect of peculiar velocity on the line-of-sight distance, and is the term which causes the usual redshift distortions (e.g, [180]). $Z_g = -\phi/(cH)$ is the positional shift caused by the gravitational redshift from the subhalo potential [71]. Two more terms give an additional redshift that depends on the peculiar velocity: $Z_{\mathrm{TD}} = \beta^2 c/(2H)$ accounts for the Transverse Doppler effect [412] and $Z_{\mathrm{LC}} = \beta_z^2 c/(2H)$ the light cone effect [181]. Because the potential well of the stellar part of the galaxy adds to the gravitational redshift, we add the component due to internal structure of galaxy as in Cappi [71], $Z_{\mathrm{galaxy}} = 10^{-5}\sigma_v^2[1 + \ln(R_0/R)]$, with $R_0 = 3R_e$ and $R = 0.05R_e$, where R_e is half-mass radius.

After adding all these components to the observed position of each galaxy in the simulation, we construct two populations of subhalos divided by median subhalo mass. We
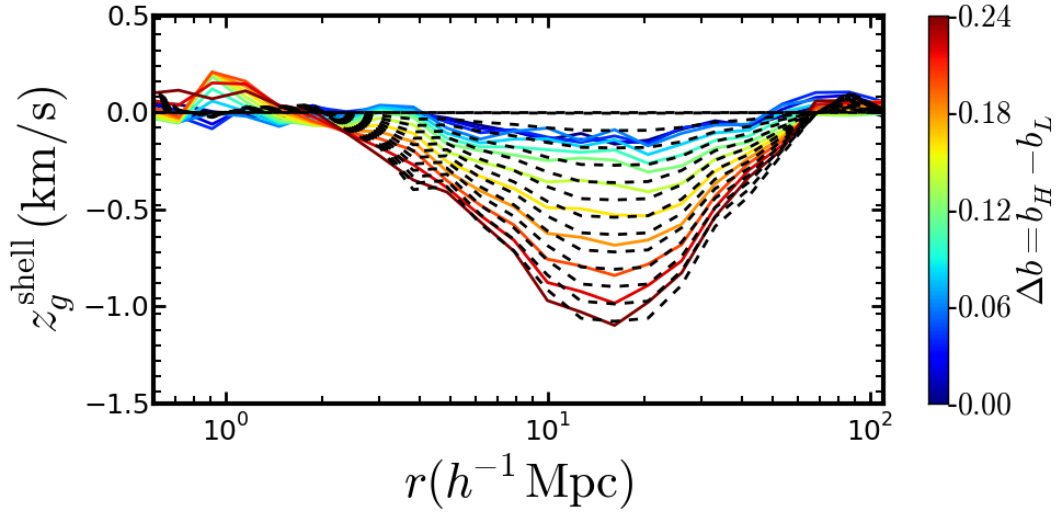
Figure 6.2: The asymmetry signal in the cross-correlation function of two galaxy populations measured from N-body simulations using the shell estimator of Equation 6.3. We show results for various values of Δb, bias difference between the two population (as indicated by the color bar). The black dashed lines show predictions of our empirical model (Equation 6.4).

measure their auto-correlation functions and define two linear bias values, b_H, and b_L for the high and low mass halves of the sample. We compute the bias in the usual fashion from the relative scaling of the large scale auto-correlation functions of subhalos and dark matter in the simulations (see [414] for details).

To measure the asymmetry in the cross-correlation function of the two samples we use the shell estimator, proposed by Croft [94]. This is simply an estimate of the centroid shift of the correlation function averaged in spherical shells, and is similar to the usual gravitational redshift profile of clusters (e.g., [399]). The shell estimator is measured from the two subsamples as follows:

$$z_g^{\text{shell}}(r) = H \sum_{h_1,h_2}^{|r_{12}-r|<\Delta r} [Z_{\text{obs}}^{h1} - Z_{\text{obs}}^{h_2}]P_\beta(h_1)P_\beta(h_2) \qquad (6.3)$$

where the sum is over all pairs of subhalos (h_1, h_2) between the two populations such that

the distance between the subhalos r_{12} lies in the radial bin between $r - \Delta r$ and $r + \Delta r$. Here $P_\beta = 1 - 6 * \beta_z$ accounts for the relativistic beaming effect on galaxy inclusion in the sample by weighting the pair in a fashion which depends on their line of sight velocities [181, 13, 168]. The above definition of shell estimator is equivalent to the definition given in equation 6.9.

Figure 6.2 shows measurements of cross-correlation function asymmetry from applying the shell estimator to our N-body simulation outputs. Lines of different colors show measurements for various values of the large-scale structure bias difference between the two populations. We have used these simulation results to develop a parametric phenomenological model for the shell estimator as follows:

$$z_g^{model}(r) = (1.5 A_{\mathrm{rel}}/0.3) z_g^{theo}(\alpha r), \tag{6.4}$$

where z_g^{theo} is measured from simulations for $\Delta b = 0.3$. Here A_{rel} and α are two free parameters which we use to scale the amplitude of the shell estimator and the position of the largest asymmetry respectively. The amplitude scaling of this model is motivated by the perturbation theory results, see equations 12 and 30 from Gaztanaga et al. [124], which show that the shell estimator should be proportional to the bias difference of the two sub-samples. We therefore set A_{rel} to be proportional to $\Delta b = b_H - b_L$. The position of the largest asymmetry depends on the mean bias of the two populations, redshift and the relative contribution of different relativistic effects. The black dashed lines in Figure 6.2 show the prediction from our model. We use $\alpha = 1$ and $A_{\mathrm{rel}} = \Delta b$. As we can see, our model captures the variations in measured signal from N-body simulations.

6.4 Data

To make our measurement of relativistic distortions in the cross-correlation function we use data from data release 12 (DR12;[298, 9]) of the Sloan Digital Sky Survey (SDSS; [407]). SDSS I, II [1] and III [115] used a drift-scanning mosaic CCD camera [132] to image 14555 square degrees of the sky in five photometric bands [122, 351, 104] to a limiting magnitude of $r < 22.5$ using the 2.5-m Sloan Telescope [134] at the Apache Point Observatory in New Mexico. The imaging data were processed through a series of software pipelines [218, 265, 248]. [6] reprocessed all of the SDSS imaging data as part of Data Release 8 (DR8). The Baryon Oscillation Spectroscopic Survey (BOSS;[96]) was designed to obtain spectra and redshifts for 1.35 million galaxies covering 10,000 square degrees of sky. These galaxies were selected from the SDSS DR8 imaging. [60] developed a tiling algorithm for BOSS that is adaptive to the density of targets on the sky. BOSS used double-armed spectrographs Smee et al. [349] to obtain the spectra and completed observations in spring 2014. BOSS obtained a homogeneous data set with a redshift completeness of more than 97% over the full survey footprint. The redshift extraction algorithm used in BOSS is described in Bolton et al. [65]. Eisenstein et al. [115] provides a summary and Dawson et al. [96] provides a detailed description of the survey design.

We use the CMASS sample of galaxies [65] from data release 12 [9]. The CMASS sample has 7,65,433 Luminous Red Galaxies (LRGs) covering 9376 square degrees in the redshift range $0.44 < z < 0.70$, which correspond to an effective volume of 10.8 Gpc^3.

6.5 Analysis Methodology

We first use the CMASS sample to obtain two galaxy sub-samples with different biases but same redshift distributions. We measure the auto-correlation function for each sub-sample,
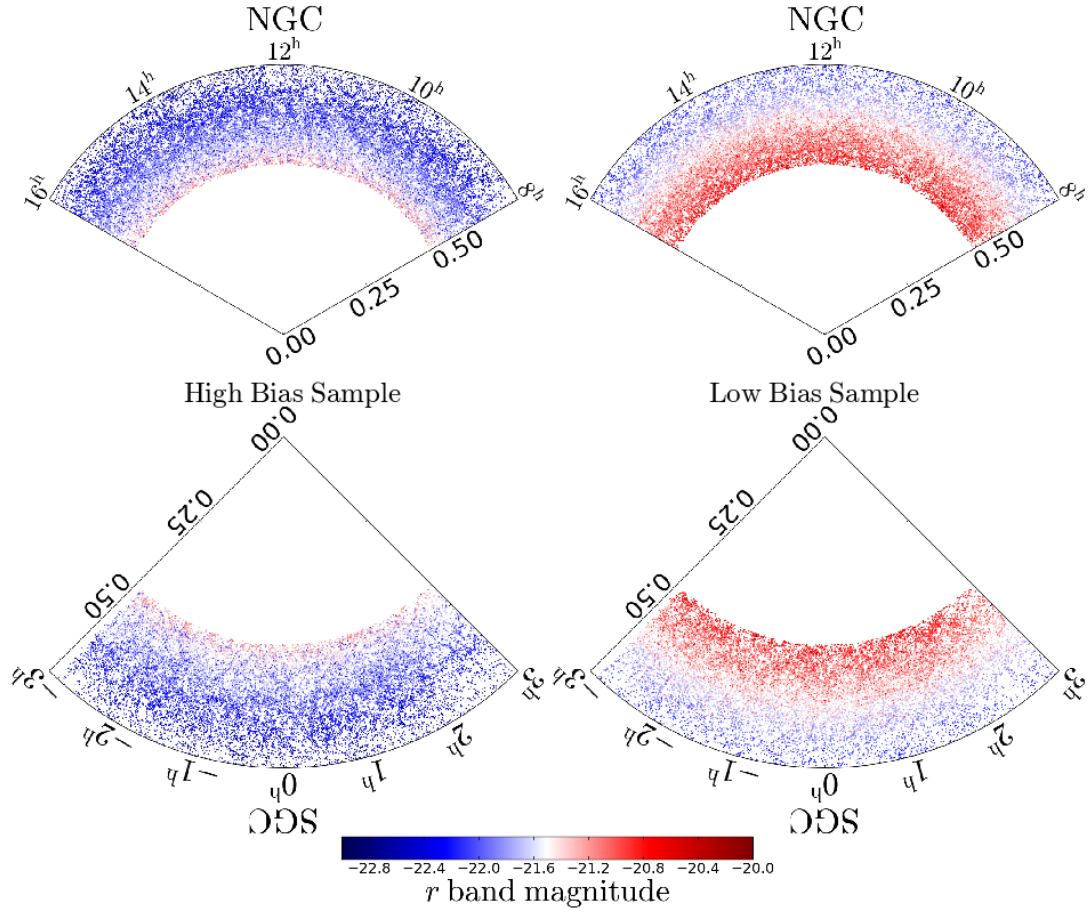
Figure 6.3: The distribution of galaxies in our CMASS sample. The radial distance in each plotted segment corresponds to the redshift of a galaxy and the angle corresponds to its right ascension (RA). The color denotes the r band magnitude of the galaxy. The top segments in each plot show the north galactic cap (NGC) and the bottom the south galactic cap (SGC) for the two sub-samples. The left panel is for high bias (more massive) subsample of the CMASS data and the right panel the lower bias (less massive) samples.
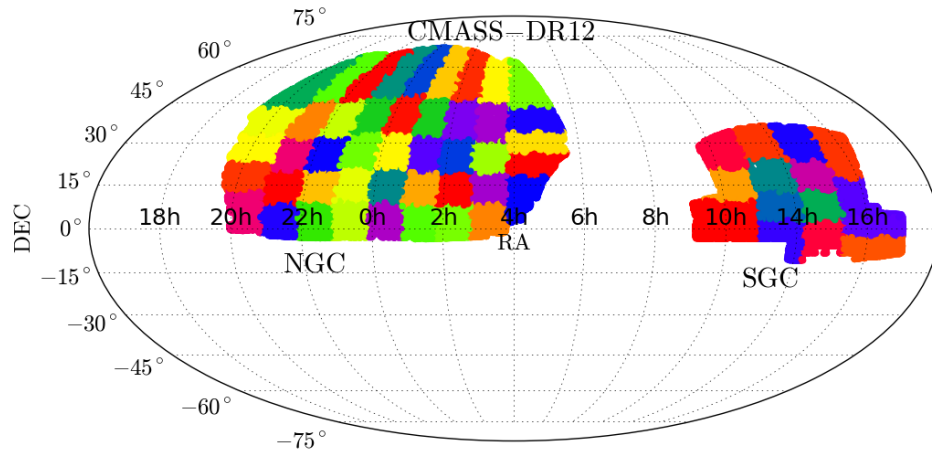
Figure 6.4: The distribution of galaxies in our CMASS sample on the sky. The two seperate regions are the NGC and SGC. Different colors correspond to different jackknife regions used in calculation of the covariance matrix. Note that the origin of RA has been shifted by $4h$ towards the left in order to make the SGC appear as a contiguous region.

and estimate their linear bias values from it. We then measure the cross-correlation function of the two sub-samples. The cross-correlation function is used to detect and quantify the line of sight asymmetry due to relativistic effects using shell estimator of equation 6.9. In this section we describe our analysis methodologies in detail.

6.5.1 Creating Galaxy sub-samples

From the SDSS CMASS DR12 sample of galaxies we would like to create two sub-samples of galaxies that occupy lower and higher mass halos. We use galaxy absolute magnitude to divide the overall sample into these two subsamples, making the assumption that brighter galaxies are associated with higher mass, and consequently higher bias halos. We make use of five different ways to divide the dataset into two sub-samples, using magnitude in the five different SDSS bands.

Our procedure is as follows: We first bin the sample into redshift bins with $\Delta z = 0.01$. In each bin, we compute the median magnitude for one of the five photometric bands (u, g, r, iz). Galaxies brighter than the median magnitude in the bin are placed into the bright subsample and fainter galaxies in the faint subsample. We repeat the process for the other four photometric bands so that we have 5 different partitions of the whole dataset into bright and faint subsamples. With this process we make sure that the two sub-samples have same redshift distribution. We found that our measurements are not sensitive to choice of Δz. We give more details of this and other tests in section 6.6.5 and Figure 6.9.

The photometric band magnitudes used in our analysis are corrected for evolution and k-correction to $z = 0.55$. The faint sub-sample contains 382711 galaxies and the bright sub-sample contains 382722 galaxies, when r band magnitudes are used to define the cut. Figure 6.3 shows the distribution of galaxies in right ascension and distance from the observer in these two CMASS subsamples. We obtain similar samples using the other photo-

metric bands.

6.5.2 Estimating the cross-correlation function

We use as a fiducial cosmology a flat ΛCDM-GR cosmological model with $\Omega_m = 0.274$, $H_0 = 0.7$,$\Omega_b h^2 = 0.0224$, $n_s = 0.95$ and $\sigma_8 = 0.8$ [20] in order to convert observed celestial coordinates (α, δ) and redshift to the position of the galaxy in three-dimensional space. These galaxy positions are used to estimate the two point statistic (cross-correlation function) of the galaxies in the two subsamples using the minimum variance, Landy-Szalay estimator [194]: citation for two population.

$$\hat{\xi}(r, \theta) = \tag{6.5}$$
$$\frac{D1D2(r,\theta) - D1R2(r,\theta) - R1D2(r,\theta) + R1R2(r,\theta)}{R1R2(r,\theta)}$$

Here $D1D2$, $D1R2$, $R1D2$ and $R1R2$ represent respectively the weighted counts of galaxy pairs from the two populations, pairs of galaxies in the first population with randoms for the second population, randoms for first population with galaxies from the second population and between randoms for two populations. We use the weighting scheme $w_{sys} = w_{star} w_{see} (w_{cp} + w_{zf} - 1)$ described in Anderson et al. [20] to account for systematic weights. Where the weight factor w_{zf} accounts for redshift failure of the nearest neighbor of a galaxy. Similarly, the weight factor w_{cp} is intended to account for a scenario where the redshift of a neighbor was not obtained because it was in a close pair. The weights w_{star} and w_{see} are to account for stellar density and the seeing effect in the galaxy sample.

The cross-correlation function depends on r, the distance between a pair of galaxies and $\mu = cos(\theta)$, where θ is the angle between the pair separation vector and the line of

sight. We define the line-of-sight direction for each pair to be the position vector that joins the observer to the mean position of that pair of galaxies. We carry out cross-correlation function measurements covering $1\,h^{-1}\mathrm{Mpc} < r < 60\,h^{-1}\mathrm{Mpc}$ with 15 logarithmic bins and $0 < \theta < \pi$ with 150 linear bins. Provided that the binning is not much finer or coarser than this, we find that our measurements are insensitive to binning choices.

6.5.3   Estimating Multipoles and Galaxy bias

We measure the 2D cross-correlation function $\xi(r, \theta)$ from the CMASS data as described in section 6.5.2. We compress the cross-correlation by projecting it onto a basis of Legendre polynomials $L_\ell(\mu)$ of order ℓ as follows:

$$\hat{\xi}_\ell(r) = \frac{2l+1}{2} \int_{-1}^{1} d\mu \hat{\xi}(r, \mu) L_\ell(\mu) \tag{6.6}$$

$$\approx \frac{2l+1}{2} \sum_k \Delta\mu_k \hat{\xi}(r, \mu) L_\ell(\mu_k), \tag{6.7}$$

where $\mu = \cos(\theta)$. The $\ell = \{0, 1, 2\}$ moments of the Legendre polynomials are given by $L_\ell(\mu) = \{1, \mu, 1/2(3\mu^2 - 1)\}$, the monopole, dipole and quadrupole respectively. We estimate the linear bias b of a sample of galaxies by fitting the model $\xi_0^{theo} = b^2 \xi_0^m$ to the observed monopole from data. We use Convolution Lagrangian Perturbation Theory (CLPT; [72]) to estimate the monopole of the matter correlation function (ξ_0^m) assuming fiducial cosmology for $z = 0.57$. We also estimate the dipole moment $\xi_{\ell=1}$ and use it as a means to detect asymmetry in the cross-correlation function [124].

185

6.5.4 Estimating the Covariance Matrix

Estimation of the covariance matrix of a summary statistic (such as the cross-correlation function) is one of the most important steps in a cosmological analysis. The covariance matrix of an observed statistic is usually computed either by sub-sampling the data or by using mock catalogues. Both methods have their limitations and regime of validity. Generally speaking, the sub-sampling methods over-estimate errors on small scale [239] and are difficult to use on large scales due to the limited volume of the observed data. On the other hand creating realistic mock catalogues in large numbers and covering large volume with high resolution requires huge computing resources. Therefore, mocks often use approximate simulations with lower spatial and temporal resolution (*e.g.* [397]). This makes small scale clustering in the mocks inaccurate and hence covariance estimated from mocks can only be used above a certain minimum scale decided by details of the method.

Because our signal of interest is on small scales ($r \sim 3 - 20 \text{h}^{-1} \text{Mpc}$) we use the sub-sampling approach here. We use the "delete one jackknife" algorithm [339] to estimate the covariance matrix. We first split the data into 61 approximately equal area regions (45 in the North Galactic cap and 16 in the South Galactic cap) as shown in Figure 6.4. A realization of data is defined by omitting one region at a time, which gives us 61 realizations. We measure the summary statistics, correlation function and shell estimator for each realization. We then estimate the covariance matrix of these summary statistics (ss) using

$$C_{i,j} = \frac{N-1}{N} \sum_{jk=1}^{N} \left(ss_i^{jk} - \bar{s}\bar{s}_i \right) \left(ss_j^{jk} - \bar{s}\bar{s}_j \right). \tag{6.8}$$

Here $C_{i,j}$ represents the covariance between bin i and j, $\bar{s}\bar{s}$ is the mean of the jackknife realizations and the sum is over all the 61 jackknife realizations. Our smallest jackknife region has an angular diameter of $\sim 8°$ which translates to $\sim 200 \text{ h}^{-1} \text{Mpc}$. This is much larger than largest scale we are using in our analysis.

6.5.5 Shell estimator: Estimating Asymmetry

As our primary measure of the redshift asymmetry in clustering caused by relativistic effects, we use a shell-averaged estimator applied to the cross-correlation function. Croft [94] proposed this estimator to quantify the effects of gravitational redshift predicted from in N-body simulations. The shell estimator is defined as follows:

$$z_g^{shell}(r) = \frac{\int_{\theta=0}^{\theta=\pi} Hr_{\parallel}[1 + \xi(r,\theta)]d\theta}{\int_{\theta=0}^{\theta=\pi}[1 + \xi(r,\theta)]rdrd\theta} \tag{6.9}$$

where $r_{\parallel}$ is the line of sight component of pair separation. We can see that z_g^{shell} measures the mean $r_{\parallel}$ weighted by the cross correlation function and is converted to km/s units through a multiplication factor of $H = 100(km/s)/(h^{-1}Mpc)$. Other quantifications of the relativistic asymmetry in clustering have been proposed, such as the imaginary part of the power spectrum [226], the dipole [67], and the anti-symmetric part of the cross-correlation function [168]. Here we focus on the shell estimator but also measure the dipole and compare conclusions derived from both.

6.6 Measurements, Null Tests and Systematics

We use the methodologies described in previous section to perform our measurements discussed here. In this section we first show the measurement of bias. We then show the measurements of shell estimator and fit the model described in section 7.3. We also perform two null tests and look at the sensitivity of our observer signal to the possible systematic.
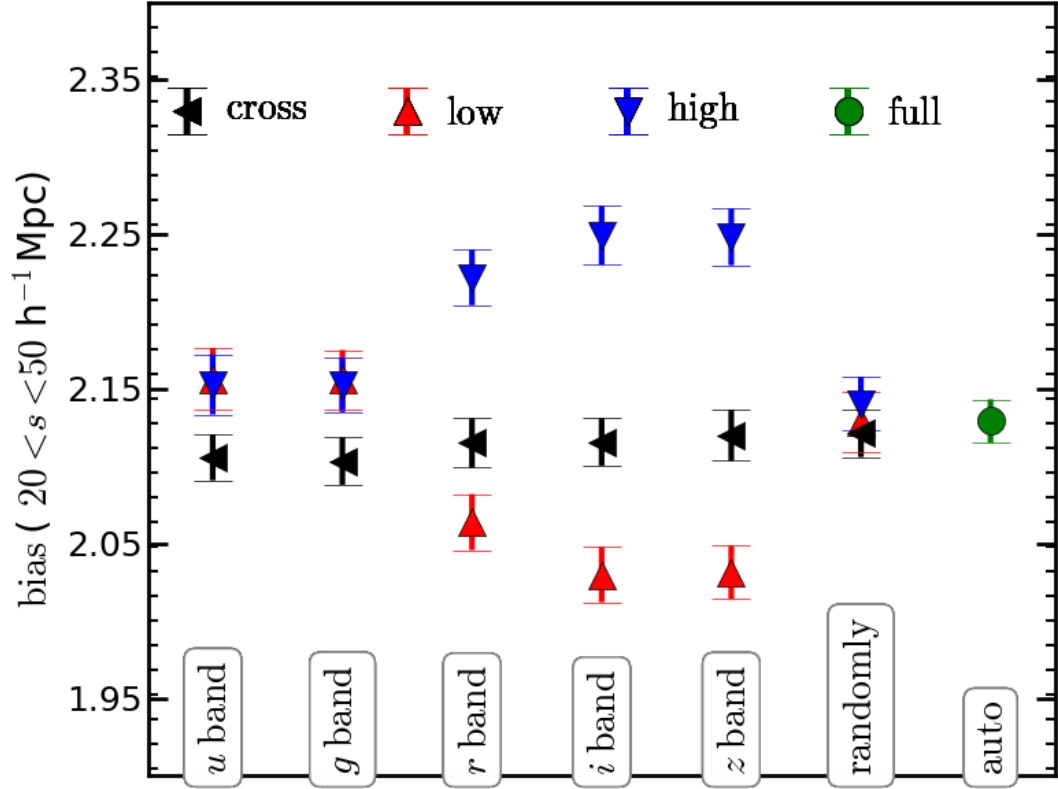
Figure 6.5: We show the bias measured for each of the sub-samples used in our analysis using scales between 20 and 50 h^{-1}Mpc. The red, blue, black and green points show bias of low mass auto-correlation, high mass auto-correlation, low-high cross-correlation and full sample auto-correlation function respectively. The split is using each of the five photometric magnitudes (u, g, r, i, z) and also a random split. The r, i and z show significantly different biases for low and high mass sample.
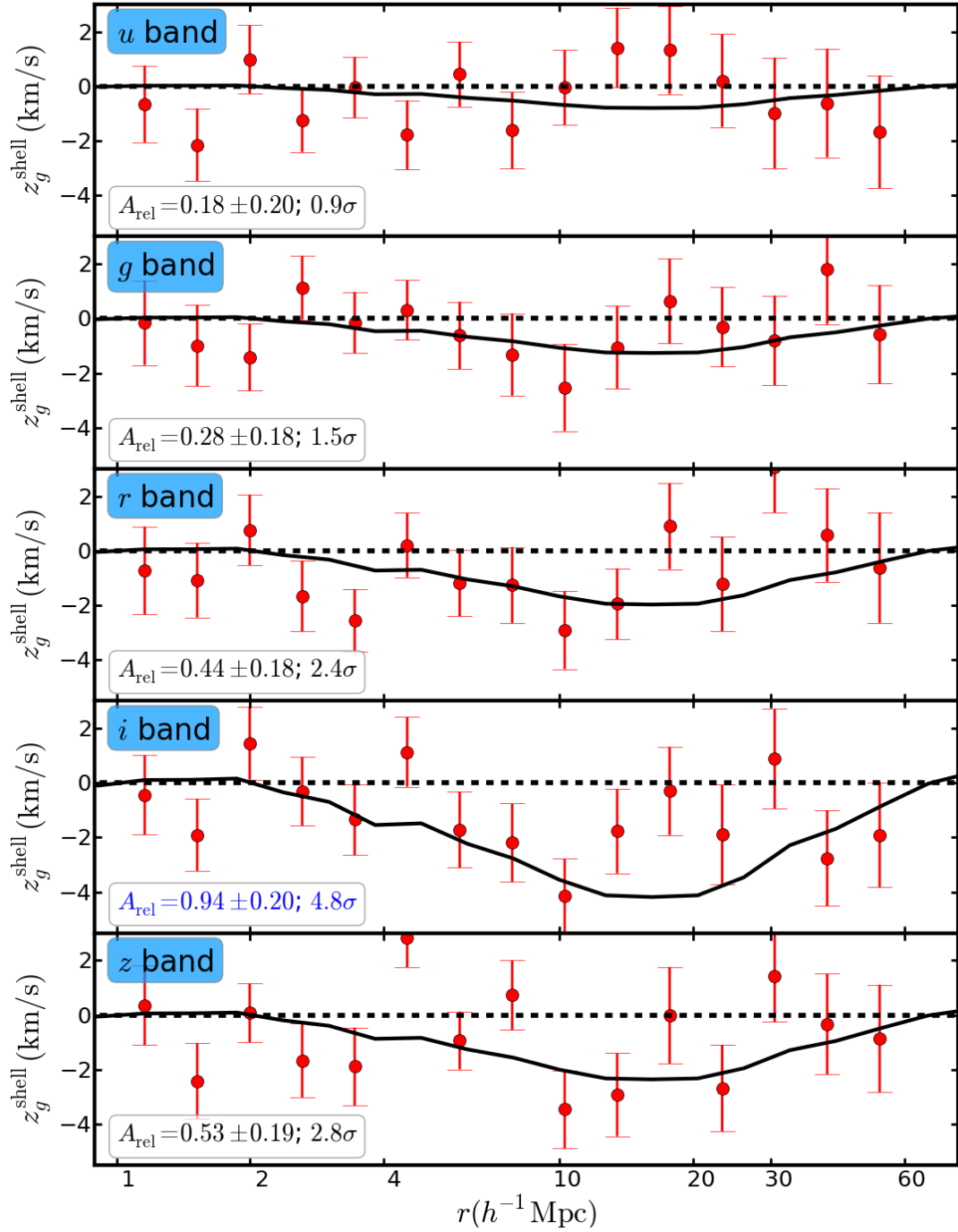
Figure 6.6: We show the measurement of shell estimator from SDSS CMASS sample. The different plots show the shell estimator measured using cross-correlation of sub-samples created by splitting the sample in two equal halves for each of u, g, r, i, z photometric bands. We detect the amplitude of relativistic asymmetry at the level of 2.4σ, 4.8σ and 2.8σ away from zeros in r, i and z bands respectively. This is consistent with our expectation from bias measurements of the 5 sub-samples as shown in Figure 6.5. The amplitude of relativistic asymmetry for u and g bands are at the level of 0.9σ and 1.5σ consistent with the expectation from biases.

6.6.1 Measurements of Bias

First we show the linear biases measured for our various samples in Figure 6.5. The galaxy bias is measured using monopole $\xi_0(s)$ as described in section 6.5.3. We use scales between $20\text{h}^{-1}\text{Mpc}$ and $50\text{h}^{-1}\text{Mpc}$ to measure bias. We show the bias of auto-correlation and cross-correlation of different sub-samples created by splitting the sample using all five photometric bands (u, g, r, i, z) and randomly. The blue points show the biases of higher mass samples, red points for lower mass samples and the black points for the cross-correlation between the lower and higher mass samples. We also show the bias of full sample using green point. The relativistic effects, dominantly gravitational redshift, breaks the line of sight symmetry of cross-correlation is proportional to the difference in biases of the two sub-samples. Therefore we expect to see relatively smaller signal for u and g bands but relatively larger signal for r, i and z photo-metric bands. We also expect no line of sight asymmetry in the cross-correlation using random split and the auto-correlation of the full sample. These two cases are used as our null tests.

6.6.2 Measurements of Shell estimator

The Figure 6.6 shows our measurements of shell estimator with best fit model. The red points show our measurement of relativistic effects including gravitational redshift $(z_g^{\text{shell}}(r))$. The solid black lines show the expected signal based on our best fit model. We have used predictions from N-body simulation to fit the measurements for each band using model described in equation 6.4. We define our likelihood function as follows

$$\mathcal{L}(A_{\text{rel}}, \alpha) = e^{-\chi^2(A_{\text{rel},\alpha})/2} / \int e^{-\chi^2(A_{\text{rel},\alpha})/2} dA_{\text{rel}} d\alpha \tag{6.10}$$

$$\chi^2(A_{\text{rel},\alpha}) = (z_g^{data} - z_g^{model})C^{-1}(z_g^{data} - z_g^{model})^T \tag{6.11}$$

where C^{-1} represents the inverse of covariance matrix obtained from jacknnife sampling as shown in equation 6.8. The likelihood is then used to estimate the mean and error on each of the model parameters as follows

$$X^\mu = \int X\mathcal{L}(A_{\rm rel}, \alpha)dA_{\rm rel}d\alpha \tag{6.12}$$

$$X^\sigma = \sqrt{\int (X - X^\mu)^2 \mathcal{L}(A_{\rm rel}, \alpha)dA_{\rm rel}d\alpha} \tag{6.13}$$

where X could be $A_{\rm rel}$ or α. The amplitude of line of sight asymmetry is zero ($A_{\rm rel} = 0$) is our null hypothesis and our alternate hypothesis is that amplitude of line of sight asymmetry is non-zero (i.e. $A_{\rm rel} \neq 0$). The detection significance quantify the difference of measured amplitude from zero in unit of standard error ($N_\sigma = A_{\rm rel}^\mu / A_{\rm rel}^\sigma$). We performed two kinds of fits to our measurement of shell estimator. First, we fit for only the amplitude of asymmetry $A_{\rm rel}$ keeping $\alpha = 1$ and in second case we fit for both the parameters. The two fits are performed to look at the sensitivity of detection significance on the extra degree of freedom in the model. Table 6.1 provdies the results for each kind of fit. The best model shown in the Figure 6.6 is with fixed α fit. We also quote the measured amplitude of line of sight asymmetry, its error and detection significance in the Figure 6.6.

The u and g bands show amplitude of gravitational redshift consistent with zero which is expected from the fact that the bias difference of the two sub-samples using these bands are small. The r, i and z bands show $A_{\rm rel}$ away from zeros at $2.4\sigma, 4.8\sigma$ and 2.8σ. These detection significance are stable if we add the second parameter α in the fit (see Table 6.1).

6.6.3 Null Tests

We perform two null tests to check for systematics. First, we divide the sample randomly in two equal halves and look at the shell estimator from the cross-correlation of the two

Table 6.1: We list our best fit parameter for each of the shell estimator measurement. We performed two fits, one with fixed α and other with free α. The table shows that the best fit value of amplitude (A_{rel}) is consistent in either case.

split	A_{rel}	α	$N\sigma$
u	0.18 ± 0.20	fixed	0.9
	-0.10 ± 0.36	2.0 ± 1.5	0.3
g	0.28 ± 0.18	fixed	1.5
	0.15 ± 0.26	2.10 ± 1.22	0.6
r	0.44 ± 0.18	fixed	2.4
	0.44 ± 0.23	0.86 ± 0.76	1.9
i	0.94 ± 0.20	fixed	4.8
	0.93 ± 0.22	1.24 ± 0.41	4.2
z	0.53 ± 0.19	fixed	2.8
	0.48 ± 0.23	1.79 ± 1.0	2.1
$random$	0.03 ± 0.21	fixed	0.1
	0.01 ± 0.23	2.49 ± 1.2	0
$auto$	0.02 ± 0.04	fixed	0.5
	0.16 ± 0.13	2.25 ± 0.39	1.2

random sub-samples. We do not expect to observe any signal, showing line of sight asymmetry, from such a measurement. Because the two sub-samples are statistically same. The top plot in Figure 6.7 show the shell estimator measurement from the random split. We obtained $A_{\rm rel} = 0.03 \pm 0.21$ which is consistent with zeros signal at 0.1σ level. We have also looked at the shell estimator from the auto-correlation of the full sample which serves as the second null test. The bottom plot in Figure 6.7 shows the measurement shell estimator from the auto-correlation of full sample. This gives $A_{\rm rel} = 0.02 \pm 0.04$ which is consistent with zero at 0.5σ level. Any problem with survey geometry, mask, wide angle effect or redshift distribution should show a non-zero signal in atleast one of these measurements. Note that this has much smaller error bar and we still obtain null result which is a strong test for many of the possible systematic effects. Both of our null tests are in excellent agreement.

6.6.4   Measurement of Dipole moment

We also measures the dipole moment of the cross-correlation for each of the photometric band as describe in section 6.5.3. Figure 6.8 shows our measurements of dipole moment. Each panel shows the dipole moment for cross-correlation for each of the photometric bands. The red points shows our measurement with jackknife error bar. The black line shows the best fit halo model prediction (see Croft [94] for details). We fit the halo model prediction for a constant amplitude which is a multiplicative factor to our fiducial halo model prediction. We find that the dipole moment also shows the non-zero signal at small scale similar to the shell estimator. But the measurement of dipole moment is more noisy than shell estimator and hence the significance of detection is slightly smaller than what we obtained using shell estimator. The plot also shows the best fit value of the halo model amplitude and it significance away from zero. We detects the amplitude of relativistic asymmetry at the level of 2.3σ ,0.9σ, 2.7σ, 2.8σ and 1.9σ away from zeros in u, g, r, i and
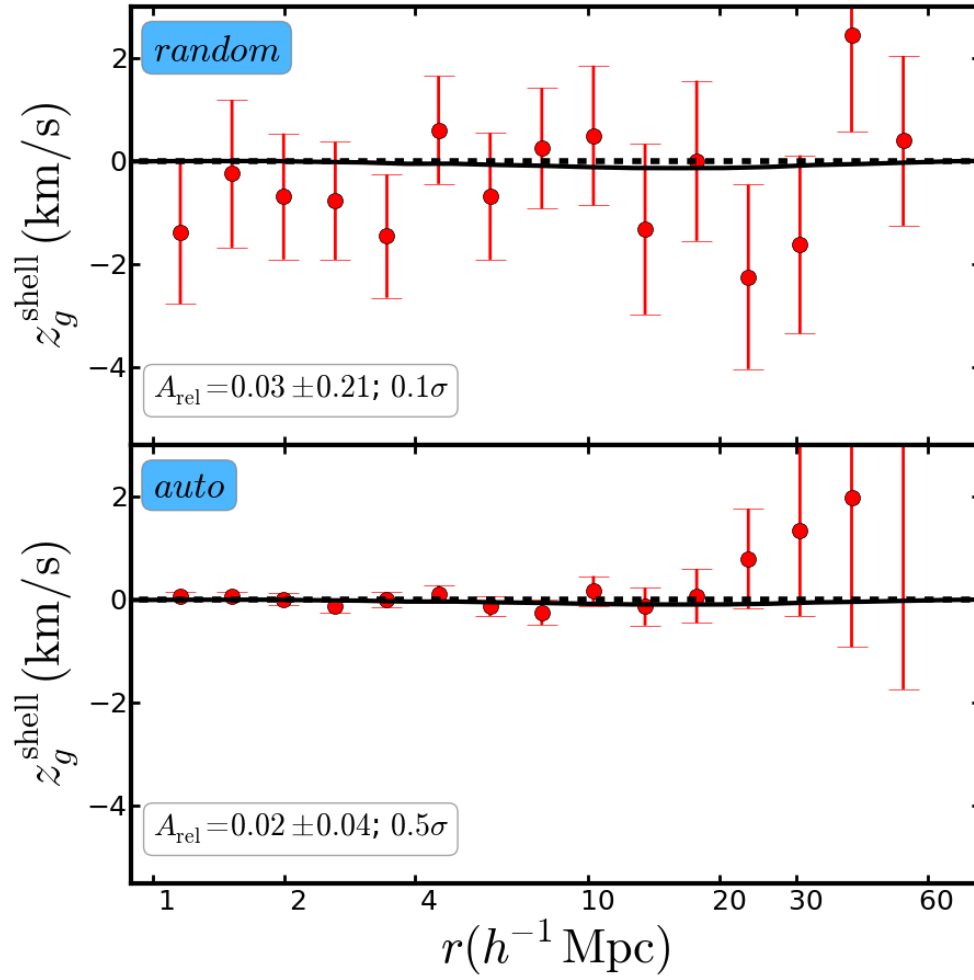
Figure 6.7: This shows our null test of zero signal to check our pipeline and various possible systematic effects. The left plot shows the shell estimator computed from cross-correlation when we split the sample randomly. The best fit signal amplitude is completely consistent with zero. The right plot shows the shell estimator computed from the auto-correlation of the full sample. Because this is an auto-correlation we do not expect to see any signal in the shell estimator. The plots show that we pass both the null tests because the best fit signals are consistent with zero.
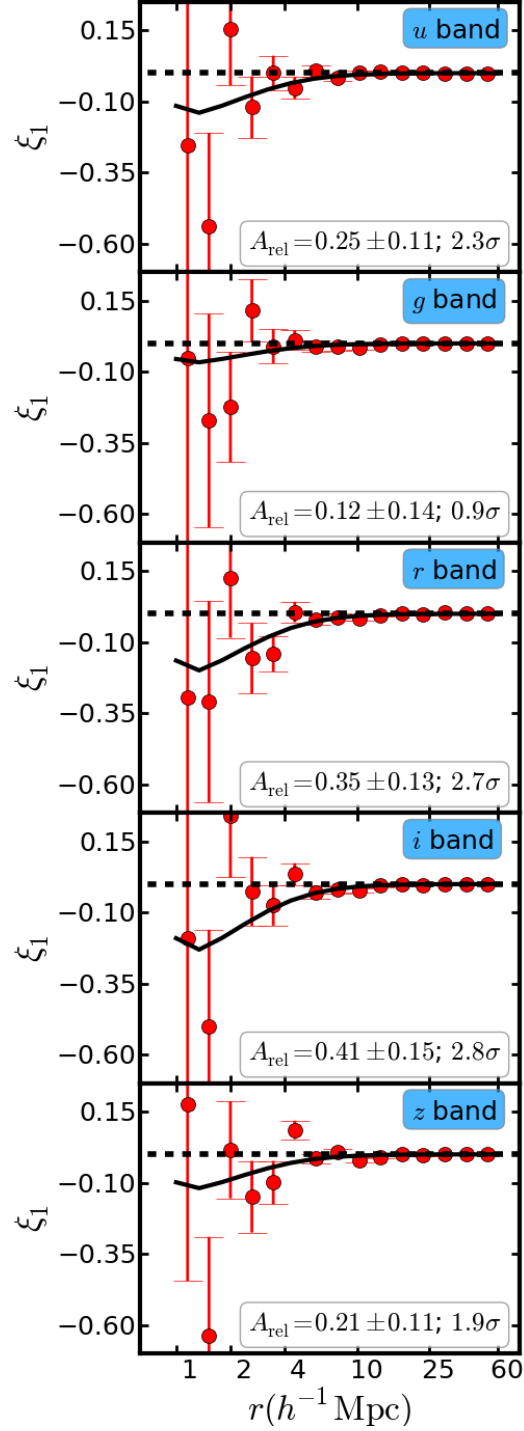
Figure 6.8: We show the dipole moment measured using cross-correlation of sub-samples created by splitting the sample in two equal halves for each of u, g, r, i, z photometric bands. We detect the amplitude of relativistic asymmetry at the level of 2.3σ, 0.9σ, 2.7σ, 2.8σ and 1.9σ away from zeros in u, g, r, i and z bands respectively.

z bands respectively. But, do not detect any dipole signal at large scale as you can see the results are entirely consistent with zero for scale above $25\text{h}^{-1}\text{Mpc}$.

6.6.5   Sensitivity to Systematics

We have used all the systematic weights suggested in the catalog which tries to removes any observational correlation that shouldn't exist in a sample like ours. We apply five different combination of systematic weights, as listed in the legend of Figure 6.9, in the measurement of cross-correlation for each of the photometric bands and null tests We then compute the shell estimator for each one of those weights for each sub-samples, making 35 different measurements. Figure 6.9 shows all of these 35 measurement. The different panels show the shell estimator measurement for different photometric bands and also the ones used for our null-test. The different colored points represent different combinations of systematic weights used in the correlation function measurement. The red points in each panel show our fiducial measurement. We found that the effect of any of these systematic weights are small. We obtain consistent measurement within 1σ independent of what systematic weights we use. This shows that our measurements are robust against observational systematic. We have also tested the effect of redshift binning while creating the sub-samples. Our fiducial bin width is $\Delta z = 0.01$, as shown using red points. Decreasing the bin width to $\Delta z = 0.005$, as shown using magenta points, doesn't change the measurement significantly. The fact that our measurements is not very sensitive to the combination of weights used or choice of redshift binning makes it stable against lack of detailed understanding of some of these systematic weights.

6.7 Discussion

We have discussed various relativistic effects which could produce line-of-sight anisotropy in a cross-correlation of two galaxies populations having different halo mass. We have used CMASS sample to measure these anisotropies. We used each of the five SDSS photometric bands to obtain two sub-samples. The biases of these sub-samples were measured by measuring the monopole of auto- and cross-correlation as described in section 6.5.3 and shown in Figure 6.5. The shell estimator described in section 6.5.5 is used to quantify the line-of-sight anisotropy due to the relativistic effects in the unit of velocity. We have used the model developed using N-body simulations and motivated by perturbation theory to fit the measured shell-estimator. The theoretical model of shell estimator is described in section 7.3 and derived from the analysis of companion paper Zhu et al. [414]. The theoretical model was fit to measurements from data in order to quantify the significance of observed non-zero signal. The covariance matrix which was estimates the uncertainties was obtained using jackknife sampling as described in section 6.5.4. Figure 6.6 shows our measurements with best fit models and detection significance. We detect the amplitude of relativistic asymmetry at the level of 2.4σ, 4.8σ and 2.8σ away from zero in r, i and z bands respectively. This is consistent with our expectation from bias measurements of the 5 sub-samples as shown in Figure 6.5. The amplitude of relativistic asymmetry for u and g bands are at the level of 0.9σ and 1.5σ, consistent with the expectation from biases. Zhu et al. [414] found that the dominant contribution in the shell estimator is due to the gravitational redshift effects. Therefore our measured signal is also a first detection of gravitational redshift in the large scale structure. Two null tests were devised to check the possibility of measuring line-of-sight anisotropy due to the survey geometry, mask effects, wide angle effect, redshift distribution etc. First null test measures the shell estimator from the cross-correlation of two randomly selected galaxy populations. This makes the two populations

statistically identical and hence we do not expect any line-of-sight-anisotropy in the cross-correlation. Second null test uses the shell estimator measured from the auto-correlation of the full sample. This has much smaller error and checks for any of possible geometrical effect to much higher precision than the statistical uncertainty in our measurement. Figure 6.9 shows our null tests being consistent with zero. This implies that any of those possible systematic effects is much below our statistical uncertainty. We have also performed a much more detailed analysis of possible systematic effects due to sample selection in a companion paper Alam et al. [13]. Another approach to look at the line-of-sight anisotropy is to use dipole moment of the cross-correlation function. We have also measured the dipole moment as described in section 6.5.3 and shown in Figure 6.8. We found similar anisotropy at small scale. We fit our dipole moments using the prediction from halo model described in Croft [94]. We detect the amplitude of relativistic asymmetry at the level of 2.3σ, 0.9σ, 2.7σ, 2.8σ and 1.9σ away from zeros in u, g, r, i and z bands respectively. We note that the detection using dipole moment is smaller and has larger scatter. This is probably caused by the fact that the shell estimator and dipole moment weights the different modes differently. Our dipole moments are completely consistent with zeros at large scale. This result is also consistent with the analysis presented in Gaztanaga et al. [124], where they didn't detect any signal using dipole moment and shell estimator at large scale.

This first detection of gravitational redshift using large scale structure is another landmark in the success story of general relativity. The future surveys with bigger volume and larger number of galaxies will be able to detect such signal with much higher significance. What can we do with such signal in future? Any suggestion?

Acknowledgments

Figure 6.9: This plot shows the effect of different systematic weights on the measurement of shell estimator for each of the five photometric bands and the two null tests. The highlight here is that our measurement is not very sensitive to the choice of systematic weights or the width of redshift bin used while creating our sub-samples. The different colored points are when we include different systematic weights.

Chapter 7

Relativistic effects on the Target Selection

Shadab Alam, Rupert A. C. Croft, Shirley Ho, Hongyu Zhu and Elena Giusarma

7.1   Abstract

In a galaxy redshift survey the objects to be targeted for spectra are selected from a parent sample observed photometrically. The observed magnitudes and colours of galaxies in this parent sample will be affected by their peculiar velocities, through relativistic Doppler and relativistic beaming effects. In this paper we compute the resulting expected changes in galaxy photometry. The magnitudes of the relativistic effects are a function of redshift, stellar mass, galaxy velocity and velocity direction. We focus on the CMASS sample from the SDSS/BOSS redshift survey, which is selected on the basis of color and magnitude. We find that 0.16% of the sample (~ 882 galaxies) has been scattered into the targeted region of color-magnitude space by relativistic effects, and conversely 0.11% of the sample ($\sim$

645 galaxies) has been scattered out. Observational consequences of these effects include an asymmetry in clustering statistics, which we explore in a companion paper. Here we compute a set of weights which can be used to remove the effect of modulations introduced into the density field inferred from a galaxy sample. We have applied these weights to the CMASS sample and looked at its clustering properties, finding that their effect is likely to be negligible for standard large scale structure BAO and redshift-space distortion analyses.

7.2 Introduction

General Relativity (GR; Einstein [111]) combined with the standard cosmological model (ΛCDM) provides the most successful theory of our universe with the minimum of external assumptions. The ΛCDM model paints a simple picture of structure formation arising from density fluctuations growing under gravity [87]. For most of the Universe's history, these perturbations obey linear perturbation theory [237, 206, 106, 219, 69, 189, 43, 192]. The density field predicted by these theories have very specific statistical properties with multiple unique features [255, 113, 34, 80]. We can measure most of the physical quantities of the universe just by comparing one, two, three and higher point statistics of the predicted matter density field. Galaxies provide us with a window on the underlying matter density field of the universe. In the limit of linear perturbations, galaxies can be assumed to form at the high-density peaks of the underlying matter density field and should have same clustering properties up to a multiplicative constant (galaxy bias) [32, 83]. Therefore creating three-dimensional maps of galaxies and studying their clustering properties provides one of the most precise ways to measure physical properties of our universe. In this paper, we address one of the complications of making these maps from galaxy redshift surveys which is usually ignored: the effect of peculiar velocities on galaxy selection.

Carrying out large galaxy surveys has been a challenging task, which was made eas-

ier by the development of CCD cameras [38]. Many astronomy projects were involved in the development and adoption of CCD technology for telescopes [25, 3, 35, 68, 122, 132]. These have led to various photometric surveys covering increasingly large parts of sky with improved depth and resolution (York et al. [407], Gladders and Yee [128], Kaiser et al. [183], Takada [366], Gilbank et al. [127] , DES[1]). Such surveys provide an excellent map of the angular distribution of galaxies, but precise measurements of the cosmological line-of-sight distance, and hence creation of three dimensional maps, requires redshifts (z). The redshift quantifies the wavelength shift of features in galaxy spectra and hence requires observing galaxy's spectral energy distributions (SED). The measurement of galaxy SED requires targeting each galaxy individually and is a very expensive process. An early large galaxy redshift surveys was the CfA redshift survey [125] which observed 22000 galaxies one at a time. Galaxy surveys targeting much large numbers of galaxies for SED measurement became possible with the advent of optical fibers combined with the ability to observe hundreds of SEDs in a single exposure. The huge increase in the number of spectra that we could observe started the era of large galaxy redshift surveys (e.g., LCRS: Shectman et al. [341], 2dF: Colless et al. [86], 6dF: Jones et al. [177], SDSS-III: Eisenstein et al. [115], WiggleZ: Blake et al. [54], DEEP2: Newman et al. [238], VIPERS: Garilli et al. [123], GAMA: Liske et al. [211]).

To make this process efficient, it is important to have prior knowledge about the location of possible targets. Therefore, generally galaxy redshift surveys require samples of objects observed photometrically to serve as parent sample. Various algorithms and knowledge of galaxy evolution models are employed to create sub-samples of such parent samples to be targeted for spectra (for example Reid et al. [298]). Generally, these selection algorithms use various magnitude and color cuts to define these subsamples. We know that the observed magnitudes and colors of galaxies are affected by their peculiar motion [369]. This

---

[1]http://www.darkenergysurvey.org/survey/

can influence the final spectroscopic galaxy target sample obtained after following the target selection rules [181]. Such effects will act to modulate the observed galaxy density in the observed sample, in a way which will be correlated with galaxy properties including redshift, mass and velocity. This could in principle introduce new features into the measured clustering of galaxies and also bias the physical properties inferred from such clustering observations.

In this paper, we examine the special relativistic effects that galaxy peculiar velocity have on their observed SEDs and the photometric quantities derived from them. We then discuss the impact of these effects on an observed sample of galaxies. We use the Sloan Digital Sky Survey III (SDSSIII) Baryon Oscillation Spectroscopy Survey (BOSS) CMASS sample from Data Release 12 (DR12) as an example to show how relativistic effects will impact target selection which uses cuts in the magnitude and color plane. We then discuss how these introduce density modulation in the observed sample. We define a weighting scheme to compensate for such modulation and look at its effect on the clustering signal. We conclude with a discussion about the impact of such effects on the large scale structure analyses. We note that we restrict ourselves here to the effect of peculiar velocities on spectroscopic target selection. This is distinct from the effect of velocities on the properties of galaxies inferred from the spectroscopic sample (e.g., Kaiser and Hudson [182], Bacon et al. [28]).

7.3   Effects of peculiar velocities on galaxy spectra

We study the relativistic effects of galaxy motion on galaxy spectra and how they affect observed galaxy flux and color. This will help us estimate the impact of such observational effects on our final observed samples. We consider two kinds of effects. The first is the redshift or blueshift applied to the spectrum due to relative motion between the observer

and galaxy. The second is the change in flux coming from relativistic boost and beaming. Note that we do not consider the impact of magnification caused by gravitational lensing [332].

7.3.1   Relativistic Doppler effect

The relativistic Doppler effect shifts the observed wavelength of a photon with respect to the emitted wavelength in a manner which depends on the line of sight velocity of the source. The observed wavelength and emitted wavelength are related by the following equation, where $\beta_{los} = v_{los}/c$ is the ratio of line of sight velocity (v_{los}) and the speed of light (c):

$$\lambda_o = \lambda_e \sqrt{\frac{1 - \beta_{los}}{1 + \beta_{los}}}. \tag{7.1}$$

Here λ_o and λ_e are the observed and emitted wavelengths respectively. The galaxy's velocity along the line of sight consists of two components. First component is the Hubble velocity due to the expansion of the universe (denoted by v_e) while the second component is due to local dynamics, the peculiar velocity and denoted by v_p. The total line-of-sight velocity of a galaxy v_{los} is given by relativistic addition of the two components so that

$$v_{los} = \frac{v_e + v_p}{1 + \frac{v_e v_p}{c^2}}. \tag{7.2}$$

The velocity due to the expansion of the universe acts to redshift the galaxy spectrum. This shift also implies that photometric bands see different parts of the spectrum for galaxies at different redshifts. Accounting for this shift leads to the well known K-correction, (see for example the case of massive galaxies [155, 58]). The K-correction can be used before applying the sample cuts or instead can be included implicitly alongside galaxy evolution models used to derive target selection algorithms. We assume that the target se-

lection has accounted for the effect of the K-correction in either way and focus on the shift in the observed flux due to the peculiar velocity of the galaxies. First, we show that the effect of shift in wavelengths due to different components of the galaxy velocity can be separated as follows:

$$\left(\frac{\lambda_o}{\lambda_e}\right)^2 = \frac{1 - \beta_{los}}{1 + \beta_{los}} \tag{7.3}$$

$$= \frac{1 - v_{los}/c}{1 + v_{los}/c} \tag{7.4}$$

$$= \frac{c^2 + v_e v_p - v_e c - v_p c}{c^2 + v_e v_p + v_e c + v_p c} \tag{7.5}$$

$$= \frac{(c - v_e)(c - v_p))}{(c + v_e)(c + v_p)} \tag{7.6}$$

$$= \left(\frac{1 - \beta_{los}^e}{1 + \beta_{los}^e}\right)\left(\frac{1 - \beta_{los}^p}{1 + \beta_{los}^p}\right) \tag{7.7}$$

Equation 7.3 shows the shift in wavelength due to the total line-of-sight velocity. Substituting equation 7.2 into 7.4 gives equation 7.5, which can be further simplified to yield equation 7.7. This shows that the Doppler shifts in wavelength due to different velocity components is separable and hence justifies our treatment to separate peculiar velocity from the velocity due to the expansion of the Universe. It is important to define the sign convention for velocity to avoid any confusion. From now on we use positive velocity and β to indicate that the line-of-sight component of galaxy peculiar velocity is toward the observer. Negative velocity will imply that the galaxy's line-of-sight component of velocity is moving away from the observer.

7.3.2 Relativistic Beaming effect

Relativistic beaming modifies the apparent brightness of a galaxy due to its peculiar motion. The peculiar motion of galaxy through the Doppler shift modifies the energy of emitted photons and the number of photons emitted per unit time . The direction in which photons are emitted is also different in the observed frame compared to the galaxy's rest frame, leading to an anisotropic pattern of emission in the observer's frame. Taken together, these effects are known as relativistic beaming. The effect on the spectral brightness can be derived using special relativity. The spectral brightness (I_ν) of a galaxy is defined to be the energy observed per unit time, per unit area of the detector, per unit frequency and per unit solid angle:

$$I_\nu = \frac{\Gamma E}{\sigma \Omega},$$

(7.8)

where Γ is the number of photons emitted per unit time, E is the energy of emitted photons, Ω is the solid angle subtended by the observed galaxy and σ is the area of the detector. Each of the quantities appearing in equation 7.8 will be modified by the peculiar motion of the galaxy in the observed frame. The spectral brightness in the observed (telescope) frame (I_ν^o) and emitted (galaxy rest) frame (I_ν^e) are related by following equation[2]:

$$\frac{I_\nu^o}{I_\nu^e} = [\gamma(1 - \beta cos(\theta))]^{-4}.$$

(7.9)

Here the Lorentz factor $\gamma = \frac{1}{\sqrt{1-\beta^2}}$ and θ is the angle the velocity vector makes with the line of sight direction. The above expression is in terms of flux per unit frequency whereas our measurements will be in flux per unit wavelengths. The spectral brightness per unit

---

[2]A detailed derivation of this equation can be found in Hogg [154]. Check equation 7.22 on page 40 of `http://cosmo.nyu.edu/hogg/sr/sr.pdf`

frequency (I_ν) can be converted to the spectral brightness per unit wavelength (I_λ) using:

$$I_\lambda = I_\nu \lambda^2 \tag{7.10}$$

Finally, the observed and emitted spectral brightness per unit wavelength can be obtained by combining equations 7.1, 7.9 and 7.10.

$$\frac{I_\lambda^o}{I_\lambda^e} = [\gamma(1 - \beta cos(\theta))]^{-4} \left(\frac{1 - \beta cos(\theta)}{1 + \beta cos(\theta)} \right). \tag{7.11}$$

It is important to note that relativistic beaming depends on both the magnitude and direction of the source velocity and not just its the line-of-sight component.

7.3.3 Effects of velocity on the observed spectra

The spectra observed for a galaxy redshift survey experience both the effects discussed in the previous two subsections: the shift in wavelength due to doppler shift and the change in flux due to relativistic beaming. The following equation describes how the observed flux per unit wavelength (f_λ^o) is related to the emitted flux per unit wavelength (f_λ^e) at wavelength (λ_e), as a function of observed wavelength (λ_o)

$$f_\lambda^o(\lambda_o, \beta, \theta) = f_\lambda^e(\lambda_e) \left[\gamma(1 - \beta cos(\theta))\right]^{-4} \left(\frac{1 - \beta cos(\theta)}{1 + \beta cos(\theta)} \right). \tag{7.12}$$

Here the galaxy is moving with peculiar velocity $v = \beta c$ along the direction at angle θ from the line-of-sight. The observed and emitted wavelengths are related by equation 7.1. We note that equations derived in the previous section are for spectral brightness whereas the observed quantity in the galaxy spectrum is spectral flux. The spectral brightness is the spectral flux per unit solid angle of the source. The solid angle in the observed and emitted frame are different due to relativistic beaming, and are related by $d\Omega^o/d\Omega^e = \gamma^2(1 -$
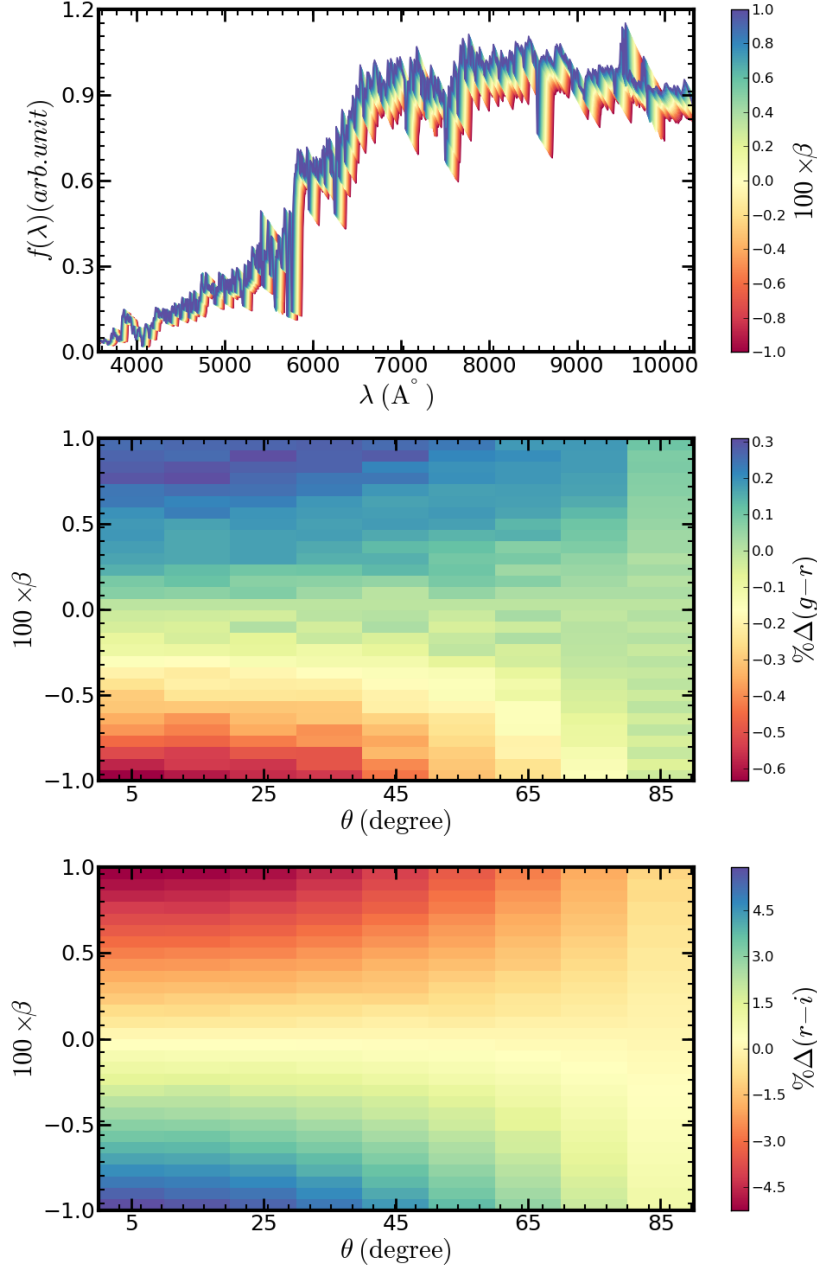
Figure 7.1: The relativistic effects on the spectra and observed color of a single galaxy. The top panel shows the flux of a galaxy SEDs on the y-axis, with x-axis showing wavelength in A° and the color scale showing velocity. Two effects are illustrated, the first being the wavelength shift and the second being the rescaling of flux for the same wavelength as the sources galaxy moves towards or away from the observer. The middle and bottom panel show the percentage change in the $g - r$ and $r - i$ colors as a function of the magnitude and direction of the galaxy velocity respectively.

$\beta cos(\theta))^2$. However, when the observed flux is measured using optical fibers with smaller angular size than the object then these fluxes are for a fixed solid angle. Therefore, the equations derived for spectral brightness are directly applicable without the extra correction (per unit solid angle). We show later that with the CMASS galaxy sample that typically only 93% of the galaxy flux falls within the fiber and hence this assumption is valid in this case.

Figure 7.1 shows the effect of relativistic beaming and relativistic doppler shift on the observed galaxy spectra and color. The top panel focuses on the galax SED. The x-axis shows the wavelength in A° and the y-axis shows the observed flux. The color scale represents the velocity of the galaxy in the unit of speed of light. The spectrum corresponding to $\beta = 0$ represents the emitted galaxy spectrum. We can clearly see the two effects discussed in the previous two sections. The relativistic Doppler shift causes the atomic lines to shift in wavelength. Relativistic beaming increases the observed flux for positive β (moving towards the observer) and decreases it for negative β (moving away from the observer). The middle and bottom panels show the percentage change in the $g - r$ and $r - i$ color as a function of different velocity magnitude (varying along the y-axis) and velocity direction with respect to the line-of-sight (x-axis). The percentage change in $g - r$ color is at the level of 0.3% when the galaxy has a peculiar velocity of 3000km/s. For realistic velocities of around 400 km/s (See section 4.5) the change is around 0.1% . For $r - i$ color the percentage change is significantly higher, at the level of 5% for 3000 km/s galaxies and $\sim 1.5\%$ for 400 km/s. This difference between color bands illustrates that the strength of the relativistic selection effects will depend on galaxy spectrum and hence galaxy type in a relatively complex way.

7.4 Effects of velocities on Selected Catalog

Most large galaxy redshift surveys feature a two-step process of photometric target selection and spectroscopic follow-up. Grism spectroscopy and other techniques for one-step generation of galaxy redshift samples have been used in the past (e.g., Schuecker [335], Momcheva et al. [233]) and will play a prominent role in the future (EUCLID: Content et al. [89], WFIRST: Spergel et al. [357], SPhereX: Bock and SPHEREx Science Team [64]). Neverthless, fiber spectrographs are also becoming larger and photometric selection of galaxy targets will be used to generate samples of tens of millions of galaxy redshifts in the next few years (cite DESI overview paper). We therefore focus in this paper on photometric target selection.

In order to obtain a reasonable target sample one must determine the properties of each object based on photometric magnitudes. This require detailed modeling of the SEDs of different kind of objects The targets of interest are then selected from a photometric sample which has predefined a depth and redshift coverage. Historically target sample selection was the result of simple magnitude cuts. Recent redshift surveys employ more complex sample selection with various cuts in the color-magnitude plane [298]. The final observed samples will also be affected by several biases due to the interplay between the sharp magnitude cut, the luminosity function and errors in the observed magnitudes. These biases are well understood and discussed in detail by e.g., Teerikorpi [369]. We are not focusing on biases of such kind, but instead we are concerned about the modulations introduced in the inferred density field due to galaxy peculiar motion.

7.4.1 Magnitude limited sample

A magnitude limited sample is one which has been selected only by applying a limiting magnitude cut. The effect of peculiar velocities on such a sample is relatively simple to

understand. The galaxies moving towards the observer will have their magnitudes boosted and those that are intrinsically just fainter than the cut will move into the sample. The galaxies moving away from an observer will have their magnitudes suppressed and hence those just above the magnitude limit will move out of the sample. We can therefore construct a simple picture in which the probability of a galaxy passing the sample cut is simply related its velocity. The constant of proportionality will depend on the true magnitude of the galaxy and its spectrum and it will always be positive. This means galaxies moving towards the observer will always have a higher probability of making the sample cut compared to galaxies moving away from the observer. This is true unless one considers an exotic galaxy SED, for example, an SED in which flux decreases with wavelength fast enough to such that the gain in flux by relativistic beaming is smaller than the reduction in flux caused by relativistic Doppler effect.

7.4.2   Color-Magnitude cuts

Most of the current and future galaxy redshift survey have a more complicated targeting algorithm than simple magnitude cuts. In a more complicated scenario where the sample selection has several color and magnitude cuts, the simplest expectation that galaxies moving towards the observer will have a higher probability of making into the sample does not hold true. The exact nature of cuts, details of spectra and the galaxy population can lead to the probabilities of including galaxies moving towards the observer being smaller than those moving away from the observer. Such effects depend on the redshift, halo mass and peculiar velocity (both magnitude and direction) of the observed galaxy. This can lead to extra structure in the number density of the observed target and affect the clustering measurements. This has been assumed to be unimportant for current and future surveys. Whether this is true is something we will address here. Some analyses of galaxy clustering rely on

partioning a sample into subsamples based on their observed properties [348, 94, 15]. The effects we model in this paper are likely to be relatively more important for these analyses, as they will have different strengths for sub-samples with different galaxy properties.

7.5 Special Case: SDSS III CMASS Sample

The SDSS III CMASS sample is one of the key target datasets where we have a large number of massive galaxies with photometric and spectroscopic observations. We use this sample as an example, computing the effects of relativistic beaming and Doppler shifting in detail. This analysis can be easily extended to other surveys. We first briefly describe the sample and introduce the relevant quantity necessary to understand the CMASS target selection.

7.5.1 CMASS Sample

We use data included in data release 12 (DR12;[298, 9]) of the Sloan Digital Sky Survey (SDSS; [407]). SDSS I, II [1] and III [115] used a drift-scanning mosaic CCD camera [132] to image 14555 square degrees of the sky in five photometric bands [122, 351, 104] to a limiting magnitude of $r < 22.5$ using the 2.5-m Sloan Telescope [134] at the Apache Point Observatory in New Mexico. The imaging data were processed through a series of SDSS pipelines [218, 265, 248]. [6] reprocessed all of the SDSS imaging data in Data Release 8 (DR8). The Baryon Oscillation Spectroscopic survey (BOSS;[96]) was designed to obtain spectra and redshifts for 1.35 million galaxies covering 10,000 square degrees of sky. These galaxies were selected from the SDSS DR8 imaging. [61] developed a tiling algorithm that is adaptive to the density of targets on the sky and this was used for targeting in BOSS. BOSS used double-armed spectrographs Smee et al. [349] to obtain the spectra. BOSS resulted in a homogeneous data set with a high redshift completeness of more than 97%
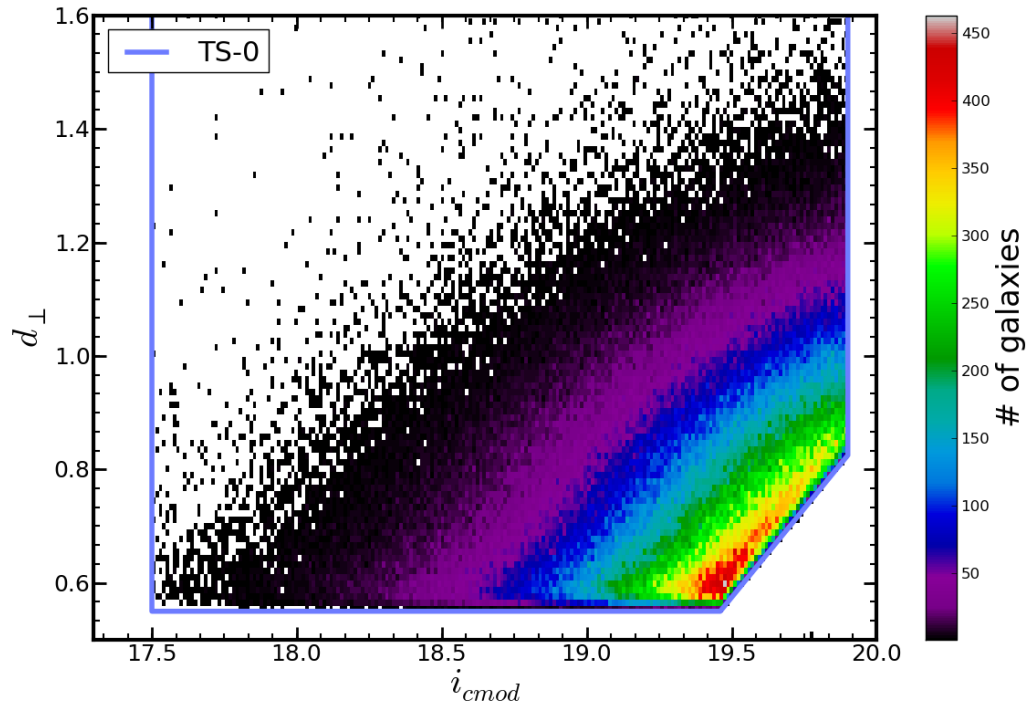
Figure 7.2: The density of galaxies in the CMASS sample in color-magnitude space. The parameter d_perp is defined in Equation 7.18. The red color indicates a high density and black shows low density. The solid blue line represents the CMASS target selection criteria.

over the full survey footprint. The redshift extraction algorithm used in BOSS is described in Bolton et al. [65]. Eisenstein et al. [115] provides a summary and Dawson et al. [96] provides a detailed description of the survey design.

We use the CMASS sample of galaxies [65] from data release 12 [9]. The CMASS sample contains 7,65,433 Luminous Red Galaxies (LRGs) covering 9376 square degrees in the redshift range $0.44 < z < 0.70$, which correspond to an effective volume of 10.8 Gpc^3. We used co-added spectra for each galaxy in our analysis [3].

CMASS Target Selection

The photometrically identified objects in the SDSS imaging catalog (Data Release 8:DR8[4]) are used as the parent sample for selecting the galaxies to be targeted for spectroscopic observations. The parent catalog covered 7606 $\deg^2$ in the Northern Galactic Cap (NGC) and 3172 $\deg^2$ in the Southern Galactic Cap (SGC). The photometric sample contains flux observed in five photometric bands (u, g, r, i, z). The target selection for the CMASS sample uses two types of magnitude provided by the SDSS imaging pipeline. The imaging pipeline fits exponential and deVaucouleurs profiles for each of the five photometric band to provide the fluxes $f_{\mathrm{exp}}^{\mathrm{band}}$ and $f_{\mathrm{deV}}^{\mathrm{band}}$ respectively. These fluxes are used to define two different kinds of flux, named "model" and "cmodel" and given by the following equations.

$$f_{\mathrm{mod,cmod}}^{\mathrm{band}} = (1 - P_{\mathrm{mod,cmod}})f_{\mathrm{exp}}^{\mathrm{band}} + P_{\mathrm{mod,cmod}}f_{\mathrm{deV}}^{\mathrm{band}}. \tag{7.13}$$

Here P_{mod} is a real number between 0 and 1, and P_{cmod} is an integer which can be either 0 or 1. The imaging pipeline fits the observed flux to obtain values of $P_{\mathrm{mod,cmod}}$. The main

---

[3]The co-added version of the spectrum used in our analysis can be downloaded from `http://data.sdss3.org/sas/dr12/boss/spectro/redux/v5_7_0/spectra/lite/`. The basic description of the SDSS optical spectra can be found over `http://www.sdss.org/dr12/spectro/spectro_basics`

[4]`http://www.sdss3.org/dr8`

difference between model and cmodel flux is that the model flux results from the use of a linear combination of exponential and deVaucouleurs profiles, whereas the cmodel flux uses the best-fitting profile. The model and cmodel fluxes are converted to magnitudes as follows:

$$\text{band} = 22.5 - 2.5 \log(f^{\text{band}}) - C_{\text{extinction}}, \tag{7.14}$$

where fluxes are in nanomaggies and band can be any of the five photometric bands u, g, r, i, z. The $C_{\text{extinction}}$ is the galactic extinction correction for the galaxy using the dust maps of Schlegel et al. [330]. The main criteria used in CMASS target selection are as follows:

$$17.5 < i_{\text{cmod}} < 19.9 \tag{7.15}$$

$$d_\perp > 0.55 \tag{7.16}$$

$$i_{\text{cmod}} < 1.6(d_\perp - 0.8) + 19.86 \tag{7.17}$$

There are several other criteria used for the target selection but they affect a very small number of objects and are not relevant for our study. The full list of target selection rules is provided in Reid et al. [298]. The quantity i_{cmod} is the cmodel magnitude for photometric band i. The quantity $d_\perp$ is a linear combination of the color $g - r$ and $r - i$ based on model magnitude as follows:

$$d_\perp = (r_{\text{mod}} - i_{\text{mod}}) - \frac{1}{8}(g_{\text{mod}} - r_{\text{mod}}), \tag{7.18}$$

where $g_{\text{mod}}, r_{\text{mod}}, i_{\text{mod}}$ are the model magnitudes for the photometric bands g, r and i respectively. The Figure 7.2 shows the distribution of galaxies in the final CMASS sample

216
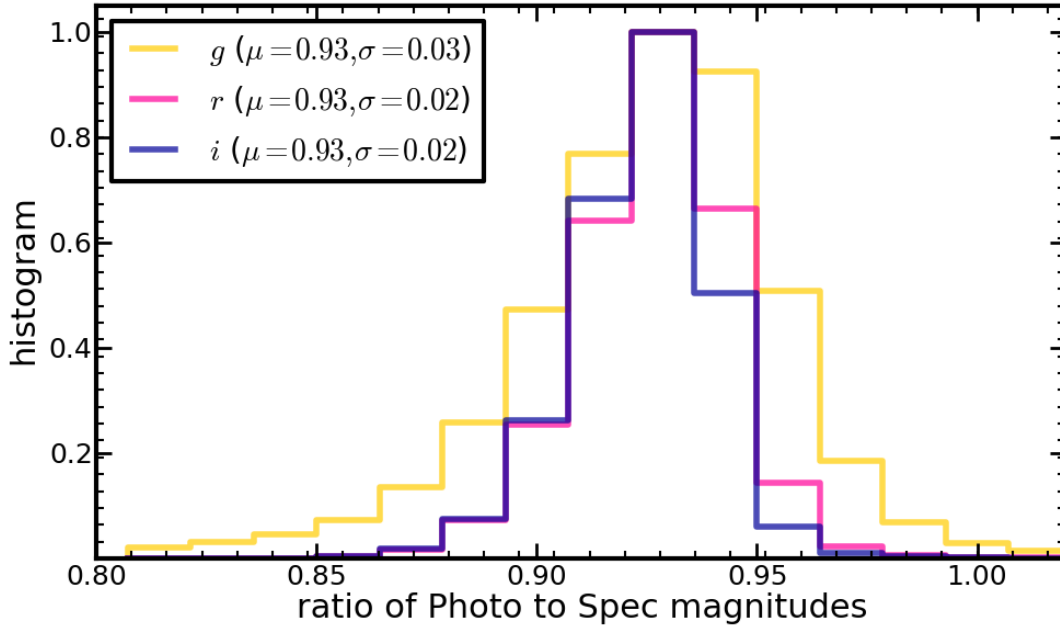
Figure 7.3: The histogram of the ratio of magnitudes from spectra to the photometric magnitude for g, r and i bands. The mean of the ratio is 0.93 which indicates that the magnitudes measured from spectra are larger (flux from spectra is smaller). This is because the fibers cover only $2'$ which is smaller than the mean size of a galaxy in the sample. This plot also shows that the scatter in this ratio of the two magnitudes is quite small.

(DR12) in the $i_{\mathrm{cmod}} - d_\perp$ plane. The solid line shows the target selection rule as stated in equation 7.15, 7.16 and 7.17.

7.5.2   Spectro-Photometry

We use SDSS observed SEDs as a template to study the relativistic effects. We transform each of the observed spectra according to equation 7.12 for a given β and θ. We then obtain the flux in different photometric bands by integrating the spectra with the response function for each band:

$$f_{\mathrm{spec}}^{\mathrm{band}} = \int d\lambda f(\lambda) R^{\mathrm{band}}(\lambda) C^{\mathrm{band}}, \qquad (7.19)$$

217

where $f(\lambda), R(\lambda)$ represents the flux and photometric band response for wavelength λ. The parameter C^{band} is the calibration factor which is obtained using the fiber flux of 10,000 galaxies. The calibration factors obtained for g, r and i bands are $((2.3, 3.3, 6.1)^{-3}$ respectively. The fiber flux is another flux provided in the SDSS imaging catalog. It represents the flux obtained in the photometric survey withing the aperture of spectroscopic fiber for each band [5]. The aperture of $2''$ in diameter is assumed for calculating fiber flux, which is appropriate for the BOSS spectrograph. The spectroscopic flux is converted to magnitude using equation 7.14. The spectroscopic magnitude is typically smaller than the corresponding photometric magnitude because fibers cover only the central part of galaxies. We have found that the spectroscopic magnitudes can be converted to photometric magnitudes using a simple multiplication factor of 0.93. The Figure 7.3 shows the histogram of the ratio of model magnitude to the spectroscopic magnitude. For each of g, r and i band the ratio of magnitudes has mean at 0.93 with a scatter of 0.03 for g band and 0.02 for both r and i band. We therefore obtain the cmodel magnitude from the spectroscopic magnitude using a multiplication factor of 0.93 ($i^{\text{spec}}_{\text{cmod}} = 0.93 i^{\text{spec}}$).

7.5.3 Magnitude and Color evolution

The local gravitational interactions of galaxies causes them to have peculiar velocities. These peculiar velocities cause the observed SEDs of galaxies to be different from the true SEDs. This can change the observed magnitude and color of galaxies. We systematically investigate these changes for grid of peculiar velocity magnitudes and directions from the line-of-sight. We transform the observed spectra of each galaxy using β values between -0.01 and 0.01 and θ between $0°$ and $90°$. We find that adding relativistic effects to spectra shifts the galaxies in the target selection plane. Not suprisingly, these shifts in color are

---

[5]http://www.sdss.org/dr12/algorithms/magnitudes/

sensitive to the galaxy spectra themselves and therefore depend on the stellar mass and redshift of galaxies. The Figure 7.4 shows the tracks of galaxies in the target selection color-magnitude plane. Each line with an arrowhead shows the path followed by the galaxies in the sample as peculiar velocity is varied. The tail of the line corresponds to the color-magnitude of the galaxy when it is moving away from the observer with $\beta = -0.01$ (speed of 3000 (km/s)) and the arrowhead correspond to the case when it is moving towards the observer with the same speed (i.e. we are showing the difference in assigning β from -0.01 (tail) to +0.01 (head). The color of the track indicates the redshift of the galaxy. Note that in the plot we only show a very small illustrative sub-sample of the full CMASS dataset, and we restrict ourselves to velocity directions directly aligned with the line-of-sight. The black thick solid line shows the CMASS target selection as described in equations 7.15, 7.16 and 7.17. We also show 3 more restrictive target selection criteria using other solid lines. The target selection criterion TS-n is given by the following equation:

$$17.5 < i_{\mathrm{cmod}} < 19.9 - 0.05n \qquad (7.20)$$

$$d_\perp > 0.55 + 0.03n \qquad (7.21)$$

$$i_{\mathrm{cmod}} < 1.6(d_\perp - 0.8 - 0.05n) + 19.86, \qquad (7.22)$$

where n is either 0,1,2, or 3, which represent different target selections TS-0,TS-1,TS-2 and TS-3 respectively. TS-0 is the actual CMASS target selection. Notice that these additional target selections are defined such that the shape of the target selection region in this plane remains unchanged. The tracks of galaxies show that the magnitudes (plotted on the x-axis) decrease when galaxies move towards the observer and increase when they moves away as per our expectation. This leads to galaxies at higher redshifts which are close to the magnitude limit of the target selection being moved inside the sample when their

velocity is towards the observer and being moved outside while their velocity is away. The color cuts can however reverse this trend as shown by the galaxies close to the lower limit of $d_\perp$, which are at lower redshifts. These galaxies move inside the sample when they have velocities away from the observer and moves outside the sample with velocities towards the observer. It should be also noticed that the effects shown in this plot are exaggerated by roughly an order of magnitude compared to the typical case for galaxies, as we are showing results for galaxy velocities as high as 3000 km/s.

7.5.4   Impact on Final Obtained Sample

Because the peculiar velocities of galaxies vary spatially, the relativistic effects will spatially modulate the observed SEDs of galaxies, which will in turn affect the observed magnitudes and colors. Therefore, a fraction of galaxies with colors and magnitudes originally within our target selection will move out of the sample and also some galaxies from outside the sample will move into it. This affects the observed number density of galaxies in the final sample. The modulations introduced in the observed number density will also be correlated with several other properties of galaxies for example stellar mass, redshift and velocity. In order to quantify these effects, we bin our sample in redshift and stellar mass. We create 10 bins in redshift between 0.4 and 0.8 and 10 bins in logarithm of stellar mass between $10^{10.8} M_\odot$ and $10^{13} M_\odot$. For each stellar mass and redshift bin, we compute the initial number of galaxies (N_{TS}^i) in the sample. We then transform the galaxies as if they were moving with velocity $v = \beta c$ along a direction at angle θ from the line-of-sight. We then reapply the target selection boundaries to count the final number of galaxies in the sample (N_{TS}^f). The relativistic effects due to peculiar motion of galaxies imply that the number of galaxies in the observed sample will be multiplied by the fraction $N_{\mathrm{TS}}^f/N_{\mathrm{TS}}^i$. Therefore, in clustering analysis if we would like to compensate for the number density modulation due
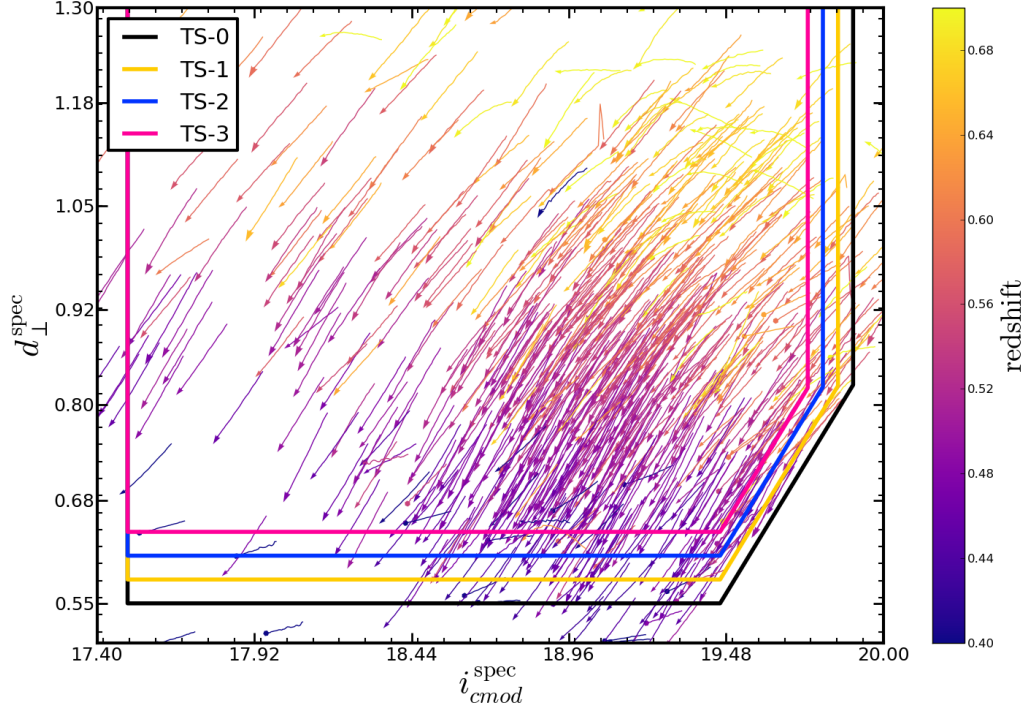
Figure 7.4: The effects of galaxy motion on observed galaxy color and magnitude. The solid thick lines of different colors show the different versions of our target selection criteria. The black solid line shows the CMASS original target selection. Other solid lines shows the variant of CMASS target selection described in equation 7.22. Each line with an arrow head shows how an individual galaxy will move in this space as we assign it a different velocity. The arrow-head shows the observed color-magnitude when galaxies are moving towards the observer with a speed of 3000 km/s and the tail point shows the color-magnitude when it moves with speed of 3000 km/s away from the observer. The color of the arrow itself indicates the redshift of the galaxy. Note that at small redshift a galaxy moving towards observer will cross the color cut to move out of the sample whereas at higher redshift the galaxy moving towards us with become brighter and cross the lower magnitude cut to move inside the sample. Note that we only show a very small illustrative sub-sample of the full CMASS dataset, and we restrict ourselves to velocity directions directly aligned with the line-of-sight.
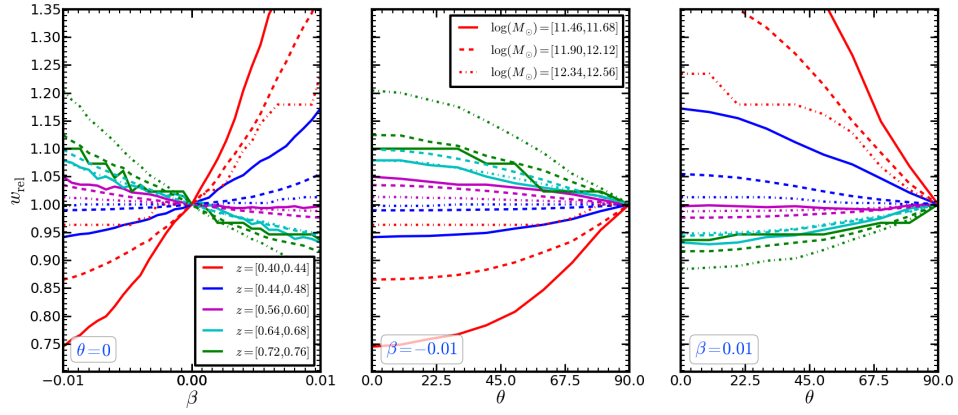
Figure 7.5: The relativistic weights for a galaxy given its redshift, stellar mass and velocity vector. The different colors indicate different redshift bins and different line-styles indicate different stellar mass bins. The left panel shows the w_{rel} with velocity of the galaxy in units of the speed of light along line-of-sight. The central and right panel shows the weight dependence on the direction of velocity from line-of-sight for $\beta = -0.01$ (v=3000 km/s away from observer) and $\beta = 0.01$ (v=3000 km/s towards the observer) respectively.

to relativistic effects we should weight each galaxy by w_{rel}, where

$$w_{\mathrm{rel}} = N_{\mathrm{TS}}^{i}/N_{\mathrm{TS}}^{f} \qquad (7.23)$$

We have obtained the w_{rel} for each bin as a function of β and θ of the galaxy. Figure 7.5 shows the weights obtained for some of the redshift and stellar mass bins as the function of β and θ. The different colors correspond to different redshift bins, while the different line styles correspond to different stellar mass bins. The left panel shows w_{rel} with β between -0.01 and 0.01 and $\theta = 0$. The value $\beta = -0.01$ corresponds to galaxies moving with a speed 3000 km/s away from the observer and $\beta = 0.01$ galaxies moving at 3000 km/s towards the observer. At higher redshifts the galaxies moving towards the observer (positive β) have weight smaller than 1. They will appear brighter and hence will be seen in larger number than if they were at rest with respect to the observer. The weight in this case is therefore smaller than unity, to compensate for the higher number of observed galaxies. The weights vary with stellar mass, galaxies with higher stellar mass having larger weights.

These trends change for lower redshifts however. Below approximately $z = 0.5$, galaxies moving towards the observer have weights larger than 1. This is due the fact that the galaxies at lower redshift are less likely to be close to the magnitude limit of the sample than they are to the color cut. When they move towards the observer they cross through the color cut and out of the sample. This causes a reverse trend with β which is different to that at higher redshifts. This can be seen in Figure 7.4 by following the tracks of these galaxies as β is varied. The middle and right panels of Figure 7.5 shows the dependence of w_{rel} on the direction of galaxy velocity θ for velocities with positive and negative β. These results show the importance of considering the full velocity vector rather than just the line-of-sight component.
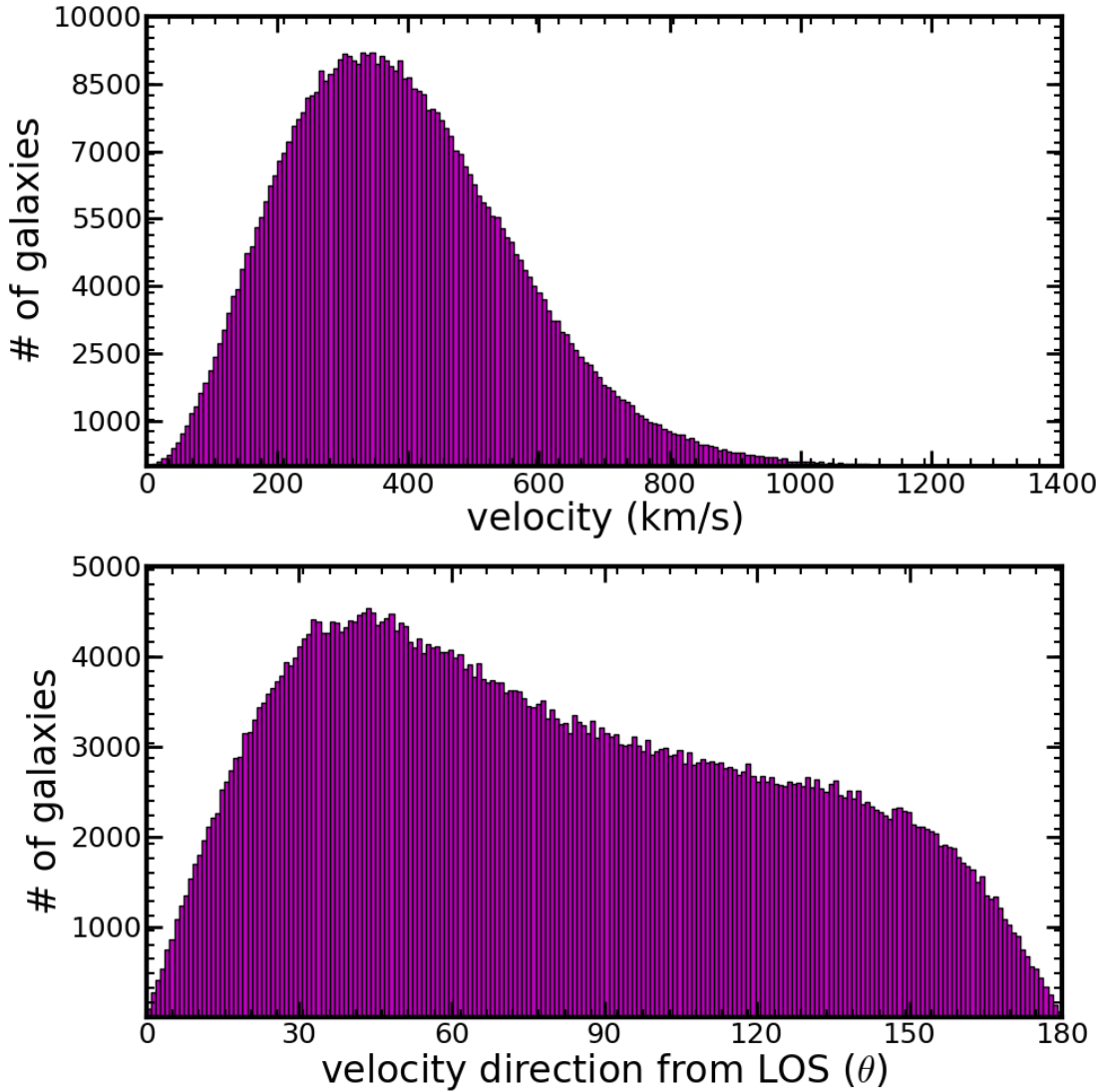
Figure 7.6: Estimated galaxy peculiar velocities in the SDSS III CMASS galaxy redshift sample. The velocity vectors for each galaxy were estimated using a perturbation theory based reconstruction algorithm. The top panel shows the distribution of the magnitudes of galaxy velocities in the sample. The bottom panel shows the distribution of velocity directions, where $\theta = 0°$ indicates that a galaxy is moving along line of sight away from observer and $\theta = 180°$ that the galaxy is moving directly towards the observer.

7.5.5   Predicting the galaxy peculiar velocities

In order to associate relativistic weights to each individual galaxy, the galaxy velocity is required. We estimate the velocity for each galaxy in the sample using a reconstruction

approach. We use a publicly available reconstruction code[6] which estimates the velocities of galaxy in our sample using perturbation theory [391, 392]. The reconstruction code first computes the number density (ρ) of galaxies on a grid using a cloud-in-cell assignment scheme . The number density is then converted to density contrast (δ) which is divided by a large scale bias b to yield the mass fluctuation in the cell. We use the value $b = 2.1$ measured in our analysis (see companion paper Alam et al. [15]). This mass fluctuation is then smoothed using a Gaussian kernel of width R_f (the smoothing scale). Our chosen value of $R_f = 10$ h^{-1}Mpc is motivated by the results of [381]. The reconstruction code then solves for the displacement field ([?]) and provides the displaced position for each galaxy [391]. We use the displaced position to obtain the peculiar velocities of galaxies using following equation:

$$\vec{v} = afH(\vec{r}_{obs} - \vec{r}_{\mathrm{recon}}), \tag{7.24}$$

where $H = 100$ (h^{-1}Mpc)/(km/s), $a = 1/(1+z)$ is the scale factor. We approximate the linear growth rate of perturbations $f = d\ln D/d\ln a$ as $f = \Omega_m(z)^{0.55}$. Figure 7.6 shows the distribution of galaxy velocities obtained using this procedure. In the top panel it can be seen that most of the galaxies have velocities between $200 - 600$km/s. The bottom panel shows the distribution of the angles between the velocities in the line of sight. The detailed shape of this distribution depends on the geometry the survey. We note that these velocities are predicted using perturbation theory which is not accurate on small scales where non-linear clustering happens. On scales below our smoothing scale, a number of galaxies will be moving significantly faster than the predicted velocity. This will be particularly true in virialized objects such as galaxy clusters. Our estimate of the strength of relativistic effects for will therefore tend to be an underestimate.

---

[6]github repo: `https://github.com/martinjameswhite/recon_code/`
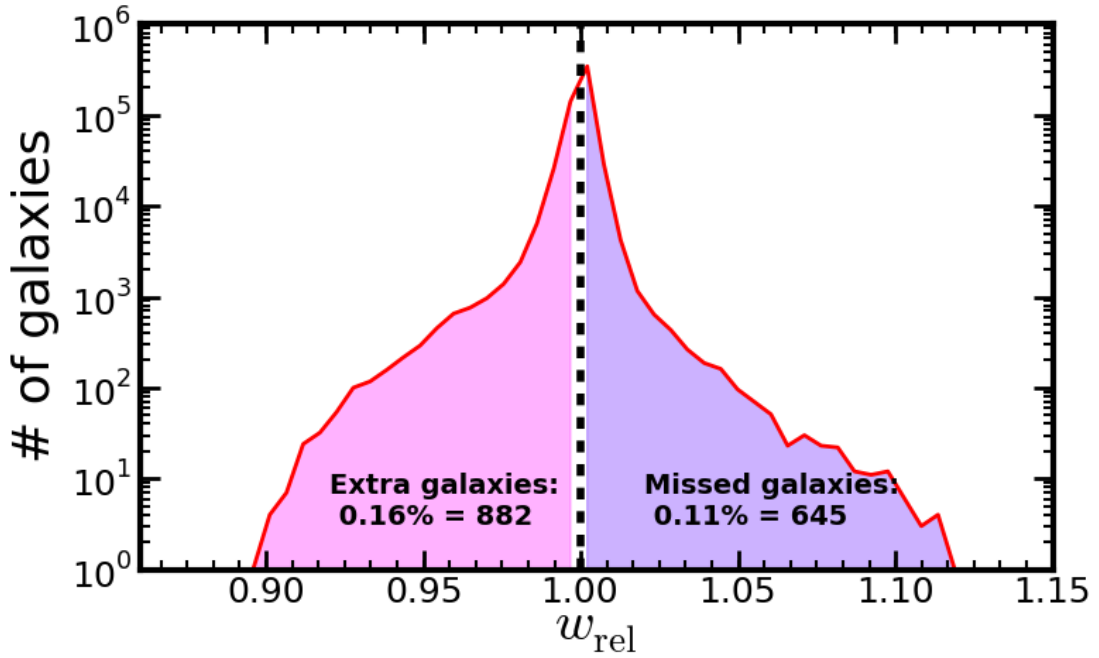
Figure 7.7: The distribution of the relativistic weights w_{rel} for the CMASS galaxy redshift sample. The x-axis is w_{rel} and the y-axis displays the binned number of galaxies on logarithmic scale. The galaxies with $w_{rel} < 1$ have higher probability of being in the sample. We estimate that 0.16% more such galaxies have been added to the sample because of their peculiar velocities. Galaxies with weights $w_{rel} > 1$ have a lower probability of being in the sample. From these we calculate that 0.11% of the sample which would be have been within the color-magnitude cuts is excluded because of the effect of peculiar velocities.
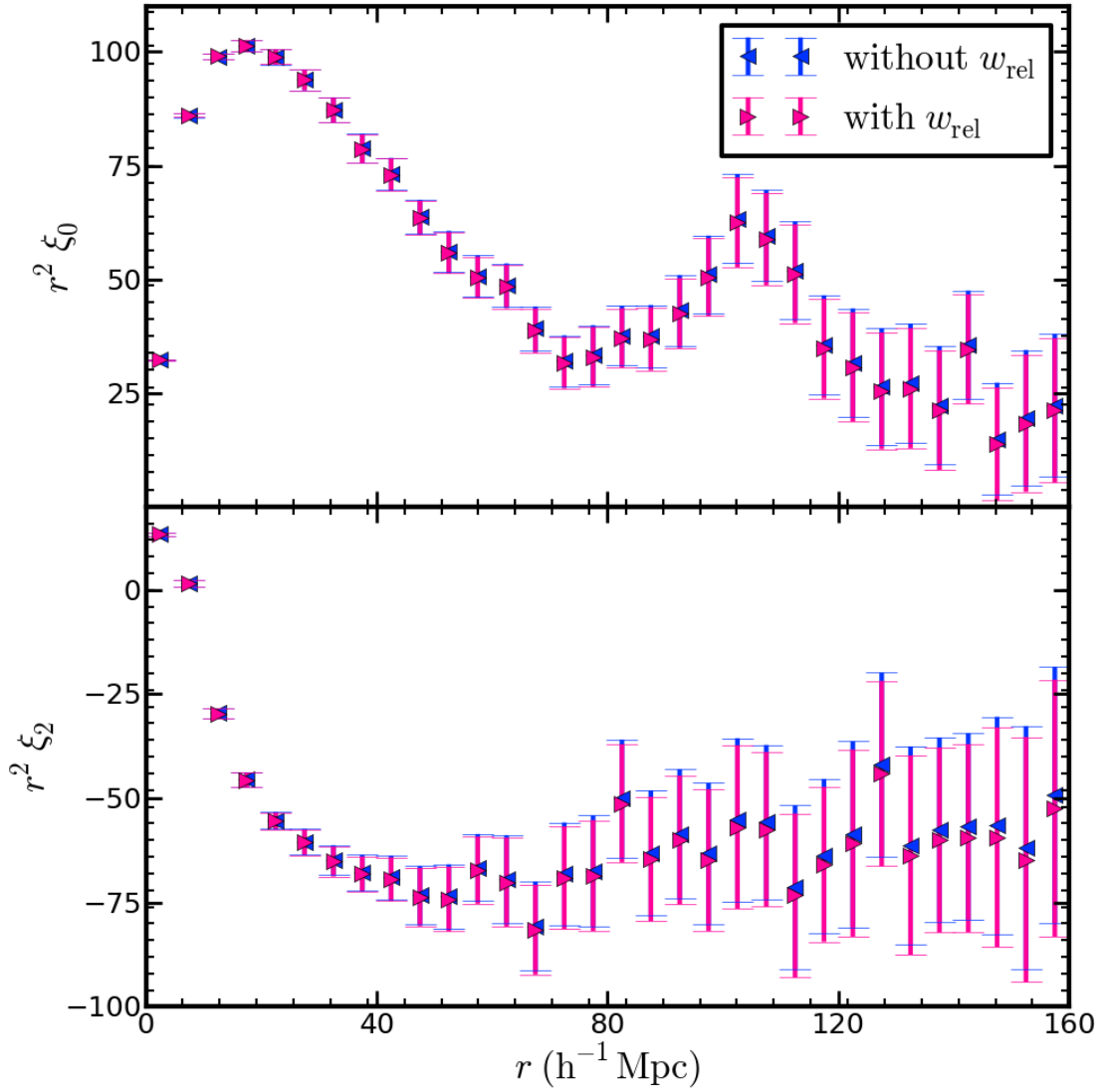
Figure 7.8: The two point galaxy auto-correlation function with and without the effect of relativistic weights. The top panel shows the monopole and the bottom panel shows the quadruple moment of the correlation function. The blue points represents the measurement without relativistic weight and the magenta points are with the relativistic weight correction.

7.5.6 Impact on Clustering

We now examine how relativistic sample selection effects alter the results of standard clustering analyses of the CMASS galaxy redshift sample. We use the observational data for

the CMASS sample to compute the weights $w_{\rm rel}$ which compensate each galaxy for the effect of Doppler shifting and beaming (see section 7.5.4). These weights are a function of the redshift, stellar mass and velocity vector of the galaxy. The relativistic correction therefore involves applying the weights before computing the two-point clustering of the galaxy sample. The galaxy catalog contains the redshift and stellar mass of each of the galaxy. We estimate the velocity vector of the galaxy using the perturbation theory approach described in section 7.5.5. Figure 7.7 shows the distribution of $w_{\rm rel}$ in the CMASS sample. We can see that the distribution of weights is not symmetric due to the fact that the luminosity function is non-uniform and hence there are more galaxies which scatter into the sample compared to those that scattering out of the sample. We estimate that around 0.16% (~ 882 galaxies) of the CMASS sample should not have been targeted and around 0.11% (~ 645 galaxies) should have been in the sample, but were not be observed.

We have computed the two-point clustering of CMASS with and without the relativistic weights. We use the Landy-szalay [194] estimator, and ther results are shown in Figure 7.8. The top panel shows the monopole of the correlation function and the bottom panel the quadruple moment.The error bars on the clustering were computed by dividing the entire sample into 61 jackknife regions, see Alam et al. [15] for more details. We find that the effects of these weights are much smaller than the statistical errors on the clustering measurement. We therefore do not expect that any of the standard large scale structure analyses(such as BAO measurement or redshift space distortions) will show significant effects in current surveys. We should bear in mind though, that as the samples get larger and probe fainter magnitudes these effects might start to become more important for future surveys.

7.6 Conclusion

We have used the SDSS III BOSS CMASS galaxy sample to examine the impact of relativistic effects on observed galaxy SEDs. We have discussed how the effects on SEDs will translate to observed fluxes and hence will impact the target selection of galaxy redshift surveys. We have found that galaxies can move both in and out of the sample depending on their peculiar motion. We have investigated these effects for the CMASS target selection as a function of redshift, stellar mass, magnitude and direction of galaxy velocity. In order to estimate the effect on clustering statistics, we have also used perturbation theory to predict the galaxy velocities from the galaxy density field. These velocities provide the information we need to gauge the impact of relativistic effects on individual galaxies.

We have computed weights that can be used to cancel out the relativistic effects on target selection. We studied the galaxy two-point correlation function with and without these weights, finding an impact on the clustering signal which is much smaller than the current statistical errors. This should not therefore affect current large scale structure analyses such as baryon acoustic oscillation measurement or estimates of the growth rate from redshift space distortions. We expect that these effects will be more significant when one is looking at galaxy clustering weighted by one of the properties which are affected by relativistic effects such as luminosity, photometric magnitude etc. We also expect these effects to be more significant when surveys are deeper and hence future surveys should be analyzed with such effects in mind.

One of the main motivations to study these effects is to understand how relativistic beaming and doppler shift modulate the density field and change galaxy clustering. If clustering statistics are chosen carefully and galaxy samples are large enough, then these effects can in principle be detected. [181] has shown that these effects can contribute to the asymmetry in galaxy clustering around clusters which is used to infer the gravitional

redshift profile (e.g., [71, 187, 399, 412, 317]). Relativistic effects on large-scale clustering have been also been computed using perturbation theory in full General Relativity (e.g., [226, 406, 67]). The results in our paper have motivated the form of the beaming effect included in a companion paper Zhu et al. [414]. We have applied them to N-body simulations in order to estimate the line-of-sight asymmetry in the non-linear scale cross-correlation function of two galaxy populations with different halo masses. The models are also used in our other companion paper Alam et al. [15], which provides the first measurement of line-of-sight asymmetry in the CMASS sample.

Bibliography

[1] K. N. Abazajian, J. K. Adelman-McCarthy, M. A. Agüeros, S. S. Allam, C. Allende Prieto, D. An, K. S. J. Anderson, S. F. Anderson, J. Annis, N. A. Bahcall, and et al. The Seventh Data Release of the Sloan Digital Sky Survey. *ApJ Suppl.*, 182:543, June 2009. doi: 10.1088/0067-0049/182/2/543.

[2] B. P. Abbott, R. Abbott, T. D. Abbott, M. R. Abernathy, F. Acernese, K. Ackley, C. Adams, T. Adams, P. Addesso, R. X. Adhikari, V. B. Adya, C. Affeldt, M. Agathos, K. Agatsuma, N. Aggarwal, O. D. Aguiar, L. Aiello, A. Ain, P. Ajith, B. Allen, A. Allocca, P. A. Altin, S. B. Anderson, W. G. Anderson, K. Arai, M. A. Arain, M. C. Araya, C. C. Arceneaux, J. S. Areeda, N. Arnaud, K. G. Arun, S. Ascenzi, G. Ashton, M. Ast, S. M. Aston, P. Astone, P. Aufmuth, C. Aulbert, S. Babak, P. Bacon, M. K. M. Bader, P. T. Baker, F. Baldaccini, G. Ballardin, S. W. Ballmer, J. C. Barayoga, S. E. Barclay, B. C. Barish, D. Barker, F. Barone, B. Barr, L. Barsotti, M. Barsuglia, D. Barta, J. Bartlett, M. A. Barton, I. Bartos, R. Bassiri, A. Basti, J. C. Batch, C. Baune, V. Bavigadda, M. Bazzan, B. Behnke, M. Bejger, C. Belczynski, A. S. Bell, C. J. Bell, B. K. Berger, J. Bergman, G. Bergmann, C. P. L. Berry, D. Bersanetti, A. Bertolini, J. Betzwieser, S. Bhagwat, R. Bhandare, I. A. Bilenko, G. Billingsley, J. Birch, R. Birney, O. Birnholtz, S. Biscans, A. Bisht, M. Bitossi, C. Biwer, M. A. Bizouard, J. K. Blackburn, C. D. Blair, D. G. Blair, R. M. Blair,

S. Bloemen, O. Bock, T. P. Bodiya, M. Boer, G. Bogaert, C. Bogan, A. Bohe, P. Bojtos, C. Bond, F. Bondu, R. Bonnand, B. A. Boom, R. Bork, V. Boschi, S. Bose, Y. Bouffanais, A. Bozzi, C. Bradaschia, P. R. Brady, V. B. Braginsky, M. Branchesi, J. E. Brau, T. Briant, A. Brillet, M. Brinkmann, V. Brisson, P. Brockill, A. F. Brooks, D. A. Brown, D. D. Brown, N. M. Brown, C. C. Buchanan, A. Buikema, T. Bulik, H. J. Bulten, A. Buonanno, D. Buskulic, C. Buy, R. L. Byer, M. Cabero, L. Cadonati, G. Cagnoli, C. Cahillane, J. Calderón Bustillo, T. Callister, E. Calloni, J. B. Camp, K. C. Cannon, J. Cao, C. D. Capano, E. Capocasa, F. Carbognani, S. Caride, J. Casanueva Diaz, C. Casentini, S. Caudill, M. Cavaglià, F. Cavalier, R. Cavalieri, G. Cella, C. B. Cepeda, L. Cerboni Baiardi, G. Cerretani, E. Cesarini, R. Chakraborty, T. Chalermsongsak, S. J. Chamberlin, M. Chan, S. Chao, P. Charlton, E. Chassande-Mottin, H. Y. Chen, Y. Chen, C. Cheng, A. Chincarini, A. Chiummo, H. S. Cho, M. Cho, J. H. Chow, N. Christensen, Q. Chu, S. Chua, S. Chung, G. Ciani, F. Clara, J. A. Clark, F. Cleva, E. Coccia, P.-F. Cohadon, A. Colla, C. G. Collette, L. Cominsky, M. Constancio, A. Conte, L. Conti, D. Cook, T. R. Corbitt, N. Cornish, A. Corsi, S. Cortese, C. A. Costa, M. W. Coughlin, S. B. Coughlin, J.-P. Coulon, S. T. Countryman, P. Couvares, E. E. Cowan, D. M. Coward, M. J. Cowart, D. C. Coyne, R. Coyne, K. Craig, J. D. E. Creighton, T. D. Creighton, J. Cripe, S. G. Crowder, A. M. Cruise, A. Cumming, L. Cunningham, E. Cuoco, T. Dal Canton, S. L. Danilishin, S. D'Antonio, K. Danzmann, N. S. Darman, C. F. Da Silva Costa, V. Dattilo, I. Dave, H. P. Daveloza, M. Davier, G. S. Davies, E. J. Daw, R. Day, S. De, D. DeBra, G. Debreczeni, J. Degallaix, M. De Laurentis, S. Déléglise, W. Del Pozzo, T. Denker, T. Dent, H. Dereli, V. Dergachev, R. T. DeRosa, R. De Rosa, R. DeSalvo, S. Dhurandhar, M. C. Díaz, L. Di Fiore, M. Di Giovanni, A. Di Lieto, S. Di Pace, I. Di Palma, A. Di Virgilio, G. Dojcinoski, V. Dolique, F. Donovan, K. L. Dooley, S. Doravari, R. Douglas, T. P. Downes, M. Drago, R. W. P. Drever, J. C. Driggers,

Z. Du, M. Ducrot, S. E. Dwyer, T. B. Edo, M. C. Edwards, A. Effler, H.-B. Eggenstein, P. Ehrens, J. Eichholz, S. S. Eikenberry, W. Engels, R. C. Essick, T. Etzel, M. Evans, T. M. Evans, R. Everett, M. Factourovich, V. Fafone, H. Fair, S. Fairhurst, X. Fan, Q. Fang, S. Farinon, B. Farr, W. M. Farr, M. Favata, M. Fays, H. Fehrmann, M. M. Fejer, D. Feldbaum, I. Ferrante, E. C. Ferreira, F. Ferrini, F. Fidecaro, L. S. Finn, I. Fiori, D. Fiorucci, R. P. Fisher, R. Flaminio, M. Fletcher, H. Fong, J.-D. Fournier, S. Franco, S. Frasca, F. Frasconi, M. Frede, Z. Frei, A. Freise, R. Frey, V. Frey, T. T. Fricke, P. Fritschel, V. V. Frolov, P. Fulda, M. Fyffe, H. A. G. Gabbard, J. R. Gair, L. Gammaitoni, S. G. Gaonkar, F. Garufi, A. Gatto, G. Gaur, N. Gehrels, G. Gemme, B. Gendre, E. Genin, A. Gennai, J. George, L. Gergely, V. Germain, Abhirup Ghosh, Archisman Ghosh, S. Ghosh, J. A. Giaime, K. D. Giardina, A. Giazotto, K. Gill, A. Glaefke, J. R. Gleason, E. Goetz, R. Goetz, L. Gondan, G. González, J. M. Gonzalez Castro, A. Gopakumar, N. A. Gordon, M. L. Gorodetsky, S. E. Gossan, M. Gosselin, R. Gouaty, C. Graef, P. B. Graff, M. Granata, A. Grant, S. Gras, C. Gray, G. Greco, A. C. Green, R. J. S. Greenhalgh, P. Groot, H. Grote, S. Grunewald, G. M. Guidi, X. Guo, A. Gupta, M. K. Gupta, K. E. Gushwa, E. K. Gustafson, R. Gustafson, J. J. Hacker, B. R. Hall, E. D. Hall, G. Hammond, M. Haney, M. M. Hanke, J. Hanks, C. Hanna, M. D. Hannam, J. Hanson, T. Hardwick, J. Harms, G. M. Harry, I. W. Harry, M. J. Hart, M. T. Hartman, C.-J. Haster, K. Haughian, J. Healy, J. Heefner, A. Heidmann, M. C. Heintze, G. Heinzel, H. Heitmann, P. Hello, G. Hemming, M. Hendry, I. S. Heng, J. Hennig, A. W. Heptonstall, M. Heurs, S. Hild, D. Hoak, K. A. Hodge, D. Hofman, S. E. Hollitt, K. Holt, D. E. Holz, P. Hopkins, D. J. Hosken, J. Hough, E. A. Houston, E. J. Howell, Y. M. Hu, S. Huang, E. A. Huerta, D. Huet, B. Hughey, S. Husa, S. H. Huttner, T. Huynh-Dinh, A. Idrisy, N. Indik, D. R. Ingram, R. Inta, H. N. Isa, J.-M. Isac, M. Isi, G. Islas, T. Isogai, B. R. Iyer, K. Izumi, M. B. Jacob-

son, T. Jacqmin, H. Jang, K. Jani, P. Jaranowski, S. Jawahar, F. Jiménez-Forteza, W. W. Johnson, N. K. Johnson-McDaniel, D. I. Jones, R. Jones, R. J. G. Jonker, L. Ju, K. Haris, C. V. Kalaghatgi, V. Kalogera, S. Kandhasamy, G. Kang, J. B. Kanner, S. Karki, M. Kasprzack, E. Katsavounidis, W. Katzman, S. Kaufer, T. Kaur, K. Kawabe, F. Kawazoe, F. Kéfélian, M. S. Kehl, D. Keitel, D. B. Kelley, W. Kells, R. Kennedy, D. G. Keppel, J. S. Key, A. Khalaidovski, F. Y. Khalili, I. Khan, S. Khan, Z. Khan, E. A. Khazanov, N. Kijbunchoo, C. Kim, J. Kim, K. Kim, Nam-Gyu Kim, Namjun Kim, Y.-M. Kim, E. J. King, P. J. King, D. L. Kinzel, J. S. Kissel, L. Kleybolte, S. Klimenko, S. M. Koehlenbeck, K. Kokeyama, S. Koley, V. Kondrashov, A. Kontos, S. Koranda, M. Korobko, W. Z. Korth, I. Kowalska, D. B. Kozak, V. Kringel, B. Krishnan, A. Królak, C. Krueger, G. Kuehn, P. Kumar, R. Kumar, L. Kuo, A. Kutynia, P. Kwee, B. D. Lackey, M. Landry, J. Lange, B. Lantz, P. D. Lasky, A. Lazzarini, C. Lazzaro, P. Leaci, S. Leavey, E. O. Lebigot, C. H. Lee, H. K. Lee, H. M. Lee, K. Lee, A. Lenon, M. Leonardi, J. R. Leong, N. Leroy, N. Letendre, Y. Levin, B. M. Levine, T. G. F. Li, A. Libson, T. B. Littenberg, N. A. Lockerbie, J. Logue, A. L. Lombardi, L. T. London, J. E. Lord, M. Lorenzini, V. Loriette, M. Lormand, G. Losurdo, J. D. Lough, C. O. Lousto, G. Lovelace, H. Lück, A. P. Lundgren, J. Luo, R. Lynch, Y. Ma, T. MacDonald, B. Machenschalk, M. MacInnis, D. M. Macleod, F. Magaña Sandoval, R. M. Magee, M. Mageswaran, E. Majorana, I. Maksimovic, V. Malvezzi, N. Man, I. Mandel, V. Mandic, V. Mangano, G. L. Mansell, M. Manske, M. Mantovani, F. Marchesoni, F. Marion, S. Márka, Z. Márka, A. S. Markosyan, E. Maros, F. Martelli, L. Martellini, I. W. Martin, R. M. Martin, D. V. Martynov, J. N. Marx, K. Mason, A. Masserot, T. J. Massinger, M. Masso-Reid, F. Matichard, L. Matone, N. Mavalvala, N. Mazumder, G. Mazzolo, R. McCarthy, D. E. McClelland, S. McCormick, S. C. McGuire, G. McIntyre, J. McIver, D. J. McManus, S. T. McWilliams, D. Meacher, G. D. Meadors,

234

J. Meidam, A. Melatos, G. Mendell, D. Mendoza-Gandara, R. A. Mercer, E. Merilh, M. Merzougui, S. Meshkov, C. Messenger, C. Messick, P. M. Meyers, F. Mezzani, H. Miao, C. Michel, H. Middleton, E. E. Mikhailov, L. Milano, J. Miller, M. Millhouse, Y. Minenkov, J. Ming, S. Mirshekari, C. Mishra, S. Mitra, V. P. Mitrofanov, G. Mitselmakher, R. Mittleman, A. Moggi, M. Mohan, S. R. P. Mohapatra, M. Montani, B. C. Moore, C. J. Moore, D. Moraru, G. Moreno, S. R. Morriss, K. Mossavi, B. Mours, C. M. Mow-Lowry, C. L. Mueller, G. Mueller, A. W. Muir, Arunava Mukherjee, D. Mukherjee, S. Mukherjee, N. Mukund, A. Mullavey, J. Munch, D. J. Murphy, P. G. Murray, A. Mytidis, I. Nardecchia, L. Naticchioni, R. K. Nayak, V. Necula, K. Nedkova, G. Nelemans, M. Neri, A. Neunzert, G. Newton, T. T. Nguyen, A. B. Nielsen, S. Nissanke, A. Nitz, F. Nocera, D. Nolting, M. E. N. Normandin, L. K. Nuttall, J. Oberling, E. Ochsner, J. O'Dell, E. Oelker, G. H. Ogin, J. J. Oh, S. H. Oh, F. Ohme, M. Oliver, P. Oppermann, Richard J. Oram, B. O'Reilly, R. O'Shaughnessy, C. D. Ott, D. J. Ottaway, R. S. Ottens, H. Overmier, B. J. Owen, A. Pai, S. A. Pai, J. R. Palamos, O. Palashov, C. Palomba, A. Pal-Singh, H. Pan, Y. Pan, C. Pankow, F. Pannarale, B. C. Pant, F. Paoletti, A. Paoli, M. A. Papa, H. R. Paris, W. Parker, D. Pascucci, A. Pasqualetti, R. Passaquieti, D. Passuello, B. Patricelli, Z. Patrick, B. L. Pearlstone, M. Pedraza, R. Pedurand, L. Pekowsky, A. Pele, S. Penn, A. Perreca, H. P. Pfeiffer, M. Phelps, O. Piccinni, M. Pichot, M. Pickenpack, F. Piergiovanni, V. Pierro, G. Pillant, L. Pinard, I. M. Pinto, M. Pitkin, J. H. Poeld, R. Poggiani, P. Popolizio, A. Post, J. Powell, J. Prasad, V. Predoi, S. S. Premachandra, T. Prestegard, L. R. Price, M. Prijatelj, M. Principe, S. Privitera, R. Prix, G. A. Prodi, L. Prokhorov, O. Puncken, M. Punturo, P. Puppo, M. Pürrer, H. Qi, J. Qin, V. Quetschke, E. A. Quintero, R. Quitzow-James, F. J. Raab, D. S. Rabeling, H. Radkins, P. Raffai, S. Raja, M. Rakhmanov, C. R. Ramet, P. Rapagnani, V. Raymond, M. Razzano, V. Re, J. Read, C. M. Reed, T. Regimbau, L. Rei, S. Reid, D. H.

Reitze, H. Rew, S. D. Reyes, F. Ricci, K. Riles, N. A. Robertson, R. Robie, F. Robinet, A. Rocchi, L. Rolland, J. G. Rollins, V. J. Roma, J. D. Romano, R. Romano, G. Romanov, J. H. Romie, D. Rosińska, S. Rowan, A. Rüdiger, P. Ruggi, K. Ryan, S. Sachdev, T. Sadecki, L. Sadeghian, L. Salconi, M. Saleem, F. Salemi, A. Samajdar, L. Sammut, L. M. Sampson, E. J. Sanchez, V. Sandberg, B. Sandeen, G. H. Sanders, J. R. Sanders, B. Sassolas, B. S. Sathyaprakash, P. R. Saulson, O. Sauter, R. L. Savage, A. Sawadsky, P. Schale, R. Schilling, J. Schmidt, P. Schmidt, R. Schnabel, R. M. S. Schofield, A. Schönbeck, E. Schreiber, D. Schuette, B. F. Schutz, J. Scott, S. M. Scott, D. Sellers, A. S. Sengupta, D. Sentenac, V. Sequino, A. Sergeev, G. Serna, Y. Setyawati, A. Sevigny, D. A. Shaddock, T. Shaffer, S. Shah, M. S. Shahriar, M. Shaltev, Z. Shao, B. Shapiro, P. Shawhan, A. Sheperd, D. H. Shoemaker, D. M. Shoemaker, K. Siellez, X. Siemens, D. Sigg, A. D. Silva, D. Simakov, A. Singer, L. P. Singer, A. Singh, R. Singh, A. Singhal, A. M. Sintes, B. J. J. Slagmolen, J. R. Smith, M. R. Smith, N. D. Smith, R. J. E. Smith, E. J. Son, B. Sorazu, F. Sorrentino, T. Souradeep, A. K. Srivastava, A. Staley, M. Steinke, J. Steinlechner, S. Steinlechner, D. Steinmeyer, B. C. Stephens, S. P. Stevenson, R. Stone, K. A. Strain, N. Straniero, G. Stratta, N. A. Strauss, S. Strigin, R. Sturani, A. L. Stuver, T. Z. Summerscales, L. Sun, P. J. Sutton, B. L. Swinkels, M. J. Szczepańczyk, M. Tacca, D. Talukder, D. B. Tanner, M. Tápai, S. P. Tarabrin, A. Taracchini, R. Taylor, T. Theeg, M. P. Thirugnanasambandam, E. G. Thomas, M. Thomas, P. Thomas, K. A. Thorne, K. S. Thorne, E. Thrane, S. Tiwari, V. Tiwari, K. V. Tokmakov, C. Tomlinson, M. Tonelli, C. V. Torres, C. I. Torrie, D. Töyrä, F. Travasso, G. Traylor, D. Trifirò, M. C. Tringali, L. Trozzo, M. Tse, M. Turconi, D. Tuyenbayev, D. Ugolini, C. S. Unnikrishnan, A. L. Urban, S. A. Usman, H. Vahlbruch, G. Vajente, G. Valdes, M. Vallisneri, N. van Bakel, M. van Beuzekom, J. F. J. van den Brand, C. Van Den Broeck, D. C. Vander-Hyde, L. van der Schaaf, J. V. van Heijningen,

A. A. van Veggel, M. Vardaro, S. Vass, M. Vasúth, R. Vaulin, A. Vecchio, G. Vedovato, J. Veitch, P. J. Veitch, K. Venkateswara, D. Verkindt, F. Vetrano, A. Viceré, S. Vinciguerra, D. J. Vine, J.-Y. Vinet, S. Vitale, T. Vo, H. Vocca, C. Vorvick, D. Voss, W. D. Vousden, S. P. Vyatchanin, A. R. Wade, L. E. Wade, M. Wade, S. J. Waldman, M. Walker, L. Wallace, S. Walsh, G. Wang, H. Wang, M. Wang, X. Wang, Y. Wang, H. Ward, R. L. Ward, J. Warner, M. Was, B. Weaver, L.-W. Wei, M. Weinert, A. J. Weinstein, R. Weiss, T. Welborn, L. Wen, P. Weßels, T. Westphal, K. Wette, J. T. Whelan, S. E. Whitcomb, D. J. White, B. F. Whiting, K. Wiesner, C. Wilkinson, P. A. Willems, L. Williams, R. D. Williams, A. R. Williamson, J. L. Willis, B. Willke, M. H. Wimmer, L. Winkelmann, W. Winkler, C. C. Wipf, A. G. Wiseman, H. Wittel, G. Woan, J. Worden, J. L. Wright, G. Wu, J. Yablon, I. Yakushin, W. Yam, H. Yamamoto, C. C. Yancey, M. J. Yap, H. Yu, M. Yvert, A. Zadrożny, L. Zangrando, M. Zanolin, J.-P. Zendri, M. Zevin, F. Zhang, L. Zhang, M. Zhang, Y. Zhang, C. Zhao, M. Zhou, Z. Zhou, X. J. Zhu, M. E. Zucker, S. E. Zuraw, and J. Zweizig. Observation of gravitational waves from a binary black hole merger. *Phys. Rev. Lett.*, 116:061102, Feb 2016. doi: 10.1103/PhysRevLett.116.061102. URL `http://link.aps.org/doi/10.1103/PhysRevLett.116.061102`.

[3] F. Abe, W. Allen, T. Banks, I. Bond, B. Carter, R. Dodd, M. Fujimoto, N. Yayashida, J. Hearnshaw, M. Honda, J. Jugaku, S. Kabe, M. Kobayashi, P. Kilmartin, A. Kitamura, T. Love, Y. Matsubara, M. Mityamoto, Y. Muraki, T. Nakamura, G. Pennycook, L. Pipe, M. Reid, H. Sato, S. Sato, T. Saito, M. Sekiguchi, D. Sullivan, Y. Watase, P. Yock, T. Yanagisawa, and M. Yoshizawa. The Moa Project. In R. Ferlet, J.-P. Maillard, and B. Raban, editors, *Variables Stars and the Astrophysical Returns of the Microlensing Surveys*, page 75, 1997.

[4] C. P. Ahn, R. Alexandroff, C. Allende Prieto, S. F. Anderson, T. Anderton, B. H.

Andrews, É. Aubourg, S. Bailey, E. Balbinot, R. Barnes, and et al. The Ninth Data Release of the Sloan Digital Sky Survey: First Spectroscopic Data from the SDSS-III Baryon Oscillation Spectroscopic Survey. *ApJ Suppl.*, 203:21, December 2012. doi: 10.1088/0067-0049/203/2/21.

[5] C. P. Ahn, R. Alexandroff, C. Allende Prieto, F. Anders, S. F. Anderson, T. Anderton, B. H. Andrews, É. Aubourg, S. Bailey, F. A. Bastien, and et al. The Tenth Data Release of the Sloan Digital Sky Survey: First Spectroscopic Data from the SDSS-III Apache Point Observatory Galactic Evolution Experiment. *ApJ Suppl.*, 211:17, April 2014. doi: 10.1088/0067-0049/211/2/17.

[6] H. Aihara, C. Allende Prieto, D. An, S. F. Anderson, É. Aubourg, E. Balbinot, T. C. Beers, A. A. Berlind, S. J. Bickerton, D. Bizyaev, M. R. Blanton, J. J. Bochanski, A. S. Bolton, J. Bovy, W. N. Brandt, J. Brinkmann, P. J. Brown, J. R. Brownstein, N. G. Busca, H. Campbell, M. A. Carr, Y. Chen, C. Chiappini, J. Comparat, N. Connolly, M. Cortes, R. A. C. Croft, A. J. Cuesta, L. N. da Costa, J. R. A. Davenport, K. Dawson, S. Dhital, A. Ealet, G. L. Ebelke, E. M. Edmondson, D. J. Eisenstein, S. Escoffier, M. Esposito, M. L. Evans, X. Fan, B. Femenía Castellá, A. Font-Ribera, P. M. Frinchaboy, J. Ge, B. A. Gillespie, G. Gilmore, J. I. González Hernández, J. R. Gott, A. Gould, E. K. Grebel, J. E. Gunn, J.-C. Hamilton, P. Harding, D. W. Harris, S. L. Hawley, F. R. Hearty, S. Ho, D. W. Hogg, J. A. Holtzman, K. Honscheid, N. Inada, I. I. Ivans, L. Jiang, J. A. Johnson, C. Jordan, W. P. Jordan, E. A. Kazin, D. Kirkby, M. A. Klaene, G. R. Knapp, J.-P. Kneib, C. S. Kochanek, L. Koesterke, J. A. Kollmeier, R. G. Kron, H. Lampeitl, D. Lang, J.-M. Le Goff, Y. S. Lee, Y.-T. Lin, D. C. Long, C. P. Loomis, S. Lucatello, B. Lundgren, R. H. Lupton, Z. Ma, N. MacDonald, S. Mahadevan, M. A. G. Maia, M. Makler, E. Malanushenko, V. Malanushenko, R. Mandelbaum, C. Maraston, D. Margala, K. L. Masters, C. K.

McBride, P. M. McGehee, I. D. McGreer, B. Ménard, J. Miralda-Escudé, H. L. Morrison, F. Mullally, D. Muna, J. A. Munn, H. Murayama, A. D. Myers, T. Naugle, A. F. Neto, D. C. Nguyen, R. C. Nichol, R. W. O'Connell, R. L. C. Ogando, M. D. Olmstead, D. J. Oravetz, N. Padmanabhan, N. Palanque-Delabrouille, K. Pan, P. Pandey, I. Pâris, W. J. Percival, P. Petitjean, R. Pfaffenberger, J. Pforr, S. Phleps, C. Pichon, M. M. Pieri, F. Prada, A. M. Price-Whelan, M. J. Raddick, B. H. F. Ramos, C. Reylé, J. Rich, G. T. Richards, H.-W. Rix, A. C. Robin, H. J. Rocha-Pinto, C. M. Rockosi, N. A. Roe, E. Rollinde, A. J. Ross, N. P. Ross, B. M. Rossetto, A. G. Sánchez, C. Sayres, D. J. Schlegel, K. J. Schlesinger, S. J. Schmidt, D. P. Schneider, E. Sheldon, Y. Shu, J. Simmerer, A. E. Simmons, T. Sivarani, S. A. Snedden, J. S. Sobeck, M. Steinmetz, M. A. Strauss, A. S. Szalay, M. Tanaka, A. R. Thakar, D. Thomas, J. L. Tinker, B. M. Tofflemire, R. Tojeiro, C. A. Tremonti, J. Vandenberg, M. Vargas Magaña, L. Verde, N. P. Vogt, D. A. Wake, J. Wang, B. A. Weaver, D. H. Weinberg, M. White, S. D. M. White, B. Yanny, N. Yasuda, C. Yeche, and I. Zehavi. The Eighth Data Release of the Sloan Digital Sky Survey: First Data from SDSS-III. *ApJ Suppl.*, 193:29, April 2011. doi: 10.1088/0067-0049/193/2/29.

[7] H. Aihara, C. Allende Prieto, D. An, S. F. Anderson, É. Aubourg, E. Balbinot, T. C. Beers, A. A. Berlind, S. J. Bickerton, D. Bizyaev, M. R. Blanton, J. J. Bochanski, A. S. Bolton, J. Bovy, W. N. Brandt, J. Brinkmann, P. J. Brown, J. R. Brownstein, N. G. Busca, H. Campbell, M. A. Carr, Y. Chen, C. Chiappini, J. Comparat, N. Connolly, M. Cortes, R. A. C. Croft, A. J. Cuesta, L. N. da Costa, J. R. A. Davenport, K. Dawson, S. Dhital, A. Ealet, G. L. Ebelke, E. M. Edmondson, D. J. Eisenstein, S. Escoffier, M. Esposito, M. L. Evans, X. Fan, B. Femenía Castellá, A. Font-Ribera, P. M. Frinchaboy, J. Ge, B. A. Gillespie, G. Gilmore, J. I. González Hernández, J. R. Gott, A. Gould, E. K. Grebel, J. E. Gunn, J.-C. Hamilton, P. Hard-

ing, D. W. Harris, S. L. Hawley, F. R. Hearty, S. Ho, D. W. Hogg, J. A. Holtzman, K. Honscheid, N. Inada, I. I. Ivans, L. Jiang, J. A. Johnson, C. Jordan, W. P. Jordan, E. A. Kazin, D. Kirkby, M. A. Klaene, G. R. Knapp, J.-P. Kneib, C. S. Kochanek, L. Koesterke, J. A. Kollmeier, R. G. Kron, H. Lampeitl, D. Lang, J.-M. Le Goff, Y. S. Lee, Y.-T. Lin, D. C. Long, C. P. Loomis, S. Lucatello, B. Lundgren, R. H. Lupton, Z. Ma, N. MacDonald, S. Mahadevan, M. A. G. Maia, M. Makler, E. Malanushenko, V. Malanushenko, R. Mandelbaum, C. Maraston, D. Margala, K. L. Masters, C. K. McBride, P. M. McGehee, I. D. McGreer, B. Ménard, J. Miralda-Escudé, H. L. Morrison, F. Mullally, D. Muna, J. A. Munn, H. Murayama, A. D. Myers, T. Naugle, A. F. Neto, D. C. Nguyen, R. C. Nichol, R. W. O'Connell, R. L. C. Ogando, M. D. Olmstead, D. J. Oravetz, N. Padmanabhan, N. Palanque-Delabrouille, K. Pan, P. Pandey, I. Pâris, W. J. Percival, P. Petitjean, R. Pfaffenberger, J. Pforr, S. Phleps, C. Pichon, M. M. Pieri, F. Prada, A. M. Price-Whelan, M. J. Raddick, B. H. F. Ramos, C. Reylé, J. Rich, G. T. Richards, H.-W. Rix, A. C. Robin, H. J. Rocha-Pinto, C. M. Rockosi, N. A. Roe, E. Rollinde, A. J. Ross, N. P. Ross, B. M. Rossetto, A. G. Sánchez, C. Sayres, D. J. Schlegel, K. J. Schlesinger, S. J. Schmidt, D. P. Schneider, E. Sheldon, Y. Shu, J. Simmerer, A. E. Simmons, T. Sivarani, S. A. Snedden, J. S. Sobeck, M. Steinmetz, M. A. Strauss, A. S. Szalay, M. Tanaka, A. R. Thakar, D. Thomas, J. L. Tinker, B. M. Tofflemire, R. Tojeiro, C. A. Tremonti, J. Vandenberg, M. Vargas Magaña, L. Verde, N. P. Vogt, D. A. Wake, J. Wang, B. A. Weaver, D. H. Weinberg, M. White, S. D. M. White, B. Yanny, N. Yasuda, C. Yeche, and I. Zehavi. The Eighth Data Release of the Sloan Digital Sky Survey: First Data from SDSS-III. *ApJ Suppl.*, 193:29, April 2011. doi: 10.1088/0067-0049/193/2/29.

[8] S. Alam, F. D. Albareti, C. Allende Prieto, F. Anders, S. F. Anderson, T. Anderton, B. H. Andrews, E. Armengaud, É. Aubourg, S. Bailey, and et al. The Eleventh and

Twelfth Data Releases of the Sloan Digital Sky Survey: Final Data from SDSS-III. *ApJ Suppl.*, 219:12, July 2015. doi: 10.1088/0067-0049/219/1/12.

[9] S. Alam, F. D. Albareti, C. Allende Prieto, F. Anders, S. F. Anderson, T. Anderton, B. H. Andrews, E. Armengaud, É. Aubourg, S. Bailey, and et al. The Eleventh and Twelfth Data Releases of the Sloan Digital Sky Survey: Final Data from SDSS-III. *ApJ Suppl.*, 219:12, July 2015. doi: 10.1088/0067-0049/219/1/12.

[10] S. Alam, S. Ho, and A. Silvestri. Testing deviations from ΛCDM with growth rate measurements from 6 Large Scale Structure Surveys at $z = 0.06$ to 1. *ArXiv e-prints*, September 2015.

[11] S. Alam, S. Ho, M. Vargas-Magaña, and D. P. Schneider. Testing general relativity with growth rate measurement from Sloan Digital Sky Survey - III. Baryon Oscillations Spectroscopic Survey galaxies. *MNRAS*, 453:1754–1767, October 2015. doi: 10.1093/mnras/stv1737.

[12] S. Alam, S. Ho, M. Vargas-Magaña, and D. P. Schneider. Testing general relativity with growth rate measurement from Sloan Digital Sky Survey - III. Baryon Oscillations Spectroscopic Survey galaxies. *MNRAS*, 453:1754–1767, October 2015. doi: 10.1093/mnras/stv1737.

[13] S. Alam, R. A. C. Croft, S. Ho, H. Zhu, and Giusarma E. GZTS paper. *xxx*, pages xx–xx, 2016. doi: xxxx.

[14] S. Alam, S. Ho, and A. Silvestri. Testing deviations from ΛCDM with growth rate measurements from six large-scale structure surveys at $z = 0.06$-1. *MNRAS*, 456: 3743–3756, March 2016. doi: 10.1093/mnras/stv2935.

[15] S. Alam, H. Zhu, R. A. C. Croft, S. Ho, and Giusarma E. GZMeasurement paper. *xxx*, pages xx–xx, 2016. doi: xxxx.

[16] C. Alcock and B. Paczynski. An evolution free test for non-zero cosmological constant. *Nature*, 281:358, October 1979. doi: 10.1038/281358a0.

[17] L. Amendola, S. Appleby, D. Bacon, T. Baker, M. Baldi, N. Bartolo, A. Blanchard, C. Bonvin, S. Borgani, E. Branchini, C. Burrage, S. Camera, C. Carbone, L. Casarini, M. Cropper, C. de Rham, C. Di Porto, A. Ealet, P. G. Ferreira, F. Finelli, J. García-Bellido, T. Giannantonio, L. Guzzo, A. Heavens, L. Heisenberg, C. Heymans, H. Hoekstra, L. Hollenstein, R. Holmes, O. Horst, K. Jahnke, T. D. Kitching, T. Koivisto, M. Kunz, G. La Vacca, M. March, E. Majerotto, K. Markovic, D. Marsh, F. Marulli, R. Massey, Y. Mellier, D. F. Mota, N. Nunes, W. Percival, V. Pettorino, C. Porciani, C. Quercellini, J. Read, M. Rinaldi, D. Sapone, R. Scaramella, C. Skordis, F. Simpson, A. Taylor, S. Thomas, R. Trotta, L. Verde, F. Vernizzi, A. Vollmer, Y. Wang, J. Weller, and T. Zlosnik. Cosmology and Fundamental Physics with the Euclid Satellite. *Living Reviews in Relativity*, 16:6, September 2013. doi: 10.12942/lrr-2013-6.

[18] L. Amendola, M. Kunz, M. Motta, I. D. Saltas, and I. Sawicki. Observables and unobservables in dark energy cosmologies. *Phys. Rev. D*, 87(2):023501, January 2013. doi: 10.1103/PhysRevD.87.023501.

[19] E. Anderson. The Problem of Time in Quantum Gravity. *ArXiv e-prints*, September 2010.

[20] L. Anderson, É. Aubourg, S. Bailey, F. Beutler, V. Bhardwaj, M. Blanton, A. S. Bolton, J. Brinkmann, J. R. Brownstein, A. Burden, C.-H. Chuang, A. J. Cuesta,

K. S. Dawson, D. J. Eisenstein, S. Escoffier, J. E. Gunn, H. Guo, S. Ho, K. Honscheid, C. Howlett, D. Kirkby, R. H. Lupton, M. Manera, C. Maraston, C. K. McBride, O. Mena, F. Montesano, R. C. Nichol, S. E. Nuza, M. D. Olmstead, N. Padmanabhan, N. Palanque-Delabrouille, J. Parejko, W. J. Percival, P. Petitjean, F. Prada, A. M. Price-Whelan, B. Reid, N. A. Roe, A. J. Ross, N. P. Ross, C. G. Sabiu, S. Saito, L. Samushia, A. G. Sánchez, D. J. Schlegel, D. P. Schneider, C. G. Scoccola, H.-J. Seo, R. A. Skibba, M. A. Strauss, M. E. C. Swanson, D. Thomas, J. L. Tinker, R. Tojeiro, M. V. Magaña, L. Verde, D. A. Wake, B. A. Weaver, D. H. Weinberg, M. White, X. Xu, C. Yèche, I. Zehavi, and G.-B. Zhao. The clustering of galaxies in the SDSS-III Baryon Oscillation Spectroscopic Survey: baryon acoustic oscillations in the Data Releases 10 and 11 Galaxy samples. *MNRAS*, 441:24–62, June 2014. doi: 10.1093/mnras/stu523.

[21] L. Anderson, É. Aubourg, S. Bailey, F. Beutler, V. Bhardwaj, M. Blanton, A. S. Bolton, J. Brinkmann, J. R. Brownstein, A. Burden, C.-H. Chuang, A. J. Cuesta, K. S. Dawson, D. J. Eisenstein, S. Escoffier, J. E. Gunn, H. Guo, S. Ho, K. Honscheid, C. Howlett, D. Kirkby, R. H. Lupton, M. Manera, C. Maraston, C. K. McBride, O. Mena, F. Montesano, R. C. Nichol, S. E. Nuza, M. D. Olmstead, N. Padmanabhan, N. Palanque-Delabrouille, J. Parejko, W. J. Percival, P. Petitjean, F. Prada, A. M. Price-Whelan, B. Reid, N. A. Roe, A. J. Ross, N. P. Ross, C. G. Sabiu, S. Saito, L. Samushia, A. G. Sánchez, D. J. Schlegel, D. P. Schneider, C. G. Scoccola, H.-J. Seo, R. A. Skibba, M. A. Strauss, M. E. C. Swanson, D. Thomas, J. L. Tinker, R. Tojeiro, M. V. Magaña, L. Verde, D. A. Wake, B. A. Weaver, D. H. Weinberg, M. White, X. Xu, C. Yèche, I. Zehavi, and G.-B. Zhao. The clustering of galaxies in the SDSS-III Baryon Oscillation Spectroscopic Survey: baryon acoustic oscillations in the Data Releases 10 and 11 Galaxy samples. *MNRAS*, 441:24–62,

243

June 2014. doi: 10.1093/mnras/stu523.

[22] L. Anderson, É. Aubourg, S. Bailey, F. Beutler, V. Bhardwaj, M. Blanton, A. S. Bolton, J. Brinkmann, J. R. Brownstein, A. Burden, C.-H. Chuang, A. J. Cuesta, K. S. Dawson, D. J. Eisenstein, S. Escoffier, J. E. Gunn, H. Guo, S. Ho, K. Honscheid, C. Howlett, D. Kirkby, R. H. Lupton, M. Manera, C. Maraston, C. K. McBride, O. Mena, F. Montesano, R. C. Nichol, S. E. Nuza, M. D. Olmstead, N. Padmanabhan, N. Palanque-Delabrouille, J. Parejko, W. J. Percival, P. Petitjean, F. Prada, A. M. Price-Whelan, B. Reid, N. A. Roe, A. J. Ross, N. P. Ross, C. G. Sabiu, S. Saito, L. Samushia, A. G. Sánchez, D. J. Schlegel, D. P. Schneider, C. G. Scoccola, H.-J. Seo, R. A. Skibba, M. A. Strauss, M. E. C. Swanson, D. Thomas, J. L. Tinker, R. Tojeiro, M. V. Magaña, L. Verde, D. A. Wake, B. A. Weaver, D. H. Weinberg, M. White, X. Xu, C. Yèche, I. Zehavi, and G.-B. Zhao. The clustering of galaxies in the SDSS-III Baryon Oscillation Spectroscopic Survey: baryon acoustic oscillations in the Data Releases 10 and 11 Galaxy samples. *MNRAS*, 441:24–62, June 2014. doi: 10.1093/mnras/stu523.

[23] L. Anderson, E. Aubourg, S. Bailey, F. Beutler, A. S. Bolton, J. Brinkmann, J. R. Brownstein, C.-H. Chuang, A. J. Cuesta, K. S. Dawson, D. J. Eisenstein, S. Ho, K. Honscheid, E. A. Kazin, D. Kirkby, M. Manera, C. K. McBride, O. Mena, R. C. Nichol, M. D. Olmstead, N. Padmanabhan, N. Palanque-Delabrouille, W. J. Percival, F. Prada, A. J. Ross, N. P. Ross, A. G. Sánchez, L. Samushia, D. J. Schlegel, D. P. Schneider, H.-J. Seo, M. A. Strauss, D. Thomas, J. L. Tinker, R. Tojeiro, L. Verde, D. Wake, D. H. Weinberg, X. Xu, and C. Yeche. The clustering of galaxies in the SDSS-III Baryon Oscillation Spectroscopic Survey: measuring D_A and H at z = 0.57 from the baryon acoustic peak in the Data Release 9 spectroscopic Galaxy sample. *MNRAS*, 439:83–101, March 2014. doi: 10.1093/mnras/stt2206.

[24] L. Anderson, E. Aubourg, S. Bailey, F. Beutler, A. S. Bolton, J. Brinkmann, J. R. Brownstein, C.-H. Chuang, A. J. Cuesta, K. S. Dawson, D. J. Eisenstein, S. Ho, K. Honscheid, E. A. Kazin, D. Kirkby, M. Manera, C. K. McBride, O. Mena, R. C. Nichol, M. D. Olmstead, N. Padmanabhan, N. Palanque-Delabrouille, W. J. Percival, F. Prada, A. J. Ross, N. P. Ross, A. G. Sánchez, L. Samushia, D. J. Schlegel, D. P. Schneider, H.-J. Seo, M. A. Strauss, D. Thomas, J. L. Tinker, R. Tojeiro, L. Verde, D. Wake, D. H. Weinberg, X. Xu, and C. Yeche. The clustering of galaxies in the SDSS-III Baryon Oscillation Spectroscopic Survey: measuring D_A and H at z = 0.57 from the baryon acoustic peak in the Data Release 9 spectroscopic Galaxy sample. *MNRAS*, 439:83–101, March 2014. doi: 10.1093/mnras/stt2206.

[25] M. Arnaud, E. Aubourg, P. Bareyre, S. Brehin, R. Caridroit, J. de Kat, G. Dispau, K. Djidi, M. Gros, and M. Lachieze-Rey. A 20 sq CM CCD mosaic camera for a dark matter search. Part 1: Mechanics, optics and cryogeny. *Experimental Astronomy*, 4: 265–278, September 1994. doi: 10.1007/BF01580786.

[26] J. Asorey, M. Crocce, and E. Gaztañaga. Redshift-space distortions from the cross-correlation of photometric populations. *MNRAS*, 445:2825–2835, December 2014. doi: 10.1093/mnras/stu1955.

[27] É. Aubourg, S. Bailey, J. E. Bautista, F. Beutler, V. Bhardwaj, D. Bizyaev, M. Blanton, M. Blomqvist, A. S. Bolton, J. Bovy, H. Brewington, J. Brinkmann, J. R. Brownstein, A. Burden, N. G. Busca, W. Carithers, C.-H. Chuang, J. Comparat, R. A. C. Croft, A. J. Cuesta, K. S. Dawson, T. Delubac, D. J. Eisenstein, A. Font-Ribera, J. Ge, J.-M. Le Goff, S. G. A. Gontcho, J. R. Gott, J. E. Gunn, H. Guo, J. Guy, J.-C. Hamilton, S. Ho, K. Honscheid, C. Howlett, D. Kirkby, F. S. Kitaura, J.-P. Kneib, K.-G. Lee, D. Long, R. H. Lupton, M. V. Magaña, V. Malanushenko, E. Malanushenko, M. Manera, C. Maraston, D. Margala, C. K. McBride, J. Miralda-

Escudé, A. D. Myers, R. C. Nichol, P. Noterdaeme, S. E. Nuza, M. D. Olmstead, D. Oravetz, I. Pâris, N. Padmanabhan, N. Palanque-Delabrouille, K. Pan, M. Pellejero-Ibanez, W. J. Percival, P. Petitjean, M. M. Pieri, F. Prada, B. Reid, J. Rich, N. A. Roe, A. J. Ross, N. P. Ross, G. Rossi, J. A. Rubiño-Martín, A. G. Sánchez, L. Samushia, R. T. G. Santos, C. G. Scóccola, D. J. Schlegel, D. P. Schneider, H.-J. Seo, E. Sheldon, A. Simmons, R. A. Skibba, A. Slosar, M. A. Strauss, D. Thomas, J. L. Tinker, R. Tojeiro, J. A. Vazquez, M. Viel, D. A. Wake, B. A. Weaver, D. H. Weinberg, W. M. Wood-Vasey, C. Yèche, I. Zehavi, G.-B. Zhao, and BOSS Collaboration. Cosmological implications of baryon acoustic oscillation measurements. *Phys. Rev. D*, 92(12):123516, December 2015. doi: 10.1103/PhysRevD.92.123516.

[28] D. J. Bacon, S. Andrianomena, C. Clarkson, K. Bolejko, and R. Maartens. Cosmology with Doppler lensing. *MNRAS*, 443:1900–1915, September 2014. doi: 10.1093/mnras/stu1270.

[29] J. S. Bagla. TreePM: A Code for Cosmological N-Body Simulations. *Journal of Astrophysics and Astronomy*, 23:185–196, December 2002. doi: 10.1007/BF02702282.

[30] J. S. Bagla. TreePM: A Code for Cosmological N-Body Simulations. *Journal of Astrophysics and Astronomy*, 23:185–196, December 2002. doi: 10.1007/BF02702282.

[31] T. Baldauf, R. E. Smith, U. Seljak, and R. Mandelbaum. Algorithm for the direct reconstruction of the dark matter correlation function from weak lensing and galaxy clustering. *Phys. Rev. D*, 81(6):063531, March 2010. doi: 10.1103/PhysRevD.81.063531.

[32] J. M. Bardeen, J. R. Bond, N. Kaiser, and A. S. Szalay. The statistics of peaks of Gaussian random fields. *ApJ*, 304:15–61, May 1986. doi: 10.1086/164143.

[33] M. Bartelmann and P. Schneider. Weak gravitational lensing. *Physics Reports*, 340: 291–472, January 2001. doi: 10.1016/S0370-1573(00)00082-X.

[34] B. Bassett and R. Hlozek. *Baryon acoustic oscillations*, page 246. 2010.

[35] F. Bauer and J. de Kat. The two EROS 4k X 8k CCD Mosaic Cameras. In J. Beletic and P. Amico, editors, *Optical Detectors for Astronomy*, volume 228 of *Astrophysics and Space Science Library*, page 191, 1998. doi: 10.1007/978-94-011-5262-4_29.

[36] R. H. Becker, X. Fan, R. L. White, M. A. Strauss, V. K. Narayanan, R. H. Lupton, J. E. Gunn, J. Annis, N. A. Bahcall, J. Brinkmann, A. J. Connolly, I. Csabai, P. C. Czarapata, M. Doi, T. M. Heckman, G. S. Hennessy, Ž. Ivezić, G. R. Knapp, D. Q. Lamb, T. A. McKay, J. A. Munn, T. Nash, R. Nichol, J. R. Pier, G. T. Richards, D. P. Schneider, C. Stoughton, A. S. Szalay, A. R. Thakar, and D. G. York. Evidence for Reionization at z~6: Detection of a Gunn-Peterson Trough in a z=6.28 Quasar. *AJ*, 122:2850–2857, December 2001. doi: 10.1086/324231.

[37] J. Bel, P. Brax, C. Marinoni, and P. Valageas. Cosmological tests of modified gravity: Constraints on F (R) theories from the galaxy clustering ratio. *Phys. Rev. D*, 91(10): 103503, May 2015. doi: 10.1103/PhysRevD.91.103503.

[38] J. Beletic and P. Amico, editors. *Optical detectors for astronomy*, volume 228 of *Astrophysics and Space Science Library*, 1998. doi: 10.1007/978-94-011-5262-4.

[39] C. L. Bennett, D. Larson, J. L. Weiland, N. Jarosik, G. Hinshaw, N. Odegard, K. M. Smith, R. S. Hill, B. Gold, M. Halpern, E. Komatsu, M. R. Nolta, L. Page, D. N. Spergel, E. Wollack, J. Dunkley, A. Kogut, M. Limon, S. S. Meyer, G. S. Tucker,

and E. L. Wright. Nine-year Wilkinson Microwave Anisotropy Probe (WMAP) Observations: Final Maps and Results. *ApJ Suppl.*, 208:20, October 2013. doi: 10.1088/0067-0049/208/2/20.

[40] C. L. Bennett, D. Larson, J. L. Weiland, N. Jarosik, G. Hinshaw, N. Odegard, K. M. Smith, R. S. Hill, B. Gold, M. Halpern, E. Komatsu, M. R. Nolta, L. Page, D. N. Spergel, E. Wollack, J. Dunkley, A. Kogut, M. Limon, S. S. Meyer, G. S. Tucker, and E. L. Wright. Nine-year Wilkinson Microwave Anisotropy Probe (WMAP) Observations: Final Maps and Results. *ApJ Suppl.*, 208:20, October 2013. doi: 10.1088/0067-0049/208/2/20.

[41] A. J. Benson, S. Cole, C. S. Frenk, C. M. Baugh, and C. G. Lacey. The nature of galaxy bias and clustering. *MNRAS*, 311:793–808, February 2000. doi: 10.1046/j. 1365-8711.2000.03101.x.

[42] A. A. Berlind and D. H. Weinberg. The Halo Occupation Distribution: Toward an Empirical Determination of the Relation between Galaxies and Mass. *ApJ*, 575: 587–616, August 2002. doi: 10.1086/341469.

[43] F. Bernardeau, S. Colombi, E. Gaztañaga, and R. Scoccimarro. Large-scale structure of the Universe and cosmological perturbation theory. *Physics Reports*, 367:1–248, September 2002. doi: 10.1016/S0370-1573(02)00135-7.

[44] M. Bersanelli, N. Mandolesi, R. C. Butler, A. Mennella, F. Villa, B. Aja, E. Artal, E. Artina, C. Baccigalupi, M. Balasini, G. Baldan, A. Banday, P. Bastia, P. Battaglia, T. Bernardino, E. Blackhurst, L. Boschini, C. Burigana, G. Cafagna, B. Cappellini, F. Cavaliere, F. Colombo, G. Crone, F. Cuttaia, O. D'Arcangelo, L. Danese, R. D. Davies, R. J. Davis, L. de Angelis, G. C. de Gasperis, L. de

La Fuente, A. de Rosa, G. de Zotti, M. C. Falvella, F. Ferrari, R. Ferretti, L. Figini, S. Fogliani, C. Franceschet, E. Franceschi, T. Gaier, S. Garavaglia, F. Gomez, K. Gorski, A. Gregorio, P. Guzzi, J. M. Herreros, S. R. Hildebrandt, R. Hoyland, N. Hughes, M. Janssen, P. Jukkala, D. Kettle, V. H. Kilpiä, M. Laaninen, P. M. Lapolla, C. R. Lawrence, D. Lawson, J. P. Leahy, R. Leonardi, P. Leutenegger, S. Levin, P. B. Lilje, S. R. Lowe, P. M. Lubin, D. Maino, M. Malaspina, M. Maris, J. Marti-Canales, E. Martinez-Gonzalez, A. Mediavilla, P. Meinhold, M. Miccolis, G. Morgante, P. Natoli, R. Nesti, L. Pagan, C. Paine, B. Partridge, J. P. Pascual, F. Pasian, D. Pearson, M. Pecora, F. Perrotta, P. Platania, M. Pospieszalski, T. Poutanen, M. Prina, R. Rebolo, N. Roddis, J. A. Rubiño-Martin, M. J. Salmon, M. Sandri, M. Seiffert, R. Silvestri, A. Simonetto, P. Sjoman, G. F. Smoot, C. Sozzi, L. Stringhetti, E. Taddei, J. Tauber, L. Terenzi, M. Tomasi, J. Tuovinen, L. Valenziano, J. Varis, N. Vittorio, L. A. Wade, A. Wilkinson, F. Winder, A. Zacchei, and A. Zonca. Planck pre-launch status: Design and description of the Low Frequency Instrument. *A&A*, 520:A4, September 2010. doi: 10.1051/0004-6361/200912853.

[45] E. Bertschinger and P. Zukin. Distinguishing modified gravity from dark energy. *Phys. Rev. D*, 78(2):024015, July 2008. doi: 10.1103/PhysRevD.78.024015.

[46] E. Bertschinger and P. Zukin. Distinguishing modified gravity from dark energy. *Phys. Rev. D*, 78(2):024015, July 2008. doi: 10.1103/PhysRevD.78.024015.

[47] F. Beutler, C. Blake, M. Colless, D. H. Jones, L. Staveley-Smith, G. B. Poole, L. Campbell, Q. Parker, W. Saunders, and F. Watson. The 6dF Galaxy Survey: z$\approx$ 0 measurements of the growth rate and σ_8. *MNRAS*, 423:3430–3444, July 2012. doi: 10.1111/j.1365-2966.2012.21136.x.

[48] F. Beutler, S. Saito, H.-J. Seo, J. Brinkmann, K. S. Dawson, D. J. Eisenstein, A. Font-

Ribera, S. Ho, C. K. McBride, F. Montesano, W. J. Percival, A. J. Ross, N. P. Ross, L. Samushia, D. J. Schlegel, A. G. Sánchez, J. L. Tinker, and B. A. Weaver. The clustering of galaxies in the SDSS-III Baryon Oscillation Spectroscopic Survey: testing gravity with redshift space distortions using the power spectrum multipoles. *MNRAS*, 443:1065–1089, September 2014. doi: 10.1093/mnras/stu1051.

[49] F. Beutler, S. Saito, H.-J. Seo, J. Brinkmann, K. S. Dawson, D. J. Eisenstein, A. Font-Ribera, S. Ho, C. K. McBride, F. Montesano, W. J. Percival, A. J. Ross, N. P. Ross, L. Samushia, D. J. Schlegel, A. G. Sánchez, J. L. Tinker, and B. A. Weaver. The clustering of galaxies in the SDSS-III Baryon Oscillation Spectroscopic Survey: testing gravity with redshift space distortions using the power spectrum multipoles. *MNRAS*, 443:1065–1089, September 2014. doi: 10.1093/mnras/stu1051.

[50] D. Bianchi, M. Chiesa, and L. Guzzo. Improving the modelling of redshift-space distortions - I. A bivariate Gaussian description for the galaxy pairwise velocity distributions. *MNRAS*, 446:75–84, January 2015. doi: 10.1093/mnras/stu2080.

[51] F. Bianchini, P. Bielewicz, A. Lapi, J. Gonzalez-Nuevo, C. Baccigalupi, G. de Zotti, L. Danese, N. Bourne, A. Cooray, L. Dunne, S. Dye, S. Eales, R. Ivison, S. Maddox, M. Negrello, D. Scott, M. W. L. Smith, and E. Valiante. Cross-correlation between the CMB Lensing Potential Measured by Planck and High-z Submillimeter Galaxies Detected by the Herschel-Atlas Survey. *ApJ*, 802:64, March 2015. doi: 10.1088/0004-637X/802/1/64.

[52] F. Bianchini, A. Lapi, M. Calabrese, P. Bielewicz, J. Gonzalez-Nuevo, C. Baccigalupi, L. Danese, G. de Zotti, N. Bourne, A. Cooray, L. Dunne, and S. Eales. Toward a tomographic analysis of the cross-correlation between Planck CMB lensing and H-ATLAS galaxies. *ArXiv e-prints*, November 2015.

[53] C. Blake, S. Brough, M. Colless, C. Contreras, W. Couch, S. Croom, T. Davis, M. J. Drinkwater, K. Forster, D. Gilbank, M. Gladders, K. Glazebrook, B. Jelliffe, R. J. Jurek, I.-H. Li, B. Madore, D. C. Martin, K. Pimbblet, G. B. Poole, M. Pracy, R. Sharp, E. Wisnioski, D. Woods, T. K. Wyder, and H. K. C. Yee. The WiggleZ Dark Energy Survey: the growth rate of cosmic structure since redshift z=0.9. *MNRAS*, 415: 2876–2891, August 2011. doi: 10.1111/j.1365-2966.2011.18903.x.

[54] C. Blake, E. A. Kazin, F. Beutler, T. M. Davis, D. Parkinson, S. Brough, M. Colless, C. Contreras, W. Couch, S. Croom, D. Croton, M. J. Drinkwater, K. Forster, D. Gilbank, M. Gladders, K. Glazebrook, B. Jelliffe, R. J. Jurek, I.-H. Li, B. Madore, D. C. Martin, K. Pimbblet, G. B. Poole, M. Pracy, R. Sharp, E. Wisnioski, D. Woods, T. K. Wyder, and H. K. C. Yee. The WiggleZ Dark Energy Survey: mapping the distance-redshift relation with baryon acoustic oscillations. *MNRAS*, 418:1707– 1724, December 2011. doi: 10.1111/j.1365-2966.2011.19592.x.

[55] C. Blake, S. Joudaki, C. Heymans, A. Choi, T. Erben, J. Harnois-Deraps, H. Hildebrandt, B. Joachimi, R. Nakajima, L. van Waerbeke, and M. Viola. RCSLenS: Testing gravitational physics through the cross-correlation of weak lensing and large-scale structure. *ArXiv e-prints*, July 2015.

[56] C. Blake, S. Joudaki, C. Heymans, A. Choi, T. Erben, J. Harnois-Deraps, H. Hildebrandt, B. Joachimi, R. Nakajima, L. van Waerbeke, and M. Viola. RCSLenS: Testing gravitational physics through the cross-correlation of weak lensing and large-scale structure. *ArXiv e-prints*, July 2015.

[57] A. Blanchard and J. Schneider. Gravitational lensing effect on the fluctuations of the cosmic background radiation. *A&A*, 184:1–6, October 1987.

[58] M. R. Blanton, J. Brinkmann, I. Csabai, M. Doi, D. Eisenstein, M. Fukugita, J. E.

251

Gunn, D. W. Hogg, and D. J. Schlegel. Estimating Fixed-Frame Galaxy Magnitudes in the Sloan Digital Sky Survey. *AJ*, 125:2348–2360, May 2003. doi: 10.1086/342935.

[59] M. R. Blanton, H. Lin, R. H. Lupton, F. M. Maley, N. Young, I. Zehavi, and J. Loveday. An Efficient Targeting Strategy for Multiobject Spectrograph Surveys: the Sloan Digital Sky Survey "Tiling" Algorithm. *AJ*, 125:2276–2286, April 2003. doi: 10.1086/344761.

[60] M. R. Blanton, H. Lin, R. H. Lupton, F. M. Maley, N. Young, I. Zehavi, and J. Loveday. An Efficient Targeting Strategy for Multiobject Spectrograph Surveys: the Sloan Digital Sky Survey "Tiling" Algorithm. *AJ*, 125:2276–2286, April 2003. doi: 10.1086/344761.

[61] M. R. Blanton, H. Lin, R. H. Lupton, F. M. Maley, N. Young, I. Zehavi, and J. Loveday. An Efficient Targeting Strategy for Multiobject Spectrograph Surveys: the Sloan Digital Sky Survey "Tiling" Algorithm. *AJ*, 125:2276–2286, April 2003. doi: 10.1086/344761.

[62] J. Blazek, R. Mandelbaum, U. Seljak, and R. Nakajima. Separating intrinsic alignment and galaxy-galaxy lensing. *JCAP*, 5:041, May 2012. doi: 10.1088/1475-7516/2012/05/041.

[63] J. Blazek, Z. Vlah, and U. Seljak. Tidal alignment of galaxies. *JCAP*, 8:015, August 2015. doi: 10.1088/1475-7516/2015/08/015.

[64] J. Bock and SPHEREx Science Team. SPHEREx: An All-Sky Spectral Survey. In *American Astronomical Society Meeting Abstracts*, volume 227 of *American Astronomical Society Meeting Abstracts*, page 147.01, January 2016.

[65] A. S. Bolton, D. J. Schlegel, É. Aubourg, S. Bailey, V. Bhardwaj, J. R. Brownstein, S. Burles, Y.-M. Chen, K. Dawson, D. J. Eisenstein, J. E. Gunn, G. R. Knapp, C. P. Loomis, R. H. Lupton, C. Maraston, D. Muna, A. D. Myers, M. D. Olmstead, N. Padmanabhan, I. Pâris, W. J. Percival, P. Petitjean, C. M. Rockosi, N. P. Ross, D. P. Schneider, Y. Shu, M. A. Strauss, D. Thomas, C. A. Tremonti, D. A. Wake, B. A. Weaver, and W. M. Wood-Vasey. Spectral Classification and Redshift Measurement for the SDSS-III Baryon Oscillation Spectroscopic Survey. *AJ*, 144:144, November 2012. doi: 10.1088/0004-6256/144/5/144.

[66] C. Bonvin. Isolating relativistic effects in large-scale structure. *Classical and Quantum Gravity*, 31(23):234002, December 2014. doi: 10.1088/0264-9381/31/23/234002.

[67] C. Bonvin, L. Hui, and E. Gaztañaga. Asymmetric galaxy correlation functions. *Phys. Rev. D*, 89(8):083535, April 2014. doi: 10.1103/PhysRevD.89.083535.

[68] O. Boulade. Wide Field Imaging at CFHT: the MEGACAM Project. In J. Beletic and P. Amico, editors, *Optical Detectors for Astronomy*, volume 228 of *Astrophysics and Space Science Library*, page 203, 1998. doi: 10.1007/978-94-011-5262-4_30.

[69] M. Bruni and D. H. Lyth. Peculiar velocity, cosmic perturbation theory and the cosmic microwave background anisotropy. *Physics Letters B*, 323:118–123, March 1994. doi: 10.1016/0370-2693(94)90279-8.

[70] M. Cacciato, F. C. van den Bosch, S. More, H. Mo, and X. Yang. Cosmological constraints from a combination of galaxy clustering and lensing - III. Application to SDSS data. *MNRAS*, 430:767–786, April 2013. doi: 10.1093/mnras/sts525.

[71] A. Cappi. Gravitational redshift in galaxy clusters. *A&A*, 301:6, September 1995.

[72] J. Carlson, B. Reid, and M. White. Convolution Lagrangian perturbation theory for biased tracers. *MNRAS*, 429:1674–1685, February 2013. doi: 10.1093/mnras/sts457.

[73] S. M. Carroll. The Cosmological Constant. *Living Reviews in Relativity*, 4:1, February 2001. doi: 10.12942/lrr-2001-1.

[74] S. M. Carroll, V. Duvvuri, M. Trodden, and M. S. Turner. Is cosmic speed-up due to new gravitational physics? *Phys. Rev. D*, 70(4):043528, August 2004. doi: 10.1103/PhysRevD.70.043528.

[75] M. Cataneo, D. Rapetti, F. Schmidt, A. B. Mantz, S. W. Allen, D. E. Applegate, P. L. Kelly, A. von der Linden, and R. G. Morris. New constraints on f (R) gravity from clusters of galaxies. *Phys. Rev. D*, 92(4):044009, August 2015. doi: 10.1103/PhysRevD.92.044009.

[76] M. Chevallier and D. Polarski. Accelerating Universes with Scaling Dark Matter. *International Journal of Modern Physics D*, 10:213–223, 2001. doi: 10.1142/S0218271801000822.

[77] C.-H. Chuang, F. Prada, F. Beutler, D. J. Eisenstein, S. Escoffier, S. Ho, J.-P. Kneib, M. Manera, S. E. Nuza, D. J. Schlegel, D. P. Schneider, B. A. Weaver, J. R. Brownstein, K. S. Dawson, C. Maraston, and D. Thomas. The clustering of galaxies in the SDSS-III Baryon Oscillation Spectroscopic Survey: single-probe measurements from CMASS and LOWZ anisotropic galaxy clustering. *ArXiv e-prints*, December 2013.

[78] G. M. Clemence. The Relativity Effect in Planetary Motions. *Reviews of Modern Physics*, 19:361–364, October 1947. doi: 10.1103/RevModPhys.19.361.

[79] T. Clifton, P. G. Ferreira, A. Padilla, and C. Skordis. Modified gravity and cosmology. *Physics Reports*, 513:1–189, March 2012. doi: 10.1016/j.physrep.2012.01.001.

[80] A. L. Coil. *The Large-Scale Structure of the Universe*, page 387. 2013. doi: 10.1007/978-94-007-5609-0_8.

[81] J. W. Colbert, H. Teplitz, H. Atek, A. Bunker, M. Rafelski, N. Ross, C. Scarlata, A. G. Bedregal, A. Dominguez, A. Dressler, A. Henry, M. Malkan, C. L. Martin, D. Masters, P. McCarthy, and B. Siana. Predicting Future Space Near-IR Grism Surveys Using the WFC3 Infrared Spectroscopic Parallels Survey. *ApJ*, 779:34, December 2013. doi: 10.1088/0004-637X/779/1/34.

[82] S. Cole and G. Efstathiou. Gravitational lensing of fluctuations in the microwave background radiation. *MNRAS*, 239:195–200, July 1989.

[83] S. Cole and N. Kaiser. Biased clustering in the cold dark matter cosmogony. *MNRAS*, 237:1127–1146, April 1989. doi: 10.1093/mnras/237.4.1127.

[84] S. Cole, K. B. Fisher, and D. H. Weinberg. Constraints on Omega from the IRAS redshift surveys. *MNRAS*, 275:515–526, July 1995.

[85] S. Cole, W. J. Percival, J. A. Peacock, P. Norberg, C. M. Baugh, C. S. Frenk, I. Baldry, J. Bland-Hawthorn, T. Bridges, R. Cannon, M. Colless, C. Collins, W. Couch, N. J. G. Cross, G. Dalton, V. R. Eke, R. De Propris, S. P. Driver, G. Efstathiou, R. S. Ellis, K. Glazebrook, C. Jackson, A. Jenkins, O. Lahav, I. Lewis, S. Lumsden, S. Maddox, D. Madgwick, B. A. Peterson, W. Sutherland, and K. Taylor. The 2dF Galaxy Redshift Survey: power-spectrum analysis of the final data set and cosmological implications. *MNRAS*, 362:505–534, September 2005. doi: 10.1111/j.1365-2966.2005.09318.x.

[86] M. Colless, B. A. Peterson, C. Jackson, J. A. Peacock, S. Cole, P. Norberg, I. K. Baldry, C. M. Baugh, J. Bland-Hawthorn, T. Bridges, R. Cannon, C. Collins, W. Couch, N. Cross, G. Dalton, R. De Propris, S. P. Driver, G. Efstathiou, R. S. Ellis, C. S. Frenk, K. Glazebrook, O. Lahav, I. Lewis, S. Lumsden, S. Maddox, D. Madgwick, W. Sutherland, and K. Taylor. The 2dF Galaxy Redshift Survey: Final Data Release. *ArXiv Astrophysics e-prints*, June 2003.

[87] G. L. Comer, N. Deruelle, D. Langlois, and J. Parry. Growth or decay of cosmological inhomogeneities as a function of their equation of state. *Phys. Rev. D*, 49: 2759–2768, March 1994. doi: 10.1103/PhysRevD.49.2759.

[88] A. Conley, J. Guy, M. Sullivan, N. Regnault, P. Astier, C. Balland, S. Basa, R. G. Carlberg, D. Fouchez, D. Hardin, I. M. Hook, D. A. Howell, R. Pain, N. Palanque-Delabrouille, K. M. Perrett, C. J. Pritchet, J. Rich, V. Ruhlmann-Kleider, D. Balam, S. Baumont, R. S. Ellis, S. Fabbro, H. K. Fakhouri, N. Fourmanoit, S. González-Gaitán, M. L. Graham, M. J. Hudson, E. Hsiao, T. Kronborg, C. Lidman, A. M. Mourao, J. D. Neill, S. Perlmutter, P. Ripoche, N. Suzuki, and E. S. Walker. Supernova Constraints and Systematic Uncertainties from the First Three Years of the Supernova Legacy Survey. *ApJ Suppl.*, 192:1, January 2011. doi: 10.1088/0067-0049/192/1/1.

[89] R. Content, R. M. Sharples, S. Blake, and R. G. Talbot. EUCLID: design of the prism DMD NIR spectrograph. In *Space Telescopes and Instrumentation 2010: Optical, Infrared, and Millimeter Wave*, volume 7731 of *Proceedings of the SPIE*, page 77312Y, July 2010. doi: 10.1117/12.857937.

[90] A. Cooray and R. Sheth. Halo models of large scale structure. *Physics Reports*, 372: 1–129, December 2002. doi: 10.1016/S0370-1573(02)00276-4.

[91] A. Cooray and R. Sheth. Halo models of large scale structure. *Physics Reports*, 372: 1–129, December 2002. doi: 10.1016/S0370-1573(02)00276-4.

[92] E. J. Copeland, M. Sami, and S. Tsujikawa. Dynamics of Dark Energy. *International Journal of Modern Physics D*, 15:1753–1935, 2006. doi: 10.1142/ S021827180600942X.

[93] M. Crocce, E. Gaztañaga, A. Cabré, A. Carnero, and E. Sánchez. Clustering of photometric luminous red galaxies - I. Growth of structure and baryon acoustic feature. *MNRAS*, 417:2577–2591, November 2011. doi: 10.1111/j.1365-2966.2011.19425. x.

[94] R. A. C. Croft. Gravitational redshifts from large-scale structure. *MNRAS*, 434: 3008–3017, October 2013. doi: 10.1093/mnras/stt1223.

[95] M. Davis and P. J. E. Peebles. A survey of galaxy redshifts. V - The two-point position and velocity correlations. *ApJ*, 267:465–482, April 1983. doi: 10.1086/ 160884.

[96] K. S. Dawson, D. J. Schlegel, C. P. Ahn, S. F. Anderson, É. Aubourg, S. Bailey, R. H. Barkhouser, J. E. Bautista, A. Beifiori, A. A. Berlind, V. Bhardwaj, D. Bizyaev, C. H. Blake, M. R. Blanton, M. Blomqvist, A. S. Bolton, A. Borde, J. Bovy, W. N. Brandt, H. Brewington, J. Brinkmann, P. J. Brown, J. R. Brownstein, K. Bundy, N. G. Busca, W. Carithers, A. R. Carnero, M. A. Carr, Y. Chen, J. Comparat, N. Connolly, F. Cope, R. A. C. Croft, A. J. Cuesta, L. N. da Costa, J. R. A. Davenport, T. Delubac, R. de Putter, S. Dhital, A. Ealet, G. L. Ebelke, D. J. Eisenstein, S. Escoffier, X. Fan, N. Filiz Ak, H. Finley, A. Font-Ribera, R. Génova-Santos, J. E. Gunn, H. Guo, D. Haggard, P. B. Hall, J.-C. Hamilton, B. Harris, D. W. Harris,

S. Ho, D. W. Hogg, D. Holder, K. Honscheid, J. Huehnerhoff, B. Jordan, W. P. Jordan, G. Kauffmann, E. A. Kazin, D. Kirkby, M. A. Klaene, J.-P. Kneib, J.-M. Le Goff, K.-G. Lee, D. C. Long, C. P. Loomis, B. Lundgren, R. H. Lupton, M. A. G. Maia, M. Makler, E. Malanushenko, V. Malanushenko, R. Mandelbaum, M. Manera, C. Maraston, D. Margala, K. L. Masters, C. K. McBride, P. McDonald, I. D. Mc-Greer, R. G. McMahon, O. Mena, J. Miralda-Escudé, A. D. Montero-Dorta, F. Montesano, D. Muna, A. D. Myers, T. Naugle, R. C. Nichol, P. Noterdaeme, S. E. Nuza, M. D. Olmstead, A. Oravetz, D. J. Oravetz, R. Owen, N. Padmanabhan, N. Palanque-Delabrouille, K. Pan, J. K. Parejko, I. Pâris, W. J. Percival, I. Pérez-Fournon, I. Pérez-Ràfols, P. Petitjean, R. Pfaffenberger, J. Pforr, M. M. Pieri, F. Prada, A. M. Price-Whelan, M. J. Raddick, R. Rebolo, J. Rich, G. T. Richards, C. M. Rockosi, N. A. Roe, A. J. Ross, N. P. Ross, G. Rossi, J. A. Rubiño-Martin, L. Samushia, A. G. Sánchez, C. Sayres, S. J. Schmidt, D. P. Schneider, C. G. Scóccola, H.-J. Seo, A. Shelden, E. Sheldon, Y. Shen, Y. Shu, A. Slosar, S. A. Smee, S. A. Snedden, F. Stauffer, O. Steele, M. A. Strauss, A. Streblyanska, N. Suzuki, M. E. C. Swanson, T. Tal, M. Tanaka, D. Thomas, J. L. Tinker, R. Tojeiro, C. A. Tremonti, M. Vargas Magaña, L. Verde, M. Viel, D. A. Wake, M. Watson, B. A. Weaver, D. H. Weinberg, B. J. Weiner, A. A. West, M. White, W. M. Wood-Vasey, C. Yeche, I. Zehavi, G.-B. Zhao, and Z. Zheng. The Baryon Oscillation Spectroscopic Survey of SDSS-III. *AJ*, 145:10, January 2013. doi: 10.1088/0004-6256/145/1/10.

[97] K. S. Dawson, D. J. Schlegel, C. P. Ahn, S. F. Anderson, É. Aubourg, S. Bailey, R. H. Barkhouser, J. E. Bautista, A. Beifiori, A. A. Berlind, V. Bhardwaj, D. Bizyaev, C. H. Blake, M. R. Blanton, M. Blomqvist, A. S. Bolton, A. Borde, J. Bovy, W. N. Brandt, H. Brewington, J. Brinkmann, P. J. Brown, J. R. Brownstein, K. Bundy, N. G. Busca, W. Carithers, A. R. Carnero, M. A. Carr, Y. Chen, J. Comparat, N. Con-

nolly, F. Cope, R. A. C. Croft, A. J. Cuesta, L. N. da Costa, J. R. A. Davenport, T. Delubac, R. de Putter, S. Dhital, A. Ealet, G. L. Ebelke, D. J. Eisenstein, S. Escoffier, X. Fan, N. Filiz Ak, H. Finley, A. Font-Ribera, R. Génova-Santos, J. E. Gunn, H. Guo, D. Haggard, P. B. Hall, J.-C. Hamilton, B. Harris, D. W. Harris, S. Ho, D. W. Hogg, D. Holder, K. Honscheid, J. Huehnerhoff, B. Jordan, W. P. Jordan, G. Kauffmann, E. A. Kazin, D. Kirkby, M. A. Klaene, J.-P. Kneib, J.-M. Le Goff, K.-G. Lee, D. C. Long, C. P. Loomis, B. Lundgren, R. H. Lupton, M. A. G. Maia, M. Makler, E. Malanushenko, V. Malanushenko, R. Mandelbaum, M. Manera, C. Maraston, D. Margala, K. L. Masters, C. K. McBride, P. McDonald, I. D. McGreer, R. G. McMahon, O. Mena, J. Miralda-Escudé, A. D. Montero-Dorta, F. Montesano, D. Muna, A. D. Myers, T. Naugle, R. C. Nichol, P. Noterdaeme, S. E. Nuza, M. D. Olmstead, A. Oravetz, D. J. Oravetz, R. Owen, N. Padmanabhan, N. Palanque-Delabrouille, K. Pan, J. K. Parejko, I. Pâris, W. J. Percival, I. Pérez-Fournon, I. Pérez-Ràfols, P. Petitjean, R. Pfaffenberger, J. Pforr, M. M. Pieri, F. Prada, A. M. Price-Whelan, M. J. Raddick, R. Rebolo, J. Rich, G. T. Richards, C. M. Rockosi, N. A. Roe, A. J. Ross, N. P. Ross, G. Rossi, J. A. Rubiño-Martin, L. Samushia, A. G. Sánchez, C. Sayres, S. J. Schmidt, D. P. Schneider, C. G. Scóccola, H.-J. Seo, A. Shelden, E. Sheldon, Y. Shen, Y. Shu, A. Slosar, S. A. Smee, S. A. Snedden, F. Stauffer, O. Steele, M. A. Strauss, A. Streblyanska, N. Suzuki, M. E. C. Swanson, T. Tal, M. Tanaka, D. Thomas, J. L. Tinker, R. Tojeiro, C. A. Tremonti, M. Vargas Magaña, L. Verde, M. Viel, D. A. Wake, M. Watson, B. A. Weaver, D. H. Weinberg, B. J. Weiner, A. A. West, M. White, W. M. Wood-Vasey, C. Yeche, I. Zehavi, G.-B. Zhao, and Z. Zheng. The Baryon Oscillation Spectroscopic Survey of SDSS-III. *AJ*, 145:10, January 2013. doi: 10.1088/0004-6256/145/1/10.

[98] A. de Felice, S. Mukohyama, and S. Tsujikawa. Density perturbations in general

modified gravitational theories. *Phys. Rev. D*, 82(2):023524, July 2010. doi: 10. 1103/PhysRevD.82.023524.

[99] S. de la Torre, L. Guzzo, J. A. Peacock, E. Branchini, A. Iovino, B. R. Granett, U. Abbas, C. Adami, S. Arnouts, J. Bel, M. Bolzonella, D. Bottini, A. Cappi, J. Coupon, O. Cucciati, I. Davidzon, G. De Lucia, A. Fritz, P. Franzetti, M. Fumana, B. Garilli, O. Ilbert, J. Krywult, V. Le Brun, O. Le Fèvre, D. Maccagni, K. Małek, F. Marulli, H. J. McCracken, L. Moscardini, L. Paioro, W. J. Percival, M. Polletta, A. Pollo, H. Schlagenhaufer, M. Scodeggio, L. A. M. Tasca, R. Tojeiro, D. Vergani, A. Zanichelli, A. Burden, C. Di Porto, A. Marchetti, C. Marinoni, Y. Mellier, P. Monaco, R. C. Nichol, S. Phleps, M. Wolk, and G. Zamorani. The VIMOS Public Extragalactic Redshift Survey (VIPERS) . Galaxy clustering and redshift-space distortions at z ≈ 0.8 in the first data release. *A&A*, 557:A54, September 2013. doi: 10.1051/0004-6361/201321463.

[100] R. de Putter and E. V. Linder. Calibrating dark energy. *JCAP*, 10:042, October 2008. doi: 10.1088/1475-7516/2008/10/042.

[101] E. Di Valentino, A. Melchiorri, V. Salvatelli, and A. Silvestri. Parametrized modified gravity and the CMB bispectrum. *Phys. Rev. D*, 86(6):063517, September 2012. doi: 10.1103/PhysRevD.86.063517.

[102] E. Di Valentino, A. Melchiorri, and J. Silk. Cosmological Hints of Modified Gravity ? *ArXiv e-prints*, September 2015.

[103] M. Doi, M. Tanaka, M. Fukugita, J. E. Gunn, N. Yasuda, Ž. Ivezić, J. Brinkmann, E. de Haars, S. J. Kleinman, J. Krzesinski, and R. French Leger. Photometric Response Functions of the Sloan Digital Sky Survey Imager. *AJ*, 139:1628–1648, April 2010. doi: 10.1088/0004-6256/139/4/1628.

[104] M. Doi, M. Tanaka, M. Fukugita, J. E. Gunn, N. Yasuda, Ž. Ivezić, J. Brinkmann, E. de Haars, S. J. Kleinman, J. Krzesinski, and R. French Leger. Photometric Response Functions of the Sloan Digital Sky Survey Imager. *AJ*, 139:1628–1648, April 2010. doi: 10.1088/0004-6256/139/4/1628.

[105] J. Dossett, B. Hu, and D. Parkinson. Constraining models of f(R) gravity with Planck and WiggleZ power spectrum data. *JCAP*, 3:046, March 2014. doi: 10.1088/1475-7516/2014/03/046.

[106] R. Durrer. Gauge Invariant Cosmological Perturbation Theory: A General Study and It's Application to the Texture Scenario of Structure Formation. *Fundamental Cosmic Physics*, 15:209–339, 1994.

[107] G. Dvali, G. Gabadadze, and M. Porrati. 4D gravity on a brane in 5D Minkowski space. *Physics Letters B*, 485:208–214, July 2000. doi: 10.1016/S0370-2693(00) 00669-9.

[108] F. W. Dyson, A. S. Eddington, and C. Davidson. A determination of the deflection of light by the sun's gravitational field, from observations made at the total eclipse of may 29, 1919. *Philosophical Transactions of the Royal Society of London A: Mathematical, Physical and Engineering Sciences*, 220(571-581):291–333, 1920. ISSN 0264-3952. doi: 10.1098/rsta.1920.0009. URL `http://rsta.royalsocietypublishing.org/content/220/571-581/291`.

[109] Giusarma E., S. Alam, H. Zhu, R. A. C. Croft, and S. Ho. GZPT paper. *xxx*, pages xx–xx, 2016. doi: xxxx.

[110] A. Einstein. Die Feldgleichungen der Gravitation . *Sitzungsberichte der Preussischen Akademie der Wissenschaften zu Berlin*, pages 844–847, 1915.

[111] Albert Einstein. Die Grundlage der allgemeinen Relativitätstheorie. *Annalen Der Physik*, 49:770–820, 1916.

[112] D. J. Eisenstein, J. Annis, J. E. Gunn, A. S. Szalay, A. J. Connolly, R. C. Nichol, N. A. Bahcall, M. Bernardi, S. Burles, F. J. Castander, M. Fukugita, D. W. Hogg, Ž. Ivezić, G. R. Knapp, R. H. Lupton, V. Narayanan, M. Postman, D. E. Reichart, M. Richmond, D. P. Schneider, D. J. Schlegel, M. A. Strauss, M. SubbaRao, D. L. Tucker, D. Vanden Berk, M. S. Vogeley, D. H. Weinberg, and B. Yanny. Spectroscopic Target Selection for the Sloan Digital Sky Survey: The Luminous Red Galaxy Sample. *AJ*, 122:2267–2280, November 2001. doi: 10.1086/323717.

[113] D. J. Eisenstein, I. Zehavi, D. W. Hogg, R. Scoccimarro, M. R. Blanton, R. C. Nichol, R. Scranton, H.-J. Seo, M. Tegmark, Z. Zheng, S. F. Anderson, J. Annis, N. Bahcall, J. Brinkmann, S. Burles, F. J. Castander, A. Connolly, I. Csabai, M. Doi, M. Fukugita, J. A. Frieman, K. Glazebrook, J. E. Gunn, J. S. Hendry, G. Hennessy, Z. Ivezić, S. Kent, G. R. Knapp, H. Lin, Y.-S. Loh, R. H. Lupton, B. Margon, T. A. McKay, A. Meiksin, J. A. Munn, A. Pope, M. W. Richmond, D. Schlegel, D. P. Schneider, K. Shimasaku, C. Stoughton, M. A. Strauss, M. SubbaRao, A. S. Szalay, I. Szapudi, D. L. Tucker, B. Yanny, and D. G. York. Detection of the Baryon Acoustic Peak in the Large-Scale Correlation Function of SDSS Luminous Red Galaxies. *ApJ*, 633:560–574, November 2005. doi: 10.1086/466512.

[114] D. J. Eisenstein, D. H. Weinberg, E. Agol, H. Aihara, C. Allende Prieto, S. F. Anderson, J. A. Arns, É. Aubourg, S. Bailey, E. Balbinot, and et al. SDSS-III: Massive Spectroscopic Surveys of the Distant Universe, the Milky Way, and Extra-Solar Planetary Systems. *AJ*, 142:72, September 2011. doi: 10.1088/0004-6256/142/3/72.

[115] D. J. Eisenstein, D. H. Weinberg, E. Agol, H. Aihara, C. Allende Prieto, S. F. An-

derson, J. A. Arns, É. Aubourg, S. Bailey, E. Balbinot, and et al. SDSS-III: Massive Spectroscopic Surveys of the Distant Universe, the Milky Way, and Extra-Solar Planetary Systems. *AJ*, 142:72, September 2011. doi: 10.1088/0004-6256/142/3/72.

[116] T. Erben, H. Hildebrandt, L. Miller, L. van Waerbeke, C. Heymans, H. Hoekstra, T. D. Kitching, Y. Mellier, J. Benjamin, C. Blake, C. Bonnett, O. Cordes, J. Coupon, L. Fu, R. Gavazzi, B. Gillis, E. Grocutt, S. D. J. Gwyn, K. Holhjem, M. J. Hudson, M. Kilbinger, K. Kuijken, M. Milkeraitis, B. T. P. Rowe, T. Schrabback, E. Semboloni, P. Simon, M. Smit, O. Toader, S. Vafaei, E. van Uitert, and M. Velander. CFHTLenS: the Canada-France-Hawaii Telescope Lensing Survey - imaging data and catalogue products. *MNRAS*, 433:2545–2563, August 2013. doi: 10.1093/mnras/stt928.

[117] W. Fang, W. Hu, and A. Lewis. Crossing the phantom divide with parametrized post-Friedmann dark energy. *Phys. Rev. D*, 78(8):087303, October 2008. doi: 10.1103/PhysRevD.78.087303.

[118] H. A. Feldman, N. Kaiser, and J. A. Peacock. Power-spectrum analysis of three-dimensional redshift surveys. *ApJ*, 426:23–37, May 1994. doi: 10.1086/174036.

[119] K. B. Fisher. On the Validity of the Streaming Model for the Redshift-Space Correlation Function in the Linear Regime. *ApJ*, 448:494, August 1995. doi: 10.1086/175980.

[120] A. Font-Ribera, P. McDonald, N. Mostek, B. A. Reid, H.-J. Seo, and A. Slosar. DESI and other Dark Energy experiments in the era of neutrino mass measurements. *JCAP*, 5:023, May 2014. doi: 10.1088/1475-7516/2014/05/023.

[121] M. Fukugita, T. Ichikawa, J. E. Gunn, M. Doi, K. Shimasaku, and D. P. Schneider.

The Sloan Digital Sky Survey Photometric System. *AJ*, 111:1748, April 1996. doi: 10.1086/117915.

[122] M. Fukugita, T. Ichikawa, J. E. Gunn, M. Doi, K. Shimasaku, and D. P. Schneider. The Sloan Digital Sky Survey Photometric System. *AJ*, 111:1748, April 1996. doi: 10.1086/117915.

[123] B. Garilli, L. Guzzo, M. Scodeggio, M. Bolzonella, U. Abbas, C. Adami, S. Arnouts, J. Bel, D. Bottini, E. Branchini, A. Cappi, J. Coupon, O. Cucciati, I. Davidzon, G. De Lucia, S. de la Torre, P. Franzetti, A. Fritz, M. Fumana, B. R. Granett, O. Ilbert, A. Iovino, J. Krywult, V. Le Brun, O. Le Fèvre, D. Maccagni, K. Małek, F. Marulli, H. J. McCracken, L. Paioro, M. Polletta, A. Pollo, H. Schlagenhaufer, L. A. M. Tasca, R. Tojeiro, D. Vergani, G. Zamorani, A. Zanichelli, A. Burden, C. Di Porto, A. Marchetti, C. Marinoni, Y. Mellier, L. Moscardini, R. C. Nichol, J. A. Peacock, W. J. Percival, S. Phleps, and M. Wolk. The VIMOS Public Extragalactic Survey (VIPERS). First Data Release of 57 204 spectroscopic measurements. *A&A*, 562: A23, February 2014. doi: 10.1051/0004-6361/201322790.

[124] E. Gaztanaga, C. Bonvin, and L. Hui. Measurement of the dipole in the cross-correlation function of galaxies. *ArXiv e-prints*, December 2015.

[125] M. J. Geller and J. P. Huchra. Mapping the universe. *Science*, 246:897–903, November 1989. doi: 10.1126/science.246.4932.897.

[126] T. Giannantonio, P. Fosalba, R. Cawthon, Y. Omori, M. Crocce, F. Elsner, B. Leistedt, S. Dodelson, A. Benoit-Levy, E. Gaztanaga, G. Holder, H. V. Peiris, W. J. Percival, D. Kirk, A. H. Bauer, B. A. Benson, G. M. Bernstein, J. Carretero, T. M. Crawford, R. Crittenden, D. Huterer, B. Jain, E. Krause, C. L. Reichardt, A. J. Ross, G. Simard, B. Soergel, A. Stark, K. T. Story, J. D. Vieira, J. Weller, T. Abbott, F. B.

Abdalla, S. Allam, R. Armstrong, M. Banerji, R. A. Bernstein, E. Bertin, D. Brooks, E. Buckley-Geer, D. L. Burke, D. Capozzi, J. E. Carlstrom, A. Carnero Rosell, M. Carrasco Kind, F. J. Castander, C. L. Chang, C. E. Cunha, L. N. da Costa, C. B. D'Andrea, D. L. DePoy, S. Desai, H. T. Diehl, J. P. Dietrich, P. Doel, T. F. Eifler, A. E. Evrard, A. Fausti Neto, E. Fernandez, D. A. Finley, B. Flaugher, J. Frieman, D. Gerdes, D. Gruen, R. A. Gruendl, G. Gutierrez, W. L. Holzapfel, K. Honscheid, D. J. James, K. Kuehn, N. Kuropatkin, O. Lahav, T. S. Li, M. Lima, M. March, J. L. Marshall, P. Martini, P. Melchior, R. Miquel, J. J. Mohr, R. C. Nichol, B. Nord, R. Ogando, A. A. Plazas, A. K. Romer, A. Roodman, E. S. Rykoff, M. Sako, B. R. Saliwanchik, E. Sanchez, M. Schubnell, I. Sevilla-Noarbe, R. C. Smith, M. Soares-Santos, F. Sobreira, E. Suchyta, M. E. C. Swanson, G. Tarle, J. Thaler, D. Thomas, V. Vikram, A. R. Walker, R. H. Wechsler, and J. Zuntz. CMB lensing tomography with the DES Science Verification galaxies. *ArXiv e-prints*, July 2015.

[127] D. G. Gilbank, M. D. Gladders, H. K. C. Yee, and B. C. Hsieh. The Red-sequence Cluster Survey-2 (RCS-2): Survey Details and Photometric Catalog Construction. *AJ*, 141:94, March 2011. doi: 10.1088/0004-6256/141/3/94.

[128] M. D. Gladders and H. K. C. Yee. The Red-Sequence Cluster Survey. I. The Survey and Cluster Catalogs for Patches RCS 0926+37 and RCS 1327+29. *ApJ Suppl.*, 157: 1–29, March 2005. doi: 10.1086/427327.

[129] A. Goobar and B. Leibundgut. Supernova Cosmology: Legacy and Future. *Annual Review of Nuclear and Particle Science*, 61:251–279, November 2011. doi: 10. 1146/annurev-nucl-102010-130434.

[130] K. M. Górski, E. Hivon, A. J. Banday, B. D. Wandelt, F. K. Hansen, M. Reinecke, and M. Bartelmann. HEALPix: A Framework for High-Resolution Discretization

and Fast Analysis of Data Distributed on the Sphere. *ApJ*, 622:759–771, April 2005. doi: 10.1086/427976.

[131] J. L. Greenstein, J. B. Oke, and H. L. Shipman. Effective Temperature, Radius, and Gravitational Redshift of Sirius B. *ApJ*, 169:563, November 1971. doi: 10.1086/ 151174.

[132] J. E. Gunn, M. Carr, C. Rockosi, M. Sekiguchi, K. Berry, B. Elms, E. de Haas, Ž. Ivezić, G. Knapp, R. Lupton, G. Pauls, R. Simcoe, R. Hirsch, D. Sanford, S. Wang, D. York, F. Harris, J. Annis, L. Bartozek, W. Boroski, J. Bakken, M. Halde-man, S. Kent, S. Holm, D. Holmgren, D. Petravick, A. Prosapio, R. Rechenmacher, M. Doi, M. Fukugita, K. Shimasaku, N. Okada, C. Hull, W. Siegmund, E. Mannery, M. Blouke, D. Heidtman, D. Schneider, R. Lucinio, and J. Brinkman. The Sloan Digital Sky Survey Photometric Camera. *AJ*, 116:3040–3081, December 1998. doi: 10.1086/300645.

[133] J. E. Gunn, M. Carr, C. Rockosi, M. Sekiguchi, K. Berry, B. Elms, E. de Haas, Ž. Ivezić, G. Knapp, R. Lupton, G. Pauls, R. Simcoe, R. Hirsch, D. Sanford, S. Wang, D. York, F. Harris, J. Annis, L. Bartozek, W. Boroski, J. Bakken, M. Halde-man, S. Kent, S. Holm, D. Holmgren, D. Petravick, A. Prosapio, R. Rechenmacher, M. Doi, M. Fukugita, K. Shimasaku, N. Okada, C. Hull, W. Siegmund, E. Mannery, M. Blouke, D. Heidtman, D. Schneider, R. Lucinio, and J. Brinkman. The Sloan Digital Sky Survey Photometric Camera. *AJ*, 116:3040–3081, December 1998. doi: 10.1086/300645.

[134] J. E. Gunn, W. A. Siegmund, E. J. Mannery, R. E. Owen, C. L. Hull, R. F. Leger, L. N. Carey, G. R. Knapp, D. G. York, W. N. Boroski, S. M. Kent, R. H. Lupton, C. M. Rockosi, M. L. Evans, P. Waddell, J. E. Anderson, J. Annis, J. C. Baren-

266

tine, L. M. Bartoszek, S. Bastian, S. B. Bracker, H. J. Brewington, C. I. Briegel, J. Brinkmann, Y. J. Brown, M. A. Carr, P. C. Czarapata, C. C. Drennan, T. Dombeck, G. R. Federwitz, B. A. Gillespie, C. Gonzales, S. U. Hansen, M. Harvanek, J. Hayes, W. Jordan, E. Kinney, M. Klaene, S. J. Kleinman, R. G. Kron, J. Kresinski, G. Lee, S. Limmongkol, C. W. Lindenmeyer, D. C. Long, C. L. Loomis, P. M. McGehee, P. M. Mantsch, E. H. Neilsen, Jr., R. M. Neswold, P. R. Newman, A. Nitta, J. Peoples, Jr., J. R. Pier, P. S. Prieto, A. Prosapio, C. Rivetta, D. P. Schneider, S. Snedden, and S.-i. Wang. The 2.5 m Telescope of the Sloan Digital Sky Survey. *AJ*, 131: 2332–2359, April 2006. doi: 10.1086/500975.

[135] J. E. Gunn, W. A. Siegmund, E. J. Mannery, R. E. Owen, C. L. Hull, R. F. Leger, L. N. Carey, G. R. Knapp, D. G. York, W. N. Boroski, S. M. Kent, R. H. Lupton, C. M. Rockosi, M. L. Evans, P. Waddell, J. E. Anderson, J. Annis, J. C. Barentine, L. M. Bartoszek, S. Bastian, S. B. Bracker, H. J. Brewington, C. I. Briegel, J. Brinkmann, Y. J. Brown, M. A. Carr, P. C. Czarapata, C. C. Drennan, T. Dombeck, G. R. Federwitz, B. A. Gillespie, C. Gonzales, S. U. Hansen, M. Harvanek, J. Hayes, W. Jordan, E. Kinney, M. Klaene, S. J. Kleinman, R. G. Kron, J. Kresinski, G. Lee, S. Limmongkol, C. W. Lindenmeyer, D. C. Long, C. L. Loomis, P. M. McGehee, P. M. Mantsch, E. H. Neilsen, Jr., R. M. Neswold, P. R. Newman, A. Nitta, J. Peoples, Jr., J. R. Pier, P. S. Prieto, A. Prosapio, C. Rivetta, D. P. Schneider, S. Snedden, and S.-i. Wang. The 2.5 m Telescope of the Sloan Digital Sky Survey. *AJ*, 131: 2332–2359, April 2006. doi: 10.1086/500975.

[136] H. Guo, I. Zehavi, and Z. Zheng. A New Method to Correct for Fiber Collisions in Galaxy Two-point Statistics. *ApJ*, 756:127, September 2012. doi: 10.1088/0004-637X/756/2/127.

[137] Y. Guo, H. C. Ferguson, M. Giavalisco, G. Barro, S. P. Willner, M. L. N. Ashby,

T. Dahlen, J. L. Donley, S. M. Faber, A. Fontana, A. Galametz, A. Grazian, K.-H. Huang, D. D. Kocevski, A. M. Koekemoer, D. C. Koo, E. J. McGrath, M. Peth, M. Salvato, S. Wuyts, M. Castellano, A. R. Cooray, M. E. Dickinson, J. S. Dunlop, G. G. Fazio, J. P. Gardner, E. Gawiser, N. A. Grogin, N. P. Hathi, L.-T. Hsu, K.-S. Lee, R. A. Lucas, B. Mobasher, K. Nandra, J. A. Newman, and A. van der Wel. CANDELS Multi-wavelength Catalogs: Source Detection and Photometry in the GOODS-South Field. *ApJ Suppl.*, 207:24, August 2013. doi: 10.1088/0067-0049/207/2/24.

[138] A. J. S. Hamilton. Measuring Omega and the real correlation function from the redshift correlation function. *ApJL*, 385:L5–L8, January 1992. doi: 10.1086/186264.

[139] A. J. S. Hamilton. Linear Redshift Distortions: a Review. In D. Hamilton, editor, *The Evolving Universe*, volume 231 of *Astrophysics and Space Science Library*, page 185, 1998.

[140] J. Han, V. R. Eke, C. S. Frenk, R. Mandelbaum, P. Norberg, M. D. Schneider, J. A. Peacock, Y. Jing, I. Baldry, J. Bland-Hawthorn, S. Brough, M. J. I. Brown, J. Liske, J. Loveday, and A. S. G. Robotham. Galaxy And Mass Assembly (GAMA): the halo mass of galaxy groups from maximum-likelihood weak lensing. *MNRAS*, 446: 1356–1379, January 2015. doi: 10.1093/mnras/stu2178.

[141] S. W. Henderson, R. Allison, J. Austermann, T. Baildon, N. Battaglia, J. A. Beall, D. Becker, F. De Bernardis, J. R. Bond, E. Calabrese, S. K. Choi, K. P. Coughlin, K. T. Crowley, R. Datta, M. J. Devlin, S. M. Duff, R. Dunner, J. Dunkley, A. van Engelen, P. A. Gallardo, E. Grace, M. Hasselfield, F. Hills, G. C. Hilton, A. D. Hincks, R. Hlozek, S. P. Ho, J. Hubmayr, K. Huffenberger, J. P. Hughes, K. D. Irwin, B. J. Koopman, A. B. Kosowsky, D. Li, J. McMahon, C. Munson, F. Nati, L. Newburgh,

M. D. Niemack, P. Niraula, L. A. Page, C. G. Pappas, M. Salatino, A. Schillaci, B. L. Schmitt, N. Sehgal, B. D. Sherwin, J. L. Sievers, S. M. Simon, D. N. Spergel, S. T. Staggs, J. R. Stevens, R. Thornton, J. Van Lanen, E. M. Vavagiakis, J. T. Ward, and E. J. Wollack. Advanced ACTPol Cryogenic Detector Arrays and Readout. *ArXiv e-prints*, October 2015.

[142] C. Heymans, L. Van Waerbeke, D. Bacon, J. Berge, G. Bernstein, E. Bertin, S. Bridle, M. L. Brown, D. Clowe, H. Dahle, T. Erben, M. Gray, M. Hetterscheidt, H. Hoekstra, P. Hudelot, M. Jarvis, K. Kuijken, V. Margoniner, R. Massey, Y. Mellier, R. Nakajima, A. Refregier, J. Rhodes, T. Schrabback, and D. Wittman. The Shear Testing Programme - I. Weak lensing analysis of simulated ground-based observations. *MNRAS*, 368:1323–1339, May 2006. doi: 10.1111/j.1365-2966.2006. 10198.x.

[143] C. Heymans, L. Van Waerbeke, L. Miller, T. Erben, H. Hildebrandt, H. Hoekstra, T. D. Kitching, Y. Mellier, P. Simon, C. Bonnett, J. Coupon, L. Fu, J. Harnois Déraps, M. J. Hudson, M. Kilbinger, K. Kuijken, B. Rowe, T. Schrabback, E. Semboloni, E. van Uitert, S. Vafaei, and M. Velander. CFHTLenS: the Canada-France-Hawaii Telescope Lensing Survey. *MNRAS*, 427:146–166, November 2012. doi: 10.1111/j. 1365-2966.2012.21952.x.

[144] C. Heymans, E. Grocutt, A. Heavens, M. Kilbinger, T. D. Kitching, F. Simpson, J. Benjamin, T. Erben, H. Hildebrandt, H. Hoekstra, and et al. CFHTLenS tomographic weak lensing cosmological parameter constraints: Mitigating the impact of intrinsic galaxy alignments. *MNRAS*, 432:2433–2453, July 2013. doi: 10.1093/mnras/stt601.

[145] H. Hildebrandt, T. Erben, K. Kuijken, L. van Waerbeke, C. Heymans, J. Coupon,

J. Benjamin, C. Bonnett, L. Fu, H. Hoekstra, T. D. Kitching, Y. Mellier, L. Miller, M. Velander, M. J. Hudson, B. T. P. Rowe, T. Schrabback, E. Semboloni, and N. Benítez. CFHTLenS: improving the quality of photometric redshifts with precision photometry. *MNRAS*, 421:2355–2367, April 2012. doi: 10.1111/j.1365-2966. 2012.20468.x.

[146] G. Hinshaw, D. Larson, E. Komatsu, D. N. Spergel, C. L. Bennett, J. Dunkley, M. R. Nolta, M. Halpern, R. S. Hill, N. Odegard, L. Page, K. M. Smith, J. L. Weiland, B. Gold, N. Jarosik, A. Kogut, M. Limon, S. S. Meyer, G. S. Tucker, E. Wollack, and E. L. Wright. Nine-year Wilkinson Microwave Anisotropy Probe (WMAP) Observations: Cosmological Parameter Results. *ApJ Suppl.*, 208:19, October 2013. doi: 10.1088/0067-0049/208/2/19.

[147] C. M. Hirata and U. Seljak. Intrinsic alignment-lensing interference as a contaminant of cosmic shear. *Phys. Rev. D*, 70(6):063526, September 2004. doi: 10.1103/PhysRevD.70.063526.

[148] C. M. Hirata, N. Padmanabhan, U. Seljak, D. Schlegel, and J. Brinkmann. Cross-correlation of CMB with large-scale structure: Weak gravitational lensing. *Phys. Rev. D*, 70(10):103501, November 2004. doi: 10.1103/PhysRevD.70.103501.

[149] C. M. Hirata, R. Mandelbaum, M. Ishak, U. Seljak, R. Nichol, K. A. Pimbblet, N. P. Ross, and D. Wake. Intrinsic galaxy alignments from the 2SLAQ and SDSS surveys: luminosity and redshift scalings and implications for weak lensing surveys. *MNRAS*, 381:1197–1218, November 2007. doi: 10.1111/j.1365-2966.2007.12312.x.

[150] C. M. Hirata, S. Ho, N. Padmanabhan, U. Seljak, and N. A. Bahcall. Correlation of CMB with large-scale structure. II. Weak lensing. *Phys. Rev. D*, 78(4):043520, August 2008. doi: 10.1103/PhysRevD.78.043520.

[151] S. Ho, C. Hirata, N. Padmanabhan, U. Seljak, and N. Bahcall. Correlation of CMB with large-scale structure. I. Integrated Sachs-Wolfe tomography and cosmological implications. *Phys. Rev. D*, 78(4):043519, August 2008. doi: 10.1103/PhysRevD. 78.043519.

[152] S. Ho, A. Cuesta, H.-J. Seo, R. de Putter, A. J. Ross, M. White, N. Padmanab-han, S. Saito, D. J. Schlegel, E. Schlafly, U. Seljak, C. Hernández-Monteagudo, A. G. Sánchez, W. J. Percival, M. Blanton, R. Skibba, D. Schneider, B. Reid, O. Mena, M. Viel, D. J. Eisenstein, F. Prada, B. A. Weaver, N. Bahcall, D. Bizyaev, H. Brewinton, J. Brinkman, L. Nicolaci da Costa, J. R. Gott, E. Malanushenko, V. Malanushenko, B. Nichol, D. Oravetz, K. Pan, N. Palanque-Delabrouille, N. P. Ross, A. Simmons, F. de Simoni, S. Snedden, and C. Yeche. Clustering of Sloan Digital Sky Survey III Photometric Luminous Galaxies: The Measurement, Sys-tematics, and Cosmological Implications. *ApJ*, 761:14, December 2012. doi: 10.1088/0004-637X/761/1/14.

[153] H. Hoekstra and B. Jain. Weak Gravitational Lensing and Its Cosmological Applica-tions. *Annual Review of Nuclear and Particle Science*, 58:99–123, November 2008. doi: 10.1146/annurev.nucl.58.110707.171151.

[154] D. Hogg, 1997. URL http://cosmo.nyu.edu/hogg/sr/sr.pdf.

[155] D. W. Hogg, I. K. Baldry, M. R. Blanton, and D. J. Eisenstein. The K correction. *ArXiv Astrophysics e-prints*, October 2002.

[156] A. Hojjati, L. Pogosian, and G.-B. Zhao. Testing gravity with CAMB and Cos-moMC. *JCAP*, 8:005, August 2011. doi: 10.1088/1475-7516/2011/08/005.

[157] A. Hojjati, L. Pogosian, and G.-B. Zhao. Testing gravity with CAMB and Cos-

moMC. *Journal of Cosmology and Astroparticle Physics*, 8:005, August 2011. doi: 10.1088/1475-7516/2011/08/005.

[158] A. Hojjati, L. Pogosian, A. Silvestri, and S. Talbot. Practical solutions for perturbed f(R) gravity. *Phys. Rev. D*, 86(12):123503, December 2012. doi: 10.1103/ PhysRevD.86.123503.

[159] C. Howlett, A. J. Ross, L. Samushia, W. J. Percival, and M. Manera. The clustering of the SDSS main galaxy sample - II. Mock galaxy catalogues and a measurement of the growth of structure from redshift space distortions at z = 0.15. *MNRAS*, 449: 848–866, May 2015. doi: 10.1093/mnras/stu2693.

[160] L.-T. Hsu, M. Salvato, K. Nandra, M. Brusa, R. Bender, J. Buchner, J. L. Donley, D. D. Kocevski, Y. Guo, N. P. Hathi, C. Rangel, S. P. Willner, M. Brightman, A. Georgakakis, T. Budavári, A. S. Szalay, M. L. N. Ashby, G. Barro, T. Dahlen, S. M. Faber, H. C. Ferguson, A. Galametz, A. Grazian, N. A. Grogin, K.-H. Huang, A. M. Koekemoer, R. A. Lucas, E. McGrath, B. Mobasher, M. Peth, D. J. Rosario, and J. R. Trump. CANDELS/GOODS-S, CDFS, and ECDFS: Photometric Redshifts for Normal and X-Ray-Detected Galaxies. *ApJ*, 796:60, November 2014. doi: 10.1088/0004-637X/796/1/60.

[161] B. Hu, M. Raveri, N. Frusciante, and A. Silvestri. Effective field theory of cosmic acceleration: An implementation in CAMB. *Phys. Rev. D*, 89(10):103530, May 2014. doi: 10.1103/PhysRevD.89.103530.

[162] W. Hu and T. Okamoto. Mass Reconstruction with Cosmic Microwave Background Polarization. *ApJ*, 574:566–574, August 2002. doi: 10.1086/341110.

[163] W. Hu and I. Sawicki. Models of f(R) cosmic acceleration that evade solar system

tests. *Phys. Rev. D*, 76(6):064004, September 2007. doi: 10.1103/PhysRevD.76. 064004.

[164] M. J. Hudson, B. R. Gillis, J. Coupon, H. Hildebrandt, T. Erben, C. Heymans, H. Hoekstra, T. D. Kitching, Y. Mellier, L. Miller, L. Van Waerbeke, C. Bonnett, L. Fu, K. Kuijken, B. Rowe, T. Schrabback, E. Semboloni, E. van Uitert, and M. Velander. CFHTLenS: co-evolution of galaxies and their dark matter haloes. *MNRAS*, 447:298–314, February 2015. doi: 10.1093/mnras/stu2367.

[165] D. Huterer and M. S. Turner. Prospects for probing the dark energy via supernova distance measurements. *Phys. Rev. D*, 60(8):081301, October 1999. doi: 10.1103/ PhysRevD.60.081301.

[166] D. Huterer, D. Kirkby, R. Bean, A. Connolly, K. Dawson, S. Dodelson, A. Evrard, B. Jain, M. Jarvis, E. Linder, R. Mandelbaum, M. May, A. Raccanelli, B. Reid, E. Rozo, F. Schmidt, N. Sehgal, A. Slosar, A. van Engelen, H.-Y. Wu, and G. Zhao. Growth of Cosmic Structure: Probing Dark Energy Beyond Expansion. *ArXiv e-prints*, September 2013.

[167] G. Hütsi. Clustering of SZ clusters on a past light-cone: acoustic oscillations and constraints on dark energy. *A&A*, 446:43–60, January 2006. doi: 10.1051/ 0004-6361:20053487.

[168] V. Iršič, E. Di Dio, and M. Viel. Relativistic effects in Lyman-α forest. *JCAP*, 2: 051, February 2016. doi: 10.1088/1475-7516/2016/02/051.

[169] M. J. Jee, J. A. Tyson, M. D. Schneider, D. Wittman, S. Schmidt, and S. Hilbert. Cosmic Shear Results from the Deep Lens Survey. I. Joint Constraints on Ω_M and σ_8 with a Two-dimensional Analysis. *ApJ*, 765:74, March 2013. doi: 10.1088/ 0004-637X/765/1/74.

[170] E. Jennings, C. M. Baugh, and S. Pascoli. Modelling redshift space distortions in hierarchical cosmologies. *MNRAS*, 410:2081–2094, January 2011. doi: 10.1111/j. 1365-2966.2010.17581.x.

[171] D. Jeong, F. Schmidt, and C. M. Hirata. Large-scale clustering of galaxies in general relativity. *Phys. Rev. D*, 85(2):023504, January 2012. doi: 10.1103/PhysRevD.85. 023504.

[172] P. Jimeno, T. Broadhurst, J. Coupon, K. Umetsu, and R. Lazkoz. Comparing gravitational redshifts of SDSS galaxy clusters with the magnified redshift enhancement of background BOSS galaxies. *MNRAS*, 448:1999–2012, April 2015. doi: 10.1093/mnras/stv117.

[173] B. Joachimi and A. Taylor. Errors on errors - Estimating cosmological parameter covariance. In A. Heavens, J.-L. Starck, and A. Krone-Martins, editors, *Statistical Challenges in 21st Century Cosmology*, volume 306 of *IAU Symposium*, pages 99–103, May 2014. doi: 10.1017/S1743921314013428.

[174] B. Joachimi, R. Mandelbaum, F. B. Abdalla, and S. L. Bridle. Constraints on intrinsic alignment contamination of weak lensing surveys using the MegaZ-LRG sample. *A&A*, 527:A26, March 2011. doi: 10.1051/0004-6361/201015621.

[175] B. Joachimi, M. Cacciato, T. D. Kitching, A. Leonard, R. Mandelbaum, B. M. Schäfer, C. Sifón, H. Hoekstra, A. Kiessling, D. Kirk, and A. Rassat. Galaxy Alignments: An Overview. *Space Science Reviews*, 193:1–65, November 2015. doi: 10.1007/s11214-015-0177-4.

[176] A. Johnson, C. Blake, J. Dossett, J. Koda, D. Parkinson, and S. Joudaki. Searching for Modified Gravity: Scale and Redshift Dependent Constraints from Galaxy Peculiar Velocities. *ArXiv e-prints*, April 2015.

[177] D. H. Jones, M. A. Read, W. Saunders, M. Colless, T. Jarrett, Q. A. Parker, A. P. Fairall, T. Mauch, E. M. Sadler, F. G. Watson, D. Burton, L. A. Campbell, P. Cass, S. M. Croom, J. Dawe, K. Fiegert, L. Frankcombe, M. Hartley, J. Huchra, D. James, E. Kirby, O. Lahav, J. Lucey, G. A. Mamon, L. Moore, B. A. Peterson, S. Prior, D. Proust, K. Russell, V. Safouris, K.-I. Wakamatsu, E. Westra, and M. Williams. The 6dF Galaxy Survey: final redshift release (DR3) and southern large-scale structures. *MNRAS*, 399:683–698, October 2009. doi: 10.1111/j.1365-2966.2009.15338.x.

[178] F. D. Kahn and L. Woltjer. Intergalactic Matter and the Galaxy. *ApJ*, 130:705, November 1959. doi: 10.1086/146762.

[179] N. Kaiser. Clustering in real space and in redshift space. *MNRAS*, 227:1–21, July 1987.

[180] N. Kaiser. Clustering in real space and in redshift space. *MNRAS*, 227:1–21, July 1987.

[181] N. Kaiser. Measuring gravitational redshifts in galaxy clusters. *MNRAS*, 435:1278–1286, October 2013. doi: 10.1093/mnras/stt1370.

[182] N. Kaiser and M. J. Hudson. On the perturbation of the luminosity distance by peculiar motions. *MNRAS*, 450:883–895, June 2015. doi: 10.1093/mnras/stv693.

[183] N. Kaiser, W. Burgett, K. Chambers, L. Denneau, J. Heasley, R. Jedicke, E. Magnier, J. Morgan, P. Onaka, and J. Tonry. The Pan-STARRS wide-field optical/NIR imaging survey. In *Ground-based and Airborne Telescopes III*, volume 7733 of *Proceedings of the SPIE*, page 77330E, July 2010. doi: 10.1117/12.859188.

[184] E. A. Kazin, M. R. Blanton, R. Scoccimarro, C. K. McBride, A. A. Berlind, N. A.

Bahcall, J. Brinkmann, P. Czarapata, J. A. Frieman, S. M. Kent, D. P. Schneider, and A. S. Szalay. The Baryonic Acoustic Feature and Large-Scale Clustering in the Sloan Digital Sky Survey Luminous Red Galaxy Sample. *ApJ*, 710:1444–1461, February 2010. doi: 10.1088/0004-637X/710/2/1444.

[185] D. Kennefick. Not Only Because of Theory: Dyson, Eddington and the Competing Myths of the 1919 Eclipse Expedition. *ArXiv e-prints*, September 2007.

[186] J. Khoury and A. Weltman. Chameleon Fields: Awaiting Surprises for Tests of Gravity in Space. *Physical Review Letters*, 93(17):171104, October 2004. doi: 10.1103/PhysRevLett.93.171104.

[187] Y.-R. Kim and R. A. C. Croft. Gravitational Redshifts in Simulated Galaxy Clusters. *ApJ*, 607:164–174, May 2004. doi: 10.1086/383218.

[188] A. Kogut, D. J. Fixsen, D. T. Chuss, J. Dotson, E. Dwek, M. Halpern, G. F. Hinshaw, S. M. Meyer, S. H. Moseley, M. D. Seiffert, D. N. Spergel, and E. J. Wollack. The Primordial Inflation Explorer (PIXIE): a nulling polarimeter for cosmic microwave background observations. *JCAP*, 7:025, July 2011. doi: 10.1088/1475-7516/2011/07/025.

[189] S. M. Kopeikin, J. Ramirez, B. Mashhoon, and M. V. Sazhin. Cosmological perturbations: a new gauge-invariant approach. *Physics Letters A*, 292:173–180, December 2001. doi: 10.1016/S0375-9601(01)00777-0.

[190] K. Koyama. Structure formation in modified gravity models. *jcap*, 3:017, March 2006. doi: 10.1088/1475-7516/2006/03/017.

[191] A. Kuntz. Cross-correlation of CFHTLenS galaxy catalogue and Planck CMB lensing using the halo model prescription. *ArXiv e-prints*, October 2015.

[192] M. Lagos, T. Baker, P. G. Ferreira, and J. Noller. A general theory of linear cosmological perturbations: scalar-tensor and vector-tensor theories. *ArXiv e-prints*, April 2016.

[193] J.-M. Lamarre, J.-L. Puget, P. A. R. Ade, F. Bouchet, G. Guyot, A. E. Lange, F. Pajot, A. Arondel, K. Benabed, J.-L. Beney, A. Benoît, J.-P. Bernard, R. Bhatia, Y. Blanc, J. J. Bock, E. Bréelle, T. W. Bradshaw, P. Camus, A. Catalano, J. Charra, M. Charra, S. E. Church, F. Couchot, A. Coulais, B. P. Crill, M. R. Crook, K. Dassas, P. de Bernardis, J. Delabrouille, P. de Marcillac, J.-M. Delouis, F.-X. Désert, C. Dumesnil, X. Dupac, G. Efstathiou, P. Eng, C. Evesque, J.-J. Fourmond, K. Ganga, M. Giard, R. Gispert, L. Guglielmi, J. Haissinski, S. Henrot-Versillé, E. Hivon, W. A. Holmes, W. C. Jones, T. C. Koch, H. Lagardère, P. Lami, J. Landé, B. Leriche, C. Leroy, Y. Longval, J. F. Macías-Pérez, T. Maciaszek, B. Maffei, B. Mansoux, C. Marty, S. Masi, C. Mercier, M.-A. Miville-Deschênes, A. Moneti, L. Montier, J. A. Murphy, J. Narbonne, M. Nexon, C. G. Paine, J. Pahn, O. Perdereau, F. Piacentini, M. Piat, S. Plaszczynski, E. Pointecouteau, R. Pons, N. Ponthieu, S. Prunet, D. Rambaud, G. Recouvreur, C. Renault, I. Ristorcelli, C. Rosset, D. Santos, G. Savini, G. Serra, P. Stassi, R. V. Sudiwala, J.-F. Sygnet, J. A. Tauber, J.-P. Torre, M. Tristram, L. Vibert, A. Woodcraft, V. Yurchenko, and D. Yvon. Planck pre-launch status: The HFI instrument, from specification to actual performance. *A&A*, 520:A9, September 2010. doi: 10.1051/0004-6361/200912975.

[194] S. D. Landy and A. S. Szalay. Bias and variance of angular correlation functions. *ApJ*, 412:64–71, July 1993. doi: 10.1086/172900.

[195] R. Laureijs, J. Amiaux, S. Arduini, J. . Auguères, J. Brinchmann, R. Cole, M. Cropper, C. Dabin, L. Duvet, A. Ealet, and et al. Euclid Definition Study Report. *ArXiv e-prints (1110.3193)*, October 2011.

[196] R. Laureijs, J. Amiaux, S. Arduini, J. . Auguères, J. Brinchmann, R. Cole, M. Cropper, C. Dabin, L. Duvet, A. Ealet, and et al. Euclid Definition Study Report. *ArXiv e-prints*, October 2011.

[197] A. Leauthaud, J. Tinker, K. Bundy, P. S. Behroozi, R. Massey, J. Rhodes, M. R. George, J.-P. Kneib, A. Benson, R. H. Wechsler, M. T. Busha, P. Capak, M. Cortês, O. Ilbert, A. M. Koekemoer, O. Le Fèvre, S. Lilly, H. J. McCracken, M. Salvato, T. Schrabback, N. Scoville, T. Smith, and J. E. Taylor. New Constraints on the Evolution of the Stellar-to-dark Matter Connection: A Combined Analysis of Galaxy-Galaxy Lensing, Clustering, and Stellar Mass Functions from z = 0.2 to z =1. *ApJ*, 744:159, January 2012. doi: 10.1088/0004-637X/744/2/159.

[198] C. D. Leonard, P. G. Ferreira, and C. Heymans. Testing gravity with E_G: mapping theory onto observations. *ArXiv e-prints*, October 2015.

[199] C. D. Leonard, P. G. Ferreira, and C. Heymans. Testing gravity with E_G: mapping theory onto observations. *ArXiv e-prints*, October 2015.

[200] M. Levi, C. Bebek, T. Beers, R. Blum, R. Cahn, D. Eisenstein, B. Flaugher, K. Honscheid, R. Kron, O. Lahav, P. McDonald, N. Roe, D. Schlegel, and representing the DESI collaboration. The DESI Experiment, a whitepaper for Snowmass 2013. *ArXiv e-prints*, August 2013.

[201] A. Lewis and S. Bridle. Cosmological parameters from CMB and other data: A Monte Carlo approach. *Phys. Rev. D*, 66(10):103511, November 2002. doi: 10. 1103/PhysRevD.66.103511.

[202] A. Lewis and S. Bridle. Cosmological parameters from CMB and other data: A Monte Carlo approach. *Phys. Rev. D*, 66(10):103511, November 2002. doi: 10. 1103/PhysRevD.66.103511.

[203] A. Lewis, A. Challinor, and A. Lasenby. Efficient Computation of Cosmic Microwave Background Anisotropies in Closed Friedmann-Robertson-Walker Models. *ApJ*, 538:473–476, August 2000. doi: 10.1086/309179.

[204] A. Lewis, A. Challinor, and A. Lasenby. Efficient Computation of Cosmic Microwave Background Anisotropies in Closed Friedmann-Robertson-Walker Models. *ApJ*, 538:473–476, August 2000. doi: 10.1086/309179.

[205] A. Lewis, A. Challinor, and D. Hanson. The shape of the CMB lensing bispectrum. *JCAP*, 3:018, March 2011. doi: 10.1088/1475-7516/2011/03/018.

[206] A. R. Liddle and D. H. Lyth. The cold dark matter density perturbation. *Physics Reports*, 231:1–105, August 1993. doi: 10.1016/0370-1573(93)90114-S.

[207] E. V. Linder. Isotropy of the microwave background by gravitational lensing. *A&A*, 206:199–203, November 1988.

[208] E. V. Linder. Exploring the Expansion History of the Universe. *Physical Review Letters*, 90(9):091301, March 2003. doi: 10.1103/PhysRevLett.90.091301.

[209] E. V. Linder. Cosmic growth history and expansion history. *Phys. Rev. D*, 72(4): 043529, August 2005. doi: 10.1103/PhysRevD.72.043529.

[210] E. V. Linder and R. N. Cahn. Parameterized beyond-Einstein growth. *Astroparticle Physics*, 28:481–488, December 2007. doi: 10.1016/j.astropartphys.2007.09.003.

[211] J. Liske, I. K. Baldry, S. P. Driver, R. J. Tuffs, M. Alpaslan, E. Andrae, S. Brough, M. E. Cluver, M. W. Grootes, M. L. P. Gunawardhana, L. S. Kelvin, J. Loveday, A. S. G. Robotham, E. N. Taylor, S. P. Bamford, J. Bland-Hawthorn, M. J. I. Brown, M. J. Drinkwater, A. M. Hopkins, M. J. Meyer, P. Norberg, J. A. Peacock, N. K. Agius, S. K. Andrews, A. E. Bauer, J. H. Y. Ching, M. Colless, C. J. Conselice,

S. M. Croom, L. J. M. Davies, R. De Propris, L. Dunne, E. M. Eardley, S. Ellis, C. Foster, C. S. Frenk, B. Häußler, B. W. Holwerda, C. Howlett, H. Ibarra, M. J. Jarvis, D. H. Jones, P. R. Kafle, C. G. Lacey, R. Lange, M. A. Lara-López, Á. R. López-Sánchez, S. Maddox, B. F. Madore, T. McNaught-Roberts, A. J. Moffett, R. C. Nichol, M. S. Owers, D. Palamara, S. J. Penny, S. Phillipps, K. A. Pimbblet, C. C. Popescu, M. Prescott, R. Proctor, E. M. Sadler, A. E. Sansom, M. Seibert, R. Sharp, W. Sutherland, J. A. Vázquez-Mata, E. van Kampen, S. M. Wilkins, R. Williams, and A. H. Wright. Galaxy And Mass Assembly (GAMA): end of survey report and data release 2. *MNRAS*, 452:2087–2126, September 2015. doi: 10.1093/mnras/stv1436.

[212] J. Liu and J. C. Hill. Cross-correlation of Planck CMB lensing and CFHTLenS galaxy weak lensing maps. *Phys. Rev. D*, 92(6):063517, September 2015. doi: 10.1103/PhysRevD.92.063517.

[213] J. Liu, A. Ortiz-Vazquez, and J. C. Hill. Constraining Multiplicative Bias in CFHTLenS Weak Lensing Shear Data. *ArXiv e-prints*, January 2016.

[214] J. C. Lopresto, C. Schrader, and A. K. Pierce. Solar gravitational redshift from the infrared oxygen triplet. *ApJ*, 376:757–760, August 1991. doi: 10.1086/170323.

[215] M. Loverde and N. Afshordi. Extended Limber approximation. *Phys. Rev. D*, 78 (12):123506, December 2008. doi: 10.1103/PhysRevD.78.123506.

[216] LSST Science Collaborations and LSST Project. LSST Science Book, Version 2.0. *ArXiv e-prints (0912.0201), http://www.lsst.org/lsst/scibook*, December 2009.

[217] R. Lupton, J. E. Gunn, Z. Ivezić, G. R. Knapp, and S. Kent. The SDSS Imaging Pipelines. In F. R. Harnden, Jr., F. A. Primini, and H. E. Payne, editors, *Astronomical*

Data Analysis Software and Systems X, volume 238 of *Astronomical Society of the Pacific Conference Series*, page 269, 2001.

[218] R. H. Lupton, J. E. Gunn, and A. S. Szalay. A Modified Magnitude System that Produces Well-Behaved Magnitudes, Colors, and Errors Even for Low Signal-to-Noise Ratio Measurements. *AJ*, 118:1406–1410, September 1999. doi: 10.1086/301004.

[219] C.-P. Ma and E. Bertschinger. Cosmological Perturbation Theory in the Synchronous vs. Conformal Newtonian Gauge. *ArXiv Astrophysics e-prints*, January 1994.

[220] R. Mandelbaum, C. M. Hirata, U. Seljak, J. Guzik, N. Padmanabhan, C. Blake, M. R. Blanton, R. Lupton, and J. Brinkmann. Systematic errors in weak lensing: application to SDSS galaxy-galaxy weak lensing. *MNRAS*, 361:1287–1322, August 2005. doi: 10.1111/j.1365-2966.2005.09282.x.

[221] R. Mandelbaum, A. Slosar, T. Baldauf, U. Seljak, C. M. Hirata, R. Nakajima, R. Reyes, and R. E. Smith. Cosmological parameter constraints from galaxy-galaxy lensing and galaxy clustering with the SDSS DR7. *MNRAS*, 432:1544–1575, June 2013. doi: 10.1093/mnras/stt572.

[222] M. Manera, R. Scoccimarro, W. J. Percival, L. Samushia, C. K. McBride, A. J. Ross, R. K. Sheth, M. White, B. A. Reid, A. G. Sánchez, R. de Putter, X. Xu, A. A. Berlind, J. Brinkmann, C. Maraston, B. Nichol, F. Montesano, N. Padmanabhan, R. A. Skibba, R. Tojeiro, and B. A. Weaver. The clustering of galaxies in the SDSS-III Baryon Oscillation Spectroscopic Survey: a large sample of mock galaxy catalogues. *MNRAS*, 428:1036–1054, January 2013. doi: 10.1093/mnras/sts084.

[223] M. Manera, R. Scoccimarro, W. J. Percival, L. Samushia, C. K. McBride, A. J. Ross, R. K. Sheth, M. White, B. A. Reid, A. G. Sánchez, R. de Putter, X. Xu, A. A. Berlind, J. Brinkmann, C. Maraston, B. Nichol, F. Montesano, N. Padmanabhan, R. A. Skibba, R. Tojeiro, and B. A. Weaver. The clustering of galaxies in the SDSS-III Baryon Oscillation Spectroscopic Survey: a large sample of mock galaxy catalogues. *MNRAS*, 428:1036–1054, January 2013. doi: 10.1093/mnras/sts084.

[224] R. Massey, T. Kitching, and J. Richard. The dark matter of gravitational lensing. *Reports on Progress in Physics*, 73(8):086901, August 2010. doi: 10.1088/0034-4885/73/8/086901.

[225] T. Matsubara. Erratum: Nonlinear perturbation theory with halo bias and redshift-space distortions via the Lagrangian picture [Phys. Rev. D 78, 083519 (2008)]. *Phys. Rev. D*, 78(10):109901, November 2008. doi: 10.1103/PhysRevD.78.109901.

[226] P. McDonald. Gravitational redshift and other redshift-space distortions of the imaginary part of the power spectrum. *JCAP*, 11:026, November 2009. doi: 10.1088/1475-7516/2009/11/026.

[227] A. Mennella, M. Bersanelli, R. C. Butler, A. Curto, F. Cuttaia, R. J. Davis, J. Dick, M. Frailis, S. Galeotta, A. Gregorio, H. Kurki-Suonio, C. R. Lawrence, S. Leach, J. P. Leahy, S. Lowe, D. Maino, N. Mandolesi, M. Maris, E. Martínez-González, P. R. Meinhold, G. Morgante, D. Pearson, F. Perrotta, G. Polenta, T. Poutanen, M. Sandri, M. D. Seiffert, A.-S. Suur-Uski, D. Tavagnacco, L. Terenzi, M. Tomasi, J. Valiviita, F. Villa, R. Watson, A. Wilkinson, A. Zacchei, A. Zonca, B. Aja, E. Artal, C. Baccigalupi, A. J. Banday, R. B. Barreiro, J. G. Bartlett, N. Bartolo, P. Battaglia, K. Bennett, A. Bonaldi, L. Bonavera, J. Borrill, F. R. Bouchet, C. Burigana, P. Cabella, B. Cappellini, X. Chen, L. Colombo, M. Cruz, L. Danese,

O. D'Arcangelo, R. D. Davies, G. de Gasperis, A. de Rosa, G. de Zotti, C. Dickinson, J. M. Diego, S. Donzelli, G. Efstathiou, T. A. Enßlin, H. K. Eriksen, M. C. Falvella, F. Finelli, S. Foley, C. Franceschet, E. Franceschi, T. C. Gaier, R. T. Génova-Santos, D. George, F. Gómez, J. González-Nuevo, K. M. Górski, A. Gruppuso, F. K. Hansen, D. Herranz, J. M. Herreros, R. J. Hoyland, N. Hughes, J. Jewell, P. Jukkala, M. Juvela, P. Kangaslahti, E. Keihänen, R. Keskitalo, V.-H. Kilpia, T. S. Kisner, J. Knoche, L. Knox, M. Laaninen, A. Lähteenmäki, J.-M. Lamarre, R. Leonardi, J. León-Tavares, P. Leutenegger, P. B. Lilje, M. López-Caniego, P. M. Lubin, M. Malaspina, D. Marinucci, M. Massardi, S. Matarrese, F. Matthai, A. Melchiorri, L. Mendes, M. Miccolis, M. Migliaccio, S. Mitra, A. Moss, P. Natoli, R. Nesti, H. U. Nørgaard-Nielsen, L. Pagano, R. Paladini, D. Paoletti, B. Partridge, F. Pasian, V. Pettorino, D. Pietrobon, M. Pospieszalski, G. Prézeau, M. Prina, P. Procopio, J.-L. Puget, C. Quercellini, J. P. Rachen, R. Rebolo, M. Reinecke, S. Ricciardi, G. Robbers, G. Rocha, N. Roddis, J. A. Rubino-Martín, M. Savelainen, D. Scott, R. Silvestri, A. Simonetto, P. Sjoman, G. F. Smoot, C. Sozzi, L. Stringhetti, J. A. Tauber, G. Tofani, L. Toffolatti, J. Tuovinen, M. Türler, G. Umana, L. Valenziano, J. Varis, P. Vielva, N. Vittorio, L. A. Wade, C. Watson, S. D. M. White, and F. Winder. Planck early results. III. First assessment of the Low Frequency Instrument in-flight performance. *A&A*, 536:A3, December 2011. doi: 10.1051/0004-6361/201116480.

[228] L. Miller, C. Heymans, T. D. Kitching, L. van Waerbeke, T. Erben, H. Hildebrandt, H. Hoekstra, Y. Mellier, B. T. P. Rowe, J. Coupon, J. P. Dietrich, L. Fu, J. Harnois-Déraps, M. J. Hudson, M. Kilbinger, K. Kuijken, T. Schrabback, E. Semboloni, S. Vafaei, and M. Velander. Bayesian galaxy shape measurement for weak lensing surveys - III. Application to the Canada-France-Hawaii Telescope Lensing Survey. *MNRAS*, 429:2858–2880, March 2013. doi: 10.1093/mnras/sts454.

[229] L. Miller, C. Heymans, T. D. Kitching, L. van Waerbeke, T. Erben, H. Hildebrandt, H. Hoekstra, Y. Mellier, B. T. P. Rowe, J. Coupon, J. P. Dietrich, L. Fu, J. Harnois-Déraps, M. J. Hudson, M. Kilbinger, K. Kuijken, T. Schrabback, E. Semboloni, S. Vafaei, and M. Velander. Bayesian galaxy shape measurement for weak lensing surveys - III. Application to the Canada-France-Hawaii Telescope Lensing Survey. *MNRAS*, 429:2858–2880, March 2013. doi: 10.1093/mnras/sts454.

[230] H. Miyatake, S. More, R. Mandelbaum, M. Takada, D. N. Spergel, J.-P. Kneib, D. P. Schneider, J. Brinkmann, and J. R. Brownstein. The Weak Lensing Signal and the Clustering of BOSS Galaxies. I. Measurements. *ApJ*, 806:1, June 2015. doi: 10.1088/0004-637X/806/1/1.

[231] H. Miyatake, S. More, R. Mandelbaum, M. Takada, D. N. Spergel, J.-P. Kneib, D. P. Schneider, J. Brinkmann, and J. R. Brownstein. The Weak Lensing Signal and the Clustering of BOSS Galaxies. I. Measurements. *ApJ*, 806:1, June 2015. doi: 10.1088/0004-637X/806/1/1.

[232] I. Mohammed, D. Martizzi, R. Teyssier, and A. Amara. Baryonic effects on weak-lensing two-point statistics and its cosmological implications. *ArXiv e-prints*, October 2014.

[233] I. G. Momcheva, G. B. Brammer, P. G. van Dokkum, R. E. Skelton, K. E. Whitaker, E. J. Nelson, M. Fumagalli, M. V. Maseda, J. Leja, M. Franx, H.-W. Rix, R. Bezanson, E. Da Cunha, C. Dickey, N. M. Förster Schreiber, G. Illingworth, M. Kriek, I. Labbé, J. Ulf Lange, B. F. Lundgren, D. Magee, D. Marchesini, P. Oesch, C. Pacifici, S. G. Patel, S. Price, T. Tal, D. A. Wake, A. van der Wel, and S. Wuyts. The 3D-HST Survey: Hubble Space Telescope WFC3/G141 grism spectra, redshifts, and emission line measurements for $\sim 100,000$ galaxies. *ArXiv e-prints*, October 2015.

[234] S. More, F. C. van den Bosch, M. Cacciato, A. More, H. Mo, and X. Yang. Cosmological constraints from a combination of galaxy clustering and lensing - II. Fisher matrix analysis. *MNRAS*, 430:747–766, April 2013. doi: 10.1093/mnras/sts697.

[235] S. More, H. Miyatake, R. Mandelbaum, M. Takada, D. Spergel, J. Brownstein, and D. P. Schneider. The Weak Lensing Signal and the Clustering of BOSS Galaxies II: Astrophysical and Cosmological Constraints. *ArXiv e-prints*, July 2014.

[236] S. More, H. Miyatake, R. Mandelbaum, M. Takada, D. N. Spergel, J. R. Brownstein, and D. P. Schneider. The Weak Lensing Signal and the Clustering of BOSS Galaxies. II. Astrophysical and Cosmological Constraints. *ApJ*, 806:2, June 2015. doi: 10. 1088/0004-637X/806/1/2.

[237] V. F. Mukhanov, H. A. Feldman, and R. H. Brandenberger. Theory of cosmological perturbations. *Physics Reports*, 215:203–333, June 1992. doi: 10.1016/ 0370-1573(92)90044-Z.

[238] J. A. Newman, M. C. Cooper, M. Davis, S. M. Faber, A. L. Coil, P. Guhathakurta, D. C. Koo, A. C. Phillips, C. Conroy, A. A. Dutton, D. P. Finkbeiner, B. F. Gerke, D. J. Rosario, B. J. Weiner, C. N. A. Willmer, R. Yan, J. J. Harker, S. A. Kassin, N. P. Konidaris, K. Lai, D. S. Madgwick, K. G. Noeske, G. D. Wirth, A. J. Connolly, N. Kaiser, E. N. Kirby, B. C. Lemaux, L. Lin, J. M. Lotz, G. A. Luppino, C. Marinoni, D. J. Matthews, A. Metevier, and R. P. Schiavon. The DEEP2 Galaxy Redshift Survey: Design, Observations, Data Reduction, and Redshifts. *ApJ Suppl.*, 208:5, September 2013. doi: 10.1088/0067-0049/208/1/5.

[239] P. Norberg, C. M. Baugh, E. Gaztañaga, and D. J. Croton. Statistical analysis of galaxy surveys - I. Robust error estimation for two-point clustering statistics. *MNRAS*, 396:19–38, June 2009. doi: 10.1111/j.1365-2966.2009.14389.x.

[240] K. Nordtvedt. Equivalence Principle for Massive Bodies. II. Theory. *Physical Review*, 169:1017–1025, May 1968. doi: 10.1103/PhysRev.169.1017.

[241] K. Nordtvedt. Testing Relativity with Laser Ranging to the Moon. *Physical Review*, 170:1186–1187, June 1968. doi: 10.1103/PhysRev.170.1186.

[242] K. Nordtvedt. A post-Newtonian gravitational Lagrangian formalism for celestial body dynamics in metric gravity. *ApJ*, 297:390–404, October 1985. doi: 10.1086/163538.

[243] Y. Omori and G. Holder. Cross-Correlation of CFHTLenS Galaxy Number Density and Planck CMB Lensing. *ArXiv e-prints*, February 2015.

[244] A. Orsi, C. M. Baugh, C. G. Lacey, A. Cimatti, Y. Wang, and G. Zamorani. Probing dark energy with future redshift surveys: a comparison of emission line and broadband selection in the near-infrared. *MNRAS*, 405:1006–1024, June 2010. doi: 10.1111/j.1365-2966.2010.16585.x.

[245] Keisuke Osumi and Shirley Ho. in preperation. *MNRAS*, 2009.

[246] N. Padmanabhan, U. Seljak, and U. L. Pen. Mining weak lensing surveys. *NewA*, 8:581–603, August 2003. doi: 10.1016/S1384-1076(03)00055-1.

[247] N. Padmanabhan, D. J. Schlegel, U. Seljak, A. Makarov, N. A. Bahcall, M. R. Blanton, J. Brinkmann, D. J. Eisenstein, D. P. Finkbeiner, J. E. Gunn, D. W. Hogg, Ž. Ivezić, G. R. Knapp, J. Loveday, R. H. Lupton, R. C. Nichol, D. P. Schneider, M. A. Strauss, M. Tegmark, and D. G. York. The clustering of luminous red galaxies in the Sloan Digital Sky Survey imaging data. *MNRAS*, 378:852–872, July 2007. doi: 10.1111/j.1365-2966.2007.11593.x.

[248] N. Padmanabhan, D. J. Schlegel, D. P. Finkbeiner, J. C. Barentine, M. R. Blanton, H. J. Brewington, J. E. Gunn, M. Harvanek, D. W. Hogg, Ž. Ivezić, D. Johnston, S. M. Kent, S. J. Kleinman, G. R. Knapp, J. Krzesinski, D. Long, E. H. Neilsen, Jr., A. Nitta, C. Loomis, R. H. Lupton, S. Roweis, S. A. Snedden, M. A. Strauss, and D. L. Tucker. An Improved Photometric Calibration of the Sloan Digital Sky Survey Imaging Data. *ApJ*, 674:1217–1233, February 2008. doi: 10.1086/524677.

[249] N. Padmanabhan, D. J. Schlegel, D. P. Finkbeiner, J. C. Barentine, M. R. Blanton, H. J. Brewington, J. E. Gunn, M. Harvanek, D. W. Hogg, Ž. Ivezić, D. Johnston, S. M. Kent, S. J. Kleinman, G. R. Knapp, J. Krzesinski, D. Long, E. H. Neilsen, Jr., A. Nitta, C. Loomis, R. H. Lupton, S. Roweis, S. A. Snedden, M. A. Strauss, and D. L. Tucker. An Improved Photometric Calibration of the Sloan Digital Sky Survey Imaging Data. *ApJ*, 674:1217–1233, February 2008. doi: 10.1086/524677.

[250] I. Pâris, P. Petitjean, É. Aubourg, N. P. Ross, A. D. Myers, A. Streblyanska, S. Bailey, P. B. Hall, M. A. Strauss, S. F. Anderson, D. Bizyaev, A. Borde, J. Brinkmann, J. Bovy, W. N. Brandt, H. Brewington, J. R. Brownstein, B. A. Cook, G. Ebelke, X. Fan, N. Filiz Ak, H. Finley, A. Font-Ribera, J. Ge, F. Hamann, S. Ho, L. Jiang, K. Kinemuchi, E. Malanushenko, V. Malanushenko, M. Marchante, I. D. McGreer, R. G. McMahon, J. Miralda-Escudé, D. Muna, P. Noterdaeme, D. Oravetz, N. Palanque-Delabrouille, K. Pan, I. Perez-Fournon, M. Pieri, R. Riffel, D. J. Schlegel, D. P. Schneider, A. Simmons, M. Viel, B. A. Weaver, W. M. Wood-Vasey, C. Yèche, and D. G. York. The Sloan Digital Sky Survey quasar catalog: tenth data release. *A&A*, 563:A54, March 2014. doi: 10.1051/0004-6361/201322691.

[251] J. A. Peacock and R. E. Smith. Halo occupation numbers and galaxy bias. *MNRAS*, 318:1144–1156, November 2000. doi: 10.1046/j.1365-8711.2000.03779.x.

[252] J. A. Peacock, S. Cole, P. Norberg, C. M. Baugh, J. Bland-Hawthorn, T. Bridges, R. D. Cannon, M. Colless, C. Collins, W. Couch, G. Dalton, K. Deeley, R. De Propris, S. P. Driver, G. Efstathiou, R. S. Ellis, C. S. Frenk, K. Glazebrook, C. Jackson, O. Lahav, I. Lewis, S. Lumsden, S. Maddox, W. J. Percival, B. A. Peterson, I. Price, W. Sutherland, and K. Taylor. A measurement of the cosmological mass density from clustering in the 2dF Galaxy Redshift Survey. *Nature*, 410:169–173, March 2001.

[253] P. J. Peebles and B. Ratra. The cosmological constant and dark energy. *Reviews of Modern Physics*, 75:559–606, April 2003. doi: 10.1103/RevModPhys.75.559.

[254] P. J. E. Peebles. *The large-scale structure of the universe*. 1980.

[255] P. J. E. Peebles and J. T. Yu. Primeval Adiabatic Perturbation in an Expanding Universe. *ApJ*, 162:815, December 1970. doi: 10.1086/150713.

[256] W. J. Percival. Large Scale Structure Observations. *ArXiv e-prints*, December 2013.

[257] W. J. Percival. Large Scale Structure Observations. *ArXiv e-prints*, December 2013.

[258] W. J. Percival, D. Burkey, A. Heavens, A. Taylor, S. Cole, J. A. Peacock, C. M. Baugh, J. Bland-Hawthorn, T. Bridges, R. Cannon, M. Colless, C. Collins, W. Couch, G. Dalton, R. De Propris, S. P. Driver, G. Efstathiou, R. S. Ellis, C. S. Frenk, K. Glazebrook, C. Jackson, O. Lahav, I. Lewis, S. Lumsden, S. Maddox, P. Norberg, B. A. Peterson, W. Sutherland, and K. Taylor. The 2dF Galaxy Redshift Survey: spherical harmonics analysis of fluctuations in the final catalogue. *MNRAS*, 353:1201–1218, October 2004. doi: 10.1111/j.1365-2966.2004.08146.x.

[259] W. J. Percival, B. A. Reid, D. J. Eisenstein, N. A. Bahcall, T. Budavari, J. A. Frieman, M. Fukugita, J. E. Gunn, Ž. Ivezić, G. R. Knapp, R. G. Kron, J. Loveday, R. H.

Lupton, T. A. McKay, A. Meiksin, R. C. Nichol, A. C. Pope, D. J. Schlegel, D. P. Schneider, D. N. Spergel, C. Stoughton, M. A. Strauss, A. S. Szalay, M. Tegmark, M. S. Vogeley, D. H. Weinberg, D. G. York, and I. Zehavi. Baryon acoustic oscillations in the Sloan Digital Sky Survey Data Release 7 galaxy sample. *MNRAS*, 401: 2148–2168, February 2010. doi: 10.1111/j.1365-2966.2009.15812.x.

[260] L. Pèrenon, F. Piazza, C. Marinoni, and L. Hui. Phenomenology of dark energy: general features of large-scale perturbations. *JCAP*, 11:029, November 2015. doi: 10.1088/1475-7516/2015/11/029.

[261] S. Perlmutter and B. P. Schmidt. Measuring Cosmology with Supernovae. In K. Weiler, editor, *Supernovae and Gamma-Ray Bursters*, volume 598 of *Lecture Notes in Physics, Berlin Springer Verlag*, pages 195–217, 2003.

[262] S. Perlmutter, G. Aldering, G. Goldhaber, R. A. Knop, P. Nugent, P. G. Castro, S. Deustua, S. Fabbro, A. Goobar, D. E. Groom, I. M. Hook, A. G. Kim, M. Y. Kim, J. C. Lee, N. J. Nunes, R. Pain, C. R. Pennypacker, R. Quimby, C. Lidman, R. S. Ellis, M. Irwin, R. G. McMahon, P. Ruiz-Lapuente, N. Walton, B. Schaefer, B. J. Boyle, A. V. Filippenko, T. Matheson, A. S. Fruchter, N. Panagia, H. J. M. Newberg, W. J. Couch, and T. S. C. Project. Measurements of Ω and Λ from 42 High-Redshift Supernovae. *ApJ*, 517:565–586, June 1999. doi: 10.1086/307221.

[263] S. Perlmutter, G. Aldering, G. Goldhaber, R. A. Knop, P. Nugent, P. G. Castro, S. Deustua, S. Fabbro, A. Goobar, D. E. Groom, I. M. Hook, A. G. Kim, M. Y. Kim, J. C. Lee, N. J. Nunes, R. Pain, C. R. Pennypacker, R. Quimby, C. Lidman, R. S. Ellis, M. Irwin, R. G. McMahon, P. Ruiz-Lapuente, N. Walton, B. Schaefer, B. J. Boyle, A. V. Filippenko, T. Matheson, A. S. Fruchter, N. Panagia, H. J. M. Newberg,

W. J. Couch, and T. S. C. Project. Measurements of Ω and Λ from 42 High-Redshift Supernovae. *ApJ*, 517:565–586, June 1999. doi: 10.1086/307221.

[264] J. R. Pier, J. A. Munn, R. B. Hindsley, G. S. Hennessy, S. M. Kent, R. H. Lupton, and Ž. Ivezić. Astrometric Calibration of the Sloan Digital Sky Survey. *AJ*, 125: 1559–1579, March 2003. doi: 10.1086/346138.

[265] J. R. Pier, J. A. Munn, R. B. Hindsley, G. S. Hennessy, S. M. Kent, R. H. Lupton, and Ž. Ivezić. Astrometric Calibration of the Sloan Digital Sky Survey. *AJ*, 125: 1559–1579, March 2003. doi: 10.1086/346138.

[266] Planck Collaboration, P. A. R. Ade, N. Aghanim, C. Armitage-Caplan, M. Arnaud, M. Ashdown, F. Atrio-Barandela, J. Aumont, C. Baccigalupi, A. J. Banday, and et al. Planck 2013 results. XVI. Cosmological parameters. *ArXiv e-prints*, March 2013.

[267] Planck Collaboration, P. A. R. Ade, N. Aghanim, M. I. R. Alves, C. Armitage-Caplan, M. Arnaud, M. Ashdown, F. Atrio-Barandela, J. Aumont, H. Aussel, and et al. Planck 2013 results. I. Overview of products and scientific results. *A&A*, 571: A1, November 2014. doi: 10.1051/0004-6361/201321529.

[268] Planck Collaboration, P. A. R. Ade, N. Aghanim, M. I. R. Alves, C. Armitage-Caplan, M. Arnaud, M. Ashdown, F. Atrio-Barandela, J. Aumont, H. Aussel, and et al. Planck 2013 results. I. Overview of products and scientific results. *A&A*, 571: A1, November 2014. doi: 10.1051/0004-6361/201321529.

[269] Planck Collaboration, P. A. R. Ade, N. Aghanim, F. Argüeso, C. Armitage-Caplan, M. Arnaud, M. Ashdown, F. Atrio-Barandela, J. Aumont, C. Baccigalupi, and et al. Planck 2013 results. XXVIII. The Planck Catalogue of Compact Sources. *A&A*, 571:A28, November 2014. doi: 10.1051/0004-6361/201321524.

[270] Planck Collaboration, P. A. R. Ade, N. Aghanim, C. Armitage-Caplan, M. Arnaud, M. Ashdown, F. Atrio-Barandela, J. Aumont, C. Baccigalupi, A. J. Banday, and et al. Planck 2013 results. XVI. Cosmological parameters. *A&A*, 571:A16, November 2014. doi: 10.1051/0004-6361/201321591.

[271] Planck Collaboration, P. A. R. Ade, N. Aghanim, C. Armitage-Caplan, M. Arnaud, M. Ashdown, F. Atrio-Barandela, J. Aumont, C. Baccigalupi, A. J. Banday, and et al. Planck 2013 results. XVII. Gravitational lensing by large-scale structure. *A&A*, 571: A17, November 2014. doi: 10.1051/0004-6361/201321543.

[272] Planck Collaboration, P. A. R. Ade, N. Aghanim, C. Armitage-Caplan, M. Arnaud, M. Ashdown, F. Atrio-Barandela, J. Aumont, C. Baccigalupi, A. J. Banday, and et al. Planck 2013 results. XV. CMB power spectra and likelihood. *A&A*, 571:A15, November 2014. doi: 10.1051/0004-6361/201321573.

[273] Planck Collaboration, P. A. R. Ade, N. Aghanim, C. Armitage-Caplan, M. Arnaud, M. Ashdown, F. Atrio-Barandela, J. Aumont, C. Baccigalupi, A. J. Banday, and et al. Planck 2013 results. XVI. Cosmological parameters. *A&A*, 571:A16, November 2014. doi: 10.1051/0004-6361/201321591.

[274] Planck Collaboration, P. A. R. Ade, N. Aghanim, C. Armitage-Caplan, M. Arnaud, M. Ashdown, F. Atrio-Barandela, J. Aumont, C. Baccigalupi, A. J. Banday, and et al. Planck 2013 results. XVI. Cosmological parameters. *A&A*, 571:A16, November 2014. doi: 10.1051/0004-6361/201321591.

[275] Planck Collaboration, P. A. R. Ade, N. Aghanim, C. Armitage-Caplan, M. Arnaud, M. Ashdown, F. Atrio-Barandela, J. Aumont, C. Baccigalupi, A. J. Banday, and et al. Planck 2013 results. XV. CMB power spectra and likelihood. *A&A*, 571:A15, November 2014. doi: 10.1051/0004-6361/201321573.

[276] Planck Collaboration, R. Adam, P. A. R. Ade, N. Aghanim, Y. Akrami, M. I. R. Alves, M. Arnaud, F. Arroja, J. Aumont, C. Baccigalupi, and et al. Planck 2015 results. I. Overview of products and scientific results. *ArXiv e-prints*, February 2015.

[277] Planck Collaboration, R. Adam, P. A. R. Ade, N. Aghanim, M. Arnaud, M. Ashdown, J. Aumont, C. Baccigalupi, A. J. Banday, R. B. Barreiro, and et al. Planck 2015 results. IX. Diffuse component separation: CMB maps. *ArXiv e-prints*, February 2015.

[278] Planck Collaboration, P. A. R. Ade, N. Aghanim, M. Arnaud, F. Arroja, M. Ashdown, J. Aumont, C. Baccigalupi, M. Ballardini, A. J. Banday, and et al. Planck 2015 results. XVII. Constraints on primordial non-Gaussianity. *ArXiv e-prints*, February 2015.

[279] Planck Collaboration, P. A. R. Ade, N. Aghanim, M. Arnaud, M. Ashdown, J. Aumont, C. Baccigalupi, A. J. Banday, R. B. Barreiro, R. Barrena, and et al. Planck 2015 results. XXVII. The Second Planck Catalogue of Sunyaev-Zeldovich Sources. *ArXiv e-prints*, February 2015.

[280] Planck Collaboration, P. A. R. Ade, N. Aghanim, M. Arnaud, M. Ashdown, J. Aumont, C. Baccigalupi, A. J. Banday, R. B. Barreiro, J. G. Bartlett, and et al. Planck 2015 results. XIII. Cosmological parameters. *ArXiv e-prints*, February 2015.

[281] Planck Collaboration, P. A. R. Ade, N. Aghanim, M. Arnaud, M. Ashdown, J. Aumont, C. Baccigalupi, A. J. Banday, R. B. Barreiro, J. G. Bartlett, and et al. Planck 2015 results. XV. Gravitational lensing. *ArXiv e-prints*, February 2015.

[282] Planck Collaboration, P. A. R. Ade, N. Aghanim, M. Arnaud, M. Ashdown, J. Aumont, C. Baccigalupi, A. J. Banday, R. B. Barreiro, J. G. Bartlett, and et al. Planck 2015 results. XIII. Cosmological parameters. *ArXiv e-prints*, February 2015.

[283] Planck Collaboration, P. A. R. Ade, N. Aghanim, M. Arnaud, M. Ashdown, J. Aumont, C. Baccigalupi, A. J. Banday, R. B. Barreiro, N. Bartolo, and et al. Planck 2015 results. XIV. Dark energy and modified gravity. *ArXiv e-prints*, February 2015.

[284] Planck Collaboration, P. A. R. Ade, N. Aghanim, M. Arnaud, M. Ashdown, J. Aumont, C. Baccigalupi, A. J. Banday, R. B. Barreiro, N. Bartolo, and et al. Planck 2015 results. XXVIII. The Planck Catalogue of Galactic Cold Clumps. *ArXiv e-prints*, February 2015.

[285] Planck Collaboration, P. A. R. Ade, N. Aghanim, M. Arnaud, M. Ashdown, J. Aumont, C. Baccigalupi, A. J. Banday, R. B. Barreiro, N. Bartolo, and et al. Planck 2015 results. XIV. Dark energy and modified gravity. *ArXiv e-prints*, February 2015.

[286] Planck Collaboration, N. Aghanim, M. Arnaud, M. Ashdown, J. Aumont, C. Baccigalupi, A. J. Banday, R. B. Barreiro, J. G. Bartlett, N. Bartolo, and et al. Planck 2015 results. XXII. A map of the thermal Sunyaev-Zeldovich effect. *ArXiv e-prints*, February 2015.

[287] Planck Collaboration, N. Aghanim, M. Arnaud, M. Ashdown, J. Aumont, C. Baccigalupi, A. J. Banday, R. B. Barreiro, J. G. Bartlett, N. Bartolo, and et al. Planck 2015 results. XI. CMB power spectra, likelihoods, and robustness of parameters. *ArXiv e-prints*, July 2015.

[288] Planck HFI Core Team, P. A. R. Ade, N. Aghanim, R. Ansari, M. Arnaud, M. Ashdown, J. Aumont, A. J. Banday, M. Bartelmann, J. G. Bartlett, E. Battaner, K. Benabed, A. Benoît, J.-P. Bernard, M. Bersanelli, J. J. Bock, J. R. Bond, J. Borrill, F. R. Bouchet, F. Boulanger, T. Bradshaw, M. Bucher, J.-F. Cardoso, G. Castex, A. Catalano, A. Challinor, A. Chamballu, R.-R. Chary, X. Chen, C. Chiang, S. Church, D. L. Clements, J.-M. Colley, S. Colombi, F. Couchot, A. Coulais, C. Cressiot,

B. P. Crill, M. Crook, P. de Bernardis, J. Delabrouille, J.-M. Delouis, F.-X. Désert, K. Dolag, H. Dole, O. Doré, M. Douspis, J. Dunkley, G. Efstathiou, C. Filliard, O. Forni, P. Fosalba, K. Ganga, M. Giard, D. Girard, Y. Giraud-Héraud, R. Gispert, K. M. Górski, S. Gratton, M. Griffin, G. Guyot, J. Haissinski, D. Harrison, G. Helou, S. Henrot-Versillé, C. Hernández-Monteagudo, S. R. Hildebrandt, R. Hills, E. Hivon, M. Hobson, W. A. Holmes, K. M. Huffenberger, A. H. Jaffe, W. C. Jones, J. Kaplan, R. Kneissl, L. Knox, M. Kunz, G. Lagache, J.-M. Lamarre, A. E. Lange, A. Lasenby, A. Lavabre, C. R. Lawrence, M. Le Jeune, C. Leroy, J. Lesgourgues, J. F. Macías-Pérez, C. J. MacTavish, B. Maffei, N. Mandolesi, R. Mann, F. Marleau, D. J. Marshall, S. Masi, T. Matsumura, I. McAuley, P. McGehee, J.-B. Melin, C. Mercier, S. Mitra, M.-A. Miville-Deschênes, A. Moneti, L. Montier, D. Mortlock, A. Murphy, F. Nati, C. B. Netterfield, H. U. Nørgaard-Nielsen, C. North, F. Noviello, D. Novikov, S. Osborne, F. Pajot, G. Patanchon, T. Peacocke, T. J. Pearson, O. Perdereau, L. Perotto, F. Piacentini, M. Piat, S. Plaszczynski, E. Pointecouteau, N. Ponthieu, G. Prézeau, S. Prunet, J.-L. Puget, W. T. Reach, M. Remazeilles, C. Renault, A. Riazuelo, I. Ristorcelli, G. Rocha, C. Rosset, G. Roudier, M. Rowan-Robinson, B. Rusholme, R. Saha, D. Santos, G. Savini, B. M. Schaefer, P. Shellard, L. Spencer, J.-L. Starck, V. Stolyarov, R. Stompor, R. Sudiwala, R. Sunyaev, D. Sutton, J.-F. Sygnet, J. A. Tauber, C. Thum, J.-P. Torre, F. Touze, M. Tristram, F. van Leeuwen, L. Vibert, D. Vibert, L. A. Wade, B. D. Wandelt, S. D. M. White, H. Wiesemeyer, A. Woodcraft, V. Yurchenko, D. Yvon, and A. Zacchei. Planck early results. VI. The High Frequency Instrument data processing. *A&A*, 536:A6, December 2011. doi: 10.1051/0004-6361/201116462.

[289] L. Pogosian and A. Silvestri. Pattern of growth in viable f(R) cosmologies. *Phys. Rev. D*, 77(2):023503, January 2008. doi: 10.1103/PhysRevD.77.023503.

[290] R. V. Pound and G. A. Rebka. Gravitational red-shift in nuclear resonance. *Phys. Rev. Lett.*, 3:439–441, Nov 1959. doi: 10.1103/PhysRevLett.3.439. URL `http://link.aps.org/doi/10.1103/PhysRevLett.3.439`.

[291] A. Pourtsidou, D. Bacon, R. Crittenden, and R. B. Metcalf. Prospects for clustering and lensing measurements with forthcoming intensity mapping and optical surveys. *ArXiv e-prints*, September 2015.

[292] A. R. Pullen and C. M. Hirata. Systematic Effects in Large-Scale Angular Power Spectra of Photometric Quasars and Implications for Constraining Primordial Non-Gaussianity. *Publications of the ASP*, 125:705–718, June 2013. doi: 10.1086/671189.

[293] A. R. Pullen, S. Alam, S. He, and S. Ho. Constraining Gravity at the Largest Scales through CMB Lensing and Galaxy Velocities. *ArXiv e-prints*, November 2015.

[294] A. R. Pullen, S. Alam, and S. Ho. Probing gravity at large scales through CMB lensing. *MNRAS*, 449:4326–4335, June 2015. doi: 10.1093/mnras/stv554.

[295] A. R. Pullen, S. Alam, and S. Ho. Probing gravity at large scales through CMB lensing. *MNRAS*, 449:4326–4335, June 2015. doi: 10.1093/mnras/stv554.

[296] M. Raveri, B. Hu, N. Frusciante, and A. Silvestri. Effective field theory of cosmic acceleration: Constraining dark energy with CMB data. *Phys. Rev. D*, 90(4):043513, August 2014. doi: 10.1103/PhysRevD.90.043513.

[297] A. Refregier. Weak Gravitational Lensing by Large-Scale Structure. *ARA&A*, 41: 645–668, 2003. doi: 10.1146/annurev.astro.41.111302.102207.

[298] B. Reid, S. Ho, N. Padmanabhan, W. J. Percival, J. Tinker, R. Tojeiro, M. White, D. J. Eisenstein, C. Maraston, A. J. Ross, A. G. Sánchez, D. Schlegel, E. Sheldon,

M. A. Strauss, D. Thomas, D. Wake, F. Beutler, D. Bizyaev, A. S. Bolton, J. R. Brownstein, C.-H. Chuang, K. Dawson, P. Harding, F.-S. Kitaura, A. Leauthaud, K. Masters, C. K. McBride, S. More, M. D. Olmstead, D. Oravetz, S. E. Nuza, K. Pan, J. Parejko, J. Pforr, F. Prada, S. Rodríguez-Torres, S. Salazar-Albornoz, L. Samushia, D. P. Schneider, C. G. Scóccola, A. Simmons, and M. Vargas-Magana. SDSS-III Baryon Oscillation Spectroscopic Survey Data Release 12: galaxy target selection and large-scale structure catalogues. *MNRAS*, 455:1553–1573, January 2016. doi: 10.1093/mnras/stv2382.

[299] B. A. Reid and M. White. Towards an accurate model of the redshift-space clustering of haloes in the quasi-linear regime. *MNRAS*, 417:1913–1927, November 2011. doi: 10.1111/j.1365-2966.2011.19379.x.

[300] B. A. Reid, W. J. Percival, D. J. Eisenstein, L. Verde, D. N. Spergel, R. A. Skibba, N. A. Bahcall, T. Budavari, J. A. Frieman, M. Fukugita, J. R. Gott, J. E. Gunn, Ž. Ivezić, G. R. Knapp, R. G. Kron, R. H. Lupton, T. A. McKay, A. Meiksin, R. C. Nichol, A. C. Pope, D. J. Schlegel, D. P. Schneider, C. Stoughton, M. A. Strauss, A. S. Szalay, M. Tegmark, M. S. Vogeley, D. H. Weinberg, D. G. York, and I. Zehavi. Cosmological constraints from the clustering of the Sloan Digital Sky Survey DR7 luminous red galaxies. *MNRAS*, 404:60–85, May 2010. doi: 10.1111/j.1365-2966. 2010.16276.x.

[301] B. A. Reid, L. Samushia, M. White, W. J. Percival, M. Manera, N. Padmanab-han, A. J. Ross, A. G. Sánchez, S. Bailey, D. Bizyaev, A. S. Bolton, H. Brew-ington, J. Brinkmann, J. R. Brownstein, A. J. Cuesta, D. J. Eisenstein, J. E. Gunn, K. Honscheid, E. Malanushenko, V. Malanushenko, C. Maraston, C. K. McBride, D. Muna, R. C. Nichol, D. Oravetz, K. Pan, R. de Putter, N. A. Roe, N. P. Ross, D. J. Schlegel, D. P. Schneider, H.-J. Seo, A. Shelden, E. S. Sheldon, A. Sim-

mons, R. A. Skibba, S. Snedden, M. E. C. Swanson, D. Thomas, J. Tinker, R. To-jeiro, L. Verde, D. A. Wake, B. A. Weaver, D. H. Weinberg, I. Zehavi, and G.-B. Zhao. The clustering of galaxies in the SDSS-III Baryon Oscillation Spectro-scopic Survey: measurements of the growth of structure and expansion rate at z = 0.57 from anisotropic clustering. *MNRAS*, 426:2719–2737, November 2012. doi: 10.1111/j.1365-2966.2012.21779.x.

[302] B. A. Reid, H.-J. Seo, A. Leauthaud, J. L. Tinker, and M. White. A 2.5 per cent measurement of the growth rate from small-scale redshift space clustering of SDSS-III CMASS galaxies. *MNRAS*, 444:476–502, October 2014. doi: 10.1093/mnras/stu1391.

[303] R. Reyes, R. Mandelbaum, U. Seljak, T. Baldauf, J. E. Gunn, L. Lombriser, and R. E. Smith. Confirmation of general relativity on large scales from weak lensing and galaxy velocities. *Nature*, 464:256–258, March 2010. doi: 10.1038/nature08857.

[304] R. Reyes, R. Mandelbaum, U. Seljak, T. Baldauf, J. E. Gunn, L. Lombriser, and R. E. Smith. Confirmation of general relativity on large scales from weak lensing and galaxy velocities. *Nature*, 464:256–258, March 2010. doi: 10.1038/nature08857.

[305] G. T. Richards, X. Fan, H. J. Newberg, M. A. Strauss, D. E. Vanden Berk, D. P. Schneider, B. Yanny, A. Boucher, S. Burles, J. A. Frieman, J. E. Gunn, P. B. Hall, Ž. Ivezić, S. Kent, J. Loveday, R. H. Lupton, C. M. Rockosi, D. J. Schlegel, C. Stoughton, M. SubbaRao, and D. G. York. Spectroscopic Target Selection in the Sloan Digital Sky Survey: The Quasar Sample. *AJ*, 123:2945–2975, June 2002. doi: 10.1086/340187.

[306] A. G. Riess, A. V. Filippenko, P. Challis, A. Clocchiatti, A. Diercks, P. M. Garnavich, R. L. Gilliland, C. J. Hogan, S. Jha, R. P. Kirshner, B. Leibundgut, M. M. Phillips,

D. Reiss, B. P. Schmidt, R. A. Schommer, R. C. Smith, J. Spyromilio, C. Stubbs, N. B. Suntzeff, and J. Tonry. Observational Evidence from Supernovae for an Accelerating Universe and a Cosmological Constant. *AJ*, 116:1009–1038, September 1998. doi: 10.1086/300499.

[307] A. G. Riess, A. V. Filippenko, P. Challis, A. Clocchiatti, A. Diercks, P. M. Garnavich, R. L. Gilliland, C. J. Hogan, S. Jha, R. P. Kirshner, B. Leibundgut, M. M. Phillips, D. Reiss, B. P. Schmidt, R. A. Schommer, R. C. Smith, J. Spyromilio, C. Stubbs, N. B. Suntzeff, and J. Tonry. Observational Evidence from Supernovae for an Accelerating Universe and a Cosmological Constant. *AJ*, 116:1009–1038, September 1998. doi: 10.1086/300499.

[308] A. G. Riess, L. Macri, S. Casertano, H. Lampeitl, H. C. Ferguson, A. V. Filippenko, S. W. Jha, W. Li, and R. Chornock. A 3% Solution: Determination of the Hubble Constant with the Hubble Space Telescope and Wide Field Camera 3. *ApJ*, 730:119, April 2011. doi: 10.1088/0004-637X/730/2/119.

[309] S. A. Rodney, A. G. Riess, L.-G. Strolger, T. Dahlen, O. Graur, S. Casertano, M. E. Dickinson, H. C. Ferguson, P. Garnavich, B. Hayden, S. W. Jha, D. O. Jones, R. P. Kirshner, A. M. Koekemoer, C. McCully, B. Mobasher, B. Patel, B. J. Weiner, S. B. Cenko, K. I. Clubb, M. Cooper, A. V. Filippenko, T. F. Frederiksen, J. Hjorth, B. Leibundgut, T. Matheson, H. Nayyeri, K. Penner, J. Trump, J. M. Silverman, V. U, K. Azalee Bostroem, P. Challis, A. Rajan, S. Wolff, S. M. Faber, N. A. Grogin, and D. Kocevski. Type Ia Supernova Rate Measurements to Redshift 2.5 from CANDELS: Searching for Prompt Explosions in the Early Universe. *AJ*, 148:13, July 2014. doi: 10.1088/0004-6256/148/1/13.

[310] A. J. Ross, S. Ho, A. J. Cuesta, R. Tojeiro, W. J. Percival, D. Wake, K. L. Masters,

R. C. Nichol, A. D. Myers, F. de Simoni, H. J. Seo, C. Hernández-Monteagudo, R. Crittenden, M. Blanton, J. Brinkmann, L. A. N. da Costa, H. Guo, E. Kazin, M. A. G. Maia, C. Maraston, N. Padmanabhan, F. Prada, B. Ramos, A. Sanchez, E. F. Schlafly, D. J. Schlegel, D. P. Schneider, R. Skibba, D. Thomas, B. A. Weaver, M. White, and I. Zehavi. Ameliorating systematic uncertainties in the angular clustering of galaxies: a study using the SDSS-III. *MNRAS*, 417:1350–1373, October 2011. doi: 10.1111/j.1365-2966.2011.19351.x.

[311] A. J. Ross, W. J. Percival, M. Crocce, A. Cabré, and E. Gaztañaga. Measuring redshift-space distortions using photometric surveys. *MNRAS*, 415:2193–2204, August 2011. doi: 10.1111/j.1365-2966.2011.18843.x.

[312] A. J. Ross, W. J. Percival, A. G. Sánchez, L. Samushia, S. Ho, E. Kazin, M. Manera, B. Reid, M. White, R. Tojeiro, C. K. McBride, X. Xu, D. A. Wake, M. A. Strauss, F. Montesano, M. E. C. Swanson, S. Bailey, A. S. Bolton, A. M. Dorta, D. J. Eisenstein, H. Guo, J.-C. Hamilton, R. C. Nichol, N. Padmanabhan, F. Prada, D. J. Schlegel, M. V. Magaña, I. Zehavi, M. Blanton, D. Bizyaev, H. Brewington, A. J. Cuesta, E. Malanushenko, V. Malanushenko, D. Oravetz, J. Parejko, K. Pan, D. P. Schneider, A. Shelden, A. Simmons, S. Snedden, and G.-b. Zhao. The clustering of galaxies in the SDSS-III Baryon Oscillation Spectroscopic Survey: analysis of potential systematics. *MNRAS*, 424:564–590, July 2012. doi: 10.1111/j.1365-2966.2012.21235.x.

[313] A. J. Ross, W. J. Percival, A. G. Sánchez, L. Samushia, S. Ho, E. Kazin, M. Manera, B. Reid, M. White, R. Tojeiro, C. K. McBride, X. Xu, D. A. Wake, M. A. Strauss, F. Montesano, M. E. C. Swanson, S. Bailey, A. S. Bolton, A. M. Dorta, D. J. Eisenstein, H. Guo, J.-C. Hamilton, R. C. Nichol, N. Padmanabhan, F. Prada, D. J. Schlegel, M. V. Magaña, I. Zehavi, M. Blanton, D. Bizyaev, H. Brewing-

ton, A. J. Cuesta, E. Malanushenko, V. Malanushenko, D. Oravetz, J. Parejko, K. Pan, D. P. Schneider, A. Shelden, A. Simmons, S. Snedden, and G.-b. Zhao. The clustering of galaxies in the SDSS-III Baryon Oscillation Spectroscopic Survey: analysis of potential systematics. *MNRAS*, 424:564–590, July 2012. doi: 10.1111/j.1365-2966.2012.21235.x.

[314] A. J. Ross, W. J. Percival, A. G. Sánchez, L. Samushia, S. Ho, E. Kazin, M. Manera, B. Reid, M. White, R. Tojeiro, C. K. McBride, X. Xu, D. A. Wake, M. A. Strauss, F. Montesano, M. E. C. Swanson, S. Bailey, A. S. Bolton, A. M. Dorta, D. J. Eisenstein, H. Guo, J.-C. Hamilton, R. C. Nichol, N. Padmanabhan, F. Prada, D. J. Schlegel, M. V. Magaña, I. Zehavi, M. Blanton, D. Bizyaev, H. Brewington, A. J. Cuesta, E. Malanushenko, V. Malanushenko, D. Oravetz, J. Parejko, K. Pan, D. P. Schneider, A. Shelden, A. Simmons, S. Snedden, and G.-b. Zhao. The clustering of galaxies in the SDSS-III Baryon Oscillation Spectroscopic Survey: analysis of potential systematics. *MNRAS*, 424:564–590, July 2012. doi: 10.1111/j.1365-2966.2012.21235.x.

[315] A. J. Ross, L. Samushia, A. Burden, W. J. Percival, R. Tojeiro, M. Manera, F. Beutler, J. Brinkmann, J. R. Brownstein, A. Carnero, L. A. N. da Costa, D. J. Eisenstein, H. Guo, S. Ho, M. A. G. Maia, F. Montesano, D. Muna, R. C. Nichol, S. E. Nuza, A. G. Sánchez, D. P. Schneider, R. A. Skibba, F. Sobreira, A. Streblyanska, M. E. C. Swanson, D. Thomas, J. L. Tinker, D. A. Wake, I. Zehavi, and G.-b. Zhao. The clustering of galaxies in the SDSS-III DR10 Baryon Oscillation Spectroscopic Survey: no detectable colour dependence of distance scale or growth rate measurements. *MNRAS*, 437:1109–1126, January 2014. doi: 10.1093/mnras/stt1895.

[316] V. C. Rubin and W. K. Ford, Jr. Rotation of the Andromeda Nebula from a

Spectroscopic Survey of Emission Regions. *ApJ*, 159:379, February 1970. doi: 10.1086/150317.

[317] I. Sadeh, L. L. Feng, and O. Lahav. Gravitational Redshift of Galaxies in Clusters from the Sloan Digital Sky Survey and the Baryon Oscillation Spectroscopic Survey. *Physical Review Letters*, 114(7):071103, February 2015. doi: 10.1103/PhysRevLett. 114.071103.

[318] S. Saito, T. Baldauf, Z. Vlah, U. Seljak, T. Okumura, and P. McDonald. Understanding higher-order nonlocal halo bias at large scales by combining the power spectrum with the bispectrum. *Phys. Rev. D*, 90(12):123522, December 2014. doi: 10.1103/PhysRevD.90.123522.

[319] J. Sakstein. Astrophysical Tests of Modified Gravity. *ArXiv e-prints*, February 2015.

[320] L. Samushia, W. J. Percival, L. Guzzo, Y. Wang, A. Cimatti, C. Baugh, J. E. Geach, C. Lacey, E. Majerotto, P. Mukherjee, and A. Orsi. Effects of cosmological model assumptions on galaxy redshift survey measurements. *MNRAS*, 410:1993–2002, January 2011. doi: 10.1111/j.1365-2966.2010.17577.x.

[321] L. Samushia, W. J. Percival, and A. Raccanelli. Interpreting large-scale redshift-space distortion measurements. *MNRAS*, 420:2102–2119, March 2012. doi: 10. 1111/j.1365-2966.2011.20169.x.

[322] L. Samushia, W. J. Percival, and A. Raccanelli. Interpreting large-scale redshift-space distortion measurements. *MNRAS*, 420:2102–2119, March 2012. doi: 10. 1111/j.1365-2966.2011.20169.x.

[323] L. Samushia, W. J. Percival, and A. Raccanelli. Interpreting large-scale redshift-

space distortion measurements. *MNRAS*, 420:2102–2119, March 2012. doi: 10. 1111/j.1365-2966.2011.20169.x.

[324] L. Samushia, B. A. Reid, M. White, W. J. Percival, A. J. Cuesta, L. Lombriser, M. Manera, R. C. Nichol, D. P. Schneider, D. Bizyaev, H. Brewington, E. Malanushenko, V. Malanushenko, D. Oravetz, K. Pan, A. Simmons, A. Shelden, S. Snedden, J. L. Tinker, B. A. Weaver, D. G. York, and G.-B. Zhao. The clustering of galaxies in the SDSS-III DR9 Baryon Oscillation Spectroscopic Survey: testing deviations from Λ and general relativity using anisotropic clustering of galaxies. *MNRAS*, 429:1514–1528, February 2013. doi: 10.1093/mnras/sts443.

[325] L. Samushia, B. A. Reid, M. White, W. J. Percival, A. J. Cuesta, G.-B. Zhao, A. J. Ross, M. Manera, É. Aubourg, F. Beutler, J. Brinkmann, J. R. Brownstein, K. S. Dawson, D. J. Eisenstein, S. Ho, K. Honscheid, C. Maraston, F. Montesano, R. C. Nichol, N. A. Roe, N. P. Ross, A. G. Sánchez, D. J. Schlegel, D. P. Schneider, A. Streblyanska, D. Thomas, J. L. Tinker, D. A. Wake, B. A. Weaver, and I. Zehavi. The clustering of galaxies in the SDSS-III Baryon Oscillation Spectroscopic Survey: measuring growth rate and geometry with anisotropic clustering. *MNRAS*, 439:3504–3519, April 2014. doi: 10.1093/mnras/stu197.

[326] L. Samushia, B. A. Reid, M. White, W. J. Percival, A. J. Cuesta, G.-B. Zhao, A. J. Ross, M. Manera, É. Aubourg, F. Beutler, J. Brinkmann, J. R. Brownstein, K. S. Dawson, D. J. Eisenstein, S. Ho, K. Honscheid, C. Maraston, F. Montesano, R. C. Nichol, N. A. Roe, N. P. Ross, A. G. Sánchez, D. J. Schlegel, D. P. Schneider, A. Streblyanska, D. Thomas, J. L. Tinker, D. A. Wake, B. A. Weaver, and I. Zehavi. The clustering of galaxies in the SDSS-III Baryon Oscillation Spectroscopic Survey: measuring growth rate and geometry with anisotropic clustering. *MNRAS*, 439:3504–3519, April 2014. doi: 10.1093/mnras/stu197.

[327] A. G. Sánchez, E. A. Kazin, F. Beutler, C.-H. Chuang, A. J. Cuesta, D. J. Eisenstein, M. Manera, F. Montesano, R. C. Nichol, N. Padmanabhan, W. Percival, F. Prada, A. J. Ross, D. J. Schlegel, J. Tinker, R. Tojeiro, D. H. Weinberg, X. Xu, J. Brinkmann, J. R. Brownstein, D. P. Schneider, and D. Thomas. The clustering of galaxies in the SDSS-III Baryon Oscillation Spectroscopic Survey: cosmological constraints from the full shape of the clustering wedges. *MNRAS*, 433:1202–1222, August 2013. doi: 10.1093/mnras/stt799.

[328] D. Schlegel, M. White, and D. Eisenstein. The Baryon Oscillation Spectroscopic Survey: Precision measurement of the absolute cosmic distance scale. In *astro2010: The Astronomy and Astrophysics Decadal Survey*, volume 2010 of *Astronomy*, page 314, 2009.

[329] D. J. Schlegel, D. P. Finkbeiner, and M. Davis. Maps of Dust Infrared Emission for Use in Estimation of Reddening and Cosmic Microwave Background Radiation Foregrounds. *ApJ*, 500:525, June 1998. doi: 10.1086/305772.

[330] D. J. Schlegel, D. P. Finkbeiner, and M. Davis. Maps of Dust Infrared Emission for Use in Estimation of Reddening and Cosmic Microwave Background Radiation Foregrounds. *ApJ*, 500:525–553, June 1998. doi: 10.1086/305772.

[331] F. Schmidt, A. Vikhlinin, and W. Hu. Cluster constraints on f(R) gravity. *Phys. Rev. D*, 80(8):083505, October 2009. doi: 10.1103/PhysRevD.80.083505.

[332] F. Schmidt, A. Leauthaud, R. Massey, J. Rhodes, M. R. George, A. M. Koekemoer, A. Finoguenov, and M. Tanaka. A Detection of Weak-lensing Magnification Using Galaxy Sizes and Magnitudes. *ApJL*, 744:L22, January 2012. doi: 10.1088/2041-8205/744/2/L22.

[333] P. Schneider. Weak Gravitational Lensing. *ArXiv Astrophysics e-prints*, September 2005.

[334] P. Schneider. Weak Gravitational Lensing. *ArXiv Astrophysics e-prints*, September 2005.

[335] P. Schuecker. The Muenster Redshift Project: improved methods for automated galaxy redshift measurement from very low-dispersion objective-prism spectra. *MN-RAS*, 279:1057–1070, April 1996. doi: 10.1093/mnras/279.4.1057.

[336] R. Scoccimarro. Redshift-space distortions, pairwise velocities, and nonlinearities. *Phys. Rev. D*, 70(8):083007, October 2004. doi: 10.1103/PhysRevD.70.083007.

[337] R. Scoccimarro, R. K. Sheth, L. Hui, and B. Jain. How Many Galaxies Fit in a Halo? Constraints on Galaxy Formation Efficiency from Spatial Clustering. *ApJ*, 546:20–34, January 2001. doi: 10.1086/318261.

[338] U. Seljak. Analytic model for galaxy and dark matter clustering. *MNRAS*, 318: 203–213, October 2000. doi: 10.1046/j.1365-8711.2000.03715.x.

[339] Jun Shao. Discussion: Jackknife, bootstrap and other resampling methods in regression analysis. *Ann. Statist.*, 14(4):1322–1326, 12 1986. doi: 10.1214/aos/1176350154. URL http://dx.doi.org/10.1214/aos/1176350154.

[340] I. I. Shapiro. Fourth Test of General Relativity. *Physical Review Letters*, 13:789–791, December 1964. doi: 10.1103/PhysRevLett.13.789.

[341] S. A. Shectman, S. D. Landy, A. Oemler, D. L. Tucker, H. Lin, R. P. Kirshner, and P. L. Schechter. The Las Campanas Redshift Survey. *ApJ*, 470:172, October 1996. doi: 10.1086/177858.

[342] E. S. Sheldon, D. E. Johnston, J. A. Frieman, R. Scranton, T. A. McKay, A. J. Connolly, T. Budavári, I. Zehavi, N. A. Bahcall, J. Brinkmann, and M. Fukugita. The Galaxy-Mass Correlation Function Measured from Weak Lensing in the Sloan Digital Sky Survey. *AJ*, 127:2544–2564, May 2004. doi: 10.1086/383293.

[343] R. K. Sheth and G. Tormen. Large-scale bias and the peak background split. *MNRAS*, 308:119–126, September 1999. doi: 10.1046/j.1365-8711.1999.02692.x.

[344] A. Silvestri and M. Trodden. Approaches to understanding cosmic acceleration. *Reports on Progress in Physics*, 72(9):096901, September 2009. doi: 10.1088/0034-4885/72/9/096901.

[345] A. Silvestri, L. Pogosian, and R. V. Buniy. Practical approach to cosmological perturbations in modified gravity. *Phys. Rev. D*, 87(10):104015, May 2013. doi: 10.1103/PhysRevD.87.104015.

[346] F. Simpson, C. Blake, J. A. Peacock, I. K. Baldry, J. Bland-Hawthorn, A. F. Heavens, C. Heymans, J. Loveday, and P. Norberg. Galaxy and mass assembly: Redshift space distortions from the clipped galaxy field. *Phys. Rev. D*, 93(2):023525, January 2016. doi: 10.1103/PhysRevD.93.023525.

[347] S. Singh, R. Mandelbaum, and S. More. Intrinsic alignments of SDSS-III BOSS LOWZ sample galaxies. *MNRAS*, 450:2195–2216, June 2015. doi: 10.1093/mnras/stv778.

[348] R. Skibba, R. K. Sheth, A. J. Connolly, and R. Scranton. The luminosity-weighted or 'marked' correlation function. *MNRAS*, 369:68–76, June 2006. doi: 10.1111/j.1365-2966.2006.10196.x.

[349] S. A. Smee, J. E. Gunn, A. Uomoto, N. Roe, D. Schlegel, C. M. Rockosi, M. A.

Carr, F. Leger, K. S. Dawson, M. D. Olmstead, J. Brinkmann, R. Owen, R. H. Bark-houser, K. Honscheid, P. Harding, D. Long, R. H. Lupton, C. Loomis, L. Anderson, J. Annis, M. Bernardi, V. Bhardwaj, D. Bizyaev, A. S. Bolton, H. Brewington, J. W. Briggs, S. Burles, J. G. Burns, F. J. Castander, A. Connolly, J. R. A. Davenport, G. Ebelke, H. Epps, P. D. Feldman, S. D. Friedman, J. Frieman, T. Heckman, C. L. Hull, G. R. Knapp, D. M. Lawrence, J. Loveday, E. J. Mannery, E. Malanushenko, V. Malanushenko, A. J. Merrelli, D. Muna, P. R. Newman, R. C. Nichol, D. Oravetz, K. Pan, A. C. Pope, P. G. Ricketts, A. Shelden, D. Sandford, W. Siegmund, A. Simmons, D. S. Smith, S. Snedden, D. P. Schneider, M. SubbaRao, C. Tremonti, P. Waddell, and D. G. York. The Multi-object, Fiber-fed Spectrographs for the Sloan Digital Sky Survey and the Baryon Oscillation Spectroscopic Survey. *AJ*, 146:32, August 2013. doi: 10.1088/0004-6256/146/2/32.

[350] S. A. Smee, J. E. Gunn, A. Uomoto, N. Roe, D. Schlegel, C. M. Rockosi, M. A. Carr, F. Leger, K. S. Dawson, M. D. Olmstead, J. Brinkmann, R. Owen, R. H. Bark-houser, K. Honscheid, P. Harding, D. Long, R. H. Lupton, C. Loomis, L. Anderson, J. Annis, M. Bernardi, V. Bhardwaj, D. Bizyaev, A. S. Bolton, H. Brewington, J. W. Briggs, S. Burles, J. G. Burns, F. J. Castander, A. Connolly, J. R. A. Davenport, G. Ebelke, H. Epps, P. D. Feldman, S. D. Friedman, J. Frieman, T. Heckman, C. L. Hull, G. R. Knapp, D. M. Lawrence, J. Loveday, E. J. Mannery, E. Malanushenko, V. Malanushenko, A. J. Merrelli, D. Muna, P. R. Newman, R. C. Nichol, D. Oravetz, K. Pan, A. C. Pope, P. G. Ricketts, A. Shelden, D. Sandford, W. Siegmund, A. Simmons, D. S. Smith, S. Snedden, D. P. Schneider, M. SubbaRao, C. Tremonti, P. Waddell, and D. G. York. The Multi-object, Fiber-fed Spectrographs for the Sloan Digital Sky Survey and the Baryon Oscillation Spectroscopic Survey. *AJ*, 146:32, August 2013. doi: 10.1088/0004-6256/146/2/32.

[351] J. A. Smith, D. L. Tucker, S. S. Allam, and A. M. Jorgensen. Southern Standard Stars for the u'g'r'i'z' System. In *American Astronomical Society Meeting Abstracts*, volume 34 of *Bulletin of the American Astronomical Society*, page #104.08, December 2002.

[352] J. A. Smith, D. L. Tucker, S. Kent, M. W. Richmond, M. Fukugita, T. Ichikawa, S.-i. Ichikawa, A. M. Jorgensen, A. Uomoto, J. E. Gunn, M. Hamabe, M. Watanabe, A. Tolea, A. Henden, J. Annis, J. R. Pier, T. A. McKay, J. Brinkmann, B. Chen, J. Holtzman, K. Shimasaku, and D. G. York. The u'g'r'i'z' Standard-Star System. *AJ*, 123:2121–2144, April 2002. doi: 10.1086/339311.

[353] K. M. Smith, O. Zahn, and O. Doré. Detection of gravitational lensing in the cosmic microwave background. *Phys. Rev. D*, 76(4):043510, August 2007. doi: 10.1103/ PhysRevD.76.043510.

[354] Y.-S. Song, W. Hu, and I. Sawicki. Large scale structure of f(R) gravity. *Phys. Rev. D*, 75(4):044004, February 2007. doi: 10.1103/PhysRevD.75.044004.

[355] Y.-S. Song, W. Hu, and I. Sawicki. Large scale structure of f(R) gravity. *Phys. Rev. D*, 75(4):044004, February 2007. doi: 10.1103/PhysRevD.75.044004.

[356] D. Spergel, N. Gehrels, J. Breckinridge, M. Donahue, A. Dressler, B. S. Gaudi, T. Greene, O. Guyon, C. Hirata, and et al. Wide-Field InfraRed Survey Telescope-Astrophysics Focused Telescope Assets WFIRST-AFTA Final Report. *ArXiv e-prints (1305.5422)*, May 2013.

[357] D. Spergel, N. Gehrels, J. Breckinridge, M. Donahue, A. Dressler, B. S. Gaudi, T. Greene, O. Guyon, C. Hirata, J. Kalirai, N. J. Kasdin, W. Moos, S. Perlmutter, M. Postman, B. Rauscher, J. Rhodes, Y. Wang, D. Weinberg, J. Centrella, W. Traub,

C. Baltay, J. Colbert, D. Bennett, A. Kiessling, B. Macintosh, J. Merten, M. Morton-son, M. Penny, E. Rozo, D. Savransky, K. Stapelfeldt, Y. Zu, C. Baker, E. Cheng, D. Content, J. Dooley, M. Foote, R. Goullioud, K. Grady, C. Jackson, J. Kruk, M. Levine, M. Melton, C. Peddie, J. Ruffa, and S. Shaklan. WFIRST-2.4: What Every Astronomer Should Know. *ArXiv e-prints*, May 2013.

[358] D. N. Spergel, R. Bean, O. Doré, M. R. Nolta, C. L. Bennett, J. Dunkley, G. Hin-shaw, N. Jarosik, E. Komatsu, L. Page, H. V. Peiris, L. Verde, M. Halpern, R. S. Hill, A. Kogut, M. Limon, S. S. Meyer, N. Odegard, G. S. Tucker, J. L. Weiland, E. Wollack, and E. L. Wright. Three-Year Wilkinson Microwave Anisotropy Probe (WMAP) Observations: Implications for Cosmology. *ApJ Suppl.*, 170:377–408, June 2007. doi: 10.1086/513700.

[359] V. Springel. The cosmological simulation code GADGET-2. *MNRAS*, 364:1105–1134, December 2005. doi: 10.1111/j.1365-2966.2005.09655.x.

[360] V. Springel, N. Yoshida, and S. D. M. White. GADGET: a code for collisionless and gasdynamical cosmological simulations. *New Astronomy*, 6:79–117, April 2001. doi: 10.1016/S1384-1076(01)00042-2.

[361] K. T. Story, D. Hanson, P. A. R. Ade, K. A. Aird, J. E. Austermann, J. A. Beall, A. N. Bender, B. A. Benson, L. E. Bleem, J. E. Carlstrom, C. L. Chang, H. C. Chi-ang, H.-M. Cho, R. Citron, T. M. Crawford, A. T. Crites, T. de Haan, M. A. Dobbs, W. Everett, J. Gallicchio, J. Gao, E. M. George, A. Gilbert, N. W. Halverson, N. Har-rington, J. W. Henning, G. C. Hilton, G. P. Holder, W. L. Holzapfel, S. Hoover, Z. Hou, J. D. Hrubes, N. Huang, J. Hubmayr, K. D. Irwin, R. Keisler, L. Knox, A. T. Lee, E. M. Leitch, D. Li, C. Liang, D. Luong-Van, J. J. McMahon, J. Mehl, S. S. Meyer, L. Mocanu, T. E. Montroy, T. Natoli, J. P. Nibarger, V. Novosad, S. Padin,

C. Pryke, C. L. Reichardt, J. E. Ruhl, B. R. Saliwanchik, J. T. Sayre, K. K. Schaffer, G. Smecher, A. A. Stark, C. Tucker, K. Vanderlinde, J. D. Vieira, G. Wang, N. Whitehorn, V. Yefremenko, and O. Zahn. A Measurement of the Cosmic Microwave Background Gravitational Lensing Potential from 100 Square Degrees of SPTpol Data. *ApJ*, 810:50, September 2015. doi: 10.1088/0004-637X/810/1/50.

[362] M. A. Strauss, D. H. Weinberg, R. H. Lupton, V. K. Narayanan, J. Annis, M. Bernardi, M. Blanton, S. Burles, A. J. Connolly, J. Dalcanton, M. Doi, D. Eisenstein, J. A. Frieman, M. Fukugita, J. E. Gunn, Ž. Ivezić, S. Kent, R. S. J. Kim, G. R. Knapp, R. G. Kron, J. A. Munn, H. J. Newberg, R. C. Nichol, S. Okamura, T. R. Quinn, M. W. Richmond, D. J. Schlegel, K. Shimasaku, M. SubbaRao, A. S. Szalay, D. Vanden Berk, M. S. Vogeley, B. Yanny, N. Yasuda, D. G. York, and I. Zehavi. Spectroscopic Target Selection in the Sloan Digital Sky Survey: The Main Galaxy Sample. *AJ*, 124:1810–1824, September 2002. doi: 10.1086/342343.

[363] M. Sullivan, J. Guy, A. Conley, N. Regnault, P. Astier, C. Balland, S. Basa, R. G. Carlberg, D. Fouchez, D. Hardin, I. M. Hook, D. A. Howell, R. Pain, N. Palanque-Delabrouille, K. M. Perrett, C. J. Pritchet, J. Rich, V. Ruhlmann-Kleider, D. Balam, S. Baumont, R. S. Ellis, S. Fabbro, H. K. Fakhouri, N. Fourmanoit, S. González-Gaitán, M. L. Graham, M. J. Hudson, E. Hsiao, T. Kronborg, C. Lidman, A. M. Mourao, J. D. Neill, S. Perlmutter, P. Ripoche, N. Suzuki, and E. S. Walker. SNLS3: Constraints on Dark Energy Combining the Supernova Legacy Survey Three-year Data with Other Probes. *ApJ*, 737:102, August 2011. doi: 10.1088/0004-637X/737/2/102.

[364] R. A. Sunyaev and I. B. Zeldovich. Microwave background radiation as a probe of the contemporary structure and history of the universe. *ARA&A*, 18:537–560, 1980. doi: 10.1146/annurev.aa.18.090180.002541.

[365] N. Suzuki, D. Rubin, C. Lidman, G. Aldering, R. Amanullah, K. Barbary, L. F. Barrientos, J. Botyanszki, M. Brodwin, N. Connolly, K. S. Dawson, A. Dey, M. Doi, M. Donahue, S. Deustua, P. Eisenhardt, E. Ellingson, L. Faccioli, V. Fadeyev, H. K. Fakhouri, A. S. Fruchter, D. G. Gilbank, M. D. Gladders, G. Goldhaber, A. H. Gonzalez, A. Goobar, A. Gude, T. Hattori, H. Hoekstra, E. Hsiao, X. Huang, Y. Ihara, M. J. Jee, D. Johnston, N. Kashikawa, B. Koester, K. Konishi, M. Kowalski, E. V. Linder, L. Lubin, J. Melbourne, J. Meyers, T. Morokuma, F. Munshi, C. Mullis, T. Oda, N. Panagia, S. Perlmutter, M. Postman, T. Pritchard, J. Rhodes, P. Ripoche, P. Rosati, D. J. Schlegel, A. Spadafora, S. A. Stanford, V. Stanishev, D. Stern, M. Strovink, N. Takanashi, K. Tokita, M. Wagner, L. Wang, N. Yasuda, H. K. C. Yee, and T. Supernova Cosmology Project. The Hubble Space Telescope Cluster Supernova Survey. V. Improving the Dark-energy Constraints above $z > 1$ and Building an Early-type-hosted Supernova Sample. *ApJ*, 746:85, February 2012. doi: 10.1088/0004-637X/746/1/85.

[366] M. Takada. Subaru Hyper Suprime-Cam Project. In N. Kawai and S. Nagataki, editors, *American Institute of Physics Conference Series*, volume 1279 of *American Institute of Physics Conference Series*, pages 120–127, October 2010. doi: 10.1063/1.3509247.

[367] M. Takada, R. S. Ellis, M. Chiba, J. E. Greene, H. Aihara, N. Arimoto, K. Bundy, J. Cohen, O. Doré, G. Graves, J. E. Gunn, T. Heckman, C. M. Hirata, P. Ho, J.-P. Kneib, O. L. Fèvre, L. Lin, S. More, H. Murayama, T. Nagao, M. Ouchi, M. Seiffert, J. D. Silverman, L. Sodré, D. N. Spergel, M. A. Strauss, H. Sugai, Y. Suto, H. Takami, and R. Wyse. Extragalactic science, cosmology, and Galactic archaeology with the Subaru Prime Focus Spectrograph. *Publications of the ASJ*, 66:R1, February 2014. doi: 10.1093/pasj/pst019.

[368] Y. Takeda and S. Ueno. Detection of Gravitational Redshift on the Solar Disk by Using Iodine-Cell Technique. *Solar Physics*, 281:551–575, December 2012. doi: 10.1007/s11207-012-0068-8.

[369] P. Teerikorpi. Observational Selection Bias Affecting the Determination of the Extragalactic Distance Scale. *ARA&A*, 35:101–136, 1997. doi: 10.1146/annurev.astro. 35.1.101.

[370] M. Tegmark. How to measure CMB power spectra without losing information. *Phys. Rev. D*, 55:5895–5907, May 1997. doi: 10.1103/PhysRevD.55.5895.

[371] The Dark Energy Survey Collaboration. The Dark Energy Survey. *ArXiv Astrophysics e-prints*, October 2005.

[372] The Planck Collaboration. The Scientific Programme of Planck. *ArXiv Astrophysics e-prints*, April 2006.

[373] J. Tinker, S. Alam, and S. Ho. Nseries Challenege mock for BOSS RSD blind challenge. *xxxx*, page xx, 2016.

[374] R. Tojeiro, A. J. Ross, A. Burden, L. Samushia, M. Manera, W. J. Percival, F. Beutler, J. Brinkmann, J. R. Brownstein, A. J. Cuesta, K. Dawson, D. J. Eisenstein, S. Ho, C. Howlett, C. K. McBride, F. Montesano, M. D. Olmstead, J. K. Parejko, B. Reid, A. G. Sánchez, D. J. Schlegel, D. P. Schneider, J. L. Tinker, M. V. Magaña, and M. White. The clustering of galaxies in the SDSS-III Baryon Oscillation Spectroscopic Survey: galaxy clustering measurements in the low-redshift sample of Data Release 11. *MNRAS*, 440:2222–2237, May 2014. doi: 10.1093/mnras/stu371.

[375] M. A. Troxel and M. Ishak. The intrinsic alignment of galaxies and its impact on

weak gravitational lensing in an era of precision cosmology. *Physics Reports*, 558: 1–59, February 2015. doi: 10.1016/j.physrep.2014.11.001.

[376] S. Tsujikawa. Matter density perturbations and effective gravitational constant in modified gravity models of dark energy. *Phys. Rev. D*, 76(2):023514, July 2007. doi: 10.1103/PhysRevD.76.023514.

[377] W. G. Unruh. Time Gravity and Quantum Mechanics. *ArXiv General Relativity and Quantum Cosmology e-prints*, December 1993.

[378] F. C. van den Bosch, S. More, M. Cacciato, H. Mo, and X. Yang. Cosmological constraints from a combination of galaxy clustering and lensing - I. Theoretical framework. *MNRAS*, 430:725–746, April 2013. doi: 10.1093/mnras/sts006.

[379] A. van Engelen, S. Bhattacharya, N. Sehgal, G. P. Holder, O. Zahn, and D. Nagai. CMB Lensing Power Spectrum Biases from Galaxies and Clusters Using High-angular Resolution Temperature Maps. *ApJ*, 786:13, May 2014. doi: 10.1088/0004-637X/786/1/13.

[380] M. Vargas Magaña, S. Ho, X. Xu, A. G. Sánchez, R. O'Connell, D. J. Eisenstein, A. J. Cuesta, W. J. Percival, A. J. Ross, E. Aubourg, S. E. D. Kirkby, M. Manera, D. P. Schneider, J. L. Tinker, and B. A. Weaver. SDSS-III Baryon Oscillation Spectroscopic Survey: Analysis of Potential Systematics in Fitting of Baryon Acoustic Feature. *ArXiv e-prints*, December 2013.

[381] M. Vargas-Magaña, S. Ho, S. Fromenteau, and A. J. Cuesta. The clustering of galaxies in the SDSS-III Baryon Oscillation Spectroscopic Survey: Effect of smoothing of density field on reconstruction and anisotropic BAO analysis. *ArXiv e-prints*, September 2015.

[382] M. Velander, E. van Uitert, H. Hoekstra, J. Coupon, T. Erben, C. Heymans, H. Hilde-brandt, T. D. Kitching, Y. Mellier, L. Miller, L. Van Waerbeke, C. Bonnett, L. Fu, S. Giodini, M. J. Hudson, K. Kuijken, B. Rowe, T. Schrabback, and E. Semboloni. CFHTLenS: the relation between galaxy dark matter haloes and baryons from weak gravitational lensing. *MNRAS*, 437:2111–2136, January 2014. doi: 10.1093/mnras/stt2013.

[383] E. Visbal and A. Loeb. Measuring the 3D clustering of undetected galaxies through cross correlation of their cumulative flux fluctuations from multiple spectral lines. *JCAP*, 11:016, November 2010. doi: 10.1088/1475-7516/2010/11/016.

[384] Z. Vlah, U. Seljak, and T. Baldauf. Lagrangian perturbation theory at one loop order: Successes, failures, and improvements. *Phys. Rev. D*, 91(2):023508, January 2015. doi: 10.1103/PhysRevD.91.023508.

[385] L. Wang and P. J. Steinhardt. Cluster Abundance Constraints for Cosmological Models with a Time-varying, Spatially Inhomogeneous Energy Component with Negative Pressure. *ApJ*, 508:483–490, December 1998. doi: 10.1086/306436.

[386] L. Wang, B. Reid, and M. White. An analytic model for redshift-space distortions. *MNRAS*, 437:588–599, January 2014. doi: 10.1093/mnras/stt1916.

[387] D. H. Weinberg, M. J. Mortonson, D. J. Eisenstein, C. Hirata, A. G. Riess, and E. Rozo. Observational probes of cosmic acceleration. *Physics Reports*, 530:87–255, September 2013. doi: 10.1016/j.physrep.2013.05.001.

[388] S. Weinberg. The cosmological constant problem. *Reviews of Modern Physics*, 61:1–23, January 1989. doi: 10.1103/RevModPhys.61.1.

[389] J. M. Weisberg, J. H. Taylor, and L. A. Fowler. Gravitational waves from an

orbiting pulsar. *Scientific American*, 245:74–82, October 1981. doi: 10.1038/ scientificamerican1081-74.

[390] M. White. The Zel'dovich approximation. *MNRAS*, 439:3630–3640, April 2014. doi: 10.1093/mnras/stu209.

[391] M. White. ZeldovichRecon: Halo correlation function using the Zeldovich approximation. Astrophysics Source Code Library, December 2015.

[392] M. White. Reconstruction within the Zeldovich approximation. *MNRAS*, 450:3822–3828, July 2015. doi: 10.1093/mnras/stv842.

[393] M. White, L. Hernquist, and V. Springel. The Halo Model and Numerical Simulations. *ApJL*, 550:L129–L132, April 2001. doi: 10.1086/319644.

[394] M. White, L. Hernquist, and V. Springel. Simulating the Sunyaev-Zeldovich Effect(s): Including Radiative Cooling and Energy Injection by Galactic Winds. *ApJ*, 579:16–22, November 2002. doi: 10.1086/342756.

[395] M. White, M. Blanton, A. Bolton, D. Schlegel, J. Tinker, A. Berlind, L. da Costa, E. Kazin, Y.-T. Lin, M. Maia, C. K. McBride, N. Padmanabhan, J. Parejko, W. Percival, F. Prada, B. Ramos, E. Sheldon, F. de Simoni, R. Skibba, D. Thomas, D. Wake, I. Zehavi, Z. Zheng, R. Nichol, D. P. Schneider, M. A. Strauss, B. A. Weaver, and D. H. Weinberg. The Clustering of Massive Galaxies at z ˜ 0.5 from the First Semester of BOSS Data. *ApJ*, 728:126, February 2011. doi: 10.1088/0004-637X/728/2/126.

[396] M. White, A. D. Myers, N. P. Ross, D. J. Schlegel, J. F. Hennawi, Y. Shen, I. Mc-Greer, M. A. Strauss, A. S. Bolton, J. Bovy, X. Fan, J. Miralda-Escude, N. Palanque-Delabrouille, I. Paris, P. Petitjean, D. P. Schneider, M. Viel, D. H. Weinberg,

C. Yeche, I. Zehavi, K. Pan, S. Snedden, D. Bizyaev, H. Brewington, J. Brinkmann, V. Malanushenko, E. Malanushenko, D. Oravetz, A. Simmons, A. Sheldon, and B. A. Weaver. The clustering of intermediate-redshift quasars as measured by the Baryon Oscillation Spectroscopic Survey. *MNRAS*, 424:933–950, August 2012. doi: 10.1111/j.1365-2966.2012.21251.x.

[397] M. White, J. L. Tinker, and C. K. McBride. Mock galaxy catalogues using the quick particle mesh method. *MNRAS*, 437:2594–2606, January 2014. doi: 10.1093/mnras/stt2071.

[398] M. White, B. Reid, C.-H. Chuang, J. L. Tinker, C. K. McBride, F. Prada, and L. Samushia. Tests of redshift-space distortions models in configuration space for the analysis of the BOSS final data release. *MNRAS*, 447:234–245, February 2015. doi: 10.1093/mnras/stu2460.

[399] R. Wojtak, S. H. Hansen, and J. Hjorth. Gravitational redshift of galaxies in clusters as predicted by general relativity. *Nature*, 477:567–569, September 2011. doi: 10.1038/nature10445.

[400] L. Xu. Constraints on f (R) gravity through the redshift space distortion. *Phys. Rev. D*, 91(6):063008, March 2015. doi: 10.1103/PhysRevD.91.063008.

[401] Lixin Xu. Constraints on $f(r)$ gravity through the redshift space distortion. *Phys. Rev. D*, 91:063008, Mar 2015. doi: 10.1103/PhysRevD.91.063008. URL `http://link.aps.org/doi/10.1103/PhysRevD.91.063008`.

[402] J. Yoo. Relativistic effect in galaxy clustering. *Classical and Quantum Gravity*, 31 (23):234001, December 2014. doi: 10.1088/0264-9381/31/23/234001.

[403] J. Yoo and U. Seljak. Wide-angle effects in future galaxy surveys. *MNRAS*, 447: 1789–1805, February 2015. doi: 10.1093/mnras/stu2491.

[404] J. Yoo and M. Zaldarriaga. Beyond the linear-order relativistic effect in galaxy clustering: Second-order gauge-invariant formalism. *Phys. Rev. D*, 90(2):023513, July 2014. doi: 10.1103/PhysRevD.90.023513.

[405] J. Yoo, A. L. Fitzpatrick, and M. Zaldarriaga. New perspective on galaxy clustering as a cosmological probe: General relativistic effects. *Phys. Rev. D*, 80(8):083514, October 2009. doi: 10.1103/PhysRevD.80.083514.

[406] J. Yoo, N. Hamaus, U. Seljak, and M. Zaldarriaga. Going beyond the Kaiser redshift-space distortion formula: A full general relativistic account of the effects and their detectability in galaxy clustering. *Phys. Rev. D*, 86(6):063514, September 2012. doi: 10.1103/PhysRevD.86.063514.

[407] D. G. York, J. Adelman, J. E. Anderson, Jr., S. F. Anderson, J. Annis, N. A. Bahcall, J. A. Bakken, R. Barkhouser, S. Bastian, E. Berman, W. N. Boroski, S. Bracker, C. Briegel, J. W. Briggs, J. Brinkmann, R. Brunner, S. Burles, L. Carey, M. A. Carr, F. J. Castander, B. Chen, P. L. Colestock, A. J. Connolly, J. H. Crocker, I. Csabai, P. C. Czarapata, J. E. Davis, M. Doi, T. Dombeck, D. Eisenstein, N. Ellman, B. R. Elms, M. L. Evans, X. Fan, G. R. Federwitz, L. Fiscelli, S. Friedman, J. A. Frieman, M. Fukugita, B. Gillespie, J. E. Gunn, V. K. Gurbani, E. de Haas, M. Haldeman, F. H. Harris, J. Hayes, T. M. Heckman, G. S. Hennessy, R. B. Hindsley, S. Holm, D. J. Holmgren, C.-h. Huang, C. Hull, D. Husby, S.-I. Ichikawa, T. Ichikawa, Ž. Ivezić, S. Kent, R. S. J. Kim, E. Kinney, M. Klaene, A. N. Kleinman, S. Kleinman, G. R. Knapp, J. Korienek, R. G. Kron, P. Z. Kunszt, D. Q. Lamb, B. Lee, R. F. Leger, S. Limmongkol, C. Lindenmeyer, D. C. Long, C. Loomis,

J. Loveday, R. Lucinio, R. H. Lupton, B. MacKinnon, E. J. Mannery, P. M. Mantsch, B. Margon, P. McGehee, T. A. McKay, A. Meiksin, A. Merelli, D. G. Monet, J. A. Munn, V. K. Narayanan, T. Nash, E. Neilsen, R. Neswold, H. J. Newberg, R. C. Nichol, T. Nicinski, M. Nonino, N. Okada, S. Okamura, J. P. Ostriker, R. Owen, A. G. Pauls, J. Peoples, R. L. Peterson, D. Petravick, J. R. Pier, A. Pope, R. Pordes, A. Prosapio, R. Rechenmacher, T. R. Quinn, G. T. Richards, M. W. Richmond, C. H. Rivetta, C. M. Rockosi, K. Ruthmansdorfer, D. Sandford, D. J. Schlegel, D. P. Schneider, M. Sekiguchi, G. Sergey, K. Shimasaku, W. A. Siegmund, S. Smee, J. A. Smith, S. Snedden, R. Stone, C. Stoughton, M. A. Strauss, C. Stubbs, M. SubbaRao, A. S. Szalay, I. Szapudi, G. P. Szokoly, A. R. Thakar, C. Tremonti, D. L. Tucker, A. Uomoto, D. Vanden Berk, M. S. Vogeley, P. Waddell, S.-i. Wang, M. Watanabe, D. H. Weinberg, B. Yanny, N. Yasuda, and SDSS Collaboration. The Sloan Digital Sky Survey: Technical Summary. *AJ*, 120:1579–1587, September 2000. doi: 10.1086/301513.

[408] D. G. York, J. Adelman, J. E. Anderson, Jr., S. F. Anderson, J. Annis, N. A. Bahcall, J. A. Bakken, R. Barkhouser, S. Bastian, E. Berman, W. N. Boroski, S. Bracker, C. Briegel, J. W. Briggs, J. Brinkmann, R. Brunner, S. Burles, L. Carey, M. A. Carr, F. J. Castander, B. Chen, P. L. Colestock, A. J. Connolly, J. H. Crocker, I. Csabai, P. C. Czarapata, J. E. Davis, M. Doi, T. Dombeck, D. Eisenstein, N. Ellman, B. R. Elms, M. L. Evans, X. Fan, G. R. Federwitz, L. Fiscelli, S. Friedman, J. A. Frieman, M. Fukugita, B. Gillespie, J. E. Gunn, V. K. Gurbani, E. de Haas, M. Haldeman, F. H. Harris, J. Hayes, T. M. Heckman, G. S. Hennessy, R. B. Hindsley, S. Holm, D. J. Holmgren, C.-h. Huang, C. Hull, D. Husby, S.-I. Ichikawa, T. Ichikawa, Ž. Ivezić, S. Kent, R. S. J. Kim, E. Kinney, M. Klaene, A. N. Kleinman, S. Kleinman, G. R. Knapp, J. Korienek, R. G. Kron, P. Z. Kunszt, D. Q. Lamb,

B. Lee, R. F. Leger, S. Limmongkol, C. Lindenmeyer, D. C. Long, C. Loomis, J. Loveday, R. Lucinio, R. H. Lupton, B. MacKinnon, E. J. Mannery, P. M. Mantsch, B. Margon, P. McGehee, T. A. McKay, A. Meiksin, A. Merelli, D. G. Monet, J. A. Munn, V. K. Narayanan, T. Nash, E. Neilsen, R. Neswold, H. J. Newberg, R. C. Nichol, T. Nicinski, M. Nonino, N. Okada, S. Okamura, J. P. Ostriker, R. Owen, A. G. Pauls, J. Peoples, R. L. Peterson, D. Petravick, J. R. Pier, A. Pope, R. Pordes, A. Prosapio, R. Rechenmacher, T. R. Quinn, G. T. Richards, M. W. Richmond, C. H. Rivetta, C. M. Rockosi, K. Ruthmansdorfer, D. Sandford, D. J. Schlegel, D. P. Schneider, M. Sekiguchi, G. Sergey, K. Shimasaku, W. A. Siegmund, S. Smee, J. A. Smith, S. Snedden, R. Stone, C. Stoughton, M. A. Strauss, C. Stubbs, M. SubbaRao, A. S. Szalay, I. Szapudi, G. P. Szokoly, A. R. Thakar, C. Tremonti, D. L. Tucker, A. Uomoto, D. Vanden Berk, M. S. Vogeley, P. Waddell, S.-i. Wang, M. Watanabe, D. H. Weinberg, B. Yanny, N. Yasuda, and SDSS Collaboration. The Sloan Digital Sky Survey: Technical Summary. *AJ*, 120:1579–1587, September 2000. doi: 10.1086/301513.

[409] P. Zhang, M. Liguori, R. Bean, and S. Dodelson. Probing Gravity at Cosmological Scales by Measurements which Test the Relationship between Gravitational Lensing and Matter Overdensity. *Physical Review Letters*, 99(14):141302, October 2007. doi: 10.1103/PhysRevLett.99.141302.

[410] P. Zhang, M. Liguori, R. Bean, and S. Dodelson. Probing Gravity at Cosmological Scales by Measurements which Test the Relationship between Gravitational Lensing and Matter Overdensity. *Physical Review Letters*, 99(14):141302, October 2007. doi: 10.1103/PhysRevLett.99.141302.

[411] G.-B. Zhao, L. Pogosian, A. Silvestri, and J. Zylberberg. Searching for modified

growth patterns with tomographic surveys. *Phys. Rev. D*, 79(8):083513, April 2009. doi: 10.1103/PhysRevD.79.083513.

[412] H. Zhao, J. A. Peacock, and B. Li. Testing gravity theories via transverse Doppler and gravitational redshifts in galaxy clusters. *Phys. Rev. D*, 88(4):043013, August 2013. doi: 10.1103/PhysRevD.88.043013.

[413] H. Zhu, S. Alam, R. A. C. Croft, S. Ho, and Giusarma E. GZHydro. *xxx*, pages xx–xx, 2016. doi: xxxx.

[414] H. Zhu, S. Alam, R. A. C. Croft, S. Ho, and Giusarma E. GZNbody . *xxx*, pages xx–xx, 2016. doi: xxxx.

[415] Y. Zu and R. Mandelbaum. Mapping stellar content to dark matter haloes using galaxy clustering and galaxy-galaxy lensing in the SDSS DR7. *MNRAS*, 454:1161–1191, December 2015. doi: 10.1093/mnras/stv2062.

[416] Y. Zu and D. H. Weinberg. The redshift-space cluster-galaxy cross-correlation function - I. Modelling galaxy infall on to Millennium simulation clusters and SDSS groups. *MNRAS*, 431:3319–3337, June 2013. doi: 10.1093/mnras/stt411.

[417] F. Zwicky. On the Masses of Nebulae and of Clusters of Nebulae. *ApJ*, 86:217, October 1937. doi: 10.1086/143864.